Diagnostic Methods for the Characterization of a Helicon Plasma Thruster

by

Mick Wijnen

A dissertation submitted by in partial fulfillment of the requirements for the degree of Doctor of Philosophy in

Fluid Mechanics interuniversity PhD program

Universidad Carlos III de Madrid

Advisors:

Pablo Fajardo Peña

Jaume Navarro Cavallé

Tutor:

Pablo Fajardo Peña

January 2023

Dedicated to my parents who raised me to be curious.

Illustration by Tania Watson

Acknowledgments

I would like first and foremost to thank my parents to whom this thesis is dedicated. You have raised me to be curious and have always stimulated my thirst for knowledge. Without your unrelenting support and patience I would not have had this education that I have been so fortunate to enjoy.

Secondly I would like to thank my thesis supervisors Pablo and Jaume. Pablo for giving me the freedom to pursue my curiosity and intuition during this thesis and Jaume for the in-depth discussions, the many hours in the lab and for the experimental data that he has contributed to this work.

I would also like to thank Tania for her love, support and the patience to put up with me while I combined founding a start-up with this thesis.

Then I would like to thank the team at IENAI, and in particular my co-founders Sara, Daniel and Javier. Thank you for your patience and for giving me the opportunity to finish my thesis. I know you have at times shielded me from some of the burdens of running the company so I could work on my thesis. When starting this thesis I would have never imagined that I would end up founding a company. But I am glad it turned out this way and I cannot wish for better partners.

Lastly I'd like to thank the many colleagues at UC3M that I have had the pleasure to work with over the years, in particular Carlos, Marco, Mario, Scherezade, Tatiana, Víctor and Xin.

Published and Submitted Content

The following publications are fully or partially included in this thesis. In the chapters where the publications below are used this is not indicated by typographic references or citations.

Journal Papers

- *Experimental characterization of a 1 kW Helicon Plasma Thruster.* J. Navarro-Cavallé, M. Wijnen, P. Fajardo. *Vacuum*, vol.**149**, pp. 69-73 (2018). DOI: 10.1016/j.vacuum.2017.11.036. Data from this work is used in chapter 3.

- *Mechanically Amplified Milli-Newton Thrust Balance for Direct Thrust Measurements of Electric Thrusters for Space Propulsion.* M. Wijnen, J. Navarro-Cavallé, P. Fajardo. *IEEE Transactions on Instrumentation and Measurement* vol.**70**, pp. 1-18 (2021). DOI: 10.1109/TIM.2020.3037305. This article is fully reproduced with minor changes in chapter 4.

Conference Proceedings

- *Mechanically amplified milli-Newton thrust balance for helicon plasma thrusters.* M. Wijnen, J. Navarro-Cavallé, P. Fajardo. *36th International Electric Propulsion Conference*, Vienna, Austria, 2019, paper: IEPC-2019-595. This conference proceeding is not used directly in this work, but contains the ground work for chapter 4.

- *Development and Characterization of the Helicon Plasma Thruster Prototype HPT05M.* J. Navarro-Cavallé, M. Wijnen, P. Fajardo. *36th International Electric Propulsion Conference*, Vienna, Austria, 2019, paper: IEPC-2019-596. Data from this work is used in chapter 3.

Other Research Merits

The following publications were published during this thesis; but are not or only tangentially related to the work in this thesis.

Journal Papers

- *CubeSat Lunar Positioning System Enabled by Novel On-Board Electric Propulsion.* M. Wijnen, N. Agüera López, S. Correyero Plaza, D. Pérez Grande. *IEEE Transactions on Plasma Science.* vol.**46**, no.**2**, pp. 319-329 (2018). DOI: 10.1109/TPS.2017.2779756

Conference Proceedings

- *Characterization of a helicon plasma thruster by means of low-resolution optical emission spectrometry.* M. Wijnen, Y. Babou, J. Navarro-Cavallé, P. Fajardo. *Space Propulsion Conference 2018*, Seville, Spain, 2018, paper: SP2018-00164.

- *Webcam based in-vacuum tomography of plasma thruster jets.* M. Wijnen, J. Navarro-Cavallé, Y. Babou, P. Fajardo. *15th International Conference on Fluid Control, Measurements and Visualization*, Naples, Italy, 2019, paper: 349.

- *Direct Thrust Measurements of the HIPATIA System Thruster Unit.* V. Gómez, M. Wijnen, J. Navarro-Cavallé, *37th International Electric Propulsion Conference*, Boston, MA, USA, 2022, paper: IEPC-2022-491.

- *Impact of the propellant temperature on the performance of externally wetted electrospray thrusters.* D. Villegas, M. Wijnen, S. Correyero, G. Arboleya, P. Fajardo, *37th International Electric Propulsion Conference*, Boston, MA, USA, 2022, paper: IEPC-2022-212.

- *Direct thrust measurements of an externally wetted electrospray thruster.* F. de Borja de Saavedra, M. Wijnen, S. Correyero, G. Arboleya, D, Pérez, *37th*

International Electric Propulsion Conference, Boston, MA, USA, 2022, paper: IEPC-2022-223.

Patents

- *Method for Manufacturing an Emitter for Electrospray Generators.* J. Noqués Sanmiquel, B. Sepulveda Martínez, P. Güell I Grau, D. Pérez Grande, M. Wijnen, J. Cruz, S. Correyero. PCT/IB2021/000394. Provisional patent.

Abstract

This thesis is dedicated to the development of several diagnostics for the characterization of electric propulsion devices in general and of RF and helicon plasma thrusters in particular.

Electric rocket propulsion is now a widely adopted technology in both scientific and commercial space missions. The lack of a fundamental limit on the specific impulse results in greatly reduced propellant consumption. However, as these systems are power limited the thrust they produce is rather low, which implies longer maneuver times. Despite this, for in-orbit maneuvers such as constellation deployment, orbit raising, orbit maintenance, drag compensation and deorbiting it is often the optimal solution.

Currently the electric propulsion market is dominated by Hall-effect and gridded ion thrusters which have been successfully used for many decades now. Despite their success these technologies have their drawbacks such as a dependency on (costly) Xenon, electrode erosion, a high cost and a need for complex cathode neutralizers. For this reason new alternative electric propulsion technologies are being developed, among them electrode-less thrusters such as RF and helicon thrusters. These devices are still in an early stage and require continued investigation to understand the underlying physical principles as well as to characterize their performance to guide iterative design.

Experimental characterization of electric thrusters in general and RF and helicon thrusters in particular depends on diagnostic methods which can be divided into indirect characterization, i.e. plasma diagnostics and direct characterization by means of direct thrust measurements, using a thrust balance. Plasma diagnostics can be further divided into electrostatic probes which can perturb the plasma, and optical diagnostics which do not. The former being inexpensive and simple, while the latter are generally costly and more complex but give access to regions of the plasma otherwise inaccessible to probes. Generally a combination of multiple diagnostic methods is required to fully characterize a thruster.

In this thesis a variety of diagnostic methods are designed, manufactured and tested. In chapter 3 several electrostatic probes are developed or procured: an RF-

compensated Langmuir probe, a Faraday probe, and emissive probe and a retarding potential analyzer. Together they give access to the following plasma parameters: plasma density, plasma potential, electron temperature, ion current density and ion energy. Furthermore, a 2D polar probe positioning system is developed to yield local measurements in the horizontal, polar plane from 0-400 mm downstream and -90 to +90 degree. The probe positions system and the probes are combined to yield 1D and 2D maps of the plasma parameters in the plume expansion of a helicon thruster. From these measurements secondary performance parameters can be derived such as utilization efficiency, divergence efficiency and divergence angle. Furthermore, several probe results are combined to produce global performance parameters such as the axial beam power, thrust efficiency, thrust and specific impulse.

Direct thrust measurements by means of a thrust balance are the golden standard for measuring thrust and, concurrently, the specific impulse in electric thrusters. Therefore in chapter 4 a novel thrust balance is developed to deal specifically with the peculiarities of helicon plasma thrusters such a a low thrust-to-weight, strong RF and magnetic fields, high heat fluxes. A new thrust balance based on the Variable Amplitude Hanging Pendulum with Extended Range (VAHPER) concept has been developed. The thrust balance includes a mechanical amplification mechanism with an angular magnification of 31 resulting in an equal improvement of the sensitivity. Using Lagrangian mechanics, we show that the TB loaded with a 5.2-kg thruster prototype behaves like a damped harmonic oscillator with a natural frequency of 0.37 Hz. A variable damping system provides damping with an optimal damping ratio of 0.78, which corresponds to a settling time of only 1.8 s. Both the model and the damping and calibration system have been validated. To accommodate the particularities of a medium power electrode-less plasma thrusters, the thrust balance design includes the following features: an optical displacement sensor, water cooling, liquid metal connectors, and dedicated vacuum-rated electronics for auto-leveling, remote (in-vacuum) calibration, and temperature monitoring. To test the thrust balance, measurements were performed on a 500-W Helicon Plasma Thruster breadboard model. When loaded with this thruster, the measured stiffness of the system was 12.67 $\pm$ 0.01 mN/mm. For this stiffness, the thrust range is 150 mN with a 0.1-mN resolution. The relative uncertainty on the thrust measurements is found to be on the order of 2%.

High power RF requires rather thick and therefore rigid coaxial cables which

interfere with the sensitivity of the thrust balance. Therefore if the RF connection has to be mechanically decoupled from the moving part of the thrust balance. In the current prototype this is achieved by mounting the RF antenna on the fixed rather than the mobile part of the balance. However, to enable this for future iterations of the thruster where the antenna will be integrated, a wireless capacitively coupled power transfer system is proposed. The solution is modeled and a first prototype is constructed and tested. Power transfer of up to 50W with a transmission efficiency of 90% is achieved. Furthermore, it is demonstrated that the performance can be tuned by varying the distance between the electrodes.

Lastly, in chapter 5 a corona model is developed for the obtention of the electron temperature from low-resolution spectroscopy data. The model is a refined implementation of the Karabadzhak-Chiu-Dressler model and considers 11 NIR lines emanating from the Xe I $2p$ levels and includes excitation from the $1s_5$ metastable level. Relevant cross section data of the KCD model is reviewed and updated were possible and 3 additional NIR lines were included. The model is implemented in MATLab to automatize processing of emission spectra. A script loads the cross sections, calculates the rate coefficients, metastable fraction and the corresponding line intensities for a range of electron temperatures. This array of line intensities as a function of electron temperature is then compared to the experimental spectra by calculating the χ^2. The temperature for which χ^2 is minimum is assumed to be the actual electron temperature. The model is validated as much as possible against data available in the work of Dressler et al. with reasonable agreement. The model is subsequently applied to spectroscopic data from the HPT05M thruster and results are compared to probe data. However, there is a yet unexplained and unacceptably large discrepancy between the probe data and the optical emission measurements. So far the model cannot be relied upon to produce accurate electron temperature measurements. Several explanations are proposed but further investigation is required.

Contents

List of Tables

List of Figures

Nomenclature

Physical Constants

ϵ_0	vacuum electric permittivity , page 19	$8.854\,187\,812\,8 \times 10^{-12}\,\mathrm{F\,m^{-1}}$
μ_0	vacuum magnetic permeability , page 26	$1.256\,637\,062\,12 \times 10^{-6}\,\mathrm{H\,m^{-1}}$
a_0	Bohr radius , page 161	$5.291\,772\,109\,03 \times 10^{-11}\,\mathrm{m}$
c	speed of light in a vacuum , page 26	$299\,792\,458\,\mathrm{m\,s^{-1}}$
e	elementary charge , page 19	$1.602\,176\,634 \times 10^{-19}\,\mathrm{C}$
h	Planck constant , page 64	$6.626\,070\,15 \times 10^{-34}\,\mathrm{J\,Hz^{-1}}$
m_e	electron mass , page 21	$9.109\,383\,701\,5 \times 10^{-31}\,\mathrm{kg}$
g_0	standard acceleration of gravity , page 2	$9.806\,65\,\mathrm{m\,s^{-2}}$

Chapter 1 - Introduction

Δv	velocity change, page 3
$\dot{m}$	mass flow rate, page 2
η	total efficiency, page 4
F	force, thrust, page 2
I_{sp}	specific impulse, page 2
m_p	propellant mass, page 3
m_{sc}	spacecraft mass, page 3
P_b	beam power, page 4
P_{in}	input power, page 4

v_{ex} exhaust velocity, page 2

Chapter 2 - Helicon Plasma Thrusters

α magnitude of wave vector, page 26

δ displacement, page 23

Γ_e electron flux, page 22

Γ_i ion flux, page 22

λ_D Debeye length, page 20

ϵ_p plasma dielectric tensor, page 25

$\mathbf{\Pi}$ pressure tensor, page 19

$\mathbf{B}$ magnetic flux density vector, page 19

$\mathbf{E}$ electric field vector, page 19

$\mathbf{H}$ magnetic field strength vector, page 26

$\mathbf{j}$ current density vector, page 34

$\mathbf{K}$ dispersion tensor, page 25

$\mathbf{k}$ wave vector, page 26

$\mathbf{u}$ velocity vector, page 19

$\mathcal{E}$ energy, page 21

ν collision frequency, page 32

ω_{ce} electron cyclotron frequency, page 24

ω_{ci} ion cyclotron frequency, page 24

ω_c cyclotron frequency, page 24

ω_{LH} lower hybrid frequency, page 29

ω_{pe} electron plasma frequency, page 23

ω_{pi} ion plasma frequency, page 23

ω_p plasma frequency, page 23

ω_{UH} upper hybrid frequency, page 29

Φ electric potential, page 19

ϕ ambipolar potential, page 41

Φ_f floating potential, page 22

Φ_p plasma potential, page 21

ψ magnetic stream function, page 41

ρ electric charge density, page 19

θ angular coordinate, page 26

a helicon source radius, page 32

c_γ adiabatic sound speed, page 24

c_s ion sound speed, see also: u_B Bohm velocity, page 42

D 'difference' term of dielectric tensor, page 25

J_m Bessel function of the m-th order, page 35

k longitudinal wave number, page 26

k_0 vacuum wave number, page 26

L left hand dielectric term, page 27

l length, page 32

M Mach number, page 41

m helicon wave azimuthal mode, page 34

m particle mass, page 19

m_i ion mass, page 21

N index of refraction, page 26

n plasma number density, page 17

n_e electron number density, page 19

n_i ion number density, page 19

P 'parallel' term of dielectric tensor, page 25

p_e electron pressure, page 24

q charge, page 19

R right hand dielectric term, page 27

R_V plasma vacuum boundary radius, page 41

S 'sum' term of dielectric tensor, page 25

T transversal wave number, page 26

T_e electron temperature, page 17

T_i ion temperature, page 21

u_B Bohm velocity, page 21

v_A Alfvén velocity, page 29

v_{ph} phase velocity, page 29

Z atomic charge number, page 19

Chapter 3 - Plasma Probes

$\dot{m}$ propellant mass flow rate, page 80

η thrust efficiency, see η chapter 1, page 93

η_u utilization efficiency, page 80

η_θ divergence efficiency, page 80

Γ_c critical (electron) flux, page 64

λ_D Debye length, page 53

$\mathcal{E}$ energy, page 57

$\mathcal{E}_i$ ion kinetic energy, page 81

Φ plasma potential, page 54

ϕ_w material work function, page 64

Φ_{dc} DC component of plasma potential, page 57

Φ_{rf} RF plasma potential oscillations, page 57

θ_D divergence angle, page 80

ξ ratio of probe radius and Debye length, see also: λ_D Debye length, page 56

A_p probe surface area, page 54

A_s probe area including sheath correction, page 55

A_w emissive probe wire area, page 64

A_x area of auxiliary electrode, page 58

C_c coaxial capacitance of capacitive probe, page 58

C_p plasma capacitance of capacitive probe, page 58

C_x sheath capacitance at auxiliary electrode, page 58

C_{cp} coupling capacitor, page 58

C_{s1} stray capacitance, page 58

F thrust, page 81

$f_e(\mathcal{E})$ electron energy distribution function, page 57

$f_i(\mathcal{E})$ ion energy distribution function, page 71

I current, page 53

I_e electron current, page 54

I_i ion current, page 54

$I_{e,th}$ thermionic electron emission current, page 64

I_{es} electron saturation current, page 54

$I_{i,ax}$ axial ion current, page 80

I_{sp} specific impulse, see I_{sp} chapter 1, page 93

j_i ion current density, page 68

M_A atomic mass (in Da), page 80

n plasma number density, page 53

n_i ion number density, page 56

r_p probe radius, page 55

R_x sheath resistance at auxiliary electrode, page 58

s sheath thickness, page 55

T temperature, page 54

T_e electron temperature, page 53

T_w wire temperature, page 63

u_B Bohm velocity, see u_B chapter 2, page 54

V voltage, page 53

Z_c parallel impedance $Z_{ck} \parallel Z_{s1}$, page 58

Z_x sheath impedance at auxiliary electrode, page 58

Z_{ck} impedance of RF choke, page 58

Z_{s1} impedance due to C_{s1}, page 58

Chapter 4 - Thruster Balance

$\bar{\bar{I}}_i$ moment of inertia tensor of element i, page 102

β rotational viscous damping factor, page 105

δ_i differential angle of element i, page 102

δ_p damper plate thickness, page 106

δ_s skin depth, page 133

κ effective torsional spring constant, page 105

κ_i torsional spring constant of element i, page 102

Λ square root of ratio of C and L, page 132

$\mathbf{B}$ magnetic field, page 106

$\mathbf{E}$ electric field, page 106

$\mathbf{F}_d$ viscous damping force, page 106

$\mathbf{F}_i$ force applied to CoM of element i, page 103

$\mathbf{J}$ current density, page 106

$\mathbf{r}_D$ position vector of eddy current damper, page 105

$\mathbf{r}_i$ position vector of CoM of element i, page 102

$\mathbf{v}$ velocity vector, page 106

$\mathcal{E}_k$ kinetic energy, page 102

$\mathcal{L}$ Lagrange function, page 102

$\mathcal{U}$ potential energy, page 102

ω angular frequency, page 130

ω_0 natural frequency, page 105

ω_i angular velocity of element i, page 102

σ electrical conductivity, page 106

σ_y uncertainty in y, page 126

$\sigma_{k_{cal}}$ uncertainty in k_{cal}, page 126

σ_{L_T} uncertainty in L_T, page 126

$\sigma_{L_{vc}}$ uncertainty in L_{vc}, page 126

τ torque, page 105

τ_0 constant offset torque, page 105

θ_i angular position of element i, page 102

ζ damping ratio, page 105

A secondary fixed pivot, page 101

B free rotational joint, page 101

b linear viscous damping factor, page 105

C equivalent capacitance, page 132

C free rotational joint, page 101

C_1 primary coupling capacitance, page 130

C_2 secondary coupling capacitance, page 130

C_D diagonal stray capacitance, page 132

C_P parallel stray capacitance, page 132

C_S series capacitance, page 132

C_{ij} (stray) capacitance between electrode i and j, page 132

C_M 'mutual' capacitance, page 132

D Eddy current damper, page 101

F_T thrust, page 105

I effective moment of inertia, page 105

k stiffness or linear spring constant, page 106

k_c coupling constant, page 132

k_{cal} calibrated stiffness, page 123

L inductance, page 130

L_1 primary inductance, page 130

L_2 secondary inductance, page 130

L_D length from Eddy current damper to pivot A, page 105

L_i distance of CoM of element i to point of rotation (A,O), page 104

L_T (perpendicular) distance from thrust vector to pivot O, page 125

L_{AE} distance from pivot A to measurement point E, page 106

L_{vc} distance from voice coil to pivot O, page 125

m_i mass of element i, page 102

n angular magnification factor, page 103

O primary fixed pivot, page 101

Q_j generalized forces, page 103

q_j generalized variable, page 103

T transmission coefficient, page 132

x horizontal Cartesian coordinate, page 103

$x_{1,0}$ equilibrium x position of element 1, page 103

y vertical Cartesian coordinate, page 103

y_A y position of pivot A, page 104

y_E vertical displacement measure at E, page 106

$y_{1,0}$ equilibrium y position of element 1, page 103

Z impedance, page 130

Z_0 characteristic impedance, 50Ω, page 132

Z_L load impedance, page 130

Chapter 4 - Optical Emission Spectroscopy

α ratio of singly to doubly charged ions, page 156

χ^2 chi-squared, relative root sum square , page 171

χ_0 first zero of zeroth order Bessel function, page 155

ΔE energy difference, page 140

$\dot{m}$ propellant mass flow rate, page 190

ϵ emission coefficient, page 145

η_u utilization efficiency, page 190

γ full-width at half-maximum of Lorentzian line profile, page 147

Γ_j Cumulative branching ratio for all transitions $2p_j \rightarrow 1s_x$ where $x \neq 5$, page 157

Γ_{ij} branching fraction of transition $i \rightarrow j$, page 152

$\hbar$ Planck constant divided by 2π, see also: h Planck constant, page 140

λ wavelength, page 140

λ_{ij} wavelength of transition $i \rightarrow j$, page 148

$\mathcal{E}$ particle kinetic energy, page 151

$\mathcal{E}_e$ electron kinetic energy, page 151

$\mathcal{E}_{i,\infty}$ ion kinetic energy at infinity, page 186

$\mathcal{L}_L$ Lorentzian line profile, page 147

$\mathcal{L}_G$ Gaussian line profile, page 148

$\mathcal{L}_V$ Voigt line profile, page 148

ν frequency, page 146

ν wave-number, page 176

ν_c cutoff wave-number, page 176

ν_{dm} metastable diffusion frequency, page 155

Ω solid angle, page 146

Φ spectral flux, page 145

π parity, page 143

σ excitation cross section, page 151

σ_G standard deviation of a Gaussian line profile, page 148

τ_i life-time of state i, page 147

τ_{ij} lifetime corresponding to transition $i \rightarrow j$, inverse of A_{ij}., page 144

A_e thruster exit area, page 190

A_m detector surface, page 146

A_p (source surface, page 146

A_s entrance slit surface, page 146

A_{ij} Einstein coefficient, probability of spontaneous emission for transition $i \rightarrow j$., page 144

b_0 RDW fitting constant, page 161

b_1 RDW fitting constant, page 161

c_0 RDW fitting constant, page 161

c_1 RDW fitting constant, page 161

c_2 RDW fitting constant, page 161

D_0 diffusion constant at standard normal density, see also n_0, page 155

D_m metastable diffusion constant, page 155

E orbital energy, page 140

g degeneracy, page 154

H instrument function, page 175

I_{ij} total emitted power of transition $i \rightarrow j$, page 148

J total angular momentum, page 142

J_λ excitation rate of emission with wavelength λ, page 156

$J_{\lambda,exp}$ measured line emission at wavelength λ, page 171

k reaction rate constant, page 151

k_1^λ rate coefficient of optical emission at wavelength λ due to doubly charged ion impact excitation from the ground state, page 156

k_1^λ rate coefficient of optical emission at wavelength λ due to singly charged ion impact excitation from the ground state, page 156

k_{e0}^λ rate coefficient of optical emission at wavelength λ due to electron impact excitation from the ground state, page 156

k_{em}^{λ} rate coefficient of optical emission at wavelength λ due to electron impact excitation from the metastable level, page 156

k_{2pm}^{j} rate coefficient of electron impact excitation from the metastable to the $2p_j$ level, page 157

k_{dm}^{k} rate coefficient of electron impact excitation from the metastable to the $3p$,$3d$ and other $1s$ levels, page 157

k_{dm}^{k} rate coefficient of electron impact ionization from the metastable level, page 157

k_{ij}^{dex} rate coefficient for deexcitation collision $j \rightarrow i$, page 154

k_{ij}^{ex} rate coefficient for excitation collision $i \rightarrow j$, page 154

k_z rate coefficient of ion impact collision for ions with charge Z, page 152

L orbital angular momentum, page 140

l azimuthal quantum number, page 140

L_z projection of orbital angular momentum, page 140

$L_{e,\Omega}$ radiance, page 145

m magnetic quantum number, page 140

m_n mass of neutral atoms, page 190

N particle population, page 144

n number density, page 155

n principle quantum number, page 140

n_0 standard normal density at $p = 1$ atm, and $T = 273$K, page 155

n_e electron number density, page 156

n_i population density of state i, page 148

n_m metastable number density, page 156

n_n neutral number density, page 156

R plasma radius, page 155

S orbital electron spin, page 142

s spin quantum number, page 141

T temperature, page 148

T_e electron temperature, page 151

T_n temperature of neutrals, page 190

T_{e0} electron temperature in the source region, page 186

u_m metastable particle velocity, page 155

V anode voltage, page 152

v_x velocity in x-direction, page 148

w arbitrary stochastic or deterministic noise, page 175

x real spectrum, page 175

y measured spectrum, page 175

z ion charge state, page 152

Acronyms

AC Alternating Current, page 130

AF-MPDT Applied field MPDT, page 6

BNC Bayonet Neill-Concelman, a type of coaxial connector, page 60

BSR B-Spline R-matrix (method), page 150

CAD Computer Assisted Drawing, page 60

CCS Confocal Chromatic Sensor, page 110

CoM Center of Mass, page 100

CP Capacitive Probe, page 61

CPT Capacitive Power Transfer, page 128

CR Collisional-Radiative, page 15

DC Direct Current, page 130

DoF Degree of Freedom, page 100

ECR Electron Cyclotron Resonance, page 8

ECRT ECR Thruster, page 8

EEDF Electron Energy Distribution Function, page 10

EM Electro-Magnetic, page 140

EMI Electro-Magnetic Interference, page 98

EO Earth Observation, page 2

EP Electric Propulsion, page 4

EP Emissive Probe, page 63

EP2 Equipo de Propulsion y Plasmas, page 14

FC Faraday Cup, page 68

FEEP Field Emission Electric Propulsion, page 5

FEM Finite Element Model, page 119

FFT Fast Fourier Transform, page 73

FP Faraday Probe, page 67

FWHM Full Width at Half Maximum, page 147

GIT Gridded Ion Thruster, page 5

HDLT Helicon Double Layer Thruster, page 49

HET Hall Effect Thrusters, page 4

HPT Helicon Plasma Thruster, page 8

HPTx HPT eXperiment(al platform), page 49

ICR Ion Cyclotron Resonance, page 40

ID Inner Diameter, page 60

ILIS Ionic Liquid Ion Source, page 6

IoT Internet of Things, page 2

IPT Inductive Power Transfer, page 128

KCD Karabadzhak-Chiu-Dressler, page 154

LANL Los Alamos National Laboratory, page 150

LDV Laser Doppler Velocimetry, page 11

LEO Low Earth Orbit, page 2

LHS Left Hand Side (of an equation), page 21

LIF Laser Induced Fluorescence, page 11

LMIS Liquid Metal Ion Source, page 6

LP Langmuir Probe, page 57

MPDT Magneto Plasma Dynamic Thruster, page 6

NIR Near Infrared part of EM spectrum (700-1400 nm), page 11

NIST National Institute of Standards and Technology, page 157

OD Outer Diameter, page 60

OES Optical Emission Spectroscopy, page 11

OML Orbital Motion Limited, page 56

PCB Printed Circuit Board, page 114

PIC Particle-in-Cell, page 47

PPT Pulsed Plasma Thruster, page 7

PPU Power Processing Unit, page 4

PTFE Polytetrafluorethylene, page 7

RDW Relativistic Distorted Wave (method), page 150

RFCLP Radio Frequency Compensated Langmuir Probe, page 60

RFEA Retarding Field Energy Analyzer, see also RPA, page 72

RFGIT Radio Frequency GIT, page 40

RFPT Radio Frequency Plasma Thruster, page 8

RHS Right Hand Side (of an equation), page 21

RMS Root Mean Square, page 114

RMSE Root Mean Square Error, page 119

RPA Retarding Potential Analyzer, page 11

RTD Resistance Temperature Detector, page 115

SLS Space Launch System, page 3

SPI Serial Peripheral Interface, page 115

SR Super Resolution, page 175

SS Stainless Steel, page 113

SSME Space Shuttle Main Engine, page 3

TB Thrust Balance, page 97

TDLAS Tunable Diode Laser Absorption Spectroscopy, page 11

TG Trivelpiece-Gould, page 32

TS Thomson Scattering, page 11

UC3M Universidad Carlos III de Madrid, page 14

UNEF ANSI standard, Extra Fine UNified screw thread, page 60

USB Universal Serial Bus, page 115

UV Ultraviolet part of EM spectrum (10-400 nm), page 11

VAHPER Variable Amplitude Hanging Pendulum with Extended Range, page 99

VASIMR VAriable Specific Impulse Magnetoplasma Rocket, page 40

VIS VISible part of EM spectrum (400-700 nm), page 158

CHAPTER

ONE

Introduction

"All civilizations become either space-faring or extinct."

— Carl Sagan

1.1 Background

Space exploration began in earnest in 1957 when the Soviet Union launched the first artificial satellite, Sputnik 1, into orbit and reached its peak about a decade later, 1969 when the United States landed the first man on the moon. Since then humans have visited the moon multiple times over, established a perpetual presence in orbit with the inauguration of the International Space Station in 2000 and launched multiple probes to other planets, such Mars, Venus, Jupiter and Saturn. Commercial use of space assets until fairly recently was limited to large geostationary communication satellites.

However one can argue that in the last few decades we have entered the age of space exploitation. The space industry is rapidly developing into a booming private industry. The miniaturization of satellites, driven by the miniaturization of consumer electronics, and the reduction in launch costs due to reusable launch vehicles and competition in the launcher market, has reduced the cost of putting an asset into orbit to the extent that even smaller start-ups can now aspire to own and operate a fleet of satellites. Commercial constellations in low-Earth orbit (LEO) for anything from Earth observation (EO), communication, internet-of-things (IoT) and other applications are becoming increasingly lucrative business models and even more exotic applications such as in-orbit manufacturing, in-orbit servicing and space mining are topics of discussion. And with the Lunar gateway project and a possible

mission to Mars effort in human space flight is also increasing.

In light of all the above, it is clear that space exploration and exploitation are experiencing a new boom. With the a record number of 1400 satellites launched only in the past year, LEO is getting more crowded. In the first half of the same year alone, SpaceX had to perform 2219 collision avoidance maneuvers. This astonishing fact alone points to a glaring fact: spacecraft needs propulsion. Not just for collision avoidance, but also for a myriad of other maneuvers such as orbit change, orbit maintenance, constellation deployment, drag compensation, formation flying, de-orbiting and deep space missions.

1.1.1 Space Propulsion

Due to the lack of a medium, in-space propulsion is necessarily rocket propulsion. That is to say a propulsion system that carries its own reaction mass. Rocket propulsion is often equated with chemical propulsion where a propellant consisting of fuel and an oxidizer are combusted in a reaction chamber after which its hot reaction products thermally expand in a bell shaped nozzle. In this process internal energy is first converted into heat which is then converted into directed kinetic energy. The thrust generated is proportional to the change in momentum, and since generally the exhaust velocity of the ejected reaction mass is constant, the thrust is proportional to the ejected mass flow rate.

$$F = \dot{m} v_{ex} \tag{1.1}$$

The exhaust velocity in chemical rocket engines is limited by the internal energy of the propellant. The highest exhaust velocity, or rather specific impulse ever measured is 542 s. The specific Impulse is the exhaust velocity scaled by the standard acceleration of standard gravity $g_0 = 9.8065$ ms^{-2} i.e.,

$$I_{sp} = \frac{v_{ex}}{g_0} \tag{1.2}$$

However this was for a tri-propellant mixture of lithium, liquid oxygen and fluorine which is an absolute nightmare in terms of toxicity and corrosiveness this is not a propellant that is used in practice. The highest achievable specific impulse in practice is for cryogenic liquid hydrogen, liquid oxygen mixture, or LOX/LH2 which is used in systems such as the Space Shuttle Main Engine (SSME) and the Space

Launch System (SLS) and which has a specific impulse of around 450 s. The reason why specific impulse a parameter of great interest for rocket propulsion has to do with what is referred to as "the tyranny of the rocket equation". The rocket equation, published by Konstantin Tsiolkovsky in 1903 states that a linear increase in the velocity increment Δv requires an exponential increase in the propellant mass. This is due to the fact that for each additional kilogram of propellant even more propellant is required to account for the increased total mass of the spacecraft.

$$\Delta v = g_0 I_{sp} \ln\left(1 + \frac{m_p}{m_{sc}}\right) \tag{1.3}$$

Looking at the above equation it quickly becomes apparent that increasing the specific impulse reduces the required propellant mass for the same Δv or results in a higher Δv for the same propellant mass. Clearly a higher specific impulse is something to be pursued, unfortunately chemical propulsion is limited by the energy densities available in nature. However, combustion with subsequent thermal expansion is not the only means of accelerating propellant mass. Propellant that is electrically charged can be accelerated by means of electric and magnetic fields. The energy for the acceleration in that case comes from an external power source and therefore the specific impulse is no longer limited by the internal energy of the propellant. Such systems are the topic of the field of electric propulsion.

1.1.2 Electric Propulsion

As aforementioned, electric propulsion (EP) is rocket propulsion whereby the propellant is accelerated by means other than a combustion process and where the power source is electric. The main advantage of electric propulsion is that there is no practical limit on the achievable specific impulse (except perhaps the speed of light c). For this reason electric propulsion is the most fuel efficient propulsion system, yielding higher Δv per kilogram of propellant mass than chemical systems. The drawback is that electric propulsion is power limited. The total amount of propulsive power it can generate is limited by the power source. For example, chemical engines use in launcher vehicles such as the Raptor 2 engine of SpaceX, can produce around 2.3 MN of thrust at 363s of specific impulse, which using Equation 1.4 equates to about 4.1GW of power. In comparison the largest power source in orbit are the solar panels that power the ISS which can generate up to 160 kW. It

should be clear that electric propulsion will never be used to power launch vehicles.

$$P_b = \frac{1}{2} g_0 I_{sp} F \tag{1.4}$$

For this reason, in general, electric propulsion provides much lower levels of thrust than chemical propulsion. Typical thrust ranges from 10s of micro-Newton up to 100s of milli-Newton, with specific impulse for electric propulsion ranging from 1000-6000 s and powers from several watts up to 10s of kW [79][96]. It has to be noted that not all power provided to an electric propulsion system is converted into propulsive power. There are losses in both the power processing unit (PPU) of the propulsion system as well as losses in the thruster itself. Therefore another important metric of electric propulsion systems is the total efficiency η which is the product of the electrical efficiency of the PPU, η_E and the thrust efficiency of the propulsion system η_T.

$$\eta = \frac{g_0 I_{sp} T}{2 P_{in}} \tag{1.5}$$

Electric propulsion can be divided into different categories, for example based on the acceleration mechanism, or based on the power coupling mechanism. In general EP can be divided into electrothermal, electrostatic and electromagnetic thrusters. How thrusters are classified depends what is taken into consideration; Hall effect thrusters (HET) for example, as we will see, can be classified as an electrostatic thruster since the acceleration mechanism is purely electrostatic. However, electromagnetic forces play an important role in the power coupling mechanism. Therefore they HETs are often categorized as electromagnetic. We will adhere to the categorization of [79] where both the acceleration and and power coupling mechanisms are taken into consideration. The following is a summary of the field of electric propulsion and the reader is referred to the excellent reviews of [79] and [96] for a more detailed overview.

Electrothermal thrusters are closest to chemical thruster in that the acceleration of the propellant relies on the thermal expansion of a hot gas (or plasma) in a bell-shaped nozzle. The difference is that the gas is not heated by a combustion process but using electrical power. Examples of electrothermal thrusters are resisto-jets which use Joule heating to heat the propellant, or arcjet thruster which use an electrical discharge to generate a hot plasma. These kinds of devices have relatively high thrust in the order of $10^1 - 10^2$ mN, but low specific impulse of 100-500 s,

comparable to chemical engines. Note that electrothermal thrusters do not require the propellant to be electrically charged.

Electrostatic thrusters rely on electrostatic acceleration of a charged propellant. One could make a further division into plasma based and field-enhanced electric propulsion (FEEP)/electrospray propulsion. The former rely on plasmas, a state of matter that is in essence a partially ionized, hot gas, where the fraction of charged particles (ions and free electrons) is substantial enough to dictate the behaviour. Most plasmas in electric propulsion are based on inert gases such as Argon, Krypton and Xenon, where the latter is the most prolific due to its superior properties. However plasmas generated from other gases or materials are certainly possible. An example of a plasma based electrostatic thruster is the gridded ion thruster (GIT) which together with the HET is the most common EP device. GITs consist of a plasma generation stage, followed by a series of electrically biased grids that establish a linear electric field that accelerates the ions in the direction of the exhaust. Charge conservation requires that a the beam of a thruster is neutralized, and therefore GITs (as well as other EP devices) have a (hollow) cathode that emits free electrons that neutralize the beam.

FEEP and electrospray devices are similar and the difference between them is mainly in type of propellant used. These types of devices do not use plasmas but rather liquid propellants from which charged particles are extracted. The extraction mechanism based on the interplay between the electric field and the surface tension near the tip of a sharp needle or capillary also referred to as the emitter. This results in the formation of Taylor cones; these conical structures are the equilibrium shape of the liquid meniscus in the presence of the electric field. Depending on the emitter geometry, electric field and the liquid properties one of two things can happen: a) the tip of the Taylor cones has as singularity which turns into a jet that breaks up into droplets, or b) the Taylor cone becomes a stable dome with an electric field high enough to greatly enhance the evaporation of ions. In practice FEEP generally refers to liquid metal ion sources (LMIS), using indium, cesium or gallium while electrospray is used for thrusters using colloids or ionic liquids; i.e. ionic liquid ion sources (ILIS); organic salts with a melting point at or below room temperature. Another difference is that FEEPs need a neutralizer while electrosprays, at least in theory could operate with an alternating polarity emitting both negative an positive ions. Electrostatic thrusters are characterized by a high specific impulse, 3000 s for

GIT and 2000-5000 s for FEEP/electrospray. On the flip side they tend to have lower thrust, $10^0 - 10^2$ mN for GIT and $10^{-2} - 10^1$ mN for FEEP/electrospray. Although needless to say this is very much dependent on their power class. On a side note, the plasma generation stage of a GIT can have many forms, including electron guns, radio-frequency heating or electron-cyclotron heating. The latter two mechanisms are clearly electromagnetic in nature, despite this the GIT is generally classified as electrostatic.

Electromagnetic thrusters use a combination of electrostatic and electromagnetic forces generate and accelerate a plasma. There is a wide variety of electromagnetic thrusters with very different working principles. The most common electromagnetic thruster is the Hall effect thruster. These thrusters consist of an annular plasma chamber with with a radial magnetic field and anode at the back generating an axial electric field. Subsequently electrons produce an azimuthal hall current due to the perpendicular **E** and **B** fields. The result is a low pressure DC-discharge with a magnetic barrier; electrons gain energy in the electric field, while their residence time is increased due to the magnetic field. These high energy electrons then ionize the neutral propellant injected from the back. The resulting ions are accelerated in the axial electric field. As with the GIT the HET uses a (hollow) cathode to produce free electrons that neutralize the beam. HET performance is generally around 1500 s of I_{sp} and thrusts in the range of $10^1 - 10^2$ mN.

Magnetoplasmadynamic thrusters (MPDT) consist of two concentric electrodes between which a high current density is generated. The resulting induced field together with the current density then generate an axially directed Lorentz force that accelerates the plasma. At lower powers the acceleration mechanism is mainly electrothermal, while at high powers it is electromagnetic. MDPTs are mostly efficient at higher powers in the 10-100 kilowatt range. However short lifetimes due to electrode erosion and the complications of testing thrusters of this power class has limited their practical use. A sub-category of MDPTs exist, which are called applied field magnetoplasmadynamic thrusters (AF-MDPT). These are MPDTs with an applied axial magnetic field. In this case the induced field is negligible and the acceleration comes from the expansion of the hot plasma in the magnetic nozzle formed by the applied field. (AF-)MPDTs have a specfic impulse in the rage $10^3 - 10^4$ s and thrust in the range of $10^{-1} - 10^1$ N. .

Ablative pulsed plasma thrusters use a solid propellant (typically polytetraflu-

oroethylene, PTFE) wedged between two electrodes. By applying a very high voltage a discharge is produced that ablates and ionizes a layer of the propellant. The pulsed discharge current is very high, $\sim$ 10 kA which is provided by a capacitor bank, and results in a perpendicular, induced magnetic field. The cross product of the discharge current and the magnetic field produces a Lorentz force that accelerates the plasma; however there is also an electrothermal contribution due to the expansion of the hot plasma. PPTs operate in a pulsed mode with a relatively high instantaneous thrust in the order of Newtons, however since the pulses last microseconds the time-averaged thrust is relatively low and dependent on the pulse frequency. Specific impulse is in the range of 1000-1500 s. A major drawback is the low efficiency $< 10\%$ due to poor propellant utilization and a large electrothermal contribution.

The last category are the electrode-less plasma thrusters. These thrusters, as the name suggests, do not have electrodes. In the most general sense they exist of a plasma chamber with a magnetic nozzle produced by either permanent magnets or a solenoid. The plasma is generated and heated by means of plasma-wave coupling after which the hot plasma expands along the magnetic nozzle. The acceleration is mainly due to the diamagnetic force between the azimuthal electron current and the magnetic circuit of the thruster although there is some electrothermal component. The most common means of plasma generation are are either by radio-frequency or by microwaves, the corresponding thruster concepts are the RF- or helicon plasma thruster (RFPT,HPT) and the electron-cyclotron resonance thruster (ECRT). The heating mechanism in the latter is electron-cyclotron resonance heating (ECR), where if the driving frequency equals the ECR frequency of the plasma, the microwave energy is efficiently transferred to the electrons. In RF and helicon discharges the radio-frequency waves couple power to the plasma, either inductively or by means of helicon waves, a particular type of electromagnetic waves that can propagate in a plasma. (Helicon waves will be explained in more detail in chapter chapter 2) The main advantage of helicon waves is that they are known to produce high plasma densities which should result in correspondingly high thrust densities. Both ECRT and HPT are still experimental thrusters without flight heritage. However their performance has been characterized somewhat. HPTs produce thrust in the order of several milli-Newton with a specific impulse of 500-1500 seconds, while their efficiency is so far still below 10% at lower powers (<1 kW) and

13-18% in the kilo-Watt range [124]. ECR thrusters have two variants: wave-guide coupled and coaxial thrusters. The former have been a topic of investigation several decades ago, with poor performance: efficiencies below 2%. The latter however is a relatively new concept that has has similar performance to the HPT, about 1 mN of thrust and up to 1000 s of specific impulse at around 50W, with 10% [139].

1.1.3 Experimental Methods

There are two ways to go about investigating electric thrusters: numerical simulation and experiments. The former is generally less resource intensive and generally provides more insight into the physics. However, in plasma physics many phenomena are coupled and therefore the physics are exceedingly complicated and cannot be captured easily in a single model. For electrode-less plasma thrusters the general approach consist of three coupled models: a wave-plasma coupling module [80][81][131][106][55]; a plasma source module [5][64][75][156][154] and a magnetic nozzle expansion module [1][4][84][85][2]. However to date no models exist that are predictive; all models require validation with experimental data. In experimental research one obtains measurements of a particular variable as a function of space, time or operating conditions. These can be macroscopic parameters such as thrust or local plasma parameters such as plasma density, electron temperature or ion velocity. The objective is usually to characterize and optimize performance, validate a model or discover heretofore unknown trends that can inform new models. Experimental methods or generally require specialized hardware and are therefore more resource intensive than numerical simulations. Few diagnostic methods can be used to measure more than one or two variables and a therefore lot of equipment is needed to fully characterize the thruster performance or plasma properties. Measurements are furthermore complicated by limitations on the validity of the experiment, conditions complicating the interpretations of the measurements, uncertainties in the measurement or perturbation of the plasma by the very measurement itself. Notwithstanding they are the closest approximation of the true behaviour of the EP device and are absolute necessary to guide design optimization and further the understanding of the underlying physics. Diagnostic methods for EP devices can generally be divided into direct thrust measurements, and plasma diagnostics methods. The latter can then be further divided into plasma probes

and non-invasive methods such as microwave and optical diagnostics.

Direct thrust measurements

Direct thrust measurements are obtained by means of a thrust balance (also referred to as 'thrust stand') and are considered the golden standard for measuring thrust in electric propulsion devices. The main principle behind them is a linear conversion of force to displacement which can then be measured. The complexity of direct thrust measurements derives from the inherently low thrust-to-weight ratio of EP devices. The thrust is generally of the order of micro- or milli-Newton while the gravitational force due to the mass of the device is in the order of Newtons. Therefore a device that is at the same time compliant enough to produce a measurable displacement while also rigid enough to sustain the weight of the device. Additional complexities are related to sources of error and noise in the measurement. Since the force and therefore the displacement to be measured is so small even the slightest perturbation can spoil the measurement including thermal drifts, ambient vibrations, misalignment and others. Despite the complexities, sensitive thrust balances have been built since the dawn of electric propulsion research. Since there is a large variety of different EP technologies with each their own peculiarities, spanning a range of power classes, thrust stands are generally tailored to a specific device and power class.

Plasma Diagnostics

Plasma diagnostics are measurement techniques used to obtain information about the state of the plasma. Most diagnostics measure one or two variables such as electron or ion density, electron temperature, plasma potential, ion current density, ion energy or velocity and many others. Often the diagnostic does not yield a direct measurement of the desired variable and some model is necessary to infer the value of the desired variable from the measurement. For example the measurement of a Langmuir probe yields a current-voltage characteristic from which the plasma density, electron temperature and plasma potential can be inferred. Other times the diagnostic does yield a direct measurement, but what is really of interest is a variable that can only be inferred from multiple time or spatially resolved measurements. For example a angular resolved ion current density profile can be used to calculate

the utilization efficiency and divergence of a thruster. Many diagnostic techniques carry over from the fields of plasma physics and plasma processing although in many cases the particularities of electric thruster plasmas require modifications to the equipment or the model used to interpret the data.

The most common, simplest and cheapest plasma diagnostics are plasma probes. In essence they are no more than a conductive element (often a rod or disc) inserted into the plasma. Generally either the potential of or the current through the conductor is measured. When measuring current this is often done while simultaneously applying a (varying) bias potential. The most common plasma probes used in electric propulsion testing are: Langmuir probes, Faraday probes, emissive probes and retarding potential analyzers. Langmuir probes measure the current extracted from the plasma as a function of a bias potential. From the resulting $I-V$ characteristic, ion density, electron density, electron temperature and plasma potential can be obtained [72]. Langmuir probes can also be used to obtain the electron energy distribution function (EEDF). Druyvestein proved that the EEDF was directly proportional to the second derivative of a Langmuir probe $I-V$ characteristic [38]. This can be obtained by twofold numerical differentiation, however this tends to be noisy and therefore rely too much on smoothing methods. However one can use the Boyd-Twiddy method to measure directly the second derivative [20][21][34].

Faraday probes consist of a cup or disc facing upstream of an ion beam. Generally the device is biased to a negative potential such that electrons are repelled ensuring that only ion current is measured. As aforementioned angular resolved profiles of the ion current density can be used to infer properties regarding the performance of the thruster [22].

Emissive probes are made of materials with a low work-function and heated to very high temperatures (>1000 K) to induce thermionic electron emission. The insertion of low temperature electrons (compared to the electron temperature of the plasma) causes the probe potential to approach the plasma potential and therefore allows for a direct measurement of the former [113].

Lastly retarding potential analyzers (RPA) can be regarded as a Faraday probe preceded by an energy filter. Using a set of transparent electrodes (i.e. grids) with a variable bias the ion current reaching the collector can be measured as a function of the bias potential. The bias potential creates an energy barrier only allowing ions of sufficient energy to pass it. The first derivative of the resulting $I-V$ characteristic

is directly proportional to the ion energy distribution function [39]. Note that the above is not an exhaustive list of plasma probes, other types exist such as capacitive probes, hairpin probes [98][17], triple probes [103] and B-dot probes [99].

Plasma probes are considered 'invasive' diagnostics; their very presence perturbs the plasma. When applied correctly they only perturb the plasma locally (which is essential for their correct operation) but do not affect the properties of the bulk plasma. However, in many cases plasma probes will also perturb the bulk plasma, precluding their use. This is particularly the case for the source region of plasma thrusters. In such cases 'non-invasive' diagnostics can be used that rely on electromagnetic radiation, generally either using the optical or micro- and millimeter wave part of the spectrum. Such methods can be further divided into passive and active diagnostics, where the latter actively probe the plasma with radiation using microwave or laser beams while the former solely measure radiation emitted by the plasma. Common techniques pertaining to the optical spectrum are optical emission spectroscopy (OES), laser-induced fluorescence laser Doppler velocimetry (LIF LDV, or simply LIF), tunable diode laser absorption spectroscopy (TDLAS) and Thomson scattering (TS).

Optical emission spectroscopy uses a spectrometer to measure the spectrum of light emitted by the plasma, generally in the range of 200-1200 nm, which includes the UV and near-infrared (NIR). The light emitted by atomic plasmas, common in EP generally consists of a unique set of emission lines, i.e. only light of a particular set of wavelengths. The wavelengths of the emission lines are related to the electronic structure of the atom and unique for each element, while their relative intensities can be related to the electron temperature of the plasma. Low-resolution OES is relatively affordable (compared to most other optical and microwave methods) but requires complex collisional radiative models to infer the electron temperature from the spectrum.

LIF LDV is an active diagnostic technique whereby the plasma is probed by as laser beam [78][148]. The wavelength of the laser is such that it induces a fluorescence in the plasma, meaning that the light emitted from ions excited by the laser occurs at a different wavelength than that of the laser. This way the measurement of the induced emission is not drowned out by the high intensity light of the laser. Fluorescent light emitted by high velocity ions experiences a Doppler shift, by measuring the magnitude of this shift the velocity of the ions

can be inferred. Another advantage of LIF is the high spatial resolution, as the measurement is constrained to the volume of intersection of the laser beam and the focal point of the collection optics.

TDLAS can be used to measure the atomic density of excited states of neutrals or ions. By sweeping the wavelength of a tunable diode laser around a known emission line of the target species the absorption as a function of wavelength can be measured. The magnitude of the absorption line is directly proportional to the density of the species. Although measurement of ground state atoms and ions would be of more interest until now no tunable diode lasers exist in the far and extreme UV range that is required for ground state absorption lines.

Incoherent Thomson scattering is a diagnostic method that can be used to accurately measure the electron temperature [140]. In Thomson scattering the plasma is probed with a laser, the light of which is then scattered by the free electrons of the plasma. However due to the thermal motion of the electrons the spectrum of the scattered light shows Doppler broadening that can be directly related to the electron temperature. The difficulty lies in preventing the high intensity laser light crowding out the measurement signal, which necessitates the use of very narrow band-stop filters. For certain plasma conditions, to be precise, when the inverse of the product of the wave number of the laser and the Debye length of the plasma is much smaller than unity the scattering of light by the electrons is coherent. In this case the method is referred to as coherent or collective Thomson scattering; the scattered light is now not only related to the electron temperature but also the electron density and this technique can be used to measure both [137].

Apart from optical diagnostics, microwave diagnostics are a common measurement method in plasma physics. The most common method in microwave interferometry. This method relies on the fact that microwaves traversing a plasma column will experience a phase shift directly proportional to the electron density. The phase shift can be obtained from the interference pattern of the microwave beam traversing the plasma with a reference beam [45][138]. A drawback of microwave interferometry is that it generally yields a line integrated measurement unless one measures along multiple chords and applies an Abel inversion. The minimum beam waist of a microwave beam is limited by the wavelength, which for microwaves is generally in the centimeter range. Higher spatial resolution can be obtained by using millimeter waves, however at these wavelengths the sensitivity of the phase shift to the plasma

density is greatly reduced. This either requires large plasma densities encountered in nuclear fusion or phase measurements with extremely high resolution. As a clever way around this conundrum one can Doppler shift the reference beam by a small amount (about 10 kHz); after mixing the reference beam and probing beam a beat signal of the same frequency as the Doppler shift is obtained that contains the same phase shift. Sampling this low frequency with a modern 1 GS/s oscilloscope then provides the required phase resolution [74].

1.2 Motivation

Electric propulsion today is dominated by HETs and GITs in all power classes [67]. These devices have flight heritage going back to the 70's of the previous century. They have good performance but are complex and costly devices that run solely on Xenon. Xenon is a rare noble gas that exists in quantities of about 87 ppb in dry air and is therefore very expensive to produce in large quantities. Furthermore the bulk of global Xenon production is concentrated in Russia and China and due to the current geopolitical situation the cost has increased even more. Both these types of thrusters also require the use of hollow cathode, which are complex and expensive devices in their own right and the primary reason these thrusters require very pure xenon propellant. Furthermore both types of thrusters suffer from erosion, mainly of the electrodes. Therefore there is a need for a thruster that can operate without a neutralizer, using alternative propellants and does not suffer from erosion with ideally equivalent or superior performance. Electrode-less thrusters can potentially meet these requirements. Although the measured performance has been inferior compared to existing technologies, electrode-less thrusters are still in the experimental phase and a better understanding of the underlying physics will pave the way for optimizing their performance.

The Electric Propulsion and Plasmas Group (EP2) at Universidad Carlos III de Madrid is currently co-developing, together with the Spanish engineering company SENER - Aeroespacial, a 500W-class helicon plasma thruster prototype, within the Horizon 2020 framework. The goal of HIPATIA (HelIcon PlasmA Thruster for In-Space Applications) project is: "to verify the function and performances of an EP system based on the helicon plasma thruster technology, for its application in non-geostationary satellites constellations and other small spacecrafts." To be able

to evaluate the performance and the effects of successive iterations on the design, diagnostic methods are an absolutely necessity.

1.3 Objectives

The objective of this thesis is to develop multiple diagnostic methods to characterise the performance of the helicon plasma thruster developed at EP2. This objective can be further divided in to three main topics: probe diagnostics, direct thrust measurements and optical diagnostics.

The main reason for developing a suite of probe diagnostics is to have both the ability to do an indirect characterization of the performance in terms of thrust, specific impulse and various partial efficiencies such as the utilization efficiency and the divergence efficiency as well as to further the understanding of magnetic nozzle physics. Multiple probe diagnostics have already been in use at EP2 for some time, however there is room for improvement on various fronts. Firstly the manufacturing of all probes can be improved to yield more robust probes with optimal performance. Furthermore, RF-compensated (a topic that will be introduced in chapter 3) Langmuir probes have been used but the efficacy of the compensation hasn't been properly investigated until now. Secondly the methods used for post-processing are currently based on previous work [142] but should be revised on more recent work [72]. Lastly, the current probe positioning system in use, although convenient for near plume measurements is sub-optimal for measurements of the far plume, particularly for Faraday probe measurements. It also does not allow for proper Langmuir probe alignment with the direction of the ions. Therefore a redesigned is planned for a system operating in polar coordinates. The tasks regarding probe diagnostics are therefore the following:

1. Improve the design of existing Langmuir, Faraday and emissive probes.
2. Verify the correct operation of the RF-compensation of the Langmuir probe
3. Improve post-processing methods for Langmuir probes
4. Develop a probe positioning system with motion in polar coordinates

The main project of this thesis is the development of thrust balance for direct thrust measurements of a helicon thruster. Apart from the complexities mentioned

in the previous section, measurements of a helicon thruster haven additional complications. Firstly the thrust-to-weight ratio is already lower than other more mature devices. In part because the prototypes have not been optimized for low mass but also due to the fact that current performance in terms of thrust is still low while the thruster itself is relatively heavy due to the solenoid or magnets required for the magnetic nozzle. Secondly, due to the currently poor efficiency as well as Joule heating of the solenoid the heat fluxes presented by the thruster are excessive and care needs to be taken so that they will not perturb the measurement. If the heat cannot be dissipated the coil temperature increases continuously limiting the time for the experiment and leading to a drift in the measuremnt due to thermal expansion. Third, the helicon plasma thruster prototype of EP2 requires a high power RF supply (>300 W) as well as high current lines (<10A) for the solenoid. This implies that the fixed and mobile parts of the balance would be bridged by thick cables that introduce an unacceptable level of stiffness to the system. And last the strong RF fields emanating from the thruster tend to interfere with nearby electronic signal lines, something that is particularly complicating in a sensitive measurement such as thrust measurements. The tasks regarding the thrust balance are then:

5. Design & manufacture a thrust balance for thrust measurements of the helicon plasma thruster prototype

6. Validate and calibrate the thrust balance setup

7. Perform a thrust measurement campaign of the HPT prototype

The fifth chapter of this thesis is devoted to the development of optical diagnostics. The main reason for this is that much of the performance of the helicon thruster is determined by what is happening inside of the source region. However, this region is inaccessible with probe diagnostics. The preferred diagnostic would have been LIF or Thomson scattering, followed by microwave diagnostics, to measure ion velocity, electron temperature and ion density respectively. Since no funds were available for any of these expensive diagnostics instead an attempt was made to develop a simple collisional-radiative (CR) model to obtain the electron temperature from low-resolution optical emission spectroscopy (OES) measurements. The tasks related to this last topic are the following:

9. Develop a CR-model of Xenon to measure the electron temperature with OES

1.4 Thesis Outline

This last section of this chapter will present the outline of this thesis. The document is divided into 6 chapters.

- Chapter 1 - this chapter - is the introduction to the rest of the work and presents the background, motivation and objectives of this thesis.
- Chapter 2 provides a review on helicon plasma thrusters and magnetic nozzles and also presents the current prototype developed at EP2.
- Chapter 3 is dedicated to the work on plasma probes; it deals with Langmuir, Faraday, emissive and capacitive probes as well as RPAs. It also includes the results of a test campaign performed with these probes.
- Chapter 4 is dedicated to the milli-Newton thrust balance developed to perform direct thrust measurements of the HPT prototype and also includes a thrust measurement campaign of the HPT prototype.
- Chapter 5 details the development of a Xenon CR model of OES measurements of the electron temperature.
- Chapter 6 - the last chapter - summarizes the previous 3 chapters, presents the conclusions of this work as well as recommendations for future work.

CHAPTER

TWO

Helicon Plasma Thruster

"It is difficult to say what is impossible, for the dream of yesterday is the hope of today and the reality of tomorrow."

— Robert H. Goddard

In this section the theory underpinning helicon plasma thrusters is summarized. It includes a short recap of relevant concepts from plasma physics, the physics of helicon waves, a review of the state of the art of helicon plasma thrusters and an overview of the HPTx prototype of EP2.

2.1 Plasma Physics

As mentioned before, plasma is regarded as the fourth state of matter. It consists in an ionized hot gas where the fraction of free charged particles - ions and electrons - is sufficiently high such that it dictates the behaviour. That is to say, its dynamics is primarily dominated by Coulomb and Lorentz forces. Most plasmas consist of positive ions and (negative) electrons, although electro-negative plasmas, with negative ions, do exist. Plasmas are defined principally by two parameters: plasma density n in m^{-3} and electron temperature T_e in eV. Figure 2.1 shows an overview of all plasmas, both artificial and naturally occurring, based on these two parameters. This includes everything from space plasmas such as the Solar corona, solar wind and the Earth's ionosphere, to low pressure discharges used in plasma processing, to fusion plasmas.

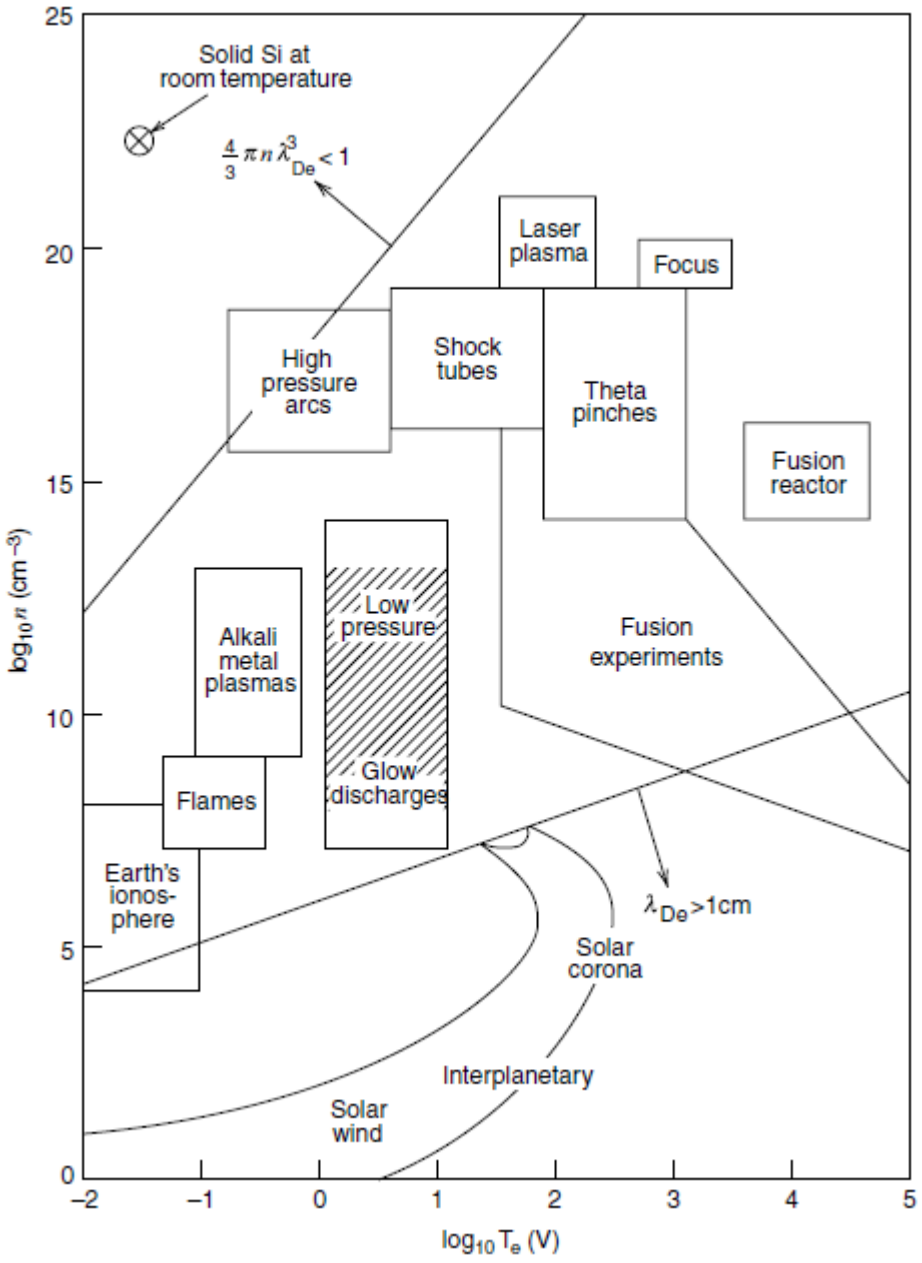

Figure 2.1: Overview of artificial an natural plasmas on a $\log T_e$ versus $\log n$ scale. From [68]

2.1.1 Quasi-neutrality

The electron temperature is a measure of the electron energy distribution function, which often (but not always) follows a Maxwell-Boltzmann distribution. The plasma density refers to the number density of particles. More precisely, one speaks of ion density and electron density, however the bulk plasma is generally quasi-neutral, that is to say:

$$e\sum_j Z_j n_j = e n_e \tag{2.1}$$

where Z_j is the atomic charge number for $j = 1, 2, ...$ and e the elementary charge. In other words the total charge density of all ions equals that of the electrons. In the case where the fraction of ions with a charge number > 1 are negligible (which is the case for many laboratory low pressure discharges), the ion density equals the electron density and one simply refers to the plasma density. Another important plasma property is the plasma potential. In absence of any time-varying magnetic fields, Faraday's law of induction and Gauss' law can be combined to yield Poisson's equation:

$$\nabla^2\Phi = -\frac{\rho}{\epsilon_0} = -\frac{e(n_i - n_e)}{\epsilon_0} \tag{2.2}$$

This states that any net charge density will produce an electric potential. Particularly the electrons in a plasma a strongly affected by (but also affect) the plasma potential.

2.1.2 Boltzmann Relation

The momentum equation for a species (i.e. ions, electrons etc.) in a plasma is given by Equation 2.3 [68, p.31].

$$mn\left[\frac{\partial \mathbf{u}}{\partial t} + (\mathbf{u}\cdot\nabla)\cdot\mathbf{u}\right] = qn\left(\mathbf{E} + \mathbf{u}\times\mathbf{B}\right) - \nabla\cdot\mathbf{\Pi} + \mathbf{f}|_c \tag{2.3}$$

Here m is the particle mass, $\mathbf{u}$ its velocity vector, q the electric charge (generally $\pm e$), $\mathbf{E}$ the electric field, $\mathbf{B}$ the magnetic field, $\mathbf{\Pi}$ the pressure tensor and $\mathbf{f}|_c$ a collisional term. For a steady state, collision-less plasma, negligible inertial forces, with an isotropic pressure, in the absence of a magnetic field and invoking the ideal gas law $p = nk_BT$ and a conservative electric field (i.e. $\mathbf{E} = -\nabla\Phi$), Equation 2.3

for electrons, reduces to:

$$\nabla \left(e\Phi - k_B T_e \ln n_e \right) = 0 \tag{2.4}$$

which leads to the Boltzmann relation for electrons:

$$n(\mathbf{r}) = n_0 \exp\left(-\frac{e\Phi(\mathbf{r})}{k_B T_e} \right) \tag{2.5}$$

Where $k_B = 8.617 \cdot 10^{-5}$ eV/$cdot$K^{-1} is the Boltzmann constant. Note that the e and k_B can be dropped when expressing T_e in eV and Φ in V, which is common practice in plasma physics and something we will do as well throughout this thesis.

2.1.3 Debye Length

When substituting the Boltzmann relation, Equation 2.5, into Poisson's equation, Equation 2.2, for a quasi-neutral plasma ($n = n_e = n_i$), obtaining the Taylor expansion for $\Phi \ll T_e$ we find:

$$\nabla^2 \Phi = \frac{en}{\epsilon_0} \frac{\Phi}{T_e} \tag{2.6}$$

the solution to which is:

$$\Phi(\mathbf{r}) = \Phi_0 \exp\left(\frac{-|\mathbf{r}|}{\lambda_D} \right) \tag{2.7}$$

The characteristic scale length λ_D is the Debye length, given by:

$$\lambda_D = \left(\frac{\epsilon_0 T_e}{en} \right)^{1/2} \tag{2.8}$$

The Debye length is the length scale over which significant space charges can exist; over length scales larger than the Debye length the plasma is quasi-neutral. It is also the length scale over which Coulomb potentials are shielded in the plasma; a particle only experiences a Coulomb force due to the charges within a sphere of radius λ_D around itself.

2.1.4 Plasma Sheaths

Most artificial plasmas on Earth are generated inside a vacuum vessel and therefore the plasma is in contact with the walls of the vessel. Near theses surfaces a plasma sheath forms, where the plasma is no longer quasi-neutral. In an electro-positive plasma the negative species, the electrons are much more mobile than the ions,

since $m_e/m_i \ll 1$ and $T_i/T_e \ll 1$. The the current density to a grounded surface is therefore predominantly negative, charging the plasma to a positive potential and resulting in a potential gradient towards the wall. In a cold plasma where $T_i \ll T_e$ the electrons will redistribute themselves leading to a density gradient on the order of the Debye length with mono-energetic ions being accelerated to the wall through the sheath potential [68, p.165]. Between the sheath and the bulk plasma there is a intermediate pre-sheath region.

For a collision-less sheath we can combine conservation of energy and continuity of ion flux to obtain an expression for the ion density:

$$n_i = n_{is}\left(1 - \frac{2e\Phi}{m_i u_s^2}^{-1/2}\right) \tag{2.9}$$

where n_{is} and u_s are the ion density and velocity at the sheath edge ($x = 0$). Plugging in this equation for n_i and the Boltzmann relation for n_e in Poisson's equation

$$\frac{1}{2}\left(\frac{d\Phi}{dx}\right)^2 = \frac{en_s}{\epsilon_0}\left[T_e \exp\frac{\Phi}{T_e} - T_e - 2\mathcal{E}_s\left(1 - \frac{\Phi}{\mathcal{E}_s}\right)^{1/2} - 2\mathcal{E}_s\right] \tag{2.10}$$

where $2e\mathcal{E} = m_i u_s^2$. Although this equation can be integrated numerically, it's sufficient to realize that the right hand side (RHS) has to be positive for a solution to exist. Expanding the RHS using a Taylor expansion, leads to the inequality $2\mathcal{E}_s \geq T_e$ or rather:

$$u_s \geq u_B = \left(\frac{eT_e}{m_i}\right)^{1/2} \tag{2.11}$$

which is the Bohm sheath criterion. As we defined $\Phi(0) = 0$ at the sheath edge, and we now have found that $u(0) = u_B$ it follows that the potential drop accelerating the ions to the Bohm velocity is $e\Phi_p = m_i u_B^2/2$ such that $\Phi_p = T_e/2$. Substituting this value in the Boltzmann relation Equation 2.5 yields:

$$n = n_0 \exp\left(-\frac{1}{2}\right) \approx 0.61 n_0 \tag{2.12}$$

In other words, the density at the sheath edge is about 0.61 times the bulk density.

Sheath voltages are often driven to high voltages such that the Boltzmann relation goes to zero $n_e \to 0$ and only ions are present in the plasma. A self-consistent solution of a high voltage sheath is the Child-Langmuir sheath. Starting with

$m_i u^2(x)/2 = -e\Phi(x)$ and $en(x)u(x) = J_0$ we can solve for $n(x)$, insert this into Poisson's equation, Equation 2.2 and after some manipulation we find [68, p.176]:

$$j_0 = \frac{4}{9}\epsilon_0 \left(\frac{2e}{m_i}\right)^{1/2} \frac{V^{3/2}}{s^2} \tag{2.13}$$

Which is the Child law for space charge limited current density in a planar diode. Substituting the explicit value $j_0 = en_s u_B$ and solving for s yields:

$$s = \frac{\sqrt{2}}{3}\lambda_{Ds} \left(\frac{2V}{T_e}\right)^{3/4} \tag{2.14}$$

with λ_{Ds} the Debyelength at the sheath edge. This last equation is of particular interest if one once to take into account the sheath expansion in Langmuir probes as we will see in chapter 3.

2.1.5 Floating Potential

When the wall in a bounded plasma is not grounded or biased, it is said to be floating and its potential will be at the floating potential. To determine the floating potential consider that the ion flux to the wall is $\Gamma_i = n_s u_B$, while the electron flux is $\frac{1}{4} n_s \bar{u}_e \exp(\Phi_f/T_e)$, where $\bar{u}_e = (8eT_e/\pi m_e)^{1/2}$ is the mean electron speed. The floating potential is the wall potential for which $\Gamma_i = \Gamma_e$, since in that case the wall is no longer accumulating charge. Equating both fluxes and rearranging yields an expression for the floating potential:"

$$\Phi_f = -\frac{T_e}{2} \ln\left(\frac{m_i}{2\pi m_e}\right) \tag{2.15}$$

2.1.6 Waves in Plasmas

Due to the presence of charged particles, plasmas couple to electric and magnetic fields. The complex interaction between fields and charges support a variety of propagating wave phenomena, which can be divided into electrostatic and electromagnetic waves. The former are always longitudinal waves while the latter always have a transversal component, but can also have a longitudinal component. Other important factors is whether the wave propagates primarily by electron or ion motions and whether it requires the presence of a magnetic field as well as the direction of the magnetic field with respect to the propagation direction.

Plasma Frequency

Imagine a slab of electrons that displace a small distance δ with respect to the immobile ions (since $m_i \gg m_e$). The electric field created by separating the ions and electrons is $E_x = en\delta/\epsilon_0$. Taking into account only Coulomb forces, the equation of motion for the electrons reads:

$$\frac{d^2\delta}{dt^2} = -\omega_{pe}\delta \tag{2.16}$$

where:

$$\omega_{pe} = \left(\frac{e^2 n_e}{\epsilon_0 m_e}\right)^{1/2} \tag{2.17}$$

This is the equation of a harmonic oscillator with natural frequency ω_{pe} and describes a sinusoidal oscillation of the electron 'cloud' with respect to the ions. In reality the ions are not immobile but also move slightly. Similarly we can define and ion plasma frequency:

$$\omega_{pi} = \left(\frac{e^2 n_i}{\epsilon_0 m_i}\right)^{1/2} \tag{2.18}$$

And the plasma frequency then is $\omega_p = (\omega_{pe}^2 + \omega_{pi}^2)^{1/2}$. However since generally $m_i \gg m_e$, $\omega_p \approx \omega_{ep}$.

Cyclotron Frequency

Consider the Lorentz force in a plasma with $\mathbf{E} = 0$ and $\mathbf{B} = \hat{z}B_0$. The equations of motion are:

$$m\frac{du_x}{dt} = qu_y B_0 \tag{2.19}$$

$$m\frac{du_y}{dt} = -qu_x B_0 \tag{2.20}$$

$$m\frac{du_z}{dt} = 0 \tag{2.21}$$

Differentiating the first equation and eliminating v_y using the second equation we find:

$$\frac{d^2u_x}{dt^2} = -\omega_c^2 u_x \tag{2.22}$$

Which again is the equation of a harmonic oscillator, this time with natural frequency:

$$\omega_c = \left(\frac{qB_0}{m}\right)^{1/2} \tag{2.23}$$

the cyclotron frequency. Both an electron cyclotron and ion cyclotron frequency exist with m_e, m_i and $q = \mp e$ respectively. The electron cyclotron resonance frequency is underpins the heating mechanism is ECR thrusters.

Langmuir Waves

Langmuir waves are longitudinal electron density fluctuations that propagate in unmagnetized plasmas or in magnetized plasmas parallel to the magnetic field $\mathbf{k} \parallel \mathbf{B}$. Consider the momentum equation, Equation 2.3 in the absence of a magnetic field and furthermore $p_e = en_eT_e$ and the adiabatic equation of state $\nabla p_e/p_e = \gamma \nabla n_e/n_e$.

$$mn_e \left[\frac{\partial \mathbf{u}_e}{\partial t} + (\mathbf{u}_e \cdot \nabla)\mathbf{u}_e \right] = -en_e\mathbf{E} - \gamma eT_e \nabla n_e \tag{2.24}$$

Suppose furthermore the small signal quantities: n_1, E_1 and u_1, such that:

$$n_e = n_0 + n_1, \qquad \mathbf{E} = \hat{x}E_1, \qquad \mathbf{u}_e = \hat{x}u_1 \tag{2.25}$$

The small signal quantities vary sinusoidally:

$$n_1, E_1, u_1 \sim \exp \mathrm{i}(\omega t - k_x x) \tag{2.26}$$

Substituting the small signal quantities into the momentum equation of Equation 2.24 as well as the continuity equation and Gauss' law we find the following three equations [68, p.102]

$$\omega n_1 - k_x n_0 u_1 = 0 \tag{2.27}$$

$$\mathrm{i}\omega m n_0 u_1 = -en_0E_1 + \mathrm{i}k_x \gamma eT_e n_1 \tag{2.28}$$

$$\mathrm{i}k_x \epsilon_0 E_1 = en_1 \tag{2.29}$$

Combining the above three equations and factoring out the first-order quantities we find the following dispersion relation:

$$\omega^2 = \omega_{pe}^2 + k_x^2 c_\gamma^2 \tag{2.30}$$

with

$$c_\gamma = \left(\frac{\gamma eT_e}{m_e} \right)^{1/2} \tag{2.31}$$

the adiabatic electron sound speed. For one-dimensional motion $\gamma = 3$

Ion Acoustic Waves

At lower frequencies ions can participate in the motion, leading to ion acoustic waves, similar to sound waves in a neutral gas. Using the same approach as above (small signal quantities) [46, p.262] the dispersion relation for ion acoustic waves can be derived.

$$\omega^2 = k^2 \left(\frac{T_e(1 + k^2\lambda_D^2)^{-1} + \gamma_i T_i}{m_i} \right) \tag{2.32}$$

Dielectric Tensor

Assume again a plasma with $\mathbf{B}_0 = \hat{z}B_{z0}$ and $\mathbf{E}_0 = 0$ and furthermore assume small sinusoidal variations of the electric field and velocity $\tilde{E}, \tilde{v}$. Plugging these into the equations of motion and solving for $\tilde{u}_x, \tilde{u}_y$ yields [68, p.111]:

$$\tilde{u}_x = -\frac{q}{m} \frac{\mathrm{i}\omega\tilde{E}_x - \omega_c\tilde{E}_y}{\omega^2 - \omega_c^2} \tag{2.33}$$

$$\tilde{u}_y = -\frac{q}{m} \frac{\mathrm{i}\omega\tilde{E}_y + \omega_c\tilde{E}_x}{\omega^2 - \omega_c^2} \tag{2.34}$$

Now consider Ampère's law:

$$\nabla \times \tilde{\mathbf{H}} = \mathrm{i}\omega\epsilon_0\tilde{\mathbf{E}} + \tilde{\mathrm{i}} \equiv \mathrm{i}\omega\epsilon_p \cdot \tilde{\mathbf{E}} \tag{2.35}$$

From which follows that the dielectric tensor ϵ_p is:

$$\epsilon_p = \epsilon_0\mathbf{K} = \epsilon_0 \begin{pmatrix} S & -\mathrm{i}D & 0 \\ \mathrm{i}D & S & 0 \\ 0 & 0 & P \end{pmatrix} \tag{2.36}$$

where $\mathbf{K}$ is the dispersion tensor with:

$$S = 1 - \frac{\omega_{pe}^2}{\omega^2 - \omega_{ce}^2} - \frac{\omega_{pi}^2}{\omega^2 - \omega_{ci}^2} \tag{2.37}$$

$$D = \frac{\omega_{ce}}{\omega} \frac{\omega_{pe}^2}{\omega^2 - \omega_{ce}^2} - \frac{\omega_{ci}}{\omega} \frac{\omega_{pi}^2}{\omega^2 - \omega_{ci}^2} \tag{2.38}$$

$$P = 1 - \frac{\omega_p^2}{\omega^2} \tag{2.39}$$

Wave Dispersion

To derive the dispersion relations of waves in magnetized plasmas we first look at Maxwell's curl equations, with sinusoidal variations $\tilde{\mathbf{E}}, \tilde{\mathbf{H}}$ and a wave vector $\mathbf{k}$:

$$\mathbf{k} \times \tilde{\mathbf{E}} = \omega\mu_0\tilde{\mathbf{H}} \tag{2.40}$$

$$\mathbf{k} \times \tilde{\mathbf{H}} = -\omega\epsilon_0\mathbf{K} \cdot \tilde{\mathbf{E}} \tag{2.41}$$

Combining these equations we get a wave equation for electromagnetic waves in plasmas:

$$\mathbf{k} \times (\mathbf{k} \times \tilde{\mathbf{E}}) + k_0^2\mathbf{K} \cdot \tilde{\mathbf{E}} = 0 \tag{2.42}$$

Note that $k_0 = \omega/c$ the propagation constant of a plane wave in vacuum, and that $c = (\epsilon_0\mu_0)^{-1/2}$ is the speed of light in vacuum. To find solutions for Equation 2.42 we first need to define the wave vector $\mathbf{k}$. We chose this to lie in the $x - z$ plane and we furthermore define an angle ϕ to be the angle between $\mathbf{k}$ and $\mathbf{B}$ such that $k = \alpha\cos\phi$ and $T = \alpha\sin\phi$, where $\alpha = |\mathbf{k}|$ and $\alpha^2 = T^2 + k^2$. Lastly the index of refraction is defined as $N = \alpha/k_0$. To solve the system of equations following from Equation 2.42 we require that the determinant is zero.

$$\det\begin{bmatrix} N^2\cos^2\phi - S & \mathrm{i}D & -N^2\cos\phi\sin\phi \\ -\mathrm{i}D & N^2 - S & 0 \\ -N^2\cos\phi\sin\phi & 0 & -N^2\sin^2\phi - P \end{bmatrix} = 0 \tag{2.43}$$

Evaluating the determinant yields biquadratic equation in N:

$$aN^4 - bN^2 + c = 0 \tag{2.44}$$

where

$$a = S\sin^2\phi + P\cos^2\phi \tag{2.45}$$

$$b = (S^2 - D^2)\sin^2\phi + PS(1 + \cos^2\phi) \tag{2.46}$$

$$c = (S^2 - D^2)P \tag{2.47}$$

There are two different solutions of N^2 for each angle ϕ corresponding to the two allowed polarizations of the electric field. Since $b^2 - 4ac$ is always positive, N^2 is real and N is either real and the wave propagates or N is imaginary and the wave is cutoff [68, p.114]. To better shed more light on the nature of the wave dispersion

it is more useful to solve for ϕ as a function of N^2. To that end we define two combinations of the dielectric components:

$$R = S - D \tag{2.48}$$

$$L = S + D \tag{2.49}$$

such that $S^2 - D^2 = RL$. Substituting the expressions of the dielectric components from Equation 2.37,2.38 we find

$$R = 1 - \frac{\omega_{pe}^2}{\omega(\omega - \omega_{ce})} - \frac{\omega_{pi}^2}{\omega(\omega + \omega_{ci})} \tag{2.50}$$

$$L = 1 - \frac{\omega_{pe}^2}{\omega(\omega + \omega_{ce})} - \frac{\omega_{pi}^2}{\omega(\omega - \omega_{ci})} \tag{2.51}$$

The biquadratic equation of 2.44 can be solved for ϕ yielding:

$$\tan^2 \phi = -\frac{P(N^2 - R)(N^2 - L)}{(N^2 - P)(SN^2 - RL} \tag{2.52}$$

Principal Waves

Using equation 2.52 we can analyze the different kinds of principal waves, their resonances $N \to \infty$ and cut-offs $N \to 0$. We consider two distinct cases $\mathbf{k} \parallel \mathbf{B}_0$ and $\mathbf{k} \perp \mathbf{B}_0$, in the former case $\phi = 0$ and the numerator of Equation 2.52 is zero and in the latter case $\phi = \pi/2$ and the denominator is zero. There are three solutions leading to the numerator being zero: $P = 0$ which are simply the plasma oscillations, $N^2 = R$ and $N^2 = L$. For the latter two cases the dispersion relation is given by:

$$N_R^2 = 1 - \frac{\omega_p^2}{(\omega - \omega_{ce})(\omega + \omega_{ci})} \tag{2.53}$$

$$N_R^2 = 1 - \frac{\omega_p^2}{(\omega + \omega_{ce})(\omega - \omega_{ci})} \tag{2.54}$$

$$\tag{2.55}$$

Which are the dispersion relations for the right hand polarized (RHP) and left hand polarized (LHP) waves. The RHP wave has a resonance at $\omega = \omega_{ce}$ and the LHP wave was a resonance at $\omega = \omega_{ci}$. The cutoffs can be found by solving

$(\omega \mp \omega_{ce})(\omega \pm \omega_{ci}) = \omega_p^2$. However since $\omega_{ce} \gg \omega_{ci}$, these can be simplified to:

$$\omega_R = \frac{\omega_{ce} + \sqrt{\omega_{ce}^2 + 4\omega_p^2}}{2} \tag{2.56}$$

$$\omega_L = -\frac{\omega_{ce} + \sqrt{\omega_{ce}^2 + 4\omega_p^2}}{2} \tag{2.57}$$

which are the cut-off frequencies for the L and R waves. When $\mathbf{k} \perp \mathbf{B}_0$ and therefore the denominator of Equation 2.52 is zero there are two solutions: either $N^2 = P$ which is called the ordinary wave, with the following dispersion relation:

$$N_O^2 = 1 - \frac{\omega_p^2}{\omega^2} \tag{2.58}$$

This is the same relation as for electromagnetic waves in un-magnetized plasmas: $\omega^2 = k^2c^2 + \omega_p^2$; it has no resonance and the cutoff is $\omega = \omega_p$. The other solution is $SN^2 = RL$ which is referred to as the extraordinary wave and has the following dispersion relation:

$$N_X^2 = \frac{\left[1 - \frac{\omega_p^2}{(\omega - \omega_{ce})(\omega + \omega_{ci})}\right]\left[1 - \frac{\omega_p^2}{(\omega + \omega_{ce})(\omega - \omega_{ci})}\right]}{1 - \frac{\omega_{pe}^2}{\omega^2 - \omega_{ce}^2} - \frac{\omega_{pi}^2}{\omega^2 - \omega_{ci}^2}} \tag{2.59}$$

From the above equation it can be immediately glanced that the cut-offs of the X wave are the same as those for the R and L waves, i.e. ω_R, ω_L. The resonances can be found by setting the numerator zero. This results in the following biquadratic equation:

$$a\omega^4 - b\omega^2 + c = 0 \tag{2.60}$$

$$a = 1 \tag{2.61}$$

$$b = \omega_{ce}^2 + \omega_{pe}^2 + \omega_{pi}^2 + \omega_{ci}^2 \tag{2.62}$$

$$c = \omega_{ce}^2\omega_{ci}^2 + \omega_{ce}^2\omega_{pi}^2 + \omega_{pe}^2\omega_{ci}^2 \tag{2.63}$$

When $b^2 \gg 4ac$, which is the case here the two roots of the quadratic equation can be expanded using a Taylor approximation resulting in $\omega^2 = b/a$ for the positive root and $\omega = c/b$ for the negative root. The positive root for the above equation, taking into account that $\omega_{pe} \gg \omega_{pi}$ and $\omega_{ce} \gg \omega_{ci}$, is then:

$$\omega_{UH}^2 \approx \omega_{pe}^2 + \omega_{ce}^2 \tag{2.64}$$

the upper hybrid resonance which is the root sum square of the electron plasma and cyclotron frequencies. The negative root is given by:

$$\omega^2 = \frac{\omega_{ce}^2\omega_{ci}^2 + \omega_{ce}^2\omega_{pi}^2 + \omega_{pe}^2\omega_{ci}^2}{\omega_{pe}^2 + \omega_{ce}^2 + \omega_{pi}^2 + \omega_{ci}^2} \tag{2.65}$$

This equation can be further simplified, by again noting that $\omega_{pe} \gg \omega_{pi}$ and $\omega_{ce} \gg \omega_{ci}$ so that $\omega_{ci}^2, \omega_{pi}^2$ can be dropped from the denominator. We further more divide both the numerator and denominator by m_e/m_i resulting in:

$$\omega^2 = \frac{\omega_{ce}\omega_{ci}\left(\omega_{ci}^2 + \omega_{pi}^2 + \omega_{pi}^2\dfrac{\omega_{ci}}{\omega_{ce}}\right)}{\omega_{pi}^2 + \omega_{ci}\omega_{ce}} \tag{2.66}$$

In the numerator we can then drop the third term inside the parenthesis since $\omega_{ce} \gg \omega_{ci}$ and if we also assume that $\omega_{pi} \gg \omega_{ci}$ which is the case for many laboratory plasmas and plasmas for materials processing [68, p.119] we find an expression for the lower hybrid frequency:

$$\frac{1}{\omega_{LH}^2} = \frac{1}{\omega_{ce}\omega_{ci}} + \frac{1}{\omega_{pi}^2} \tag{2.67}$$

A summary of all principle waves is found in Table 2.1 and a plot of the dispersion relation can be seen in Figure 2.2. It can be seen that for very low frequencies $\omega \ll \omega_{ci}$ the wave dispersion for the L,R and X wave all reduce to [68]:

$$\alpha^2 = k_0^2\left(1 + \frac{\omega_{pi}^2}{\omega_{ci}^2}\right) \tag{2.68}$$

For reasonably high densities such that $\omega_{pi} \gg \omega_{ci}$ the 1 can be disregarded and the phase velocity $v_{ph} = \omega/k$ is the Alfvén velocity:

$$v_A = \frac{\omega_{ci}}{\omega_{pi}}c = \frac{B_0}{\sqrt{\mu_0 m_i n_i}} \tag{2.69}$$

2.1.7 Helicon Waves

Helicon waves are a type of whistler waves that propagate in a bounded plasma. Whistlers are quasi-longitudinal (i.e. $\phi \simeq 0$) R waves in the frequency range $\omega_{LH} \ll$

Wave	Cut-offs ($k = 0$)	Resonances ($k = \infty$)
R wave	$\omega \approx \dfrac{\omega_{ce} + \sqrt{\omega_{ce}^2 + 4\omega_p^2}}{2}$	$\omega = \omega_{ce}$
L wave	$\omega \approx \dfrac{-\omega_{ce} + \sqrt{\omega_{ce}^2 + 4\omega_p^2}}{2}$	$\omega = \omega_{ci}$
X wave	Both as above	$\omega_{UH}^2 \approx \omega_{pe}^2 + \omega_{ce}^2$ and $\omega_{LH}^{-2} \approx \omega_{pi}^{-2} + (\omega_{ce}\omega_{ci})^{-2}$ for $\omega_{pi} \gg \omega_{ci}$
O wave	$\omega = \omega_p$	None

Table 2.1: Summary of principal waves.

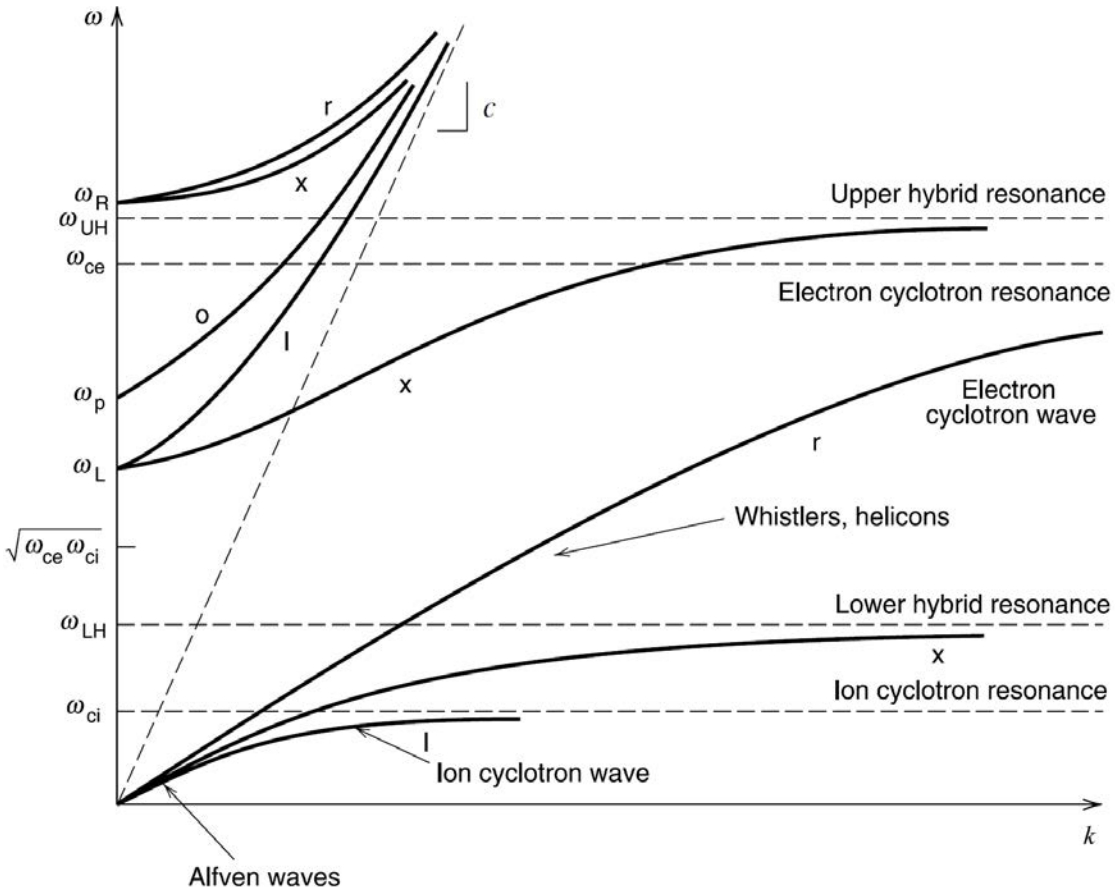

Figure 2.2: Wave dispersion for principal waves in plasmas.

$\omega \ll \omega_{ce}$. To be able to derive the dispersion relation we need to go back to the bi-quadratic equation for N^2, Equation 2.44. Introducing $\xi = N^2 - 1$, rewriting the equation in terms of ξ^{-1} and solving for ξ^{-1} leads to Equation 2.73 [13, p.198]. Note that since $\omega \gg \omega_{LH}$ we have neglected the ion motion, dropping the terms with ω_{ci}, ω_{pi}.

$$N^2 = 1 + \left[\frac{2(a - b + c)}{b - 2a \pm \sqrt{b^2 - 4ac}}\right] \tag{2.70}$$

where a, b, c are a defined earlier. Writing this in terms of the dielectric components and dividing both the numerator and denominator by $1 - S$ we find:

$$N^2 = 1 - \left[\frac{2\left(1 - S - \dfrac{D^2}{1-S}\right)P}{2P + \left(S + \dfrac{D^2}{1-S} + \dfrac{S-P}{1-S}\right)\sin^2\phi \pm \Lambda}\right] \tag{2.71}$$

$$\Lambda = \left[(\frac{S^2 - D^2 - SP}{1-S})^2 \sin^4\phi + 4\frac{D^2P^2}{1-S}\cos^2\phi\right]^{1/2} \tag{2.72}$$

If we substitute equations 2.37 - 2.39 for the dielectric components (but ignoring the part due to ion motion) we find:

$$N^2 = 1 - \left[\frac{2\dfrac{\omega_{pe}^2}{\omega^2}\left(1 - \dfrac{\omega_{pe}^2}{\omega^2}\right)}{2\left(1 - \dfrac{\omega_{pe}^2}{\omega^2}\right) - \dfrac{\omega_{ce}^2}{\omega^2}\sin^2\phi \pm \Lambda}\right] \tag{2.73}$$

$$\Lambda = \left[\frac{\omega_{ce}^4}{\omega^4}\sin^4\phi + 4\frac{\omega_{ce}^2}{\omega^2}\left(1 - \frac{\omega_{pe}^2}{\omega^2}\right)^2\cos^2\phi\right]^{1/2} \tag{2.74}$$

Equation 2.73 is the Altar-Appleton-Hartree dispersion relation and it conveniently shows how the refraction index N deviates from the vacuum dispersion $N^2 = 1$. For the dispersion of quasi-longitudinal waves the equation can be expanded around $\phi = 0$. In that case Λ reduces to only the term with $\cos^2\phi$, substituting this in Equation 2.73 and simplifying yields, for the R wave (i.e. $+\Lambda$):

$$N_r^2(\phi) = 1 - \left[\frac{1 - S - \dfrac{D^2}{1-S}}{1 - \left|\dfrac{D}{1-S}\cos\phi\right|}\right] \tag{2.75}$$

where the minus sign in the denominator results from the fact that $P < 1$, assuming that $\omega < \omega_{pe}$. Substituting the expressions for the dielectric components yields:

$$N_r^2(\phi) = 1 - \frac{\omega_{pe}^2/\omega^2}{1 - \left|\frac{\omega_{ce}}{\omega}\cos\phi\right|} \tag{2.76}$$

Now in the case that $\omega_{LH} \ll \omega \ll \omega_{ce}$ and furthermore $\omega_{pe}^2 \gg \omega\omega_{ce}$ this reduces to:

$$N^2 \approx \frac{\omega_{pe}^2}{\omega\omega_{ce}\cos\phi} \tag{2.77}$$

Rewriting this in terms of k, ω yields:

$$\alpha = \frac{\omega}{k}\frac{n_0 e\mu_0}{B_0} \tag{2.78}$$

Which is the basic dispersion relation for helicon waves [31]. Helicon waves occur in axially magnetized plasmas confined in a long cylinder, i.e. $a \ll l$ where R is the radius and l the length and the wave number α is therefore of order a^{-1}. In such a cylinder the boundary condition for a waves with $ka \ll 1$ is [31]:

$$mkJ_m(Ta) = 0 \tag{2.79}$$

For the lowest radial mode, $m = 1$, the Bessel root is 3.83 and we find:

$$n_0 \approx \frac{3.83}{e\mu_0 a}\frac{kB_0}{\omega} \tag{2.80}$$

In other words the density is proportional to the magnetic field, for a given cylinder and frequency.

Trivelpiece-Gould Waves

Helicon waves are excited together with second type of wave; electrostatic electron cyclotron waves named Trivelpiece-Gould (TG) waves. These waves are excited near the radial boundary of the plasma. If we go back to Equation 2.75 but now substitute the dielectric components including collisional damping, with ν the collision frequency:

$$S = 1 - \frac{\omega + \mathrm{i}\nu}{\omega}\frac{\omega_{pe}^2}{(\omega + \mathrm{i}\nu)^2 - \omega_{ce}^2} \tag{2.81}$$

$$D = \frac{\omega_{ce}}{\omega}\frac{\omega_{pe}^2}{(\omega + \mathrm{i}\nu)^2 - \omega_{ce}^2} \tag{2.82}$$

$$P = 1 - \frac{\omega_{pe}^2}{\omega(\omega + \mathrm{i}\nu)} \tag{2.83}$$

with the same assumptions as before, $\omega_{LH} \gg \omega \gg \omega_{ce}$ and $\omega_{pe}^2 \gg \omega\omega_{ce}$ we find:

$$N_r^2(\phi) \approx \frac{\omega_{pe}^2}{\omega[\omega_{ce}\cos\phi - (\omega + \mathrm{i}\nu)]} \tag{2.84}$$

This can be solved for ω to find the dispersion relation:

$$\omega = \frac{\alpha^2 c^2}{\omega_{pe}^2 + \alpha^2 c^2}\left(\omega_{ce}\cos\phi - \nu\right] \tag{2.85}$$

The above equation suggests a characteristic length, or 'anomalous skin depth' c/ω_{pe} [110]. In the limits $\alpha c \ll \omega_{pe}$ and $\alpha c \gg \omega_{pe}$ this reduces to:

$$\omega = \omega_{ce}\frac{\alpha k c^2}{\omega_{pe}^2} - \mathrm{i}\nu\frac{\alpha^2 c^2}{\omega_{pe}^2} \tag{2.86}$$

$$\omega = \omega_{ce}\frac{k}{\alpha} - \mathrm{i}\nu \tag{2.87}$$

The former are 'long' waves that are weakly damped which are the helicon waves; if we disregard the imaginary component we find again the dispersion relation of Equation 2.78. The latter are 'short', heavily damped waves that are the TG-waves. The anomalous skin depth is the reason why the TG-waves which are excited at the boundary do not penetrate into the core of the plasma.

Alternatively we can also solve Equation 2.85 for k, which yields a quadratic equation, with solution:

$$\alpha = \frac{k}{2\delta}\left[1 \mp \left(1 - \frac{4\delta k_w^2}{k^2}\right)^{1/2}\right] \approx \frac{k}{2\delta}\left[\mp\left(1 - \frac{2\delta k_w^2}{k^2}\right)\right] \approx \begin{cases} k_w^2/k \\ k/\delta \end{cases} \tag{2.88}$$

with

$$k_w^2 = \frac{\omega n_0 e \mu_0}{B_0} \qquad \text{and} \qquad \delta = \frac{\omega + \mathrm{i}\nu}{\omega_c} \tag{2.89}$$

where the negative sign is the helicon wave dispersion while the positive sign is the TG-wave dispersion. Again it is apparent that the TG-waves are damped while the helicon waves are not.

Wave Pattern

To derive the wave pattern we begin with Maxwell's equations and the assumption that all varying quantities are of the form: $\exp \mathrm{i}(m\theta + kz - \omega t)$.

$$\nabla \cdot \mathbf{B} = 0 \tag{2.90}$$

$$\nabla \times \mathbf{B} = \mu_0(\mathbf{j} - \mathrm{i}\omega\epsilon_0\mathbf{E}) = -\mathrm{i}\omega\epsilon_0\mathbf{K}\mathbf{E} \tag{2.91}$$

$$\nabla \times \mathbf{E} = -\mathrm{i}\omega\mathbf{B} \tag{2.92}$$

Furthermore, the plasma current, neglecting the ion motion, is $\mathbf{j} = -en\mathbf{u}$ and the continuity equation $\nabla \cdot \mathbf{j} = 0$. The equation of motion for the electrons is:

$$-i\omega m_e\mathbf{u} = -e\left(E + \mathbf{u} \times \mathbf{B}_0\right) - m_e\nu\mathbf{u} \tag{2.93}$$

Solving the above equation for $\mathbf{E}$ and substituting the expression for $\mathbf{j}$ we find:

$$\mathbf{E} = \frac{B_0}{en_0}\left[\mathrm{i}\delta\mathbf{j} + \hat{\mathbf{z}} \times \mathbf{j}\right] \tag{2.94}$$

where δ is as specified in the previous paragraph. If we now combine the Maxwell's equation above with our newfound expression for $\mathbf{E}$ while neglecting the displacement current in the curl $\mathbf{B}$ equation we can find:

$$\mathrm{i}\omega\mathbf{B} = \frac{B_0}{en_0\mu_0}\left[\mathrm{i}\delta\nabla \times \nabla \times \mathbf{B} + \nabla \times [\hat{\mathbf{z}} \times (\nabla \times \mathbf{B})]\right] \tag{2.95}$$

realizing that the last term is $ik\nabla \times \mathbf{B}$ this becomes:

$$\delta\nabla \times \nabla \times \mathbf{B} - k\nabla \times \mathbf{B} - k_w^2\mathbf{B} = 0 \tag{2.96}$$

This equation can be factored into:

$$(\alpha_1 - \nabla\times)(\alpha_2 - \nabla\times)\mathbf{B} = 0 \tag{2.97}$$

with α_1, α_2 the roots of

$$\delta\alpha^2 - \alpha - k_w^2 = 0 \tag{2.98}$$

which is the quadratic equation that follows from Equation 2.85 and the solution of which is given by Equation 2.88. The general solution of Equation 2.96 is $\mathbf{B} = \mathbf{B}_1 + \mathbf{B}_2$ where $\nabla \times \mathbf{B}_1 = \alpha_1$ and $\nabla \times \mathbf{B}_2 = \alpha_2$. Taking the curl of these last two expressions and using Equation 2.90 we can write:

$$\nabla^2\mathbf{B}_1 + \alpha_1^2\mathbf{B}_1 = 0 \tag{2.99}$$

$$\nabla^2\mathbf{B}_2 + \alpha_2^2\mathbf{B}_2 = 0 \tag{2.100}$$

for the helicon wave, $\alpha_1 = k_w^2/k$. We can write out the wave equation above for the z-component:

$$\frac{\partial^2 B_z}{\partial r^2} + \frac{1}{r}\frac{\partial B_z}{\partial r} + \left(T^2 - \frac{m^2}{r^2}\right) B_z = 0 \tag{2.101}$$

The r, θ components can be obtained from $\nabla \times \mathbf{B}_1 = \alpha_1$ and yield:

$$\mathrm{i}\frac{m}{r} B_z - \mathrm{i} B_\theta = \alpha B_r \tag{2.102}$$

$$\mathrm{i}k B_r - \frac{\partial B_z}{\partial r} = \alpha B_\theta \tag{2.103}$$

Equation 2.101 is the Bessel equation with solution:

$$B_z(r) C J_m(Tr) \tag{2.104}$$

After some manipulation we find the expressions for the wave fields [29]:

$$B_r = \frac{2A}{T}\left[\frac{\alpha m}{r} J_m(Tr) + k J_m'(Tr)\right] \cos(m\theta + kz - \omega t) \tag{2.105}$$

$$B_\theta = -\frac{2A}{T}\left[\frac{km}{r} J_m(Tr) + \alpha J_m'(Tr)\right] \sin(m\theta + kz - \omega t) \tag{2.106}$$

$$B_z = 2AT J_m(Tr) \sin(m\theta + kz - \omega t) \tag{2.107}$$

$$E_r = \frac{\omega}{k} B_\theta \tag{2.108}$$

$$E_\theta = -\frac{\omega}{k} B_r \tag{2.109}$$

$$E_z = 0 \tag{2.110}$$

where A is the amplitude. From the above equations it is clear that the $\mathbf{E}$ and $\mathbf{B}$ fields are orthogonal at each section $z = \text{const.}$. The z-component of $\mathbf{E}$ is zero, but B_z is not to ensure $\nabla \cdot \mathbf{B} = 0$. The divergence of E is therefore not zero, but instead $\nabla \cdot \mathbf{E} = \omega\alpha/k B_z$.

The lowest two modes $m = 0, \pm 1$ of the helicon waves are the most relevant. The wave pattern for the $m = 0$ mode is:

$$B_r = -AkJ_1(Tr) \cos\psi \tag{2.111}$$

$$B_\theta = A\alpha J_1(Tr) \sin\psi \tag{2.112}$$

$$B_z = 2AT J_0(Tr) \sin\psi \tag{2.113}$$

$$E_r = A\omega\frac{\alpha}{k} J_1(Tr) \sin\psi \tag{2.114}$$

$$E_\theta = A\omega J_1(Tr) \cos\psi \tag{2.115}$$

$$E_z = 0 \tag{2.116}$$

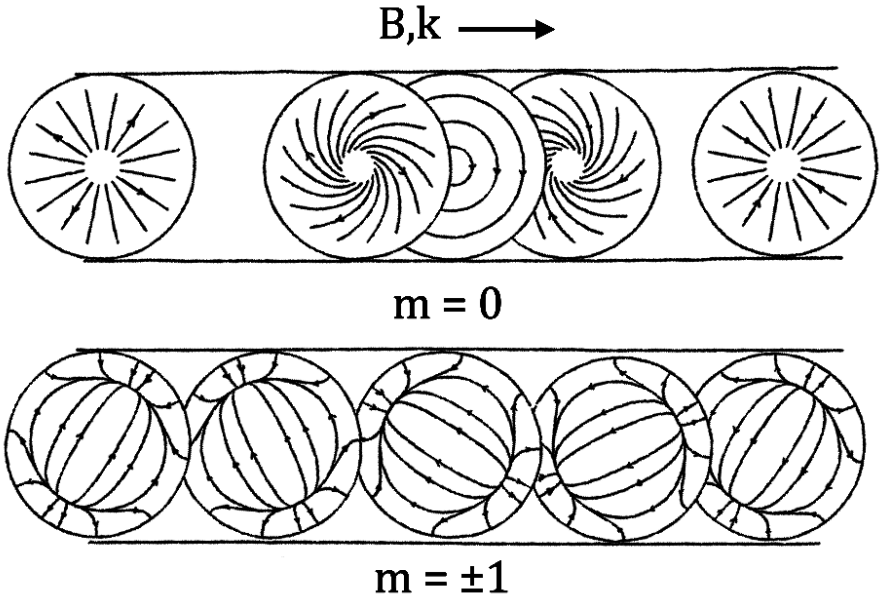

Figure 2.3: Electric field pattern of helicon wave $m = 0$ and $m = \pm 1$. Image from [29].

where $\psi = kz - \omega t$. For $\psi = 0$ the electric field is purely azimuthal and for $\psi = \pi/2$ it is purely radial, in between the fields lines form a spiral. As can be seen in Figure 2.3.

The $m = +1$ mode has a field pattern that does not change with position, but does change with the value of $|k_z/\alpha|$. The electric field pattern is given by:

$$E_r = -\frac{A}{T}\frac{\omega}{k}\left[\alpha J_1'(Tr) + \frac{k}{r}J_1(Tr)\right]\sin(\theta + kz - \omega t) \tag{2.117}$$

$$E_\theta = -\frac{A}{T}\frac{\omega}{k}\left[\frac{\alpha}{r}J_1(Tr) + kJ_1'(Tr)\right]\cos(\theta + kz - \omega t) \tag{2.118}$$

$$E_z = 0 \tag{2.119}$$

The field at $kz - \omega t = 0$ can be written as:

$$E_r = E_0(\zeta J_0 - J_2)\sin\theta \tag{2.120}$$

$$E_\theta = E_0(\zeta J_0 + J_2)\cos\theta \tag{2.121}$$

with $\zeta = (\alpha + k)/(\alpha - k)$, Which produces (for $k\alpha = 1/3$) the pattern shown in Figure 2.3. Substituting $\nabla \times \mathbf{B}_1 = \alpha_1 \mathbf{B}_1$ in Equation 2.91 yields: $\mathbf{j} = (\alpha_1/\mu_0)\mathbf{B}$. For dielectric walls the boundary condition is $j_r = B_r = 0$ which is equivalent to $E_\theta = 0$. The radial wave number T is there for obtained from $E_\theta(a) = 0$. Furthermore the

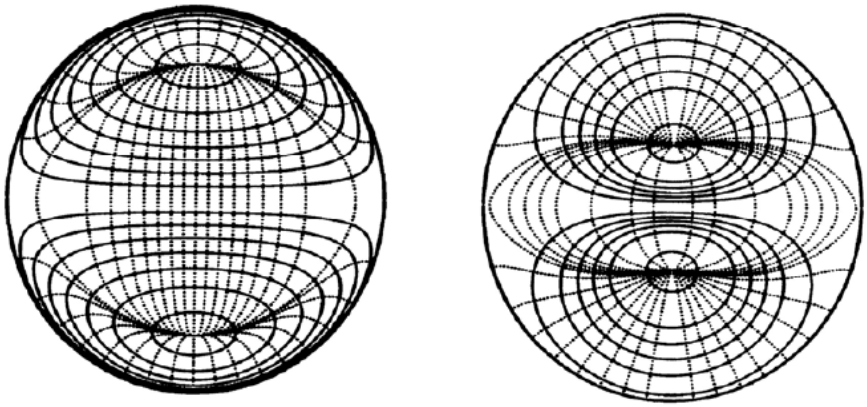

Figure 2.4: Electric field pattern in the r, θ plane of helicon wave $m = +1$ (left) and $m = -1$ (right). Image from [31].

pattern has a separatrix at $r = r_0$ where $E_r(r_0) = 0$. As is apparent from Figure 2.4 there is a rotating transversal electric field at the center, moving along the column. For $m = +1$ this is right hand polarized, while for $m = -1$ it is left hand polarized. The electric field pattern for $m = +1$ and $m = -1$ is somewhat different as can be seen in Figure 2.4.

2.2 Helicon Plasma Sources

Helicon plasma sources have been investigated since the discovery of helicon waves in plasmas in 1965 [66]. Major contributors to helicon research have been Boswell et al., Chen et al., Scime et al., Shinohara et al. and Shamrai et al. [31]. A review of helicon sources by Chen can be found in [31] and a more recent review by Shinohara in [114]. For a detailed review on helicon sources the reader is referred to these to excellent works. Here we will present a summary of the most salient features of helicon sources.

Helicon sources are plasma sources where the main heating and ionization mechanism are helicon waves. Helicon sources consist of a dielectric cylinder, with an axial applied magnetic field and an RF antenna. Antennas used in helicon sources are designed to excite the $m = +1$ mode, and work by coupling to the traveling, rotating transversal electric field. Various types of antennas have been developed over the years. Most antennas are a Nagoya type-III antennas (see Figure 2.5) or a modification therefore. The principle is as follows: the rising current J entering

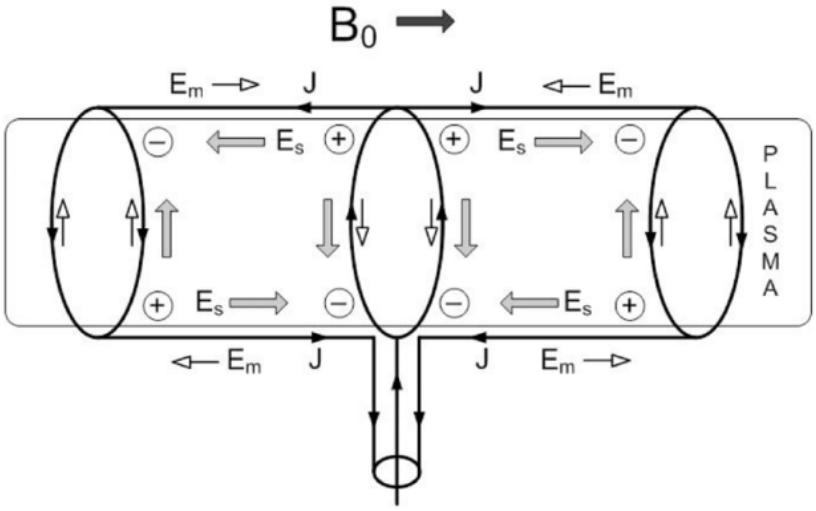

Figure 2.5: Schematic of the working principle of a Nagoya type-III antenna for the excitation of helicon waves. Image from [31].

through the center ring, splitting at the top, moving towards the end rings, where is flows down and then recombines at the center. The rising current, flowing outward in the top horizontal leg, generates an opposing electric field E_m which drives electrons to the outer rings, while in the bottom leg where the current flows towards the center it drives the electrons towards the center. This creates a pattern of spaces charges, marked $+, -$ which in turn create a longitudinal and transversal electric field E_s. This field is supposed to couple to the transverse field of the $m = +1$ mode.

Other types of antennas can be seen in Figure 2.6. The Boswell antenna, (b), is a Nagoya antenna split in two halves so it can be placed around the source without breaking the vacuum. The half-helical antenna, (e) is a (right-hand) twisted Nagoya antenna, which better matches the rotating pattern of the $m = +1$ mode. A spiral antenna, (f) was used by Little and Choueiri [69]. Another novel antenna type is the birdcage antenna, originally developed for MRI scanners but applied to plasma sources by Guittienne et al. [48] and applied to helicon thrusters by Romano et al. [104]. Birdcage antennas include capacitors to produce a resonance at the desired frequency an produce rotating, transversal electric fields. Furthermore, if designed well they present a real, or almost fully real impedance to the RF source. All other antennas present themselves as inductive impedances and require a matching

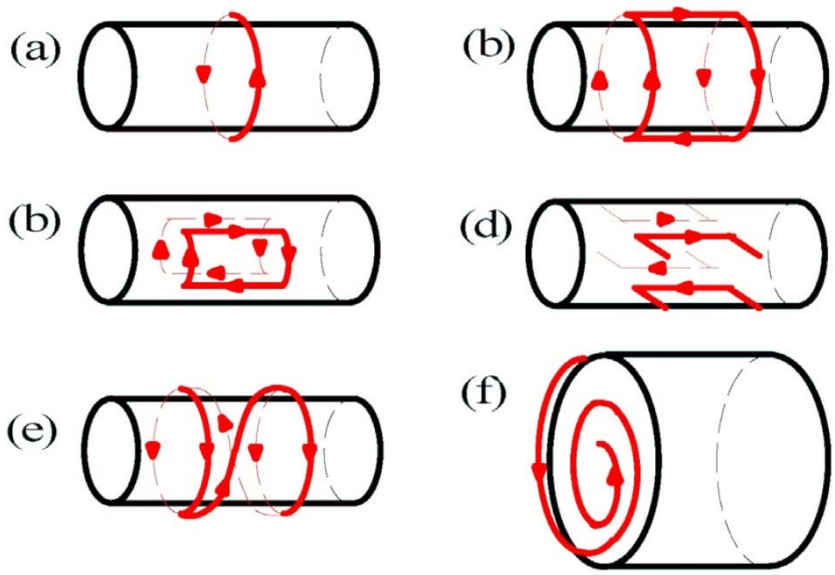

Figure 2.6: Different types of antennas used in helicon sources. Image from [114].

network for efficient power transfer from the RF generator to the antenna. Typical operating frequencies are those within the ISM band, particularly 13.56 MHz and its harmonics 27.12 MHz and 40.68 MHz.

Helicon plasmas are of interest because of the high plasma densities $n \sim 10^{-19}$ m^{-3}, they can generate. When varying the RF power to the plasma, density jumps can be distinguished which are related to a change in power coupling mechanism. At very low power < 200W a capacitively coupled plasma is generate, with typically $n \sim 10^{-15}$ m^{-3}, with increasing power, coupling becomes inductive, resulting in a density jump, and magnitudes of $n \lesssim 10^{17}$ m^{-3}, at even larger power another density jump occurs with densities of $10^{18} - 10^{19}$ m^{-3} corresponding to the helicon mode [114][31]. Further density jumps can occur corresponding to different resonances of the bounded helicon wave. Density jumps can also occur with increasing magnetic field [31]. Another characteristic of helicon sources is a density profile that is centred on the axis of the plasma column [31] and a color change in the emitted light attributed to and increase ion density. In argon discharges this results in a distinct bright blue discharge, while in xenon it produces a bright green/white discharge. Corresponding spectral measurements show a relative increase of emission lines coming from Ar II (or Xe II) in these modes.

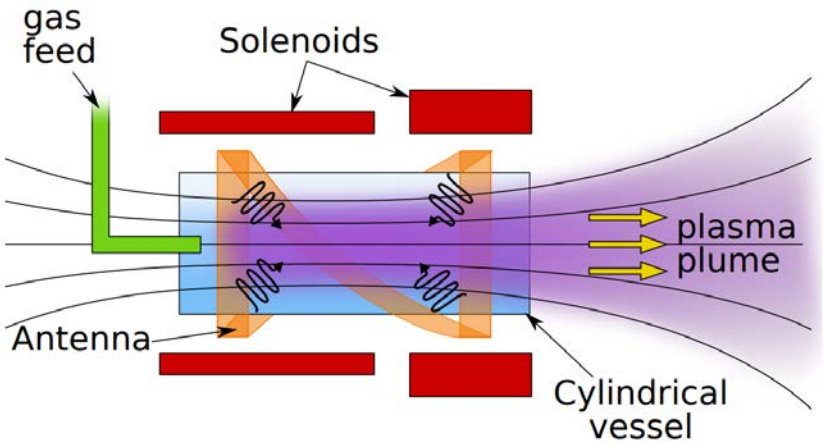

Figure 2.7: Schematic of a helicon thruster.

2.3 Helicon Plasma Thrusters

Helicon plasma thrusters are simply thrusters that are based on helicon sources. This includes two-stage technologies such as RF gridded ion thrusters (RFGIT) [144], helicon hall thrusters [109] as well as the 'VAriable Specific Impulse Magnetoplasma Rocket' (VASIMR) [25]: a 200 kW ion ion cyclotron resonance (ICR) thruster based on a 30 kW helicon ionization stage. However we will focus on single stage helicon thrusters that consist of a helicon source only. In the two-stage thrusters the plasma is generated by the helicon source and accelerated by a secondary mechanism, electrostatic (RF-GIT), hall-effect or ICR, in single stage helicon thrusters the acceleration mechanism is a magnetic nozzle, a concept which will be explained in detail the next section.

Single stage helicon plasma thrusters are in essence a helicon plasma source with an open end. It consists of a dielectric tube, open at one end and closed at the other end; a gas injection port generally at the closed end; a helicon antenna enveloping the cylinder; and a magnetic circuit, either by means of a solenoid or permanent magnets, that produces an axial magnetic field. A schematic of the principle can be seen in Figure 2.7.

2.3.1 Magnetic Nozzles

Although not specific to helicon thrusters, the magnetic nozzle is the main mechanism for generating thrust of HTPs. The general principal is as follows, magnetized electrons expanding along a divergent magnetic field will exchange their thermal, azimuthal velocity into parallel (along the magnetic field line) velocity, accelerating downstream. This in turn produces an ambipolar electric field that will drag the ions along. A magnetic nozzle thus converts electron thermal motion into ion kinetic motion, albeit not perfectly. The force is due to the magnetic force between the electron diamagnetic current and the magnetic circuit of the thruster.

A 1D expansion model was already reported in 1968 by Andersen et al. Combining the equation for conservation of energy $\bar{M} = \sqrt{M_0^2 - 2\bar{\phi}}$, the continuity equation $\hat{R}_V(\hat{z})\bar{n}\bar{M} = M_0$, and the Boltzmann relation $\bar{n} = e^{\bar{\phi}}$ leads to the following implicit equation for $\bar{\phi}$:

$$R_V^2(\hat{z})e^{\hat{\phi}}\sqrt{M_0^2 - 2\phi} = M_0 \tag{2.122}$$

Once solved for $\bar{\phi}$, $\bar{n}$, $\bar{M}$ can also be calculated. The variables are radially average non-dimensional: $\bar{M} = u_i/c_s$ the ion Mach number ($c_s = \sqrt{T_e/m_i}$), $\bar{n} = n/n_0$ and $\bar{\phi} = e\phi/T_e$. Furthermore $\hat{R}_V(\hat{z})$ is the plasma radius at position $\hat{z}$ which is taken to be the radius of the magnetic flux tube (for which the magnetic stream function $\psi(z,r) = \text{const.}$) originating at the throat of the magnetic nozzle, such that $\psi(z, R_V) = \psi(0, R)$; both $\hat{R}_V$ and $\hat{z}$ are normalized with R. Note that for the magnetic stream function $\partial\psi/\partial z = -rB_r$ and $\partial\psi/\partial r = rB_z$. For a single loop with radius R_L and current I the stream function is given by:

$$\psi(z,r) = \frac{\mu_0 I R_L}{4\pi}\sqrt{(R_L + r)^2 + z^2}\,[(2-m)K(m) - 2E(m)] \tag{2.123}$$

with $m = 4R_L r[(R_L + r)^2 + z^2]^{-1}$ and K, E the complete elliptical integrals of the first and second kind.

The 1D model does describe the axial expansion rather well but a 2D model is needed for insight into any other features. Ahedo and Merino developed an axisymmetric 2D model of a supersonic expansion in a magnetic nozzle based on the method of characteristics [3]

The model solves the continuity and momentum equations for species electrons

and ions in a steady-state collision-less plasma.

$$\nabla \cdot (n_j \mathbf{u}_j) = 0 \tag{2.124}$$

$$m_j n_j \mathbf{u}_j \cdot \nabla \mathbf{u}_j = -\nabla n_j T_j - q_j n_j \nabla \phi + q_j n_j \mathbf{u}_j \times \mathbf{B} \tag{2.125}$$

with n_j, m_j, q_j, T_j and $\mathbf{u}_j$ the density, atomic mass, charge, temperature and velocity of species $j = i, e$ and ϕ and $\mathbf{B}$ the ambipolar potential and magnetic field respectively.

Since the model assumes axisymmetry ($\partial/\partial\theta = 0$) the velocity can be separated in a longitudinal and azimuthal component $\tilde{\mathbf{u}} = \mathbf{u} - u_\theta \mathbf{1}_\theta$.

After some manipulation the following system of 3 differential equations:

$$u_{ri}\frac{\partial \ln n}{\partial r} + u_{zi}\frac{\partial \ln n}{\partial z} + \frac{\partial u_{ri}}{\partial r} + \frac{\partial u_{zi}}{\partial z} = -\frac{u_{ri}}{r} \tag{2.126}$$

$$u_{ri}\frac{\partial u_{ri}}{\partial r} + u_{zi}\frac{\partial u_{ri}}{\partial z} + c_s^2\frac{\partial \ln n}{\partial r} = -(u_{\theta e} - u_{\theta i})\Omega_i \cos\alpha + \frac{u_{\theta i}^2}{r} \tag{2.127}$$

$$u_{ri}\frac{\partial u_{zi}}{\partial r} + u_{zi}\frac{\partial u_{zi}}{\partial z} + c_s^2\frac{\partial \ln n}{\partial z} = (u_{\theta e} - u_{\theta i})\Omega_i \sin\alpha \tag{2.128}$$

$$\tag{2.129}$$

and 4 algebraic equations:

$$T_e \ln n - e\phi = H_e(\psi) \tag{2.130}$$

$$u_{\theta e} = -\frac{r}{e}\frac{dH_e}{d\psi} r m_i u_{\theta i} + e\psi = D(\psi_i) \tag{2.131}$$

$$\frac{n u_{\parallel e}}{B} = G_e(\psi) \tag{2.132}$$

are found. Note that here two different reference are used, cylindrical $\{\mathbf{1}_z, \mathbf{1}_r, \mathbf{1}_\theta\}$ and magnetic $\{\mathbf{1}_\parallel, \mathbf{1}_\perp, \mathbf{1}_\theta\}$. Furthermore Ω_i is the ion cyclotron frequency and α the angle of the local magnetic field vector. ψ is the magnetic stream function as defined earlier and ψ_i is the ion stream function, defined similarly, such that $\partial\psi_i/\partial z = -r u_{ri}$ and $\partial\psi_i/\partial r = r u_{zi}$. $D(\psi)$ is the value of the conserved ion angular momentum, $G_e(\psi)$ the ratio of electron to magnetic flux, and $H_e(\psi)$ the electron Bernoulli function, along a magnetic stream tube. Note also that the plasma is assumed quasi-neutral $n_e = n_i \equiv n$, isotropic, and that $\mathbf{E} = -\nabla\phi$. These 7 equations are a closed system for determining $n, \phi, \mathbf{u}_i, \mathbf{u}_e$. All variables can be normalized with R, c_s, T_e and n_0. The model furthermore requires as a boundary

conditions the radial distributions at the throat, i.e. $z = 0$ as well as the magnetic stream function ψ or (equivalently) magnetic field $\mathbf{B}$.

Throat conditions considered in the model are: a) supersonic ions $\hat{u}_{zi} = M_0 \simeq 1$; b) current-free $\hat{u}_{ze} = \hat{u}_{zi}$; c) axial flow $\hat{u}_{re} = \hat{u}_{ri} = 0$; d) constant potential $\hat{\phi} = 0$; e) density distribution $\hat{n} = J_0(a_0\sigma\hat{r}$ where σ controls the non-uniformity; d) Hall-current distribution $\hat{j}_{\theta e} = -\hat{\Omega}_{i0}^{-1} a_0 J_1(a_0\sigma\hat{r})$ and $\hat{u}_{\theta e} = -\hat{j}_{\theta e}/\hat{n}$; e) zero swirl current $\hat{u}_{\theta i} = 0$. With these parameters $D(\psi_i), H_e(\psi), G_e(\psi)$ and $dH_e/d\psi$ can the differential equations are then integrated from $z = 0$ to close to the turning point of the nozzle, $z = z_F$.

The three parameters controlling the entrance conditions are the non-uniformity σ, the ion magnetization $\hat{\Omega}_{i0} = \Omega_{i0} R c_s^{-1}$ and the divergence of the nozzle R_L/R

Ahedo and Merino compared the uniform $\sigma = 0$ and highly non-uniform $\sigma = 0.99$ cases and found that the results of the former agree well with the 1D model. For the non-uniform case both the ion current density is found to concentrate itself on-axis (as opposed to being uniform in the 1D model) which is good for thrust and ion-detachment. The also found a separation of the magnetic streamtubes ψ and the ion streamtubes ψ_i where the latter are less divergent. This points to ion detachment from the magnetic nozzle which is necessary for thrust. As the magnetic field lines are closed, if ions, like the electrons would follow the magnetic field lines the would curve back onto the device and the net momentum flux would be zero. Furthermore the separation of the magnetic, i.e. electron stream tubes and ion stream tubes also implies that the plasma is not locally current-free, i.e. $\mathbf{j} \neq 0$ even though it is globally current-free i.e. $\nabla \cdot \mathbf{j} = 0$. And lastly it induces a swirl current $j_{\theta i}$ opposite to the Hall current $j_{\theta e}$ that will degrade performance somewhat.

The thrust F generated by the magnetic nozzle can be written as:

$$F = 2\pi \int_0^{R_V(z)} drr(nm_i u_{zi}^2 + p_e) \tag{2.133}$$

where the first term of the integrand is the axial ion momentum flux and the second term is the electron pressure. If we combine the electron and ion momentum equation, and use the continuity equation to write the ion inertial term as a dyadic tensor we get:

$$\nabla \cdot (nm_i \mathbf{u}_i \mathbf{u}_i) + \nabla(n_e T_e) = en(\mathbf{u}_e - \mathbf{u}_i) \times \mathbf{B} \tag{2.134}$$

If we now take the volume integral over the volume V and use the divergence

theorem we get:

$$\oint_{\partial V}(nm_i\mathbf{u}_i\mathbf{u}_i\cdot\hat{\mathbf{n}})dS+\oint_{\partial V}n_eT_ed\mathbf{S}=\int_V-\mathbf{j}_\theta\times\mathbf{B} \tag{2.135}$$

The z-component of this equation is:

$$\begin{aligned}F&=2\pi\int_0^{R_V}drr(nm_iu_{zi}^2+n_eT_e)\\&=2\pi\int_0^{R}drr(nm_iu_{zi}^2+n_eT_e)+\int_{A_V}p_e\sin\alpha dS-\int_V-j_\theta B_rdV\\&=F_0+F_v+F_s\end{aligned}$$

where A_V is the lateral surface of the magnetic nozzle (with $\mathbf{1}_\perp$ the normal vector). The thrust therefore consists of three contributions: F_0 the thrust generated at the throat coming from the source, F_v the magnetic thrust due to the volume hall current and the F_s the magnetic thrust due to a surface current on the edge of the magnetic nozzle. Where the surface Hall current is postulated to be $j_{\theta,s}=-(p_e/B)|_{z,R_V(z)}$. Note that since plasma at the throat is sonic, i.e. $u_{zi}(z=0)=c_s$ that the momentum flux at the throat is equal to $2nT_e$ where 50% or n_eT_e is due to the electron pressure and the other 50% from the ion kinetic energy. From the above equation it should also be clear that the main source of thrust is are the volume and surface diamagnetic current j_θ,$j_{\theta,s}$. Justifying its classification as an electromagnetic thruster. Furthermore it shows that the swirl current $j_{\theta,i}$ reduces the performance since it reduces j_θ.

Deriving the energy equation from the momentum equation we find for the ion axial power, i.e. the axial flow of axial kinetic energy, integrated over the volume:

$$P_{zi}(z)=2\pi\int_0^{R_v(z)}\frac{1}{2}nm_iu_{zi}^3rdr \tag{2.136}$$

$$=2\pi\int_0^{R}\frac{1}{2}nm_iu_{zi}^3rdr+\int_V u_{zi}\frac{\partial p_e}{\partial z}dV-\int_V u_{zi}j_\theta B_rdV \tag{2.137}$$

$$=P_{zi,0}+P_{zi,th}+P_{zi,m} \tag{2.138}$$

while the total ion kinetic power we get from:

$$\nabla\cdot(\frac{1}{2}nm_iu_i^2\mathbf{u}_i)=-\mathbf{u}_i\cdot\nabla p_e+\mathbf{u}_i\cdot(\mathbf{j}_\theta\times\mathbf{B}) \tag{2.139}$$

which integrated over the volume yields:

$$P_i(z) = 2\pi \int_0^{R_v(z)} \frac{1}{2} n m_i u_i^2 u_{zi} r dr \tag{2.140}$$

$$= 2\pi \int_0^{R} \frac{1}{2} n m_i u_i^2 u_{zi} r dr + \int_V \mathbf{u}_i \cdot \nabla p_e dV - \int_V \mathbf{u}_i \cdot (\mathbf{j}_\theta \times \mathbf{B}) dV \tag{2.141}$$

$$= P_{i,0} + P_{i,th} + P_{i,m} \tag{2.142}$$

2.3.2 Thruster Source Model

The plasma thruster source region of a long cylinder $R \ll L$ with a purely axial $\mathbf{B} = B_0 \hat{\mathbf{z}}$ magnetic field, was modelled using an axisymmetric 2D fluid model with three species (ions, electrons, neutrals) by Ahedo and Navarro-Cavallé [5] by decoupling the radial and axial equations and solving the continuity equation and the momentum equation.

$$\nabla \cdot (n_e \mathbf{u}_e) = \nabla \cdot (n_i \mathbf{u}_i) = -\nabla \cdot (n_n \mathbf{u}_n) = n_e n_n R_{ion} \tag{2.143}$$

$$\nabla \cdot (m_j n_j \mathbf{u}_j \mathbf{u}_j) = -\nabla p_j + q_j(-\nabla \phi + \mathbf{u}_j \times \mathbf{B}) - \mathbf{S}_j \tag{2.144}$$

with m_j the particle mass, n_j the density, $\mathbf{u}_j$ the velocity vector, $\mathbf{B}$ the magnetic field vector, ϕ the ambipolar potential (assuming $\mathbf{E} = -\nabla\phi$), $p_j = T_j n_j$ the pressure, R_{ion} the ionization rate and $\mathbf{S}_j$ a collisional term. They assumed: 1) axial symmetry $\partial/\partial\theta = 0$ 2) cold neutrals $T_n = 0$, $\mathbf{u}_n$ 3) negligble ion pressure $p_i \ll p_e$ 4) longitudinal ambipolarity $\mathbf{j} - j_\theta \hat{\mathbf{z}} = 0$ such that $u_{zi} = u_{ze} \equiv u_z$ and $u_{ri} = u_{re} \equiv u_r$ 4) density profile $n(z,r) = n_z(z) n_r(z,r)$ with $(2/R^2)\int_0^R r n_r(r,z) dr = 1 \quad \forall \quad z$ 5) $\phi(z,r) = \phi_z(z) + \phi_r(z,r)$ with $\phi_r(z,0) = 0 \quad \forall \quad z$ 6) unmagnetized ions $u_{\theta i} \ll u_{\theta e} \equiv u_\theta$ 7) neglecting longitudinal electron enertia, but maintaining azimuthal electron inertia through $u_{\theta e}$ 8) Ordering of spatial gradients: $\partial n_r/\partial z \ll \partial n_r/\partial r$. $\partial \phi_r/\partial z \ll \partial \phi_r/\partial r$, $\partial(u_r, u_\theta)/\partial z \ll \partial(u_r, u_\theta)/\partial r$ and $\partial u_z/\partial r \ll \partial u_z \partial z$. This results in a set of 5 axial equations determining $n_z, n_n, u_z, u_n, \phi_z$ and 4 radial equations that determine $n_r, u_r, u_\theta, \phi_r$ which are coupled only through the wall recombination frequency $\nu_w(z)$. The boundary conditions are $u_r = u_\theta = \ln(n_r/n_r(z,0)) = \phi_r = 0$, $u_r(z,R) = c_s$ with $c_s = \sqrt{T_e/m_i}$ the Bohm velocity, for the radial equations and $u_n(0) = u_{n0}$, $u_z(0) = -c_s$ and $u_z(L) = c_s$.

Integrating the equation for a given set of representative operational parameters they found that a) neutral density depletes along the axial direction b) ion density has a peak some distance after the injection point with a positive gradient before and

a negative gradient after; c) ions move towards the back wall left of the density peak and towards the exit after the peak; d) electron collisions frequency decrease towards the exit, due to neutral depletion, resulting in a more magnetized plasma near the exit; e) for strong magnetization the radial velocities are low in the bulk plasma and increase sharply near the radial walls. i.e. plasma magnetization concentrates velocity gradients near the chamber wall and idem for the radial electric field; f) radial gradients of the plasma density are maintained by the radial Lorentz force due to azimuthal electron current; g) for weak magnetization the radial wall losses are not negligible (something also found by [64]) and h) constant-velocity lines in the r, z plane are good approximations for iso-potential lines showing that ion acceleration is driven by the ambipolar electric field.

In terms of the performance the model looks at utilization efficiency $\eta_u = \dot{m}_i(L)/\dot{m}$ and production efficiency $\eta_p = \dot{m}_i(L)/\dot{m}_i$ in other words the ratio of the mass flow rate of ions leaving the thruster to the total mass flow rate injected into the thruster and the ratio of the mass flow rate of ions leaving the thruster to by the total mass flow rate of ions produced (i.e. those leaving the thruster as well as those to the back and radial walls). Both utilization and production efficiency were found to increase with the magnetic field saturating at the maximum value for $B > 600G$ while the utilization efficiency depends also on the electron temperature, where higher temperatures both result in reaching the maximum value for lower magnetic fields as well as a higher maximum value.

The model also looked at the total efficiency where. It solves the following power balance:

$$\nabla \cdot (\dot{\mathbf{P}} + E_{ion} n \mathbf{u}_i + \phi \mathbf{j}) = \dot{P}_a \tag{2.145}$$

where the second term is the ionization loss, with E_{ion} the ionization energy and the third term is losses due to Joule heating; $\dot{P}_a$ is the absorbed power density. The first term is the plasma power density:

$$\dot{\mathbf{P}}(z, r) = \frac{1}{2} n_n u_n^2 \mathbf{u}_n + \frac{1}{2} n [m_i u_i^2 \mathbf{u}_i + (m_e u_{\theta e}^2 + 5T_e)] \mathbf{u}_e + \mathbf{q}_e \tag{2.146}$$

The power balance can be integrated over the volume which is equal to a integral over the boundaries. The balance then becomes $P_{wall} + P_{beam} + P_{ion} = P_a$. where P_{wall} are losses to the wall, P_{ion} are losses due to ionization and P_{beam} is the power leaving thruster and going into the beam, which can be further divided into P_i and P_e the power carried by the ions and electrons respectively. Since the thrust is

generated by the axial momentum flux of the ions, the 'useful' power P_{iz} is carried by the axial ion kinetic energy flux $m_i u_{zi}^3$. The total efficiency is then P_{zi}/P_a which can be further divided into partial efficiencies:

$$\eta = \frac{P_{beam}}{P_a}\frac{P_i}{P_{beam}}\frac{P_{zi}}{P_i} = \eta_{cham}\eta_{conv}\eta_{div} \tag{2.147}$$

Where η_{cham} is the chamber efficiency, η_{conv} is the conversion efficiency i.e. the conversion of electron energy to ion kinetic energy and η_{div} the divergence efficiency. At the exit of the thruster $\eta_{div} = 1$ however in the plume expansion, as we have seen in the previous section on magnetic nozzles, this will be less than unity. The conversion efficiency will also vary along the nozzle as electron thermal energy is converted into ion kinetic energy.

The model of Ahedo and Navarro-Cavallé provide insight in the parametric scaling of the source region. Main draw backs are the assumptions of a purely axial magnetic field and the separation in axial and radial dynamics as well as the assumption of a uniform electron temperature. Particle-in-cell (PIC) or hybrid schemes could overcome these issues. Furthermore coupling to a 2D model of the plasma-wave interaction is necessary to provide a more realistic model of the power deposition.

Zhou et al. [154] adapted a 2D axisymmetric hybrid-PIC code originally developed for Hall-effect thrusters to the helicon thruster topology, most notably by employing algorithms for solving a magnetic field aligned mesh. The electrons are treated as a fluid while the ions are solved with a PIC model. Zhou et al. simulated a thruster similar to the prototype under investigation in this thesis, with $L = 60$ mm, $R = 12.5$ mm, a magnetic field of $B_0 = 1200$G, assuming a Gaussian power density profile, centered on the magnetic throat with a total RF power of $P_a = 300$W and running with xenon. The following conclusions were reached: a) plasma densities peaks near the back wall at $5{\cdot}10^{19}$ m^{-3}, decaying radially inside the source region due to wall losses and in the plume due to expansion; b) electron temperatures are around $T_e = 7 - 14$ eV with a maximum on-axis near the peak of the power density. c) plasma potential is maximum near the back wall corresponding to the plasma density peak and the total potential drop is about 50V, or about $3T_e$. (Note that based on kinetic modelling, as we will see in the next section, for Xenon this expected to about $8T_e$. The discrepancy here is likely due to the incomplete plume expansion of the model); d) ion motion is governed by the electric field, while

electrons are attached to the magnetic streamlines. The sum $\tilde{\mathbf{j}}_e + \tilde{\mathbf{j}}_i$ of the longitudinal ($\tilde{\mathbf{j}} = \mathbf{j} - j_\theta \hat{\mathbf{z}}$) although globally zero, locally is non-zero, i.e. local ambipolarity is not fulfilled; e) the azimuthal current is almost exclusively due to electron motion and has contributions due to electric field and pressure gradient drift, where the latter dominates; f) power fluxes to the back wall are about an order of magnitude larger than to the radial walls (however the radial walls have a larger surface area) and impact energies are about a factor 2 higher at the back wall. g) the solution is sensitive to the anomalous cross-field transport parameter where $\alpha_{ano} = 0.02$ provided the best agreement with experimental results. h) an anomalous cooling parameter, a collision frequency ν_q was needed to reproduce the electron cooling in the plume, in fact $\nu_q = 0$ results in a (non-physical) isothermal expansion, while $\nu_q \sim 10^9$ s^{-1} reproduces the polytropic cooling with $1.15 < \gamma < 1.25$ observed in experiments and kinetic modelling. i) variations in the power deposition map, e.g. homogeneous heating instead of a Gaussian profile, produces mild changes in the plasma response, mostly affecting the location of the electron temperature peak although the magnitude is comparable.

2.3.3 Helicon Thruster Prototypes

Helicon thruster technology although relatively new, has been and still is being investigated by many research groups around the world. The earliest work was done by Charles and Boswell at the Australian National University in Canberra. Early publications of Charles and Boswell refer to a Helicon Double-Layer Thruster (HDLT) as a thin double layer structure was observed experimentally in the exhaust plume in which most of the acceleration happened, as opposed to gradual ambipolar acceleration along the magnetic nozzle. Double layers do not impart additional thrust, nor do they affect the final downstream divergence [83]. Many later experiments, including at EP2 do not show evidence for a double layer. It is thought that this is possibly related to facility effects. Experiments of Charles and Boswell were performed on thrusters coupled to relatively small diffusion chamber while more experiments are performed with thrusters completely immersed in large vacuum chambers. Takahashi was a visiting fellow at ANU and subsequently started a line of research at Tohoko University in Sendai, Japan, working mostly on high power (>1 kW) helicon thrusters. A second center of investigation in Japan is the

research group of Shinohara at the Institute of Engineering of the Tokyo University of Agriculture and Technology. In the USA research on helicon thrusters has been performed at Georgia Tech, Atlanta, by Williams and Walker, at the University of Michigan by Shabshelowitz and Gallimore, at Massachusetts Institute of Technology by Batischev [11] and by Little [69] and Choueiri at Princeton University. However, the latter two have not presented any direct thrust measurements. The US company Phase Four is developing an RF (helicon) thruster and has published some performance data. In Europe, some work has been done by Harle and Pottinger at the Surrey Space Centre of the University of Surrey in the UK, by Trezzolani and Pavarin at the Advanced Space Propulsion group at Padova University, Italy and the spin-off company T4i and by Navarro-Cavallé at the Space Propulsion and Plasmas group of Universidad Carlos III de Madrid, Spain. This thesis is part of the latter research effort. In Table 2.2 below an overview can be found of published performance data by the aforementioned research groups. It is mostly a duplicated of Table 1 of [121] with some additional data points.

2.3.4 EP^2 Prototypes

The HPTx is an experimental platform developed by EP2 (jointly with SENER Aeroespacial). It is a laboratory breadboard model that allows for several operational parameters to be varied among which: RF power, mass flow rate, magnetic field. It consists of a solenoid with about 50 G/A that can handle currents of up to 30A; a 25 mm inner diameter, 120 mm long quartz tube; a ceramic injector at the back of this tube and a half-turn helical antenna fed by an RF power generator operating at a frequency of 13.56 MHz. Between the power generator and the thruster is a matching circuit to reduce power reflections due to impedance mismatch. A schematic of the prototype can be seen in Fig. 2.8 and the operational parameters are tabulated in Tab. 2.3. More details on the HPTx and its predecessors can be found in [90, 92]. For the purpose of validating the thrust balance it is important to note that the thruster weighs 5.2 kg and is mounted to the balance using a mechanical interface that weighs 1.7 kg.

Table 2.2: Overview of performance results of helicon plasma thruster prototypes.

	Authors	Group	Year	P_{rf} [W]	F [mN]	I_{sp} [s]	F/P_{rf} [mN/kW]	η [%]	prop.
[123]	Takahashi et al.	Tohoko	2011	900	3.0	510	3.3	0.8	Ar
[101]	Pottinger et al.	Surrey	2011	650	2.8	286	4.3	0.6	Kr
[122]	Takahashi et al.	Tohoko	2011	800	6.0	816	7.5	3.0	Ar
[130]	Charles et al.	Canberra	2012	800	5.0	680	6.3	2.1	Ar
[125]	Takahashi et al.	Tohoko	2013	1000	11.0	1559	11.0	8.4	Ar
[107]	Shabshelowitz et al.	Michigan	2013	1500	11.0	160	7.3	0.6	Ar
[143]	Williams et al.	Atlanta	2013	600	6.0	136	10.0	0.7	Ar
[143]	Takahashi et al.	Tohoko	2013	2000	15.0	2126	7.5	7.8	Ar
[28]	Charles et al.	Canberra	2013	900	6.0	696	6.7	2.3	Xe
[50]	Harle et al.	Surrey	2013	400	1.1	187	2.8	0.3	Ar
[126]	Takahashi et al.	Tohoko	2014	2000	20.0	2721	10.0	13.3	Ar
[129]	Takahashi et al.	Tohoko	2015	6000	58.0	2818	9.7	13.3	Ar
[63]	Kuwahara et al.	Tokyo	2017	3000	40.0	459	13.3	3.0	Xe
[95]	Oshio et al.	Tokyo	2017	1000	6.0	510	6.0	1.5	Ar
[115]	Siddiqui et al.	Phase Four	2017	100	5.0	146	50.0	3.6	Xe
[135]	Trezzolani et al.	Padova	2017	150	1.4	714	9.3	3.3	Xe
[136]	Trezzolani et al.	Padova	2017	70	0.9	867	12.1	5.2	Xe
[121]	Takahashi et al.	Tohoko	2018	6000	67.0	3256	11.2	17.8	Ar
[116]	Siddiqui et al.	Phase Four	2018	440	6.2	1350	14.1	9.3	Xe
[47]	Gómez et al.	Madrid	2022	350	3.9	325	11.2	1.8	Xe

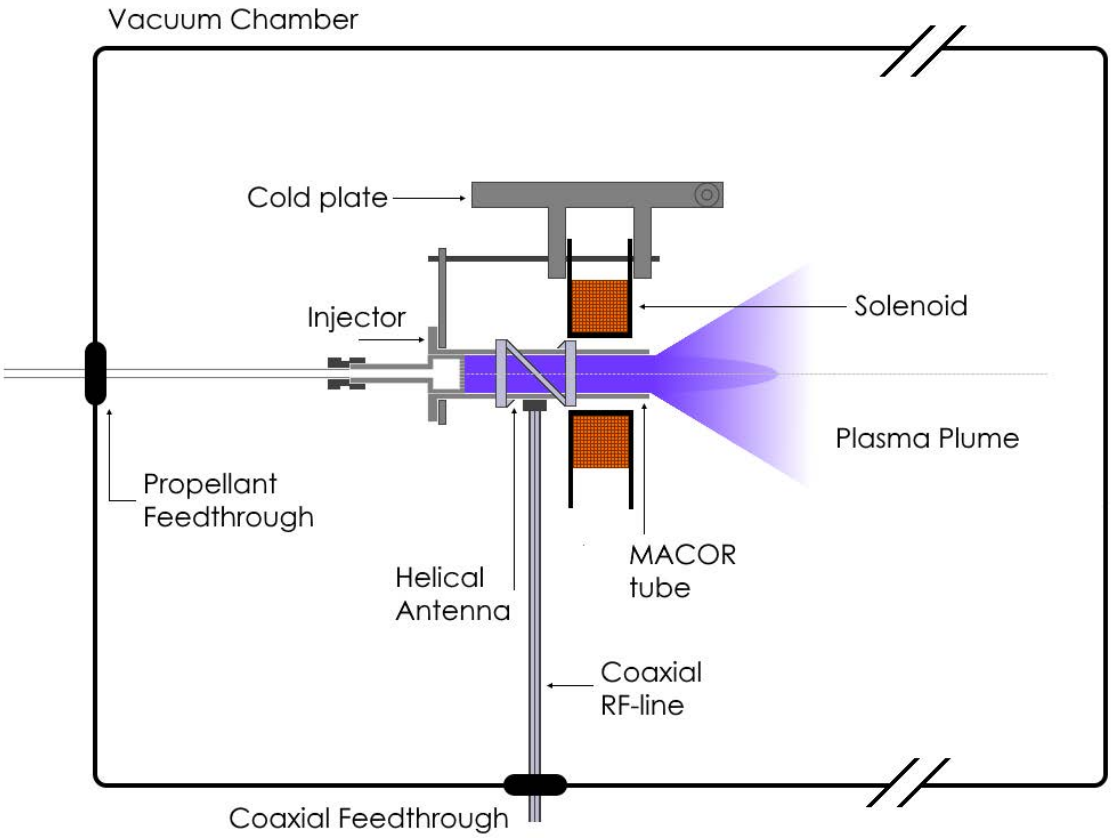

Figure 2.8: Schematic of the HPTx setup.

Table 2.3: HPTx operational parameters.

parameter	nominal	range	unit
RF power	450	300-600	W
B-field	1000	0-1500	G
mfr, Xe	10	5-30	sccm
mfr, Ar	20	10-50	sccm

CHAPTER

THREE

Plasma Probes

"History proves abundantly that pure science, undertaken without regard to applications to human needs, is usually ultimately of direct benefit to mankind."

— Irving Langmuir

3.1 Langmuir Probes

3.1.1 Theory

The Langmuir probe was the first plasma diagnostic ever developed and is named after its inventor, and pioneer of plasma physics, Irving Langmuir. The working principle is simple, yet elegant. It consists of a metallic surface emerged in the plasma, connected in series with a current meter and a voltage source. The second terminal of the voltage source is connected to the plasma chamber which acts as the electrical ground. From the current-voltage characteristic or $I-V$ curve, n, T_e, Φ and $f_e(\mathcal{E})$ may be obtained.[68, p.185]

The bulk of the plasma is quasi-neutral; the non-neutral regions between the surface and the plasma is called the sheath. A plasma sheath can be of the order of 10-100 Debye lengths [68, p.175], which is defined as:

$$\lambda_D = \left(\frac{\epsilon_0 k_B T_e}{e^2 n} \right)^{1/2} \tag{3.1}$$

With ϵ_0 the permittivity of free space, k_B the Boltzmann constant and e the elementary charge. The Debye length is the characteristic length over which the Coulomb potential of charges are shielded. Due to their higher mobility the electron

flux to the surface initially exceeds the ion flux, negatively charging the surface. The resulting change in potential of the surface results in a redistribution of the electrons following the Boltzmann relation.

$$n(\mathbf{r}) = n_0 \exp\left(-\frac{q\Phi(\mathbf{r})}{k_B T}\right) \tag{3.2}$$

When the ion and electron fluxes are equal the surface is said to be at floating potential, Φ_f, and the net current to the surface is zero.

Unless the surface is at the plasma potential there exists a potential drop between the bulk plasma and the surface. Ions are then accelerated through this potential drop. For a collision-less sheath and cold ions ($T_i = 0$) it was found that the sheath is only stable when the ions are accelerated to at least the Bohm velocity $u \geq u_B = (k_B T_e/m_i)^{1/2}$ [68, p.169].

The probe can also be biased with a voltage V repelling either ions or electrons and resulting in a net current. Assuming a Maxwellian electron distribution function and cold ions ($T_i = 0$) we can give an expression for the collected current. Since electrons are repelled following eq. 3.2 the total electron current is:

$$I_e = I_{es} \exp\left[\frac{e\,(\Phi - V)}{k_B T_e}\right] \tag{3.3}$$

Here I_{es} is the electron saturation current, which is given by the random flux times the probe area:

$$I_{es} = \frac{1}{4} e n A_p \left(\frac{8 k_B T_e}{\pi m_e}\right)^{1/2} \tag{3.4}$$

where A_p is the probe surface area and the term in parentheses is the mean velocity of the Maxwell-Boltzmann distribution with temperature T_e. In the case of a planar probe for a voltage $V \geq \Phi$ the electron current is equal to the saturation current. In the sheath, ions approaching the probe surface are almost mono-energetic (since we assumed $T_i \simeq 0$) and reach the probe with uniform velocity u_B. The total ion current collected by the probe is therefore:

$$I_i = -\alpha_0 e n A_p u_B \tag{3.5}$$

where $\alpha_0 = e^{-1/2}$ is a correction accounting for the fact that the density at the sheath edge is a factor $e^{-1/2} \approx 0.61$ lower than the bulk density [68, p.172]. The total current collected by a probe is then the sum of the electron and ion currents

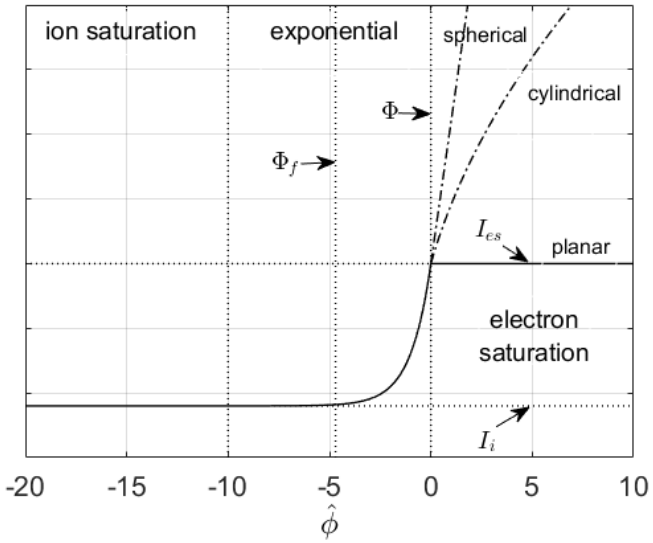

Figure 3.1: Sketch of an ideal Langmuir probe $I - V$ curve.

$I = I_e + I_i$. A sketch of the $I - V$ curve can be seen in figure 3.1. Note that the abscissa displays the normalized potential $\hat{\phi} = e(V - \Phi)/k_B T_e$.

The aforementioned approach is only valid for an infinite plane. Real probes however are finite and often cylindrical. However when the probe parameter $\xi = r_p/\lambda_D$ which is the ratio of probe radius to Debye length is sufficiently large $\xi \geq 50$, the aforementioned approach remains valid [72]. This regime is referred to as the thin-sheath limit. However the assumption of a constant ion and electron saturation current is incorrect since the sheath expands with increasing voltage following the Child-Langmuir law [68, p.177] resulting in a sheath thickness s:

$$s = \frac{\sqrt{2}}{3}\lambda_D \left[\frac{2e\,(V - \Phi)}{k_B T_e}\right]^{3/4} \tag{3.6}$$

The correction for the sheath area A_s of a cylindrical probe being:

$$A_s = A_p \left(1 + \frac{s}{r_p}\right) \tag{3.7}$$

The plasma in an electric thruster plume expands into the vacuum and the plasma density decreases with increasing distance from the thruster exit. Although the electron temperature can decrease as well, due to electron cooling [76, 70, 86, 132] the net effect is an increase in Debye length downstream. The probe parameter ξ is therefore not constant and the aforementioned assumption not always valid. The

opposite limit, the thick-sheath limit more often referred to as the orbital motion limit (OML) is defined as $\xi < 3$ and here a different theory applies.[68, p.192] For a cylindrical probe with a thick sheath $\xi > 3$ the angular momentum of the collected species has to be taken into account. In the limit of high voltage $|\Phi - V| \gg T_e$ the collected current can be expressed as:

$$I_j = \frac{en_j A_p}{\pi} \left[\frac{2e\left(\Phi - V\right)}{m_j} \right]^{1/2} \tag{3.8}$$

where $j = i, e$. Often the probe parameter is in the transitional regime $3 < \xi < 50$, where no closed form of the collected current is available and numerical solutions are required. The most complete set of results were obtained by Laframboise [65]. These numerical results have been parametrized for use in post-processing of LP probe data. The latest parametrization of Narasimhan and Steinbrüchel [89], valid for the aformentioned regime, provides the ion collection current for $T_i \ll T_e$ from a power series fit to Laframboise's results.

$$I_i(V, \lambda_D) = en_i A_p \left(\frac{k_B T_e}{2\pi m_i} \right)^{1/2} a \left(\frac{\Phi - V}{k_B T_e} \right)^b \tag{3.9}$$

$$a = 1.18 - 0.0080 \cdot \xi^{1.35} \tag{3.10}$$

$$b = 0.0684 + \left[0.722 + 0.928 \cdot \xi\right]^{-0.729} \tag{3.11}$$

A similar parametrization exists for electron saturation current in the transitional regime [72], however this is only necessary for determining n_e if the plasma potential is not well defined; otherwise equating $I(\Phi)$ with eq. 3.4 yields n_e.

The plasma potential can be determined from the inflection point of the $I - V$ characteristic. The abrupt transition from the electron retarding regime to the electron saturation regime is often clearly visible and referred to as the 'knee' of the curve. The plasma potential is usually obtained by finding the location of the maximum in the first derivative of the $I - V$ curve. However noise in the numerical differentiation or a poorly defined peak in more complex plasmas can lead to poor accuracy.

Often the electron energy distribution function is assumed to be Maxwellian, however in the case of magnetized electrons, large anisotropic ion velocities, wall-effects and anomalous transport the actual distribution may deviate. The Langmuir probe can be used to determine the actual distribution function. Druyvestein proved

in 1930 that the distribution function $f(\mathcal{E})$ was proportional to the second derivative of the $I-V$ characteristic [38]. The Druyvestein method can therefore be used to determine $f_e(\mathcal{E})$ [68, p.191]:

$$f_e(\mathcal{E}) = \frac{2}{e^2 A_p} \left(2 m_e e \mathcal{E}\right)^{1/2} \frac{d^2 I_e}{d\mathcal{E}^2} \tag{3.12}$$

where $\mathcal{E} = \Phi - V$. Note that this is the second derivative of the electron current, so one has to first subtract the computed ion current before differentiating. From the distribution function the electron density and temperature can then be determined by taking the zeroth and second moments of the distribution [72].

The post-processing methodology outlined above has been implemented in a MATLAB script which is duplicated in section A.1. This script makes a first guess of the plasma parameters based on the thick sheath limit to estimate the Debye length and the probe parameter ξ. Then it iterates using the appropriate model (thick sheat, OML or the parametrization of Narasimhan and Steinbrüchel) until it converges on a ion density and electron temperature. The plasma potential is obtained from the peak in the first derivate. Furthermore the EEDF is also calculated and its zeroth an first moment are calculated for comparison.

RF-compensation

The application to radio-frequency plasmas complicates the interpretation of LP measurements. Strong RF-fields propagate through the plasma and result in a locally oscillating plasma potential $\tilde{\Phi} = \Phi_{dc} + \Phi_{rf}(t)$. Since the RF frequency 3-300 MHz usually exceeds the bandwidth of the Langmuir probe acquisition by several orders of magnitude. The measured $I-V$ curve is in fact a time-average over many RF-periods and due to the non-linear response of the current voltage relationship this $I-V$ curve is not representative of the DC behavior [18]. Most importantly the slope of the exponential part decreases resulting in a erroneously high reading of the electron temperature.

There are two approaches to mitigate this problem, passive filtering using RF-chokes [120, 40, 42] or active compensation where the RF feed signal is added to the probe signal to cancel the RF fluctuations. Although both methods agree quite well [8], the latter method is more elaborate and best applied to more homogeneous RF discharges encountered in plasma processing. For a thorough understanding of

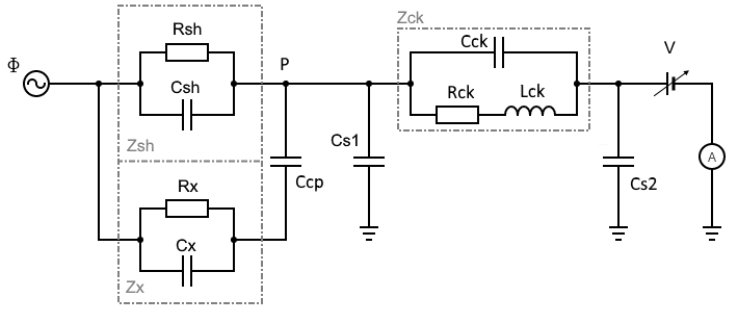

Figure 3.2: Equivalent circuit for RF-compensated Langmuir probe.

the underlying physics and the application to double probes the reader is referred to the recent work of Caneses [23]. In the present case the passive method of Sudit and Chen [120] was chosen for its simplicity.

The working principle as shown in figure 3.2 is as follows. By placing a notch filter (choke) with a resonance at the RF frequency in series with the probe, a voltage divider is formed by the resistance of the plasma sheath and the impedance of the filter. Proper compensation requires that the oscillations at the probe tip (point P in fig. 3.2) are much smaller than $k_B T_e/e$. The problem is that a stray capacitance C_{s1} cannot be avoided. The resulting stray impedance is Z_{s1} is very small at high frequencies. Since it's parallel to Z_{ck}, the resulting equivalent impedance $Z_{s1} \parallel Z_{ck}$ is smaller than Z_{ck} reducing the effect of the chokes. To mitigate this an auxiliary electrode with an area A_x much larger than the probe tip is capacitively coupled to the probe tip through a sufficiently large capacitor C_{cp}. The condition for compensation then reads:

$$Z_c \gg Z_x \left(\frac{e|\Phi_{rf}|}{k_B T_e} - 1 \right) \tag{3.13}$$

where $Z_c = \min(Z_{ck}, Z_{s1})$. For calculating Z_{sh} the following expressions can be used:

$$R_x = \frac{dI}{dV} \approx \frac{k_B T_e}{I_i} \frac{A_p}{A_x} \tag{3.14}$$

$$C_x \approx \frac{A_x}{2^{5/4}} \frac{\epsilon_0}{\lambda_D} \left[\frac{e(\Phi - V)}{k_B T_e} \right]^{3/4} \tag{3.15}$$

where the second equality holds at the floating potential (i.e. $I_e + I_i = 0$). Note

that the expression for C_x is an approximation in the absence of RF [30]. The approximation in R_x is only strictly valid at $V = \Phi_f$.

LP measurements in the plume of the HPT operating with argon at 450 W input power and a magnetic field of 1000 G showed that on the center-line, a 100 mm downstream of the exit plane the plasma density is 1.26 $\cdot 10^{17}$ m^{-3} and the electron temperature 9.6 eV from which it follows that $\lambda_D = 6.5$ μm. Using the dimensions given in the next paragraph we can calculate the resistance and capacitance in the sheath of the auxiliary electrode: $R_x = 3.7$ kΩ and $C_x = 8$ pF. (Note that the term in brackets in equation 3.15 in the case of argon is about 4.7 when $V = \Phi_f$.) At 13.56 MHz the total impedance $Z_x = 10$ kΩ. The stray capacitance is estimated to be 1 pF [120] leading to an impedance of $Z_c = 12$ kΩ. In the equality 3.13, considering the condition 'much larger than' ($\gg$) as > 10 then yields $\Phi_{rf} < 2.2 k_B T_e/e = 21.1$ V. As will be shown in section 3.7 the amplitude of the RF potential is $\Phi_{rf} = 12.9$ V under the same conditions. Since the density drops almost an order of magnitude over the plume the probes' capacity to filter diminishes and the condition of 3.13 read $\Phi_{rf} <$ 15.4 V. However as can be seen from figure 3.19 in section 3.7 downstream the potential oscillations decrease as well and $\Phi_{rf} = 5$ V. It can be concluded that the potential oscillations are successfully filtered in the whole plume (for the conditions of figure 3.19.)

3.1.2 Construction

The RF-compensated LP consists of the current collecting tip, a secondary electrode and the RF-choke circuit. It has a ceramic (Alumina) housing and is terminated with a male BNC connector. The tip is made of a 32 mm long, 0.256 mm diameter tungsten rod which is crimped to the terminal of the RF choke. The tungsten rod is inserted in a 20 mm long alumina tube with 1.3 mm OD and 0.512 mm inner diameter (ID), leaving about 2 mm of the tip exposed. The alumina tube is then inserted in a larger, 10 mm long, 3.96 mm outer diameter (OD) alumina rod with dual bores of 1.3 mm diameter. A 22 nF capacitor is soldered to the terminal of the RF chokes, close to where the tungsten rod is crimped. The other terminal of the capacitor is inserted into the second bore of the dual bore alumina rod. It is soldered to a piece of copper tape that is then wrapped around the thin alumina tube and serves as the secondary electrode. With a 1.4 mm diameter and 10 mm

Figure 3.3: CAD drawing of RF-compensated Langmuir probe.

length the exposed surface area is 44 mm^2 about 27.5 times the area of the tip.

In total the probe contains 4 chokes soldered in series, two with a resonance at 13.56 MHz and two at 27.12 MHz. The terminal of the last RF-choke is soldered to the pin of a male BNC connector which terminates in a 3/8-32 UNEF thread. An aluminium adaptor is machined consisting of a 10 mm long, 7.95 mm OD cylinder continuing in a 9 mm long, 14 mm OD cylinder. The inside of the widest part is tapped with a 3/8-32 UNEF thread; the thinner part has 6 mm ID bore. The whole assembly is inserted into a 82 mm long, 7.95 mm ID, 11 mm OD alumina tube. The aluminium adapter is glued to the alumina tube using epoxy and the joint is covered in aluminium tape to protect the epoxy from exposure to the plasma. On the other end the dual bore alumina rod extends about 5 mm from the large alumina tube. The surrounding gap is filled with a zirconium paste, taking care that the probe tip is centered. A CAD drawing of the probe is shown in Figure 3.3 and a cross-section to show the internal configuration, in figure 3.4.

3.2 Capacitive Probes

3.2.1 Theory

Capacitive probes (CP) are particular to RF plasmas and are used to measure the local RF potential. The name refers to the fact that the probe is capacitively coupled to the plasma; this also means it draws no net current. The capacitive probe consists of a wire connected to a 50Ω resistance, terminated in a coaxial connector. The shield of the connector is extended with a conductive cylinder which is concentric with the center wire and extends beyond the resistance, leaving only the tip of the wire exposed. The outer cylinder is then enshrouded with a dielectric, covering also

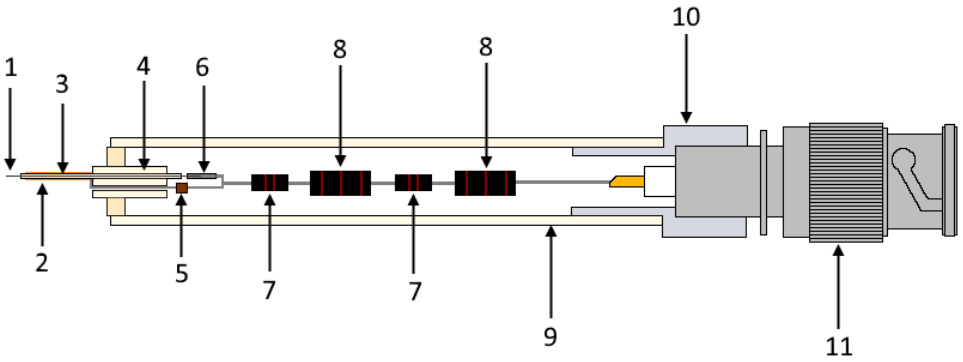

Figure 3.4: Schematic cross-section of RF-compensated Langmuir probe. Numbered parts: 1) tungsten tip; 2) secondary electrode (copper tape); 3) single bore alumina rod; 4) double bore alumina rod; 5) coupling capacitor; 6) crimp ferule; 7) 13.56 MHz choke; 8) 27.12 MHz choke; 9) alumina tube; 10) custom aluminium adapter; 11) BNC connector.

the open end of the cylinder and the wire tip. The wire and resistor are electrically shielded by the cylinder, while the short wire tip is capacitively coupled through the dielectric. A schematic of the probe can be seen in Figure 3.6 along with an equivalent circuit. Note that C_p is the capacitance between the wire tip and the plasma, and C_c is the capacitance of the shielded part and the coaxial cable.

From the equivalent circuit it can be seen that the probe connected to an oscilloscope with a 50 Ω input forms a voltage divider. The impedance is constant at a given frequency and therefore the relationship between the RF potential and the voltage measured at the oscilloscope is linear. Since the plasma is highly non-linear, harmonics of the RF frequency can be generated [30],[42]. The impedance of the voltage divider at each harmonic will be different. To obtain the relationship between the RF potential and the measured voltage the probe is calibrated using the same method as used in [42]. The resulting coefficients are shown in table 3.1 and agree well with those obtained in [42]. The calibration constants clearly scale with the inverse of the frequency, as expected.

3.2.2 Construction

The probe is based on a pyrex test tube of 95 mm length with a 12 mm outer diameter and a 9.6 mm inner diameter, which serves as the dielectric shroud. A

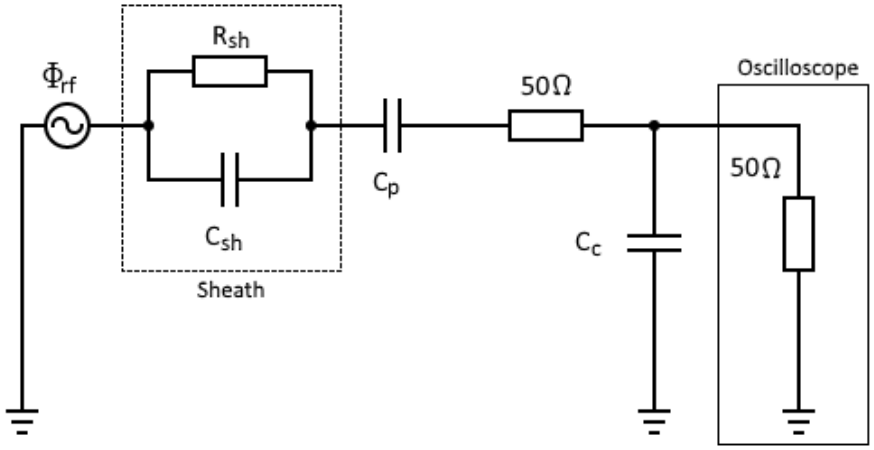

Figure 3.5: Equivalent circuit of capacitive probe.

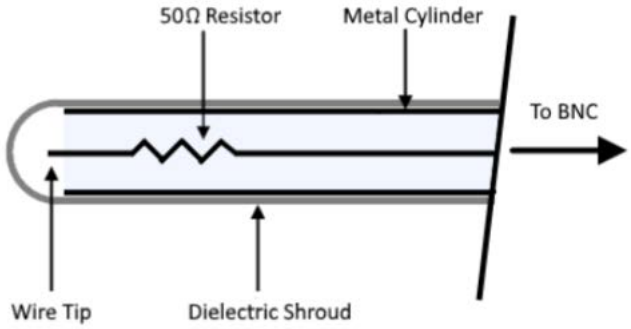

Figure 3.6: Schematic of capacitive probe.

Table 3.1: Capacitive probe calibration.

Frequency [MHz]	**Calibration constant**	$\|\mathbf{\Phi_{rf}}\|$**[V]**
13.56	1029	13.01
27.12	511	0.567
40.68	328	0.013

Figure 3.7: CAD drawing of Capacitive probe.

hollow aluminium cylinder was machined to fit the test tube, with a length of 90 mm, a 9.5 mm outer diameter and 6 mm inner diameter. At one end the cylinder has a 9 mm long and 14 mm diameter extension, with an inside 3/8-32 UNEF thread to fit a threaded male bulkhead BNC connector. A 60 mm long, 1 mm diameter bare copper wire was soldered to the solder pin of the BNC connector. A 50Ω resistor was soldered to the wire. On the other end another 15 mm of copper wire was soldered. The length of the wire was chosen such that the tip was situated at the center of the spherical end of the test tube. To ensure that the wire would remain centered three PTFE spacers of 30 mm length were machined to fit the aluminium tube and the wire. A CAD drawing of the probe is shown in Figure 3.7.

3.3 Emissive Probes

3.3.1 Theory

Emissive probes (EP) essentially are Langmuir probes heated to the point of thermionic emission. Emissive probes emit electrons with a half-Maxwellian distribution with a temperature T_w equal to that of the wire. Since generally $T_w \ll T_e$ the exponent in the Boltzmann relation of the emitted electrons is much more sensitive to potential differences. Emissive probes can therefore measure the plasma potential more accurately. [112] There are several methods for measuring Φ with an EP and they can be found in the extensive review on EP's [112] and their use in electric propulsion testing [113]. In this paper we focus on the floating potential method in the limit of high emission.

As mentioned before any unbiased conductive exposed to the plasma will charge

up negatively (with respect to the plasma potential). When electrons are emitted from the probe surface the negative charge on the probe is reduced and the voltage drop over the sheath decreases. If the emitted current is sufficiently high the floating potential will approach the plasma potential.

For a Maxwellian xenon plasma, without emission, the difference between the floating potential and the plasma potential is about $5.8k_BT_e/e$ [68, p.172]. By inducing an emission current this potential difference can be reduce. However it was found that at best an emissive probe will float about $1.5k_BT_e/e$ below[1] [113, 53].

The advantage of the emissive probe over the Langmuir probe is then that a single measurement of the floating potential will suffice, instead of taking an $I-V$ characteristic. Furthermore, emissive probes provide an accurate measurement of the plasma potential even in cases where the Langmuir probe measurement might fail, such as flowing or magnetized plasmas. The disadvantage is that the emissive probe can potentially perturb the plasma more since it adds electrons to the plasma with a different distribution function. The floating potential method is particularly susceptible to this as it relies on large emission currents. Keeping the filament, and therefore the total emission current small, minimizes these problems.[113].

The thermionic emission is given by the Richardson-Duschman equation.

$$I_{e,th} = \lambda_R A_0 T_w^2 A_w \exp\left(\frac{-e\phi_w}{k_B T_w}\right) \tag{3.16}$$

$$A_0 = \frac{4\pi m_e k_B^2 e}{h^3} = 1.20173 \cdot 10^6 \ Am^{-2}K^{-1} \tag{3.17}$$

here T_w is the wire temperature, ϕ_w the work function of the material, A_w the surface area, m_e the electron mass, $h = 6.626 \cdot 10^{-34}$ kg·m^2·s^{-1} Planck's constant and $\lambda_R \in (0,1)$ a material specific parameter.

According to [53] the probe floats nearest to the plasma potential when the ratio between the emitted and incident current reaches a critical value Γ_c.

$$\Gamma_c = 1 - 8.3\sqrt{\frac{m_e}{m_i}} \tag{3.18}$$

For a xenon plasma this means that the emitted current is 0.98 times the incident current. For example, from eq. 3.3 the incident current density to a probe at

[1]Note that this consists of $1k_BT_e/e$ as calculated by [53] and the $0.5k_BT_e/e$ drop over the pre-sheath to accelerate the ions to Bohm velocity.

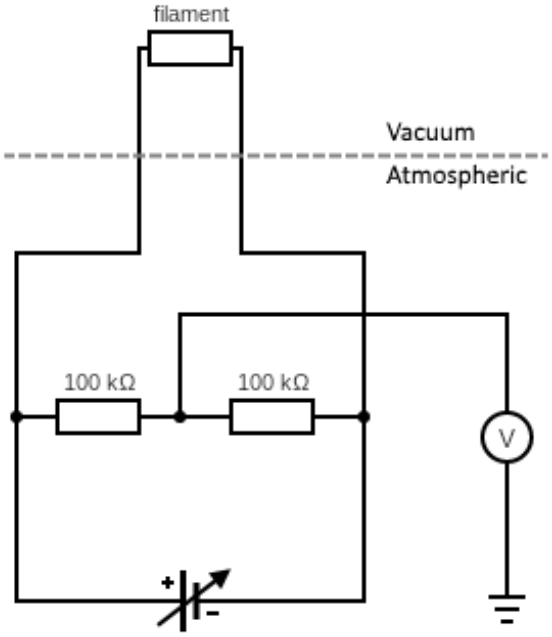

Figure 3.8: Schematic of emissive probe setup.

$1.5k_BT_e/e$ below the plasma potential, in a plasma with $T_e = 5$ eV and $n = 10^{17}$ m^{-3} is about 138 mA·cm^{-2}. A Thoriated Tungsten filament with $A_G = 3.0$ A·cm^{-2}·K^{-1} and $\phi_w = 2.63$ V [49] will produce the same current when at about 1700 K. The probe material needs to be able to withstand such high temperatures, which is why thoriated tungsten is used. Thoriated tungsten has a lower work function than regular tungsten and the same melting point of 3695 K.

To be able to reach such high temperatures a thoriated tungsten filament is heated by Joule heating. To measure the plasma potential using the floating point method the filament of the probe is connected in series with a floating power supply. Two relatively large resistors ~ 100 kΩ are connected in parallel with the filament, but outside of the vacuum chamber. The potential between the two resistors is then equal to that of the mid-point of the filament and is therefore connected to a Volt-meter. A schematic of the setup is shown in Figure 3.8. The probe is then positioned in an area where the plasma density is highest and the heating current is slowly increased while measuring the floating potential. The floating potential will initially increase and then saturate when it is near the plasma potential as can be seen in Figure 3.9. The heating current is then set to the value right after the knee and the probe is swept through the plasma to obtain potential profiles.

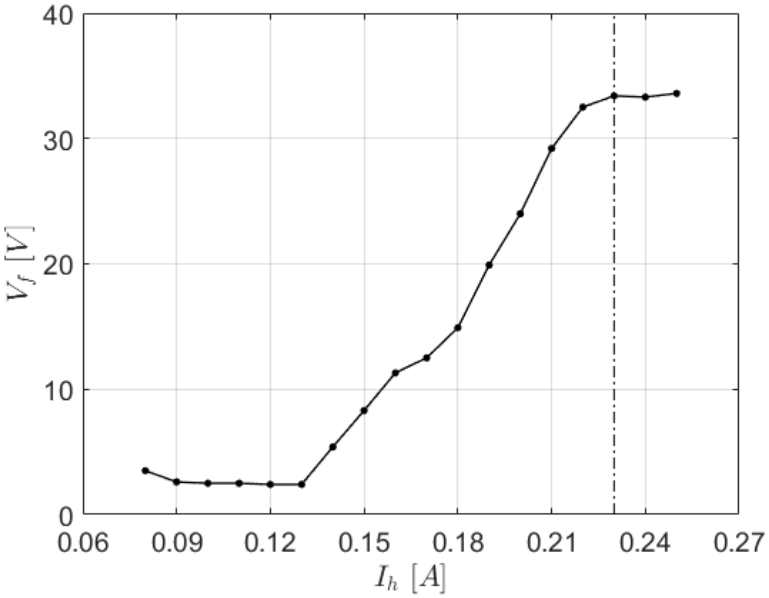

Figure 3.9: Floating potential of an EP as a function of heating current.

3.3.2 Construction

The emissive probe is centered around a thin filament with a low work function, that can withstand a high temperature, above 1500K. In this case a 50 μm thoriated-tungsten filament was used. Both ends of the 4 cm long filament were wrapped in a bare, stranded copper wire, by twisting the copper wire around it. This ensure a good electrical and thermal contact. The stranded wire is about 120 mm and each end is inserted in an aluminium-oxide dual bore rod. The rod has a 4 mm diameter and two 1.3 mm diameter bores. The wire is inserted such that the only part protruding from the rod is a semicircle of the exposed filament. On the other end the stranded wires extend about 6 mm and are soldered to a two pole connector. A 10 mm diameter aluminium cylinder is machined to accommodate the ceramic rod and has a tapped bore (M9x0.5) to insert the connector. The aluminium cylinder needs to be wrapped in Kapton tape to prevent drawing a large current from the plasma. A CAD drawing of the probe can be seen in Figure 3.10 and a cross-section in figure 3.11.

Figure 3.10: CAD drawing of Emissive probe.

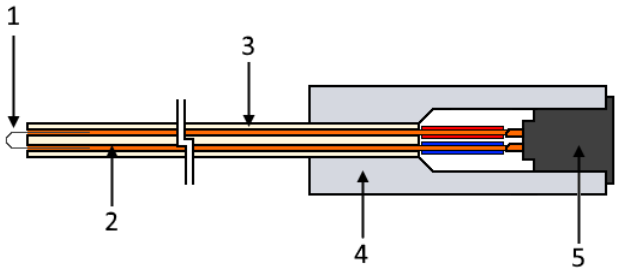

Figure 3.11: Schematic cross-section of Emissive probe. Numbered parts: 1) tungsten filament; 2) copper leads; 3) double bore alumina tube; 4) aluminium housing; 5) connector.

3.4 Faraday Probes

3.4.1 Theory

Faraday probes (FP) measure current densities in flowing plasmas. In electric propulsion particularly they are used for measuring the ion current density, as that is the species that carries the momentum. In essence Faraday probes consist of a (circular) conducting surface, its normal parallel to the flow. The surface is biased to a sufficiently negative potential to ensure that all electrons are repelled and only ions are collected. The measured current, divided by the probe area then yields the current density. A schematic of the FP setup is shown in Figure 3.12.

The problem with a single conducting surface is that the effective collection area changes with the bias potential, due to edge effects [22]. To overcome this problem, FP's generally have a guard-ring: a concentric ring of the same material as the collector, biased to the same potential, but its collected current not contributing to the measurement. If sized correctly the field over the collector remains flat and the effective collection area will be independent of the bias voltage [79].

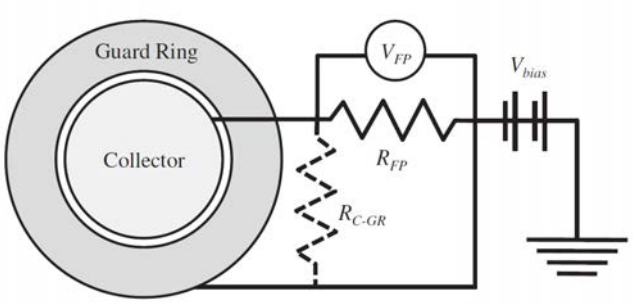

Figure 3.12: Schematic of Faraday probe setup. (from ref. [22])

Another solution is the Faraday cup (FC) which consists of a metal cylinder with on one side the collector and on the other side a collimator. The collimator is a conductive disc with a small orifice that is electrically isolated from the cylinder and collector. Due to the collimator the probe has a collection angle less than 2π str and only ions with a narrow range of ion velocity vectors can reach the collector [79]. The collected current is therefore lower than that of a Faraday probe with guard-ring of comparable size. Most importantly the cup design inherently makes the collected current independent of the bias voltage.

To size the FP one has to look at the width of the plasma sheath; the sheath should not exceed the guard-ring diameter (or the orifice of the FC). The sheath width can be estimated using the Child-Langmuir law [68, p.176].

$$j_i = \frac{4}{9}\epsilon_0\sqrt{\frac{2e}{m_i}}\frac{\Delta V^{3/2}}{s^2} = enu_i \tag{3.19}$$

here $\Delta V = \Phi - V$. The space-charge limited current density is equated to the incoming ion current and solved for the sheath width s.

$$s = \frac{\sqrt{2}}{3}\lambda_D\left(\frac{2e\Delta V}{k_B T_e}\right)^{3/4} \tag{3.20}$$

For sheaths in stationary plasmas the boundary condition for the velocity of the ions is the Bohm velocity, $u_i = u_B$. However, in a thruster plume the ions are supersonic. One could instead use $u_i = Mu_B$ (M being the Mach number) as a boundary condition scaling the resulting sheath width with M^{-2}. Clearly the Bohm boundary condition is an overestimation, but will be used as an upper limit. For the plasma under consideration it was found that the sheath width is less than 2 mm within the first 500 mm of the plume. The upper limit on the dimension is

Figure 3.13: CAD drawing of the Faraday probe.

set by the maximum current that can be measured by the current meter, which for the Keithley 6517B used in this work is 10 mA. Based on models [82] and previous experiments current densities are expected to be below 10 mA $\cdot$ cm^{-2}; requiring a collector/collimator area of less than 1 cm^2.

3.4.2 Construction

For the FP a collector size of 10 mm diameter was chosen with a guard-ring of 23 mm outer diameter, 11 mm inner diameter. Both collector and guard-ring are 6 mm thick and machined from aluminium. On the backside the collector has a M2 tapped, blind hole in the center; the guard-ring has 3 similar holes at a 7.5 mm distance from the center and equispaced. Collector and guard ring are mounted concentrically on a 3 mm thick, 25 mm diameter Macor disc with through holes corresponding to the aforementioned tapped holes. Both are secured with copper plated M2 bolts. Two wires are soldered to the copper plated bolts - one to the collector and one to the guard-ring - and subsequently covered with a drop of epoxy. The Macor disc is press-fitted into a 12 mm long, 25 mm diameter aluminium cup. The back of the cup is extended with a 125 mm long, 12 mm diameter aluminium tube. At the other end of the tube a 2-pole connector is inserted to which the collector and guard-ring wires are soldered. Note that the long tube is included to ensure that the front area of the FP is at the same position as the tip of the other probes when mounted on the translational stage. A CAD drawing of the probe and a longitudinal cross-section are shown in Figure 3.13 and 3.14.

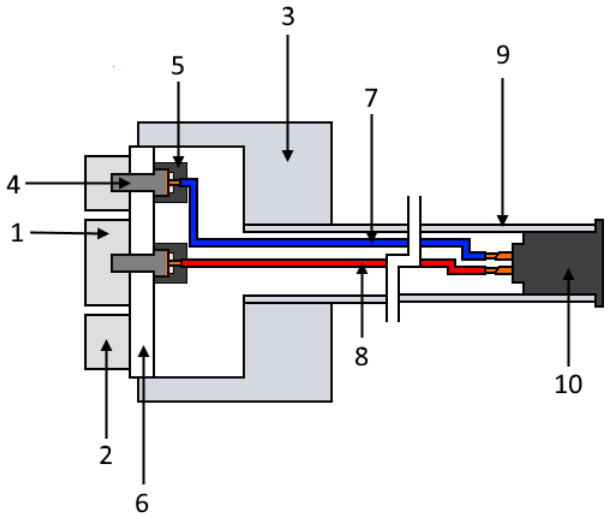

Figure 3.14: Schematic cross-section of the Faraday probe. Numbered parts: 1) collector; 2) guard-ring; 3) aluminium housing; 4) M2 copper plated screws; 5) epoxy; 6) Macor disc; 7) guard-ring wire; 8) collector wire; 9) aluminium tube; 10) connector.

3.5 Retarding Potential Analyzer

3.5.1 Theory

Retarding potential analyzers (RPA) are used to measure the ion velocity distribution function. They are similar to Faraday probes with the added feature of a retarding grid. By biasing the grid to different potentials only a part of the ion flux will be collected, depending on their energy. The relation between collected current and bias potential can then be used to derived the ion energy distribution function and by extension the velocity distribution function.

RPAs generally have several grids, all of the same dimensions (orifice diameter, and grid diameter). The first grid (G_0) reduces the sampling diameter to below the Debye length to prevent plasma forming inside the probe. The second grid (G_1) is biased at a negative potential, typically $-60\ V$ w.r.t G_0, to repel electrons. The third grid (G_2) is swept over positive potentials to discriminate positive ions based on their energy. The fourth (G_3) and last grid is biased negatively again, typically at $-10\ V$ w.r.t. G_0, to prevent any secondary electrons emitted by the collector upon ion impact to escape. The four grids are followed by a collecting

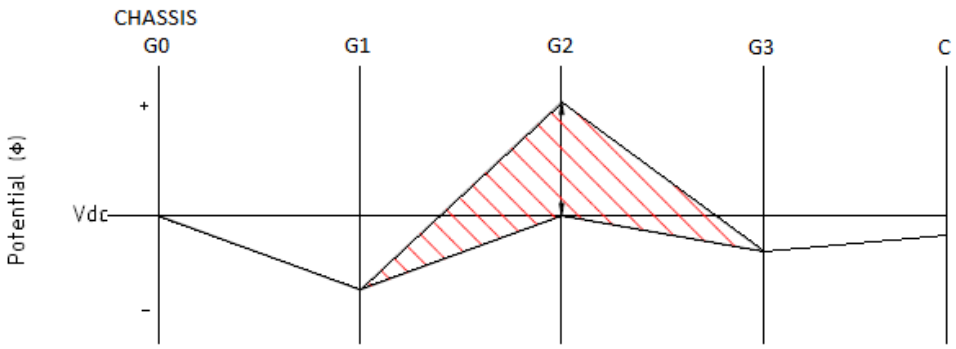

Figure 3.15: Bias potentials in an RPA. From ref. [60]

electrode, biased typically at $-40\ V$ w.r.t. G_0, to attract the ions. If mounted to a grounded structure G_0 is generally at ground potential i.e. $V = 0$. The distribution of potentials on the grids is illustrated in Figure 3.15. A species in a plasma can be described by a distribution function $f(\mathbf{r}, \mathbf{v}, t)$. Measuring at a point in space, $\mathbf{r}$, and time t one can speak of the local velocity distribution function $f(\mathbf{v})$. The zeroth moment of this distribution function gives the plasma density n, while the first moment of the distribution yields the mean velocity. For a species in thermal equilibrium the velocity distribution is Maxwellian.

The raw data of the RPA is the $I - V$ curve, which contrary to that of the Langmuir probe consists solely of ion current. Dividing by the probe area yields the ion flux $j_i = enu_i$. Taking also in account that the ion energy $\mathcal{E} = m_i u_i^2/2 = eV$ the ion flux can be expressed as follows:

$$j_i = \frac{e^2 n_i}{m_i} \int_{eV}^{\infty} f_i(\mathcal{E}) d\mathcal{E} \tag{3.21}$$

By biasing the grid at different potentials the RPA measures the voltage dependent ion flux $j_i(V)$. From the above equation it then immediately follows that its first derivative is proportional to the velocity distribution function.

$$\frac{dj_i}{dV} = -\frac{e^2 n_i}{m_i} f_i(\mathcal{E}) \tag{3.22}$$

Lastly, integrating the $j_i(V)$ profile furthermore provides the local ion flux j_i similar to the Faraday probe measurement.

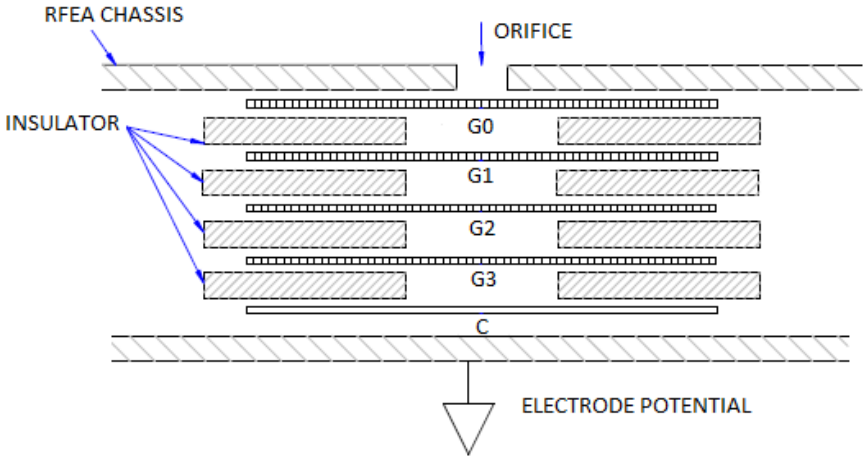

Figure 3.16: Bias potentials in an RPA. From ref. [60]

3.5.2 Construction

The RPA currently in use at the EP^2 lab is a commercially available Impedans Semion Retarding Field Energy Analyzer (RFEA). In parallel, EP2 is developing a novel RPA system. The Impedans Semion button probe is a circular disc of 50 mm diameter and 5 mm thickness and contains four grids as mentioned before. The frontal surface has 37 orifices of 0.8 mm diameter. All grids have a 50% transmission and 20 μm orifices. The total collection surface is therefore 4.56 mm^2 A schematic of the grids is shown in Figure 3.16. The Impedans Semion consists of a button probe as described above, a feed-through and an electronics unit. It can measure ion fluxes up to 220 A$\cdot$ m^{-1} and ion energies up to 2 kV.

3.6 Translational Arm

To obtain spatially resolved measurements of the thruster exhaust plume the diagnostics are mounted on a translational arm. Because of the conical shape of the plume a polar coordinate system is preferable as this allows the diagnostics to be aligned with the direction of the flow as much as possible. This justifies the assumption of zero drift velocities for the plasma species in Langmuir probe measurements and obviates the need for geometrical corrections in Faraday probe measurements. It cannot be stressed enough that alignment of the probe is paramount to the

validity of the results. Particularly for the interpretation of Langmuir probe measurements which are already heavily dependent on underlying models.

Previous, otherwise excellent work on probe measurements in electric thruster plumes often report local measurements at different positions but fail to elucidate how the probe was positioned [12]. Others briefly mention the translational system that was used or merely show an image.[35] Sometimes translational systems with a Cartesian topology are used that fail to ensure probe alignment with the flow. [127] Some systems are only 1D, and provide either on-axis downstream measurements or azimuthal measurements at a single downstream position.[108] Our current system provides a 2D envelop of $\pm 90°$ and 0-400 mm.

The main issue with mechanical systems in vacuum is that the lubricant of regular bearings will quickly evaporate rendering the bearings useless. Therefore, in this design, all components are vacuum rated, while custom parts incorporate IGUS® [2], lubricant free bearings. The arm system is mounted on a rectangular frame consisting of 45 × 45 mm extruded aluminium profiles. Both the azimuthal axis and the radial axis are driven by vacuum rated stepper motors, that can provide up to 2 Nm of torque and have a 200 step/revolution resolution. The rotational axis is connected to the azimuthal motor by means of a planetary gearbox, with a gear ratio of 1:180. The axle of the gearbox is coupled to the azimuthal axis of the arm by means of a timing belt with a gear ratio of 1:2, resulting in an azimuthal resolution of $5 \cdot 10^{-3}$ degrees. A rotary encoder is mounted to the bottom side of the axis of the arm, to track the azimuthal position. This allows for continuous azimuthal sweeps. The radial axis consists of a linear guide, driven by a 12 mm pitch lead screw, thus having a 60 μm resolution. At the distal end of the radial axis two small wheels are mounted that roll along a semi-circular aluminium strip which is mounted on the frame. This prevents the radial axis from tipping downwards due to the weight of the diagnostics. The the radial carriage a 15 mm thick aluminium plate is mounted on top which there is a 20 × 20 mm extruded aluminium profile which support a small 5 mm thick aluminium strip that holds the diagnostics. Currently up to three different diagnostics can be mounted on the arm. The system is also outfitted with limit-switches to be able to zero the position of the arm system in-situ. A CAD drawing of the system can be seen in Figure 3.17.

[2] IGUS®: https://www.igus.com

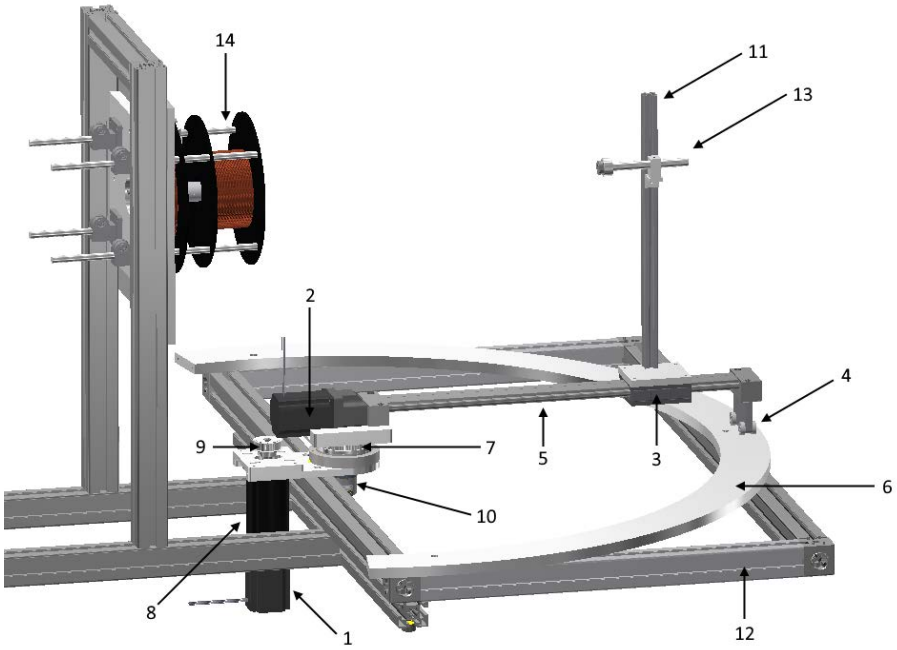

Figure 3.17: CAD drawing of the custom translational arm system. Numbered parts: 1) azimuthal motor; 2) radial motor; 3) radial carriage; 4) azimuthal carriage; 5) lead screw module; 6) rails; 7) azimuthal bearing; 8) gearbox; 9) timing belt pulley; 10) rotary encoder; 11) aluminium profile; 12) frame; 13) probe; 14) thruster.

3.7 Thruster Performance Estimation

In this section we present the measurements of the different probe and show how they can be used to determine the thruster performance. We start with the capacitive probe as this diagnostic does not provide a measure of the thruster performance but is used to assess the validity of the RF-compensation of the Langmuir probe.

To measure the oscillations of the plasma potential the CP is mounted on the probe arm and measurements are taken on-axis at different downstream positions. The measurements are obtained with an oscilloscope. Post processing is done by means of a fast Fourier transform (FFT) so it is key to obtain a waveform with a sufficient amount of periods to guarantee a good resolution in the Fourier spectrum. With sample time of 2 ns a waveform of 2712 periods is obtained. Figure 3.18 shows the FFT of the waveform obtained at 100 mm downstream of the HPT operating at 450 W. The peaks have been scaled such that the amplitude of the base frequency is equal to one. Although up to 6 harmonics can be seen only the first harmonic is relevant as the relative amplitude of the others is below 1% The first harmonic has an amplitude about 8% compared to the base frequency. To obtain the amplitude of the plasma oscillations these values have to be scaled by the coefficients of table 3.1 reducing further the contributions of the first harmonic to 4%. It is therefore sufficient to only look at plasma oscillations at the base frequency. A plot of the amplitude of Φ_{RF} on-axis, at different downstream positions is shown in Figure 3.19. It can be seen that the RF component of the plasma potential linearly increases from 5 V far downstream to about 12 V at a 100 mm and then sharply increases to almost 30 V at 50 mm. When positioned at 50 mm from the thruster exit the probe can be seen to visually perturb the plasma, bringing the validity of this measurement into question. Since no LP measurements are obtained closer than 100 mm downstream we discard this point. In any case it is clear from this plot that the RF compensated probe has to be able to filter at least 12 V of RF potential oscillations.

The Langmuir probe is used to measure the $I - V$ curve of the plasma. An example plot taken on the center line of the HPT plume about 200 mm downstream, is shown in Figure 3.20. The solid line is the $I - V$ curve, while the dashed line denotes the derivative. For voltages below zero the current is negative and of the order of micro-Amps, corresponding to ion collection. The curve crosses zero

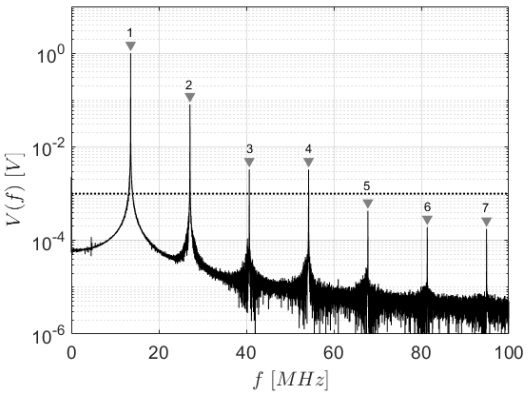

Figure 3.18: FFT of a waveform obtained with a CP.

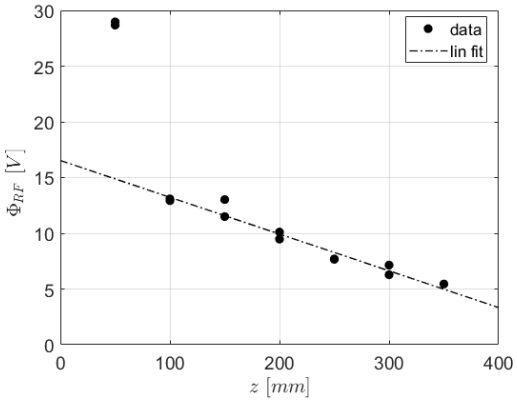

Figure 3.19: Amplitude of Φ_{RF} downstream in the HPT plume.

at $\Phi_f = 11.9$ V and then increases exponentially into the milli-Amp range. The characteristic knee is not appreciable in this graph; despite this the clear maximum in the derivative denotes the plasma potential at 32.5 V. Figure 3.21 shows a close up of the ion-collection region together with a fit of both the thin-sheath theory (solid) and thick-sheath theory (dash-dotted) of which the latter seems a better fit. Figure 3.22 shows a close up of the logarithm of the electron current (obtained by subtracting the fitted ion-current) near the plasma potential. The solid line is a linear fit to obtain the slope, its inverse being proportional to the electron temperature. The plasma parameters obtained from this particular data-set are an ion density of $3.9 \cdot 10^{16}$ m^{-3}, electron temperature of 4.9 eV and plasma potential of 32.5 V.

The EP probe like the other probes is swept through the plasma to obtain the plasma potential profile, both in azimuthal and axial direction. In Figure 3.23 the axial profile on the center line of the thruster is shown. Note that this measurement is already corrected with a concurrent measurement of the electron temperature.

In electrode-less thrusters like the HPT [91] that rely on ambipolar acceleration the ions are accelerated along the axial potential drop. The energy balance for ions thus reads:

$$m_i u_i^2 = m_i u_{i,0}^2 + 2e(\Phi - \Phi_0) \tag{3.23}$$

Linearly extrapolating the potential profile to the thruster exit ($z = 0$) and assuming that ions are sonic at the exit [7] , $u_{i,0} = u_B$ the plasma potential profile can be

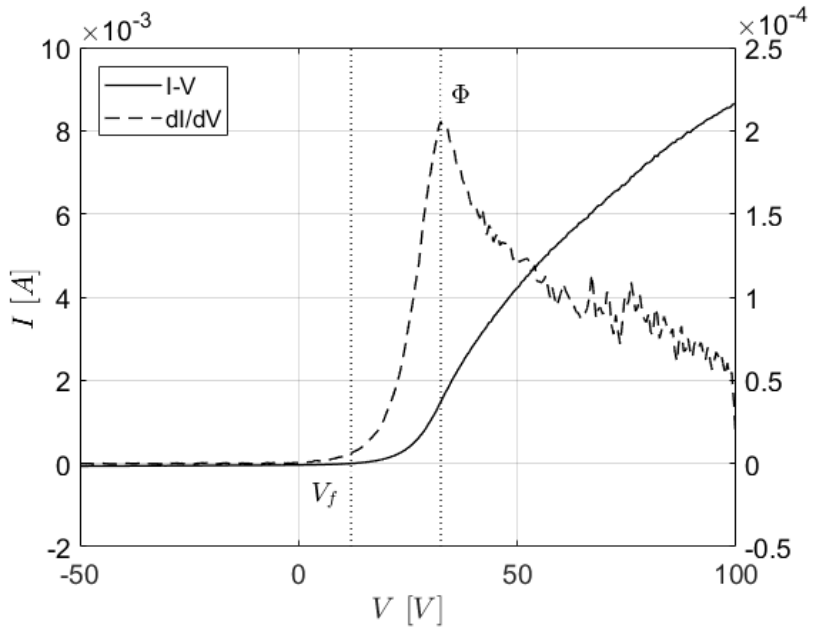

Figure 3.20: $I - V$ curve (solid) and first derivative (dashed).

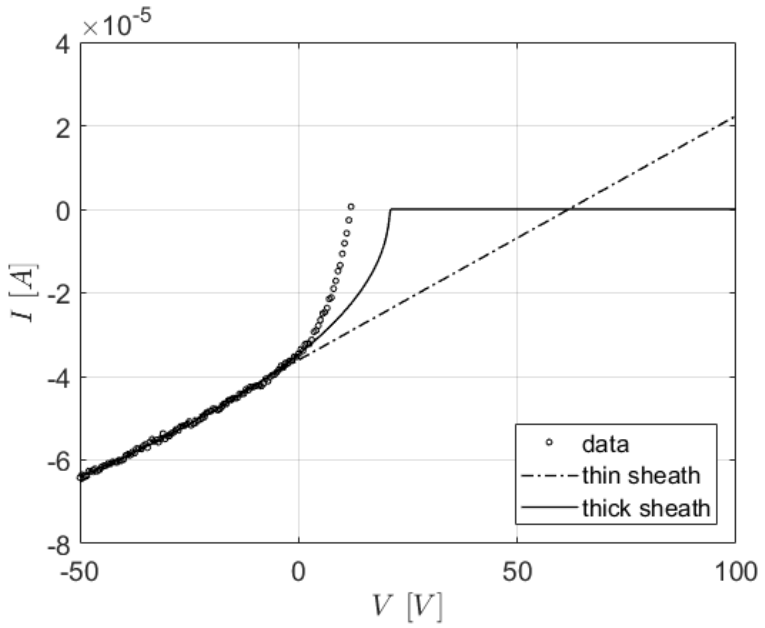

Figure 3.21: Ion current: data (dots), thin sheath theory (solid), thick sheath theory (dash-dotted).

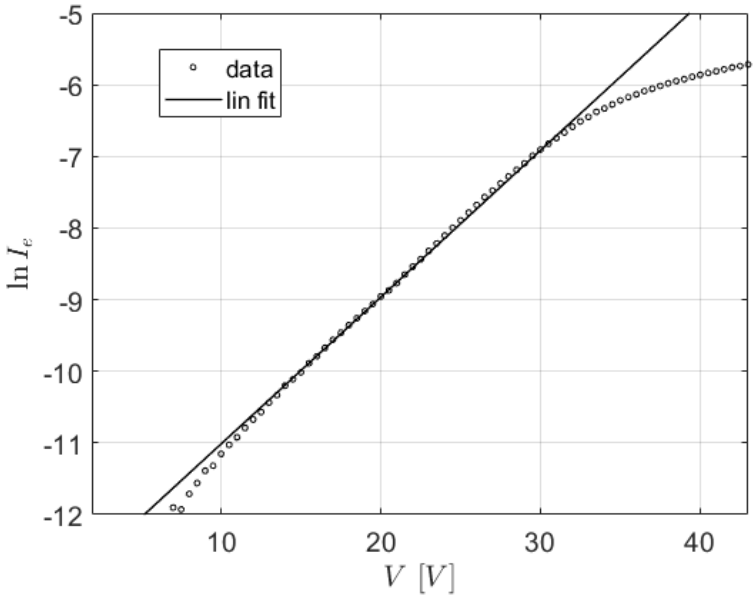

Figure 3.22: Logarithm of electron current: data (dots), linear fit (solid).

translated into an ion Mach profile, as shown in Figure 3.24. Linear extrapolation to $z = 0$ is of course a rough approximation. A better solution is to measure the ion velocity distribution with an RPA at a single point of the Φ profile and use the mean velocity to convert the plasma potential to the ion velocity. Note that the continuing acceleration of ions over the length of the plume is characteristic of thrusters that a use magnetic nozzle.

Faraday probes are mostly swept through the plasma along the radial or azimuthal direction to obtain the angular/radial distribution of the ion current density. Figure 3.25 shows an azimuthal FP scan of the HPT helicon plasma thruster is shown. The measurement was taken at 300 mm from the thruster exit, between $\pm 70°$. Usually sweeps are performed from $\pm 90°$, however in the current configuration the power supply of the thruster impaired the motion of the translation stage. Assuming axi-symmetry this profile can be integrated to obtain the total ion current, which for this case is 0.47 A.

$$I_i = \pi R^2 \int_{-\pi/2}^{\pi/2} j_i(\theta) \sin\theta d\theta \tag{3.24}$$

By dividing the ion current by the elementary charge, e, and multiplying with the atomic mass, M_A, one obtains the mass flow rate of ions, $\dot{m}_i$. Dividing this by

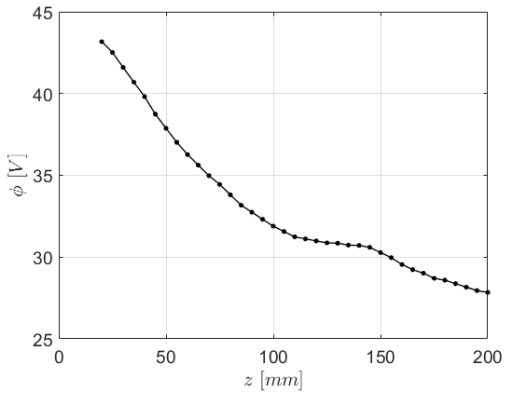

Figure 3.23: Axial EP scan of the HPT, from 50 mm to 200 mm downstream.

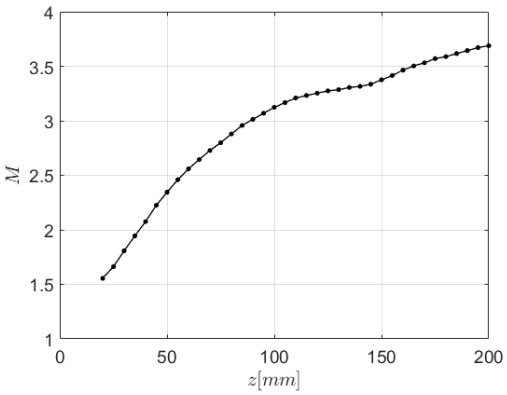

Figure 3.24: Axial ion Mach profile obtained from fig. 3.23 and equation 3.23.

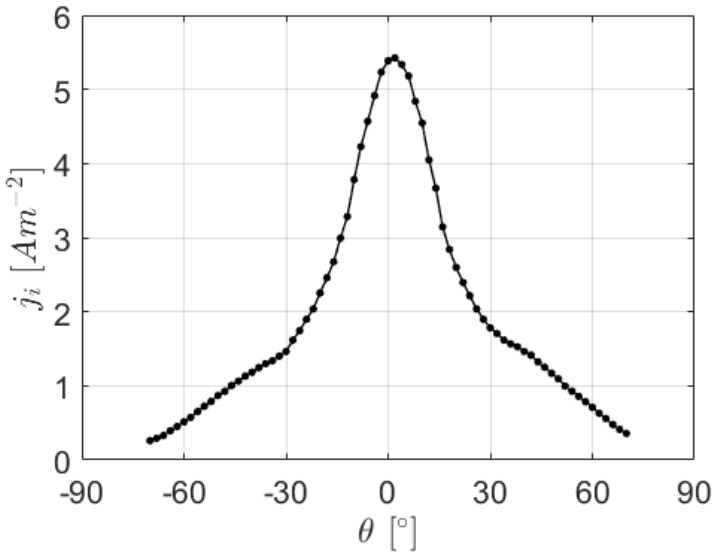

Figure 3.25: Azimuthal FP scan taken at 300 mm downstream of the HPT operating with 20 sccm of argon.

the mass flow rate of neutrals, $\dot{m}$, injected into the thruster yields the utilization efficiency, η_u, a relevant parameter for thruster characterization. For the plot of figure 3.25 η_u is about 32.4%. Another relevant parameter is the divergence angle. Difference in divergence of momentum and divergence of ion current are mainly due to spatial variation in ion charge species fractions [22]. Since the fraction of multiply charged ions is generally small the divergence momentum can be found by calculating the divergence of ion current. From the azimuthal current distribution one can obtain the axial current.

$$I_{i,ax} = 2\pi R^2 \int_0^{\pi/2} j_i(\theta) \cos\theta \sin\theta d\theta \tag{3.25}$$

The divergence half-angle θ_D is then the arccosine of the charge flux weighted average cosine $\langle \cos\theta \rangle_j$, in this case $\theta_D = 38°$.

$$\theta_D = \cos^{-1}(\langle \cos\theta \rangle_j) = \cos^{-1}\left(\frac{I_{i,ax}}{I_i}\right) \tag{3.26}$$

From the divergence angle the divergence efficiency can be calculated.

$$\eta_\theta = \cos^2(\theta_D) \tag{3.27}$$

Another interesting feature that can be studied with 2D Faraday probe scans is ion detachment, an important phenomenon in magnetic nozzles. By taking azimuthal ion current density profiles at different axial positions and plotting the normalized radii of 30-60-90% ion flux tubes together with the corresponding magnetic flux tubes the ion detachment can be visualized. [71]

The RPA is used to obtain in formation about the energy of the ions in the plume. Figure 3.26 shows data obtained with the RPA from the plume of the HPT. The very pronounced and narrow peak shows that the ions are nearly mono-energetic with a most probable energy of 115.5 eV. The average energy can be found by taking the first moment of the distribution and is about 103.6 eV. The spread in the distribution can be explained by the fact that there exists a potential gradient inside the ionization region; the ions therefore don't all experience the exact same potential drop; another explanation is the presence of low energy ions created by charge-exchange collisions with the background gas. The data of Figure 3.26 were obtained while operating with xenon. The potential drop in a magnetic nozzle is

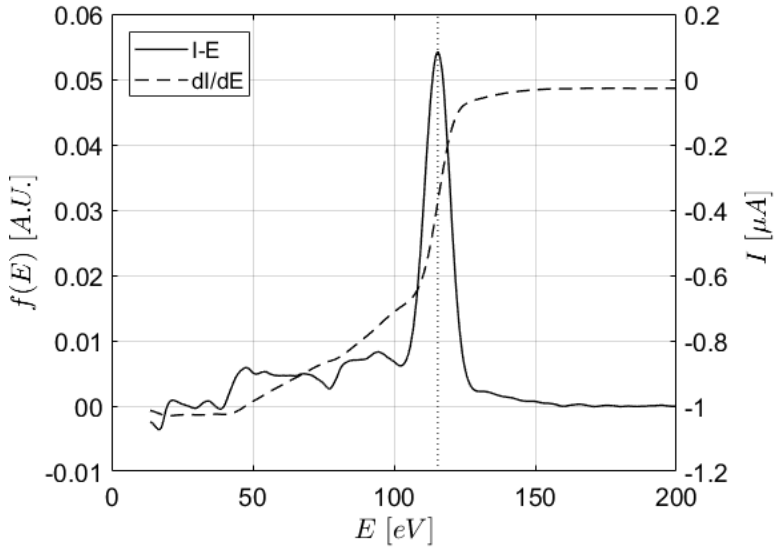

Figure 3.26: $I-V$ curve (solid) and ion energy distribution function (dashed) as obtained with the Impedans Semion RPA

finite and dependent on the ion/electron mass ratio. For xenon the total potential drop is about $8T_e$.[76] The energy of 103.6 eV then implies an electron temperature of about 13 eV which agrees well with corresponding Langmuir probe measurements [3]. Note that at this energy the ions have a velocity of about 12 km·s^{-1}.

The RPA measurements can be combined with the FP and LP measurements to estimate the thrust. The total thrust at a downstream position z is the sum of the local electron pressure and the ion momentum flux integrated over a hemispherical surface. Assuming axi-symmetry this can be written as:

$$F(z) = \pi z^2 \int_{-\pi/2}^{\pi/2} n(z,\theta) \left[k_B T_e(z,\theta) + m_i u_{zi}^2(z,\theta)\right] \sin\theta d\theta \tag{3.28}$$

Here $n(z,\theta)$ and $T_e(z,\theta)$ can be measured with the Langmuir probe. The second term on the right hand side can be measured by combining RPA and FP measurements. Since $j_i = enu_i$ and $\mathcal{E}_i = m_i u_i^2/2$ we can write the thrust as:

$$F(z) = \pi z^2 \int_{-\pi/2}^{\pi/2} \left[n(z,\theta) k_B T_e(z,\theta) + m_i \frac{j_i(z,\theta)}{e} \sqrt{\frac{2\mathcal{E}_i(z,\theta)}{m_i}} \cos^2\theta\right] \sin\theta d\theta \tag{3.29}$$

[3] Note that this would be the electron temperature inside the source which is higher than at the position of the measurement in Figure 3.20

Measurements of $\mathcal{E}_i$ at different angles shows that the corresponding axial velocity u_{iz} is independent of the angle up to at least $\pm 20°$. Beyond that the IEDF signal becomes weak and noisy. Corresponding FP measurements show that the majority of the current is within the same cone. As a first estimation one can therefore use the on-axis value of $\mathcal{E}_i$.

Furthermore, sufficiently downstream the pressure term becomes negligible. At the thruster exit planes both terms contribute 50% of the thrust, however conversion of electron thermal energy into ion kinetic energy results in an increase of the momentum term at the expense of the pressure term.

3.8 Thruster Test Campaign Results

In this section we present results from a test campaign performed with plasma probes. The campaign was performed in the Q4 of 2018 and Q1 of 2019 on the HPTx prototype, using both argon and xenon as propellant. The prototype described in subsection 2.3.4 consist of Macor or quartz plasma chamber with a 20 mm inner diameter, a single solenoid, and a half helical antenna. The nominal power is 450W, but can be comfortably varied between 300-600W. The magnetic field can be varied from 0-1500G and the propellant mass flow rate can be varied from 2.5-20 sccm for xenon and from 10-40 sccm for argon.

The measurements consisted of a combination of Langmuir probe, Faraday probe and RPA measurements in the polar plane from -90° to +90° and up to 400 mm downstream of the thruster exit. Although the probes can be put practically in the exit plane of the thruster, doing so perturbs the plasma. Therefore 100-150 mm downstream is the closest practical approach, depending on the operating point.

Using the RFCLP the plasma density in the plume of the HPTx with a nominal operating point of 450W, 1000G and 20 sccm of argon has been characterized. In Figure 3.27 the plasma density on-axis at different downstream positions is shown for four different case: nominal operation, increased magnetic field: 1500G, inverse polarity of the magnetic field (i.e. 1000G but with the opposite direction) and at 600W. As discussed in section 2.2 the $m = +1$ mode is excited preferentially, which for a right handed antenna is in the direction north-south. In the nominal case the $m = +1$ wave travels downstream (towards the exit) while in the inverse case it travels upstream.

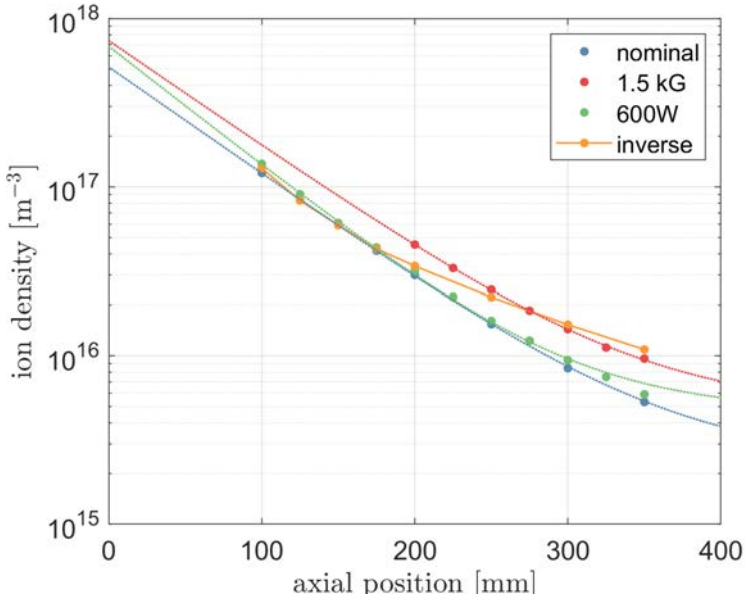

Figure 3.27: On-axis plasma density at different downstream positions in the plume of the HPTx nominally operating at 450W, 1000G and 20 sccm argon.

The dashed lines are a empirical fit with a function of the form $f(x) = a\exp(-bx)+c$ which seems to be a reasonable choice except for the case of opposite polarity. Several things can be gleaned from this plot: firstly, increasing the RF power does not increase the plasma density with respect to the nominal case. This could indicate that the utilization efficiency is already close to maximum and any extra power is wasted. Secondly, increasing the magnetic field by 50% does increase the plasma density by about 50% however the factor b in the exponent is similar for both cases. For the reverse polarity it seems that upstream the plasma density is similar to the nominal case, while downstream the plasma density remains elevated. This is indicative of less acceleration, which will become later in this section when discussing the temperature and plasma potential for this case.

In Figure 3.28 the downstream evolution of the plasma density at different azimuthal angles, $\pm 20°$ and $\pm 40°$ for the nominal case is shown, while in Figure 3.29 the azimuthal evolution is shown at 100 mm and 150 mm downstream for the nominal case and at 150 mm for the case with increase magnetic field. From Figure 3.28 it is clear that the plasma density decreases off-axis something that is also seen in the azimuthal plot. The dotted lines in Figure 3.29 are Gaussian fits, which agree well with the data in the range $\pm 30°$; beyond that the plasma density is somewhat

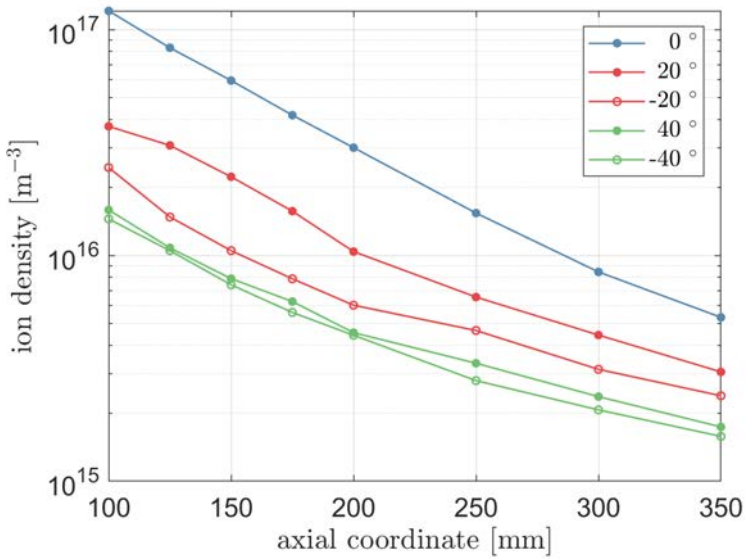

Figure 3.28: Plasma density at different downstream positions on- and off-axis, in the plume of the HPTx nominally operating at 450W, 1000G and 20 sccm argon.

constant. This is partially due the fact that there is an ambient plasma density created by charge-exchange collisions. However the magnitude of the density beyond $\pm 30°$ and the fact that it decreases downstream and increases with the magnetic field implies these wings are part of the expansion. Furthermore visually certain bands can be seen off axis that could correspond to these wings in the azimuthal density profile.

What is furthermore interesting is in Figure 3.29 is that the density decreases from 100 mm to 150 mm downstream which is congruent with the previous plots. However, when the magnetic fields is increase the plasma density is increased, but mainly near the axis, up to $\pm 15°$, implying some sort of focusing effect.

Lastly to better visualize the density, the data of Figure 3.28 can be recast in a contour plot, here shown in Figure 3.30

Since plasma density, electron temperature and plasma potential are all obtained from Langmuir probe measurements, the above plots are repeated below for the latter two variables. First we will discuss the electron temperature.

In Figure 3.31 we can see that as with plasma density, increase the temperature does not have a noticeably effect on the on-axis evolution of the electron temperature. Increasing the magnetic field however, increases the temperature, over the

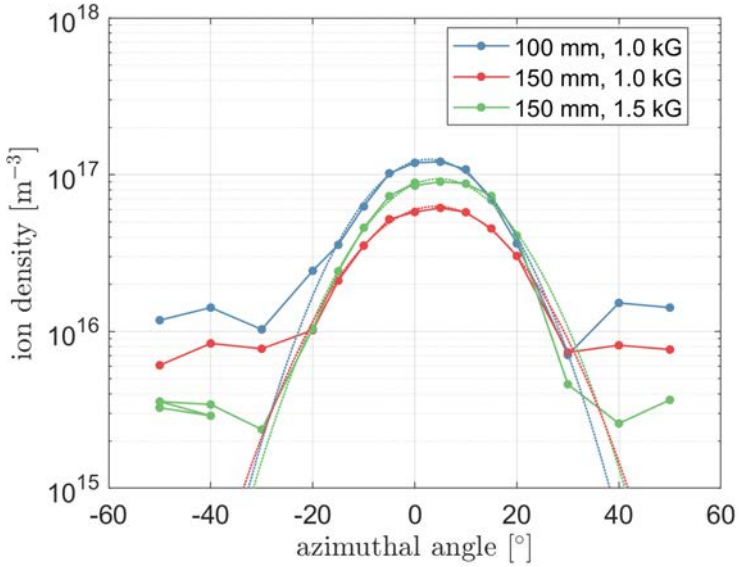

Figure 3.29: Plasma density at different azimuthal positions, at 100 and 150 mm downstream in the plume of the HPTx nominally operating at 450W, 1000G and 20 sccm argon.

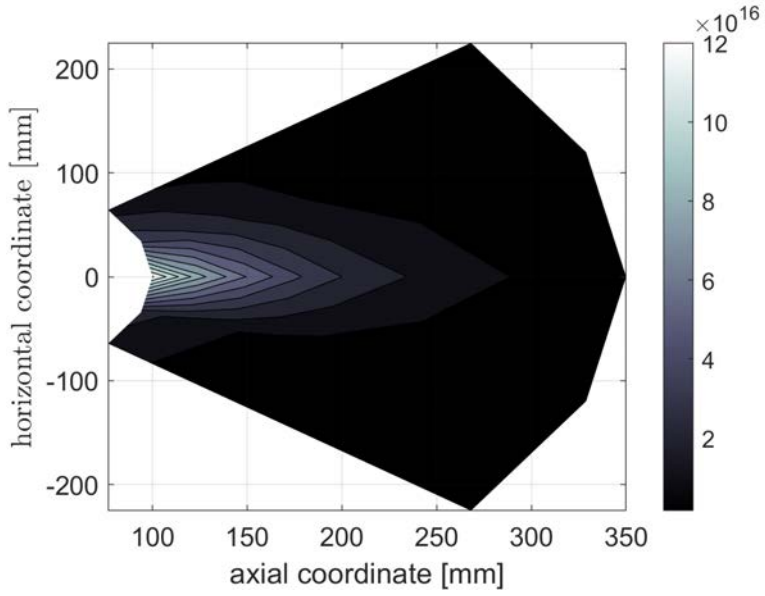

Figure 3.30: Plasma density map of the plume of the HPTx, operating at 450W, 1000G and 20 sccm argon.

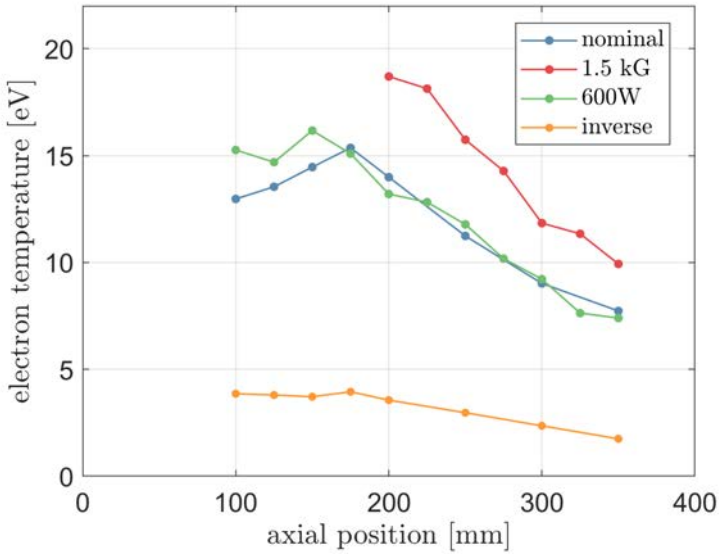

Figure 3.31: On-axis electron temperature at different downstream positions in the plume of the HPTx nominally operating at 450W, 1000G and 20 sccm argon.

whole range, by about 3-5 eV. Inverting the polarity however results in a significantly lower electron temperature with maximum of 4 eV, compared to 15 eV and 20 eV for the nominal and high field case. This also points to a reduced plasma acceleration in the reversed polarity case. Another noteworthy detail is the fact that for the nominal and 600W case the temperature seems to have a maximum around 150-200 mm, rather than decreasing monotonously. The explanation for this will be given when discussing the 2D temperature map below.

The azimuthal evolution of the electron temperature in Figure 3.32 shows a markedly different picture from the density plots. There seems to be a double peaked profile, where the maxima occur at around $\pm 20°$ at 100 mm and $\pm 15°$ at 150 mm. Furthermore, the temperature increases downstream, in agreement with Figure 3.31 and increases with increased magnetic field. The origin of the double peaked profiles could be that the RF power is coupled not homogeneously but rather in a cylindrical shell closer to the walls of the plasma chamber. In the simulations of Zhou [153] these off-axis maxima off the electron temperature are also observed. Furthermore, it seems that downstream the peaks move towards the axis and merge. This can be more clearly observed in the 2D electron temperature map of Figure 3.33. It can be observed that while the temperature decreases downstream,

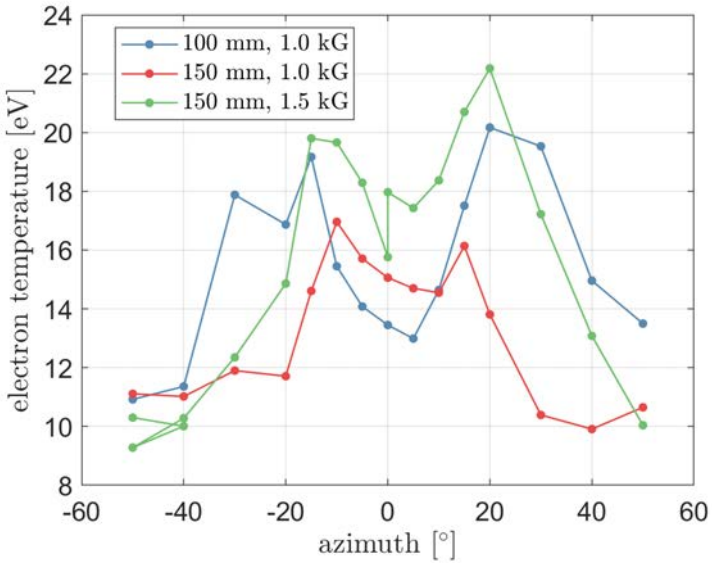

Figure 3.32: Electron temperature at different azimuthal positions, at 100 and 150 mm downstream in the plume of the HPTx nominally operating at 450W, 1000G and 20 sccm argon.

the off-axis peaks that occur near the thruster merge on-axis downstream, resulting in an increase of the on-axis temperature. These two opposing trends produce the peak in the electron temperature that was observed in Figure 3.31.

Lastly we present the plasma potential plots, axial, azimuthal and a 2D map. In Figure 3.34 the on-axis evolution of the plasma potential can be seen. In all cases the plasma potential decreases monotonically downstream. Increasing the RF power seems to have little effect, except for the fact that the nominal case has a higher potential upstream. Increasing the magnetic field increases both the overall potential and the rate at which it decreases. While the inverse polarity has significantly lower potential overall and also decreases slower. The potential drop over the 100-350 mm range is 44V and 34V for the nominal and 600W case respectively and only 12V for the inverse polarity. For the high field case only data for the 200-350 mm range is available, where the drop is 40V. The potential drop is equivalent to the increase in kinetic energy of the ions. Here again it is clear that the reverse polarity results in poor acceleration, while increased magnetic field leads to increased acceleration of the ions. The later fact can be verified by looking at RPA measurements; in Figure 3.35 the IEDF obtained on axis at 300 mm and 400

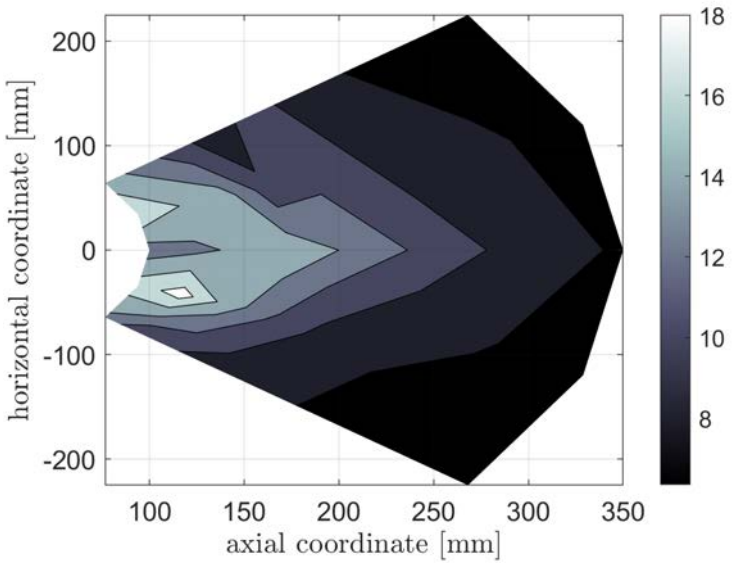

Figure 3.33: Electron temperature map of the plume of the HPTx, operating at 450W, 1000G and 20 sccm argon.

mm and at 1000G and 1500G is shown. Note that the dashed lines represent the most probably and mean energy of each of the distributions. For an ideal Gaussian distribution these energies should overlap, however, there is a significant population of disperse, lower energy ions most likely a product of charge exchange collisions. Two insights can be obtained from this graph. First increasing the magnetic field to 1500G results in an increase of about 17 eV in both the mean and most probable ion energy. Secondly ions are further accelerated between 300 and 400 mm resulting in a subsequent increase of another 5 eV. The reduced area under the curve at 400 mm corresponds to the lower overall density further down stream.

Along the azimuthal direction the plasma potential also shows a double peaked profile, somewhat similar to the electron temperature. However in this case it seems that the peaks are more pronounced downstream, rather than upstream. Furthermore it can be seen that increasing the magnetic field seems to both raise and focus the plasma potential profile; the latter effect should improve the divergence.

We will now discuss the Faraday probe result. In Figure 3.37 four azimuthal current density profiles can be seen, obtained 300 mm downstream in the plume of the HPTx operating at 400W and with different mass flow rates of both xenon and argon, and with magnetic fields of 1000G and 1500G. Several things can be gleaned

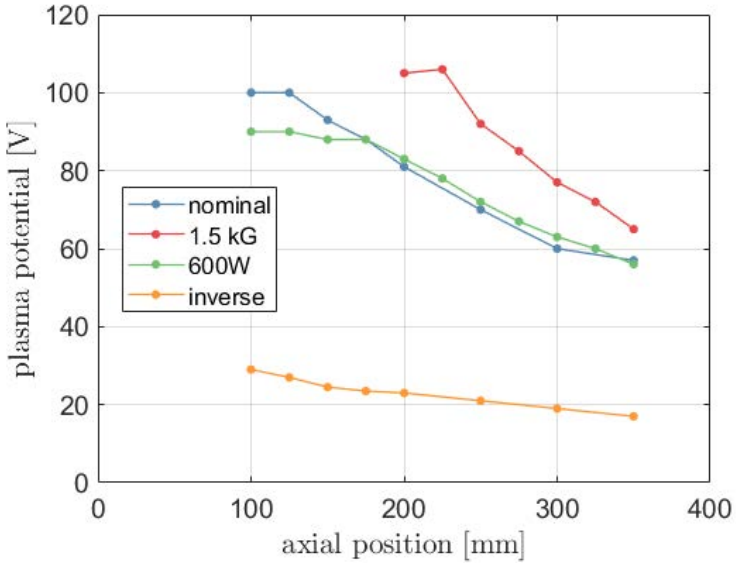

Figure 3.34: On-axis plasma potential at different downstream positions in the plume of the HPTx nominally operating at 450W, 1000G and 20 sccm argon.

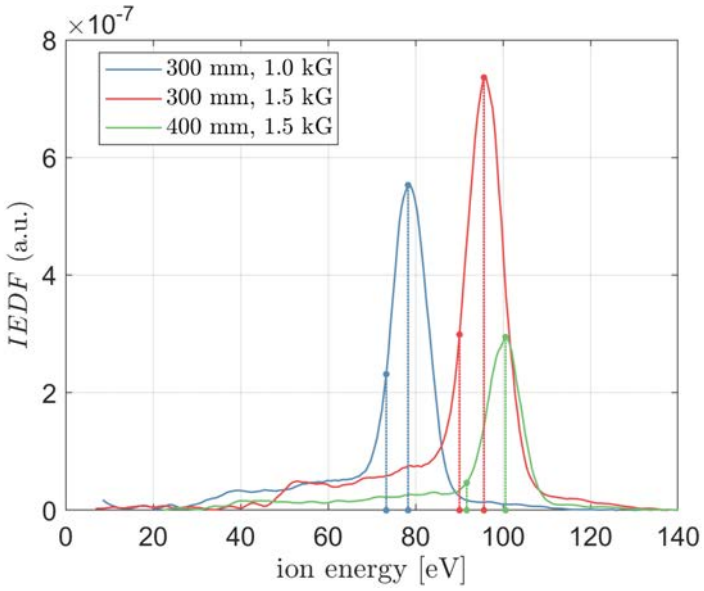

Figure 3.35: On-axis ion energy distribution function (IEDF) at different downstream positions in the plume of the HPTx operating at 450W and 20 sccm argon.

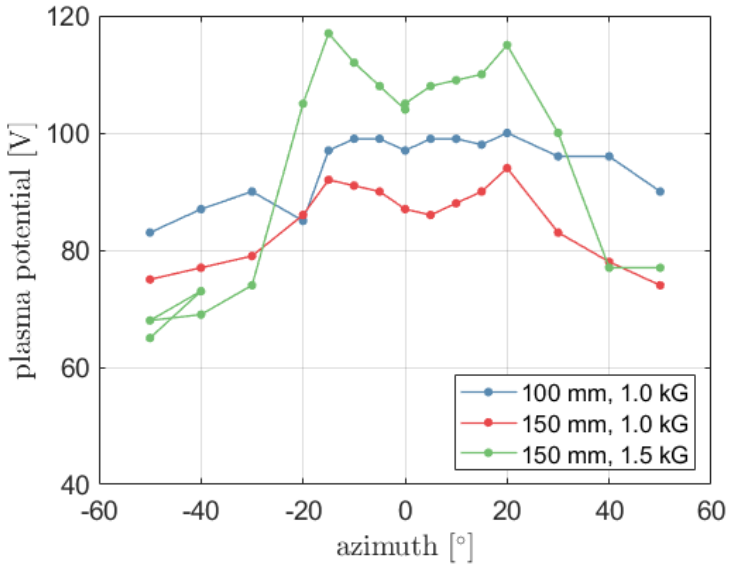

Figure 3.36: Plasma potential at different azimuthal positions, at 100 and 150 mm downstream in the plume of the HPTx nominally operating at 450W, 1000G and 20 sccm argon.

from this plot. Firstly, for a fixed magnetic field strength and increase in the mass flow rate results in larger overall current densities, regardless of the propellant type. Secondly, reducing the magnetic field decreases the overall current density. We can furthermore calculate the utilization efficiencies of these curves which are 51% for 20 sccm of argon at 1500G and 40% at 1000G; for xenon they are 80% at 10 sccm and about 100% for 5 sccm. From this we conclude that the utilization efficiency is proportional to the magnetic field and inversely proportional to the mass flow rate. It is of interest to normalize the current density profiles with the peak value to better compare the shape of the curves. This is shown in Figure 3.38. It can be seen that near the axis, up to about $\pm 20°$ the profiles overlap. This is taken as an indication that the beam profile is determined by the shape of the magnetic field rather than the magnitude or other operational parameters. Further off axis for the 1000G case it can be seen that there is some widening of the plume. In the 5 sccm xenon case the shoulders of the profile seem elevated. In Figure 3.37 it can be seen that for the other cases the magnitude of the current density in the wings is similar despite differences in mass flow rate, while for the 5 sccm xenon case it is actually lower in absolute terms. However, in relative terms it is elevated.

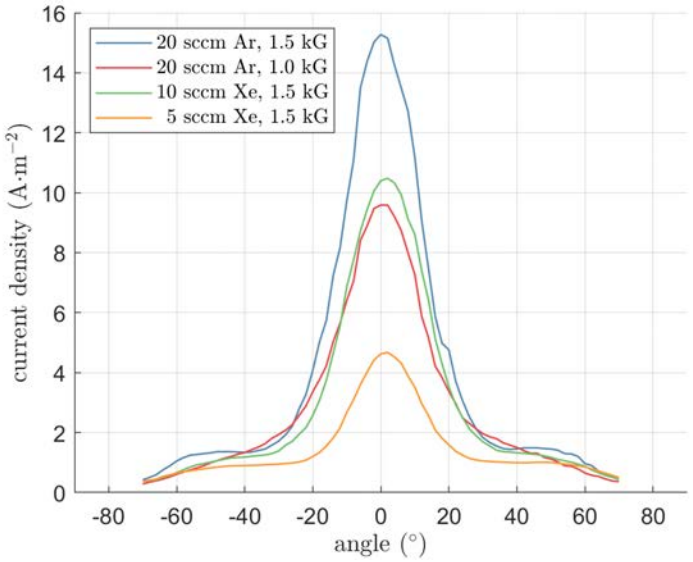

Figure 3.37: Azimuthal current density profiles 300 mm downstream in the plume of the HPTx operating with 400W of RF power.

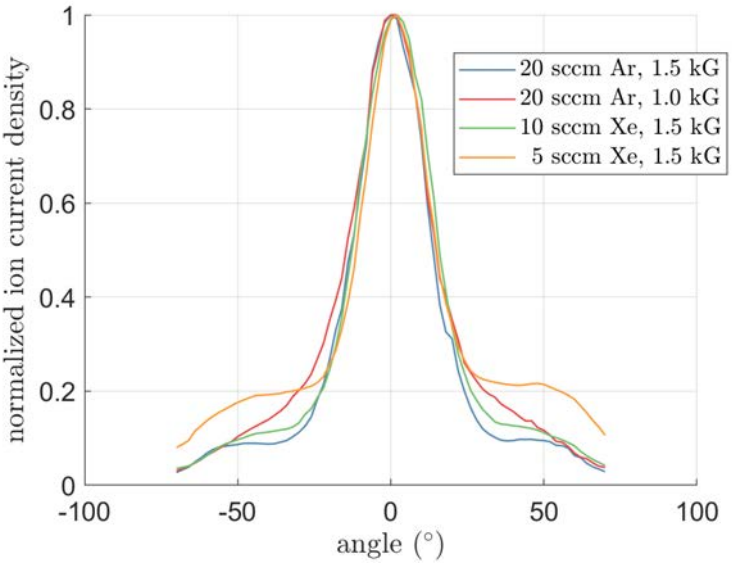

Figure 3.38: Normalized azimuthal current density profiles 300 mm downstream in the plume of the HPTx operating with 400W of RF power.

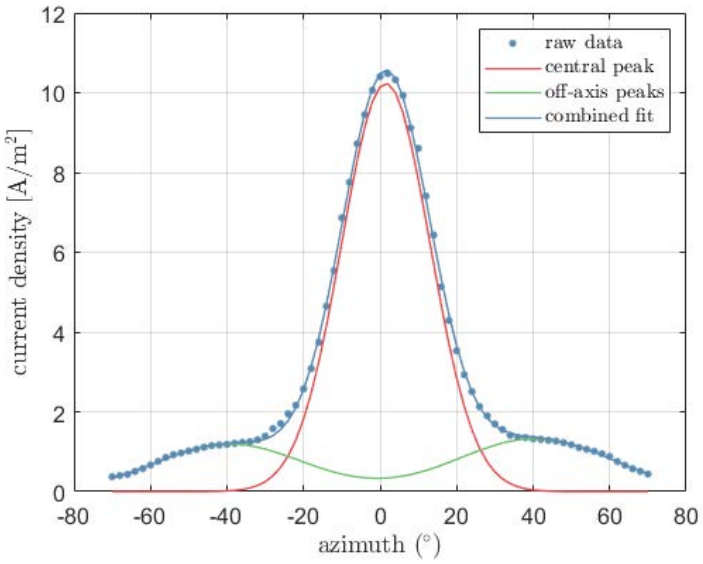

Figure 3.39: Triple Gaussian fit of the azimuthal current density profile of Figure 3.37, corresponding to 10 sccm Xe.

We can take a closer look at the wings of the current density profiles; with some effort it can be shown that they are well fitted with a triple Gaussian as can be appreciated in Figure 3.39. The central Gaussian has a half-width at half maximum (HWHM) of 16-18° while the two smaller Gaussians centered at ±40° have each a HWHM of around 26-28°. This means that the beams consists of a central beam and a second annular beam at about 40°. This fitting can be performed for all current density profiles of Figure 3.37. The parameters of the off-axis peaks are found to differ somewhat depending on the operating point (mass flow rate, magnetic field, etc.) However the HWHM of the central peak seems to be independent of the operating point and rather a feature of the magnetic topology. In fact, normalized (with the peak value) curves of different operating points result in a similar curve for the near axis (±20°) range. Decreasing the magnetic field seems to shift the off-axis peaks more towards the center to around ±30°. The amplitude of these off-axis peaks varies between 10-20% of the central peak, depending on the mass flow rate and the magnetic field.

To be able to extract propulsive performance figures the Faraday probe data needs to to be complemented by RPA data. For this reason RPA measurements were taken at several azimuthal positions for the above cases. The results are

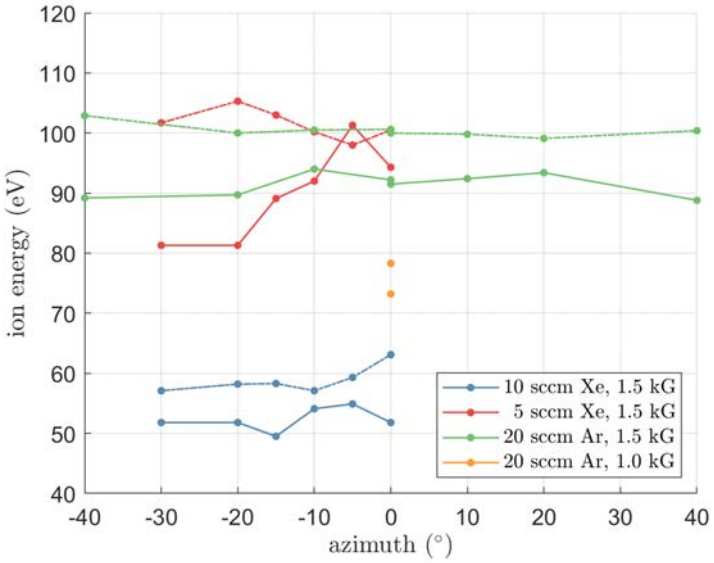

Figure 3.40: Mean (solid) and most probable (dashed) ion energy at different azimuthal positions, 300 mm downstream in the plume of the HPTx operating with 400W of RF power.

plotted in Figure 3.40. In general it can be said that the most probably energy is higher than the mean energy, so we will use the latter for a conservative estimate. Furthermore, except for the case of 5 sccm of xenon, the azimuthal ion energy profile is rather flat and we can approximate it with a constant value. Even in the exceptional case this yields good results, as can be seen in Figure 3.41.

Integrating the resulting energy flux density profiles yields the beam power, from which thrust, specific impulse and thrust efficiency can be obtained. The results are reported in Table 3.2 below. Note that the uncertainty reported in the thrust, specific impulse and efficiency is solely due to the uncertainty in the ion energy (due to taking the azimuthal average) and does not include other error sources. Also note that the efficiency is calculated taking only the RF power into account, i.e., the power dissipated in the solenoid is not considered here.

Surprisingly the cases operating with argon seem to yield better performance despite expectations to the contrary (because of the lower ionization energy of xenon). Decreasing the magnetic field worsens the performance, while decreasing the mass flow rate seems to improve the performance. The thrust and efficiency seem at least to be in the ball park as will become clear in the next chapter on thrust

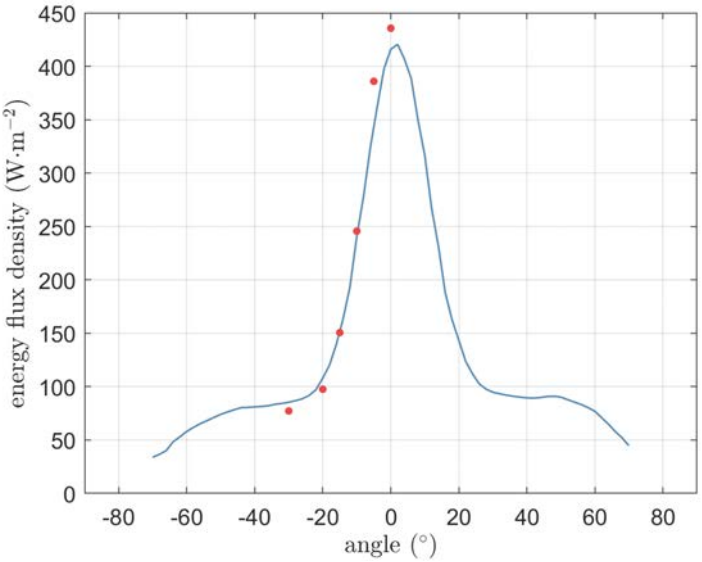

Figure 3.41: Comparison of energy flux density obtained with using the average azimuthal ion energy and the ion energy as a function of the azimuth for the case of 5 sccm Xe, 1500G, 400W.

measurements. Note that these results are only a preliminary characterization of a few selected operating points. A full characterization of the thruster is outside of the scope of this work.

Table 3.2: Performance estimates based on combined RPA and FP measurements of the plume of the HPTx operating at 400W and 1500G (†1000G).

	$\dot{m}$ [sccm]	[mg/s]	$\mathcal{E}_i$ [eV]	F [mN]	I_{sp} [D]	η [%]	η_u [%]	θ_D [°]
Ar	20	0.6	91±2	8.1±0.1	1370±20	13.5±0.3	51	36
Ar†	20	0.6	73	6.4	1090	8.5	40	36
Xe	10	1.0	52±2	6.8±0.1	710±10	5.6±0.2	80	36
Xe	5	0.5	90±8	4.9±0.2	1027±10	6.2±0.2	100	42

CHAPTER
FOUR

Thrust Balance

"I regarded as quite useless the reading of large treatises of pure analysis: too large a number of methods to pass at once before the eyes. It is in the works of application that one must study them; one judges their utility there and appraises the manner of making use of them."
— Joseph-Louis Lagrange

4.1 State of the Art

Direct thrust measurements of plasma thrusters have been common place in the EP community. While thrust measurements for chemical rocket motors are quite straight forward and based on load cells, thrust measurements of EP devices are more elaborate. EP devices also usually only operate in a high vacuum environment ($p \sim 10^{-5}$ mbar) confining experiments to a vacuum chamber. Due to their inherent low thrust-to-weight ratio they require both a rigid structure to support their weight as well as a sensitive, i.e. compliant structure that is able to transduce the low thrust values to a measurable signal. The solution of these opposite requirements is reffered to as a thrust balance (TB) and generally comes in the form of a pendulum, either simple [24, 52], inverted [145, 59] or torsional [147, 9, 33] that converts thrust into displacement which is then measured. Each of these configurations has its advantages and disadvantages, which are summarized in Tab. 4.1.

The simple pendulum is the simplest solution. It is naturally stable under external perturbations but also has the lowest sensitivity. Furthermore, its sensitivity is dependent on the pendulum length which is limited by the dimensions of the vacuum chamber that has to contain it. The inverted pendulum is the most common type of

Table 4.1: Advantages and disadvantages of thrust balance types.

Design	Advantage	Disadvantage
Simple Pendulum	Stable under external perturbations	Lowest sensitivity, depends on pendulum length
Inverted Pendulum	High sensitivity	Sensitivity depends on flexures, prone to changes
	Compact	Compact
Torsional Pendulum	Superior sensitivity, independent of mass	Asymmetric arrangement

TB [97]. It is less stable than the simple pendulum, but has better sensitivity which is governed by the stiffness of the supporting flexures. The sensitivity is therefore much less dependent on the thruster mass. However, the stiffness of the flexures are prone to changes for instance, thermal drifts either due to changes in ambient temperature or due to thruster heat loads. Thermal management in a vacuum environment is challenging due to the lack of convection and the heat dissipated from the thruster can easily affect the thrust balance, including the flexures.

The inverted pendulum is also more compact than a simple pendulum. This has the advantage that the performance is less limited by the vacuum chamber dimensions. The disadvantage is that it also places the thruster, which is a source of heat and electro-magnetic interference (EMI), close to any sensitive components. This is of particular concern for a RF thrusters like the HPT where heat dissipation and EMI are significant.

The torsional pendulum has superior sensitivity. Since the plane of motion is perpendicular to the gravitational force the sensitivity is independent of the thruster mass. However the horizontal, often asymmetric, arrangement is not always easy to manage inside the limited space of a vacuum chamber. It would also place the thruster closer to the side walls of the chamber, resulting in plume-wall interaction that degrades thruster performance. These limitations are of particular concern for larger thrusters; torsional balances have therefore been most successfully applied for testing micro-propulsion devices, those providing continuous thrust as well as pulsed thrusters.

Polzin et al. [100] proposed a modification of the hanging pendulum that was dubbed the Variable Amplitude Hanging Pendulum with Extended Range (VAHPER). It includes a secondary, horizontal arm that is mechanically coupled to the main pendulum arm and results in a mechanical amplification of the displacement. The displacement measurement is performed on the secondary arm which allows for placing the sensor far away from the thruster without losing sensitivity. In their design, it was furthermore possible to change the location of the pivot of the secondary arm and thereby vary the amplification factor.

In this work we present a new thrust balance developed by the EP2 research group of UC3M, based on the design of Polzin, to perform direct thrust measurements on an experimental helicon thruster platform.

HPTs [27, 11, 123] are electrode-less thrusters that use helicon waves to produce high density plasmas. These waves are excited at frequencies in the Megahertz range, typically 13.56 MHz in the presence of an applied magnetic field [29]. HPTs rely furthermore on magnetic nozzles for plasma acceleration by converting the thermal electron energy into ion kinetic energy. Thrust is generated by the magnet repulsion between diamagnetic plasma currents and the magnetic circuit of the thruster [77, 79].

EP2 has been studying these devices for the past ten years, both theoretically [3, 5, 131, 152, 155] and experimentally [90, 92]. The current experimental platform, the HPTx, developed jointly by EP2 and SENER Aeroespacial is a flexible platform for investigating the effect of different design and operational parameters on the performance as well as the underlying physics. It can operate with either solenoids or permanent magnets, uses different propellants such as Argon and Xenon and can operate with up to 1 kW of RF power.

To date, all experimental characterization of the HTPx has been performed mainly with electrostatic probes. Current performance estimates are about 5-8 mN of thrust, 750-1200s of specific impulse and 7-10% of efficiency [90, 92]. However, electrostatic probes only provide indirect measurements of thrust and specific impulse. The need for reliable thrust measurements has driven the development of a new TB, designed to primarily accommodate the HPTx prototype but also applicable to other thruster types.

The HPTx weighs about 5 kg thus has an estimated thrust-to-weight ratio of only 2 mN/kg, produces strong RF fields, requires electrical currents of up to 30

A, and presents thermal heat loads of up 1.5 kW. This imposes a set of stringent requirements on the design of the thrust balance. In this article we will present both a theoretical analysis of the TB design and its technical implementation as well as validation & calibration results and some preliminary thrust measurements.

The rest of the article is structured as follows. In section 4.2 a novel analysis of the dynamic response of this type of balance, using the Lagrange formalism, is introduced as well as a model for the damping system. Section 4.3 details the technical implementation of all the features of the thrust balance. Here we also introduce briefly the vacuum facility and the thruster. In section 4.5 we present results on the validation of the dynamical model, the damping system and the calibration method as well as actual thrust measurements obtained with the HPTx. The article ends with a discussion on the obtained results and the conclusions.

4.2 Modelling

We start with defining our system. As can be seen in Fig. 4.1, the reference frame is centered at O with the x-axis rightwards, the y-axis upwards and the z-axis out of the plane. The mechanism consists of three articulated rigid elements numbered $1, 2, 3$. The first element is an upside-down L-shaped component suspended at its corner from the fixed frame at O, by means of a flexure bearing with torsional spring constant κ_1. The second element, a straight beam, is anchored to the fixed frame at point A, also by a flexure bearing with constant κ_2. The joints in point O and A have one degree of freedom (DoF): rotation about z. The primary and secondary elements are interconnected with a third element, another straight beam, joined at B and C by flexure bearings with κ_3, κ_4, respectively. Points B and C have 3 DoF each, rotation around z and translation in the $x-y$ plane. The thruster, with mass M, is suspended from the bottom of element 1, while a counterweight with mass m is attached to the right end of element 2.

The positions of the centers of mass (CoM) of all elements i are noted $\mathbf{r_i}$, where we numbered the thruster and the counterweight 4 and 5, respectively. The point of element 2 where the displacement is measured is labeled E. Point D is the point where the damping force acts. Whereas point O and A are fixed to the reference frame, points B, C, D and E can move; when *not* in their initial position (i.e. when the vertical part of element 1 is parallel to the local gravity vector) they are denoted

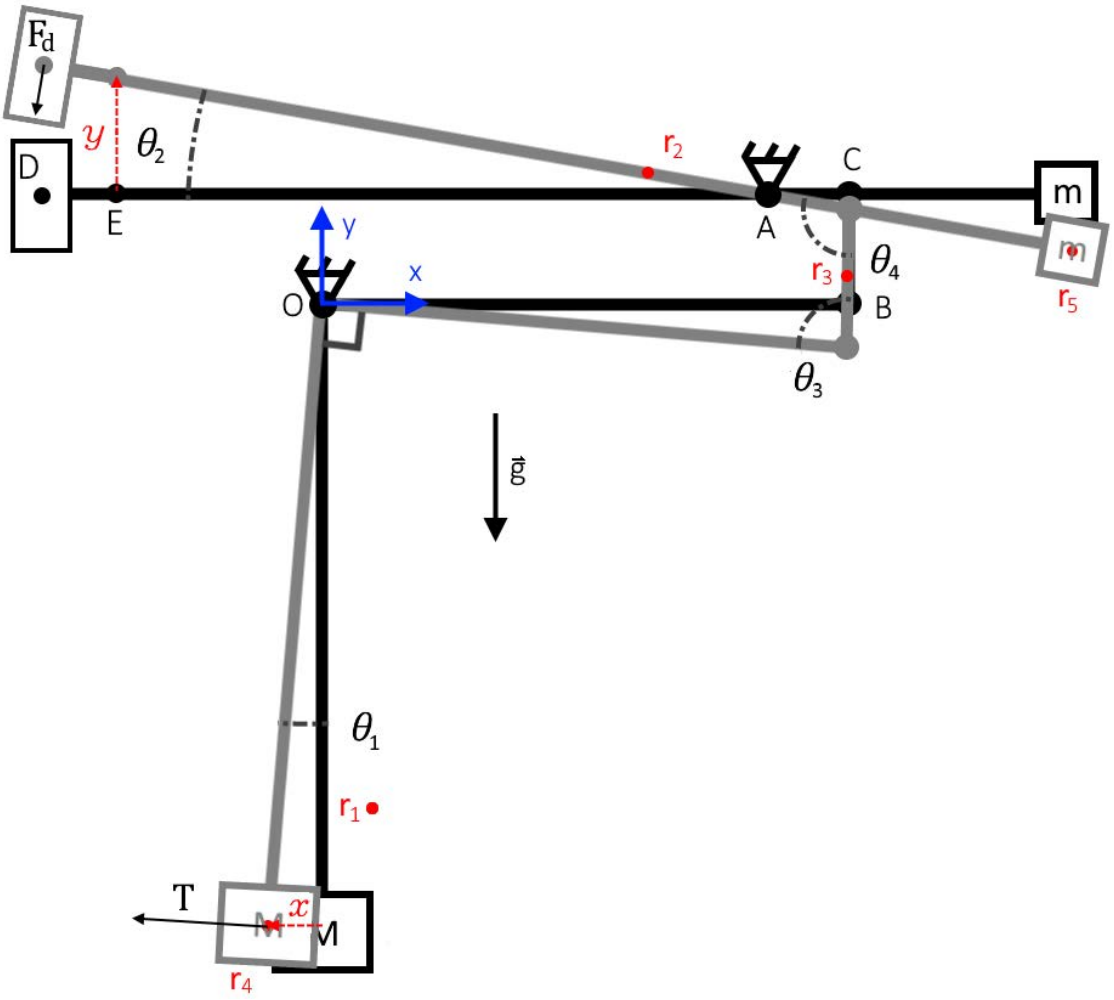

Figure 4.1: Schematic of the thrust balance mechanism.

with a prime i.e. B', C', D', E' (this would correspond to the positions colored in grey in Fig. 4.1). There are four relevant angles, $\theta_1, \theta_2, \theta_3$ and θ_4 as shown in Fig. 4.1. Lastly, it has to be noted that the gravity vector is pointing in the $-y$ direction.

The quantity of interest in conventional pendulum balances is the horizontal displacement of r_4 - here denoted x - and how it is related to the applied force T. In reference [100] it was shown that in this particular arrangement the vertical displacement of E, denoted y, is a constant multiple of x. However, as the relationship between x, y is dependent on the centre of thrust of the thruster, it makes more sense to speak of the relationship between the angles θ_1, θ_2, as this is independent of the thruster. It can be shown that $\theta_2 = n\theta_1$, as we will see later. For the interested

reader we have reproduced the equations from the static analysis of [100] using our nomenclature; they can be found in appendix B.1. When looking at eq. (B.1)-(B.8) in appendix B.1 it becomes apparent that the angles θ_i are all a function of $\theta_1 \equiv \theta$ (here we have dropped the subscript for clarity). For the following analysis it is convenient to work with the differential angles $\delta_i(\theta) = \theta_i(\theta) - \theta_i(0)$ referred to the equilibrium position $\theta = 0$. The equilibrium positions for the angles θ_i are $\theta_1 = \theta_2 = 0$ and $\theta_3 = \theta_4 = \pi/2$.

To find the dynamic response of the system we can analyze it using Lagrangian mechanics. We consider the system formed by 5 elements. To simplify the calculations somewhat, we will neglect the motion of the connecting element $i = 3$, which is a reasonable approximation, considering its size and mass compared to the other elements. When considering small angles (as we will do), element 3 ideally experiences no rotational motion, further justifying this approximation. We first define the Lagrange function of the full system:

$$\mathcal{L} = \mathcal{E}_k - \mathcal{U} \tag{4.1}$$

with $\mathcal{E}_k$ the kinetic energy and $\mathcal{U}$ the potential energy which are defined as:

$$\mathcal{E}_k = \frac{1}{2} \sum_i m_i \dot{r}_i^2 + \omega_i^T \bar{\bar{I}}_i \omega_i \tag{4.2}$$

$$\mathcal{U} = \sum_i \frac{1}{2} \kappa_i \delta_i^2 + m_i \mathbf{g} \cdot \mathbf{r}_i \tag{4.3}$$

here $\mathbf{r}_i$ are the position vectors of the centers of mass of the 5 elements, and $\dot{\mathbf{r}}_i$ their time derivatives, m_i are the corresponding masses. The ω_i are the angular velocities of the rigid elements (only defined for $i = 1, 2$) and $\mathbf{I}_i$ is the corresponding inertia matrix. Lastly, κ_i are the torsional spring constants of the four pivots and $\mathbf{g} = -g\,\hat{\mathbf{y}}$ is the gravitational acceleration.

Now we consider the Euler-Lagrange equation, which reads:

$$\frac{d}{dt}\left(\frac{d\mathcal{L}}{d\dot{q}_j}\right) - \frac{d\mathcal{L}}{dq_j} = Q_j \tag{4.4}$$

where q_j are the generalized variables and Q_j are the generalized forces:

$$Q_j = \sum_i \mathbf{F}_i \cdot \frac{\partial \mathbf{r}_i}{\partial q_j} \tag{4.5}$$

As we will see, all quantities in eq. (4.2) and (4.3) are a function of the angle θ and its time derivative $\dot{\theta}$, only. This angle is the single generalized coordinate that determines this system. Although the other quantities are non-linear functions of θ, since $\theta \ll 1°$, and we are interested in motion around the point $\theta = 0$, these functions can be linearized.

The positions $\mathbf{r}_i$ are dependent on θ and θ_2 only. The linearized angle θ_2 and linearized differential angles are given in eq. (4.6a)-(4.6d) below. Using these expressions, eq. (4.4) can be expressed in terms of θ only.

$$\delta_1(\theta) = \theta + \mathcal{O}(\theta^2) \tag{4.6a}$$

$$\delta_2(\theta) = n\theta + \mathcal{O}(\theta^2) \equiv \theta_2 \quad \text{with} \quad n = 1 + n_3 + n_4 \tag{4.6b}$$

$$\delta_3(\theta) = \theta_3'(0)\theta + \mathcal{O}(\theta^2) \equiv n_3\theta \tag{4.6c}$$

$$\delta_4(\theta) = \theta_4'(0)\theta + \mathcal{O}(\theta^2) \equiv n_4\theta \tag{4.6d}$$

Note that the prime denotes $d/d\theta$. The derivation of the various terms in the linearized equations can be found in appendix B.2.

Going back to eq. (4.4) we can substitute $q_j = \theta$. For now we consider a system without forcing or damping, so that $Q_j = 0$. This results in the following equation.

$$\frac{d}{dt}\left(\frac{d\mathcal{L}}{d\dot{\theta}}\right) - \frac{d\mathcal{L}}{d\theta} = 0 \tag{4.7}$$

Solving this equation will yield the equation of motion for the system. To solve this equation all $\mathbf{r}_i, \dot{\mathbf{r}}_i$ need to be known and are, for this purpose, tabulated in Tab. 4.2. The angular velocities are $\omega_1 = -\dot{\theta}$ and $\omega_2 = -n\dot{\theta}$ and zero for all other i. $L_i = |\mathbf{r}_i|$ are the lengths from the center of mass of element i to A, or to O for $i = 1, 4$. There is one exception: the center of mass of the L-shaped component ($i = 1$) has both an x and a y component in the equilibrium position, which are denoted $x_{1,0}$ and $y_{1,0}$. Calculation of $\mathbf{r}_1$ furthermore requires a rotation matrix as can be seen in Tab. 4.2.

We now write out the terms of the Lagrange function. The different components are: the linear kinetic energy,

$$\sum_{i=1}^{N} \frac{1}{2} m_i \dot{r}_i^2 = \frac{1}{2}(m_1 L_1^2 + m_2 n^2 L_2^2 + m_4 L_4^2 + m_5 n^2 L_5^2)\dot{\theta}^2 \tag{4.8}$$

Table 4.2: Position and linear velocity for elements i.

i	$\mathbf{r}_i$	$\dot{\mathbf{r}}_i$
1	$\begin{bmatrix} \cos\theta & \sin\theta \\ -\sin\theta & \cos\theta \end{bmatrix} \begin{bmatrix} x_{1,0} \\ y_{1,0} \end{bmatrix}$	$-\begin{bmatrix} \sin\theta - \cos\theta \\ \cos\theta \quad \sin\theta \end{bmatrix} \begin{bmatrix} x_{1,0} \\ y_{1,0} \end{bmatrix} \dot{\theta}$
2	$\mathbf{r}_A - L_2(\cos n\theta\,\hat{\mathbf{x}} - \sin n\theta\,\hat{\mathbf{y}})$	$L_2(\sin n\theta\,\hat{\mathbf{x}} + \cos n\theta\,\hat{\mathbf{y}})n\dot{\theta}$
3	-	-
4	$-L_4(\sin\theta\,\hat{\mathbf{x}} + \cos\theta\,\hat{\mathbf{y}})$	$-L_4(\cos\theta\,\hat{\mathbf{x}} - \sin\theta\,\hat{\mathbf{y}})\dot{\theta}$
5	$\mathbf{r}_A + L_5(\cos n\theta\,\hat{\mathbf{x}} - \sin n\theta\,\hat{\mathbf{y}})$	$-L_5(\sin n\theta\,\hat{\mathbf{x}} + \cos n\theta\,\hat{\mathbf{y}})n\dot{\theta}$

the rotational kinetic energy,

$$\sum_{i=1}^{N} \frac{1}{2} I_i \omega_i^2 = \frac{1}{2}(I_1 + n^2 I_2)\dot{\theta}^2 \tag{4.9}$$

the gravitational potential energy,

$$\begin{aligned} \sum_{i=1}^{N} m_i \mathbf{g} \cdot \mathbf{r}_i \quad = - \quad & g[m_1(y_{1,0}\cos\theta - x_{1,0}\sin\theta) \\ & +m_2(y_A + L_2 \sin n\theta) \\ & -m_4 L_4 \cos\theta \\ & +m_5(y_A - L_5 \sin n\theta)] \end{aligned} \tag{4.10}$$

and the elastic potential energy.

$$\sum_{i=1}^{N} \frac{1}{2} \kappa_i {\delta_i}^2 = \frac{1}{2}(\kappa_1 + n^2\kappa_2 + n_3^2\kappa_3 + n_4^2\kappa_4)\theta^2 \tag{4.11}$$

From these equations it is evident that the kinetic energy is only dependent on $\dot{\theta}$ and the potential energy is only dependent on θ, as expected. The Euler-Lagrange equation (4.4) for this system can now be written as:

$$\begin{aligned} & (m_1 L_1^2 + m_2 n^2 L_2^2 + m_4 L_4^2 + m_5 n^2 L_5^2 + I_1 + n^2 I_2)\ddot{\theta} \\ + \quad & (\kappa_1 + n^2\kappa_2 + n_3^2\kappa_3 + n_4^2\kappa_4 - g m_1 y_{1,0} + g m_4 L_4)\theta \\ = \quad & g(n m_2 L_2 - m_1 x_{1,0} - n m_5 L_5) \end{aligned} \tag{4.12}$$

Note that the trigonometric functions are linearized, i.e. $\sin x \simeq \theta$ and $\cos x \simeq 1$ (for both $x = \theta$ and $x = n\theta$) in the gravitational term. Also note that $y_{1,0} < 0$, so

the gravitational term of the first element is positive. It is interesting to see that the spring force of the flexures at A and C is multiplied by a factor n^2 (which is equal to n_4^2 and about 10^3 as shown in appendix B.2). The above expression represents a harmonic oscillator with an effective moment of inertia I, an effective torsional spring constant κ and a constant offset τ_0:

$$I\ddot{\theta} + \kappa\theta = \tau_0 \tag{4.13}$$

The constant term is $\tau_0 = gm_1x_{1,0} + gnm_5L_5 - gnm_2L_2$ which are the gravitational torques. For the balance to be in the equilibrium position ($\theta = 0$) it is required that τ_0 is zero. This reflects the purpose of the counterweight; as its distance to the pivot A, L_5, is variable, it can be used to balance out the system by choosing L_5 such that $\tau_0 = 0$.

Now we will include the external forces. As shown in Fig. 4.1 there are two forces applied to the system, F_T the thrust operating at r_4 and $F_D = -b\dot{\mathbf{r}}_D$ the damping force, which acts on point D and is opposite and proportional to its velocity. To include these forces we now consider them as generalized forces Q_j:

$$Q_4 = \mathbf{F} \cdot \frac{\partial \mathbf{r}_4}{\partial \theta} = F_T L_4 \tag{4.14}$$

$$Q_D = \mathbf{F} \cdot \frac{\partial \mathbf{r}_D}{\partial \theta} = -bn^2 L_D^2 \dot{\theta} \tag{4.15}$$

where $\mathbf{r}_D = \mathbf{r}_A - L_D(\cos n\theta\ \hat{\mathbf{x}} - \sin n\theta\ \hat{\mathbf{y}})$. The new equation of motion then becomes:

$$I\ddot{\theta} + \beta\dot{\theta} + \kappa\theta = \tau(t) + \tau_0 \tag{4.16}$$

with $\beta = bn^2L_D^2$ being the torsional viscous damping factor, and $\tau = F_T L_4$ the torque due to the thrust. It is now perfectly clear that in first approximation the balance behaves as a damped harmonic oscillator.

The equation of motion for the damped harmonic oscillator can be normalized as follows.

$$\ddot{\theta} + 2\zeta\omega_0\dot{\theta} + \omega_0^2\theta = \frac{\tau}{I}, \qquad \zeta = \frac{\beta}{2\sqrt{\kappa I}}, \qquad \omega_0 = \sqrt{\frac{\kappa}{I}} \tag{4.17}$$

Here we have introduced the damping ratio ζ and the natural angular frequency ω_0.

The other property of interest is the stiffness k of the system: the relationship between the measured displacement y_E and the applied thrust F_T, such that $F_T = ky_E$. In a steady state the equation of motion reduces to:

$$\kappa\theta = F_T L_4 \tag{4.18}$$

Combining this with eq. (4.6b) and (B.1) (from appendix B.1) which we can simplify as $y = L_{AE}\theta_2$ we can find an expression for k.

$$k = \frac{\kappa}{nL_4 L_{AE}} \tag{4.19}$$

To have a response that closely follows the step input of the applied thrust and to prevent the system from oscillating eternally, a damping force is required. Generally damping ratios of $0.4 < \zeta < 0.8$ give a good step response [97]. The damping is realized by means of Eddy current damping, which is contact-less and well suited for vacuum.

The principle is as follows. When a conductor moves through a magnetic field, Eddy currents are induced inside the conductor. Due to the magnetic field, the moving charges that make up these currents experience a Lorentz force which is proportional to and in opposite direction of the velocity. The induced current density and the resulting force are:

$$\mathbf{J} = \sigma\left(\mathbf{E} + \mathbf{v} \times \mathbf{B}\right) \qquad\qquad \mathbf{F}_d = \int_V \mathbf{J} \times \mathbf{B}\mathrm{dV} \tag{4.20}$$

For a thin plate of thickness δ_p we can approximate the problem in 2D, assuming the current density and magnetic field constant over this dimension (z). For a velocity in the y-direction $\mathbf{v} = v_y\hat{y}$ and a homogeneous axial magnetic field in the z-direction $\mathbf{B} = B_z\hat{z}$, with pole projection S. Ignoring the electric field for now, the Lorentz force is then proportional to:

$$F_d \propto -\sigma v S \delta_p B_z^2 \tag{4.21}$$

A sketch of the fields and current density is shown in figure 4.2. Due to the sharp gradient in the magnetic field at the edges of the pole projection area, charge accumulation occurs here. This charge results in an electric field perpendicular to the direction of motion of the conductor, in a way similar to the Hall-effect. Inside the pole projection area this electric field is opposite the component $\mathbf{v} \times \mathbf{B}$

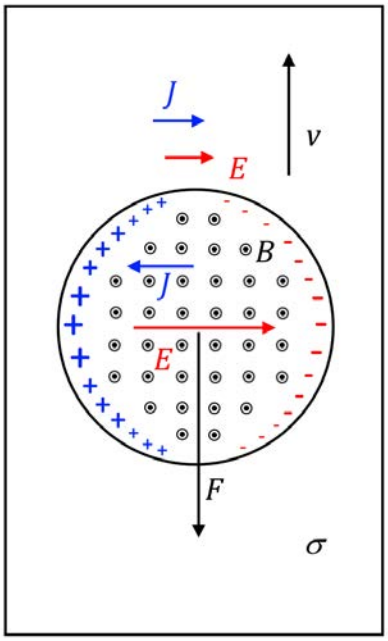

Figure 4.2: Sketch of electric and magnetic fields and current densities in they eddy current damper. Note that the currents in reality flow in closed loops.

and here effectively limits the induced current density. Outside the pole projection area the electric field is the sole reason for the induced current density. Knowing both **B** and **E** the current density **J** and correspondingly the force can be solved for. Furthermore, to ensure that the current density normal to the boundaries of the conductor is zero the method of image currents can be used. This problem was solved analytically by Bae [10] for square magnets. For circular magnets the integrals involved are rather complicated and it's more convenient to solve it with commercial FEM software. We modeled the damping system of the thrust balance using Comsol's magnetic and electric field (mef) module. The system was modeled using the dimensions and properties detailed in section 4.3.3, the results are reported in section 4.5.

4.3 Technical Implementation

4.3.1 Structure

The thrust balance structure as shown in Fig. 4.1 can also be recognized in Fig.4.3 (although mirrored). Point O and A are the pivots, item 2 in Fig. 4.3. These pivots are anchored to a large aluminium plate (top white plate in Fig. 4.3). (As opposed to pivots B and C, not labeled in this figure, which are freely moving as was explained in section 4.2). This plate is placed on top of another aluminium plate (grey, bottom). The relative attitude of the top plate with respect to the bottom-plate is controlled by the leveling system described in the next section.

The bottom plate is suspended from the roof of the vacuum chamber (not shown for clarity). It also includes the interface for the power lines, gas lines and cooling water lines (items, 14, 15, 16 respectively).

The secondary arm and the intermediate link are custom machined aluminium parts. The primary arm is a combination of a machined aluminium part, an extruded 30 mm x 60 mm extruded aluminium profile and a gun-drilled cold plate (item 9). The cold-plate doubles as the thermal and the mechanical interface for the thruster. The pivots are C-flex type G10 for the main pivot (2 bearings at O) and D10 for the other pivots (2 bearings at A, 1 bearing each at B, C).

The system further includes a calibration rig (items 7,8), liquid metal connectors (item 13) a viscous damping system (item 5) and an optical displacement sensor (item 6) which will be elaborated on in the rest of this section.

4.3.2 Leveling system

To be able to align the surface normal of the upper plate with the gravity vector the system uses two motorized screw-jacks (item 12 in Fig. 4.3) in conjunction with a two-axis inclinometer. The screw-jacks are fixed to the upper aluminium plate with the lead-screw projecting down, towards the bottom plate and are connected to the bottom plate by means of spherical joints (item 19 in Fig. 4.3). Both joints allow for 3 rotational degrees of freedom (DoF) and one of the joints allows for one additional (linear) DoF. The screw-jacks allow for varying the distance between both plates, separately at each point of contact. Both plates are connected at a third point by a rod of a fixed distance ending in a 4 DoF (3 rotational, 1 linear) joint. All joints

are implemented using custom, lubricant-less bearings. This arrangement allows for controlling the pitch and roll of the top plate with respect to the bottom plate. The pitch is changed by co-rotating both screw-jacks, i.e. by generating a common change in the distance between the two plates at each contact point, while roll is changed by counter-rotating, i.e. by generating a differential change. Control of the screw-jacks is informed by the inclinometer that measures the angle with respect to the vertical.

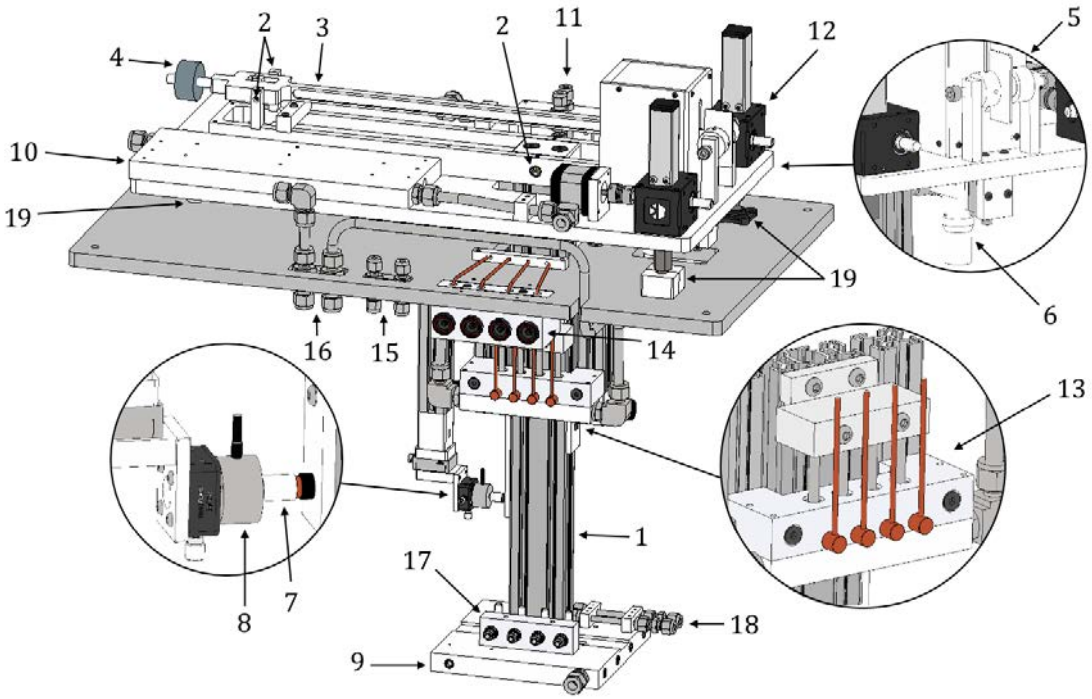

Figure 4.3: CAD drawing of the thrust balance design. 1) Primary arm. 2) Pivots O and A 3) Secondary arm. 4) Counterweight. 5) Eddy current damper. 6) Displacement sensor. 7) Voice coil. 8) Load cell. 9) Water cooled mounting plate. 10) Water cooled electronics plate. 11) Propellant line mounting point. 12) Motorized screw jack for auto-leveling. 13) Liquid metal connectors. 14) Power supply user interface (UI). 15) Propellant line UI. 16) Cooling water UI. 17) Power supply thruster interface. 18) Propellant supply thruster interface. 19) Pivot points for auto-leveling system.

4.3.3 Damping System

The implementation of the damping system consists of a conductive plate attached at the end of the secondary arm. Here the displacement (and hence the velocity) is the largest. Furthermore, including the damping force on the secondary arm takes advantage of the mechanical amplification. As can be seen from eq. (4.15) the damping scales with $n^2 \sim 10^3$. In this way, up to critical damping can be achieved for any thruster, with only a modest damping system.

The magnetic field is applied by two aligned permanent magnets on each side of the plate. The damping force scales with the conductivity of the metal. Of all affordable metals, copper has the highest conductivity of any metal, but it also has a high mass density. The added mass, with a considerable arm ($L_{AE} \sim 0.5$m), leads to an undesirable increase in the moment of inertia of the second arm. Pure aluminium has 60% the conductivity of copper but is only 30% as dense, making it the preferred option. The reported conductivity of the alloy that was used, Al5745, is $2.04 \cdot 10^7$S/m. However, when we measured the conductivity it was found to be closer to $1.59 \cdot 10^7$S/m.

The conductive plate is made of aluminium and has the following dimensions: 30 mm x 60 mm x 2 mm. The two cylindrical magnets are 20 mm diameter, 5 mm thick, NdFeB grade N42 (maximum energy product 42 MGOe) magnets with a remanence of 1.3T and are spaced a distance s apart. To be able to vary the magnetic field strength, and thereby the damping, s is variable by means of small lead-screws.

4.3.4 Displacement Sensing

The quantity that must be measured is the displacement of point E (in Fig. 4.1). There are many different displacement sensors available: inductive, capacitive, interferometry, triangulation etc. For this particular balance we wanted a sensor that was impervious to EMI as the strong RF fields of a Helicon thruster are known to wreak havoc on (sensitive) electrical systems. The current design is outfitted with a confocal chromatic sensor CCS-Prima from STIL.

Confocal chromatic sensors [105] consist of a white light source, a system of lenses (the 'optical pen') and a spectrometer. The white light is refracted by the optical pen; the focal distance is wavelength dependent. An object will reflect the

wavelength with a focal distance corresponding to the position of the reflecting surface. By measuring the wavelength of the reflected light with a spectrometer, and given the relationship between the focal distance and wavelength, the distance of the object to the optical pen can be inferred.

The optical pen is mounted on the top plate, pointing upwards, about 25 mm distance from the horizontal arm. This distance can be controlled by a vacuum-rated manual linear translation stage. The optical pen is connected to the light source and spectrometer by an optical fiber, passing the vacuum/ambient barrier by means of an optical feed-through. Both the emitted and reflected light are coupled through the same fiber. The in-vacuum path only consist of passive elements (fiber, optical pen) while the light source, spectrometer and other electronics reside outside of vacuum chamber far away from the RF fields of the thruster. The range and resolution can be changed by changing the optical pen. For this particular application we are using the CL5-MG20 optical pen which has a measurement range of 12 mm and a resolution of 0.4 μm. It is unaffected by a tilt of the reflecting surface of up to 14° far exceeding the maximum deflection angle $\theta_2 < 3°$.

4.3.5 Calibration System

Since the stiffness of the thrust balance is dependent upon the mass of the thruster, additional stiffness from gas and cooling lines as well as thermal drifts, it is important that the thrust balance can be calibrated repeatedly, preferably in-situ without breaking the vacuum. Calibration is done by applying a known force while measuring the displacement, for a range of loads spanning the desired measurement range.

We have chosen a calibration system based on a voice coil. Voice coils consist of a small solenoid and a permanent magnet. The interaction of the magnetic fields of the solenoid and the magnet results in a repulsive force, linearly proportional to the current applied to the solenoid. The force per current ratio is constant only over a short part of the stroke length, and dependent on the relative position of the solenoid and the magnet. The actual force per current ratio could very well differ from the one specified by the manufacturer. Calculating the applied force from the applied current using the specified force per current ratio can therefore introduce an error. The voicecoil used is a Moticont LVCM-010-013-10 with a reported force

per current of 0.29 N/A.

In the current design, the magnet of the voice coil is instead mounted on a calibrated load cell.This allows for directly measuring the applied force, circumventing the uncertainties in the force per current ratio. The load cell used is a custom version of the Novatech F329 with an extended range, up to 200 mN. Although the load cell is calibrated, its sensitivity can change slightly under loading, especially when loaded horizontally.

4.3.6 Gas-line & Power Feeds

The power and propellant supplies are generally separated from the thruster in an experimental setting; therefore both power supply and gas lines are needed between the fixed and mobile parts of the thrust balance. For the power lines, we opted for 4 supply lines which could power up to 2 electromagnets or for example the anode, keeper and the heater of a HET. For this purpose we also included a secondary gas line to, in the future, be able to operate thrusters that need a hollow cathode for neutralization, such as a HET or GIT.

The electromagnet on the HPTx is fed with up to 30 A, requiring at least gauge 10 wires (2.6 mm ⌀) according to MIL-STD-975. We settled for 3 mm ⌀ enamelled copper cables that can handle temperatures up to 200°C. Due to their considerable diameter these wires would add excessive stiffness to the system. To mechanically decouple the power lines from the system we included liquid metal connectors (item 13, Fig. 4.3). These consist of a metal receptacle filled with a liquid metal and metal rod partially submerged in the metal liquid. The receptacle is mounted on the fixed part of the thrust balance while the rods are mounted on the primary arm. As the viscous drag is negligible, the rod can move freely with respect to the receptacle while maintaining the electrical contact.

In the past, mercury was used as the liquid metal but this is undesirable because of its toxicity. Instead we used galinstan, an eutectic mixture of gallium, indium and tin. It is liquid at room temperature $T_{fus} = -19°\mathrm{C}$, has an electrical conductivity of $3.46{\cdot}10^6$ S/m and a vapour pressure of less than 10^{-8} mbar at 500 °C meaning, that it is suitable for testing in high vacuum. The problem with Galinstan is that it embrittles aluminium and other metals. Certain stainless steels (SS) and refractory metals have good resistance against embrittlement.

Although stainless steel (SS) is the most economic option, to accommodate the high currents we chose molybdenum for its higher conductivity $1.87{\cdot}10^7$ S/m, about 13 times that of SS. The receptacles are 15 mm diameter, 23 mm long cylinders with a 12 mm diameter, 12 mm deep cylindrical cavity.

We simulated the resistive dissipation in the liquid to see whether any notable heating would occur. The total dissipation in the liquid amounts to only 12 mW while the dissipation in the receptacle is little over 14 mW and that in the rod is 175 mW.

To minimize the impact of the gas-lines and to ensure that their impact is linear and limited to an increase in the overall stiffness we opted for thin walled PTFE (polytetrafluoroethylene) tubes of 6 mm outer diameter and 4 mm inner diameter. These tubes are mechanically fixed at two ends: at the top plate and at the cold plate and run parallel to the vertical part of the primary arm. In this way their contribution to the overall stiffness can be approximated with the Euler-Bernoulli beam bending theory. The equivalent torsional stiffness of two 480 mm tubes with a Young's modulus of 0.6 GPa is found to be 0.40 Nm/rad. As we will see later, this is less than 1% of the total torsional stiffness of the system. The overall stiffness of the balance was also calibrated before and after installing the gas-lines and no significant increase in the stiffness was found.

4.3.7 Thermal Management

The HPTx prototype operates in the 0.3-1 kW range with an efficiency of around 10 %. The electromagnet has a resistance of about 0.8 Ω resulting in an Ohmic heating power of 720 W at 30 A. However, this increases with time due to the resistance increasing with temperature. The thermal loads to the balance are therefore of the order of 1-1.5 kW; the need for thermal management is obvious. Moreover, with such high heat fluxes radiative cooling and/or a thermal block would not suffice. The equilibrium temperature would far exceed the rated temperatures of some of the thruster components. Instead we have opted for water cooling.

To realise this, three separate water cooled cold-plates are installed: one integrated in the thruster mounting plate (item 9, Fig. 4.3), a second one on the top plate (item 10, Fig. 4.3), to cool the electronics and a smaller one passing by the liquid connectors. All three cold-plates are connected in series by means of 10 mm

⌀ SS and PU (polyurethane) tubing. For a total cooling line length of about 10 m and a differential pressure of 4.5 bar we estimate a flow rate of 17.5 L/min and Reynolds number of $4.6{\cdot}10^4$ implying turbulent flow. The thermal resistance of the mounting cold plate is about 5.0 °C/kW, that of the electronics plate 3.9 °C/kW and for the liquid connector cooling 24.8 °C/W providing sufficient cooling.

To minimize the effect of the cooling lines to and from the cold plate, the flow direction is kept perpendicular to the plane of motion of the balance. In this way the thrust balance will not be sensitive to any reaction forces of the water on the cooling lines. For that reason the cold-plate is also symmetric w.r.t. the centre line. To reduce the effect on the overall stiffness, the cooling lines run in semi-circular loops on each side of the centre line, from the top plate to the cold plate and back. The are made of 12 mm outer diameter, 10 mm inner diameter PU tubing. The overall stiffness of the balance was also calibrated before and after installing the cooling lines and only a small increase on the stiffness was found, on the order of a few percent.

The problem with water cooling is that the turbulent flow might cause vibrations which introduce noise into the measurement. Although water cooling is used in the shroud (an immobile part) of the thrust stand of [145], as far as we are aware there is no thrust balance design with water cooling of the mobile part(s). We found that the water cooling indeed introduces noise, increasing the RMS noise level from 0.5 μm to 2.9 μm. However, it also reduced the thermal drifts of the thrust balance and prevented both the thruster and balance from overheating.

4.3.8 Data Acquisition and Control

The thrust balance is controlled by an on-board micro-controller. This reduces the amount of electrical feed-through connections (not including those for the thruster) to a minimum, 2 pins for power and 2 for data.

The electronics are exposed to the vacuum environment. Care is to taken to avoid the use of electrolytic capacitors which can lose their electrolyte over time due to evaporation. To prevent overheating the PCBs are mounted on the aforementioned cold plate. A metal cover is placed over the electronics to prevent EMI.

The electronics are based on two Arduino micro-controllers and are divided over

two PCBs, the main board containing the master Arduino Due and a secondary board with the slave Arduino Nano. The secondary board is mounted on top of the thruster mounting plate and further contains an accelerometer (ADXL355), 8 PT1000 resistance temperature detector (RTD) signal conditioners and a variable current source to power the voice coil of the calibration system. The main board also contains an accelerometer, 8 PT1000 signal conditioners as well as a dual axis inclinometer (ADIS16209), 3 stepper motor controllers and a signal conditioner for the load cell. Master and slave are connected by 6 wires using the SPI protocol. The master Arduino is connected to a PC by an RS485 to USB adaptor.

The stepper motors drive the screw-jacks mentioned in section 4.3 and together with the inclinometers allow for control of the pitch and roll of the top plate such that it can be maintained level with the local horizontal at all times. The accelerometers allow for measuring ambient vibrations which can be used to enhance the post-processing. The RTDs are used to track thermal drifts of various parts of the thrust balance. A block diagram of the full data & acquisition system can be seen in Fig. 4.4.

4.4 Experimental Setup

To validate the thrust balance performance various measurements were performed, including some preliminary measurements using the HPTx. Ideally the thrust measurements would be compared to those of an already validated thrust balance. However, these are not yet available, mainly because most existing thrust balances are not compatible with the HPTx platform, which is one of the main drivers for the current work. What is available however, are combined probe measurements that can give an estimate of the thrust and specific impulse. These measurements estimate a thrust in the order of 5-8 mN.

The vacuum facility that houses the thrust balance is a 3.5 m long, 1.5 m diameter stainless steel vacuum chamber at the EP2LAB at UC3M. The chamber has two magnetically levitated turbo-molecular pumps and three cryo-panels. The ultimate pressure is $5 \cdot 10^{-7}$ mbar; the background pressure with 10 sccm of Xenon is about $1.8 \cdot 10^{-5}$ mbar.

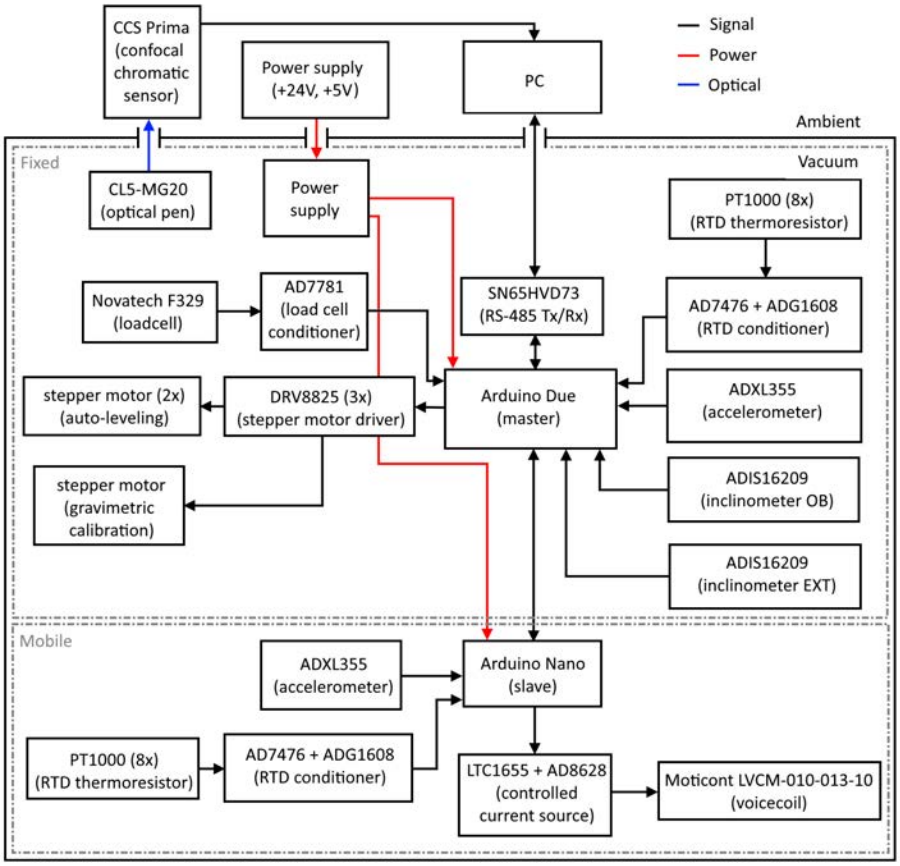

Figure 4.4: Block diagram of data acquisition & control system.

Table 4.3: Mass and moment of inertia of all elements i

i	m_i [kg]	L_i [mm]	I_i [kg·m^2]
1	3.626	375.0	$150 \cdot 10^{-3}$
2	0.237	116.9	$6.86 \cdot 10^{-3}$
3	-	-	-
4	6.9	647.0	-
5	0.271	97.4	-

Table 4.4: Dimensions of the schematic thrust balance.

Point	x [m]	y [m]	κ [N·m/rad]
O	0.000	0.000	0.19160
A	0.300	0.045	0.02330
B	0.310	0.000	0.01165
C	0.310	0.045	0.01165
D	-0.185	0.045	-
E	-0.120	0.045	-
M	0.000	0.674	-

4.5 Results

4.5.1 Validation

To validate the model we simulated the response for our particular balance and compared it to the measured response. All relevant properties and dimensions of the balance are tabulated in Tab. 4.3 and 4.4. The moments of inertia and the masses of all elements are obtained from a CAD model of the balance. Note that the mass of the primary arm includes the 1.7 kg cold-plate and that the mass of the thruster here includes the 1.7 kg mechanical interface. The resulting center of mass is almost aligned with the vertical part of the arm; $x_{1,0} = 2.0$, $y_{1,0} = -375.0$ mm.

For the dimensions in Tab. 4.4 the linearization (see. appendix B.2) yields the following values: $\theta_3'(0) = -1$ which means that $n = \theta_4'(0) = 31.0$. The result

$n = 31.0$ is also found using the static analysis in appendix B.1, confirming the accuracy of the linearization.

Using equations (4.12) and (4.13) and the data in Tab. 4.4 and 4.3, we can calculate the effective moment of inertia $I = 13.0$ kg·m^2, and the effective torsional stiffness $\kappa = 47.1$ N·m/rad of the unloaded thrust balance. This results in a natural frequency of 0.30 Hz for the pendulum motion, equivalent to a period of about 3.3 seconds. When loaded with the HPTx the results are 15.9 kg·m^2, 90.9 N·m/rad, 0.38 Hz and 2.39 s.

To validate the dynamic response of the designed thrust balance, Fig. shows 4.5 the calculated and measured response of the thrust balance when excited with a stepped load. The thrust balance was excited by the voice coil by stepping the applied current nearly instantaneously from zero to some constant value. The response was normalized and centred on $t = 0$, when the step is applied, and then fitted using the step response function for an under-damped harmonic oscillator.

$$A(t) = 1 - e^{-\zeta\omega_0 t}\left[\frac{\sin\left(\sqrt{1-\zeta^2}\omega_0 t + \cos^{-1}\zeta\right)}{\sqrt{1-\zeta^2}}\right] \tag{4.22}$$

The resulting values are $\omega_0 = 2.56$ rad/s corresponding to 0.41 Hz and $\zeta = 0.57$. The plot of the model is generated using the same value for ζ. The relative difference in frequency between the measured and calculated response is about 8%.

The stiffness of the balance changes linearly with thruster mass. The static model, using eq. (B.9) and the dimensions and stiffness from Tab. 4.4 predicts a stiffness of $k = 0.753 \cdot M + 4.06$ mN/mm, ranging from about 4.8 N/m for a 1 kg thruster to about 42 mN/mm for a 50 kg thruster. For the HPTx weighing 5.2 kg, plus 1.7 kg of the cold plate and another 1.7 kg of the mechanical interface, a stiffness of 10.5 mN/mm is expected. Using eq. (4.19) our model predicts a stiffness of 10.4 mN/mm. Both values agree within less than 0.1%.

To validate the model of the damping system we simulated the damping coefficient b for varying magnet spacing s with Comsol's magnetic and electric field (mef) module using the parameters described in section 4.3.3. We also measured the damping ratio ζ by fitting eq. (4.22) to the measured step response for the same spacing s. For each s we performed two square pulses, fitting eq. (4.22) on the positive edge and also on the negative edge (after multiplying by -1), resulting

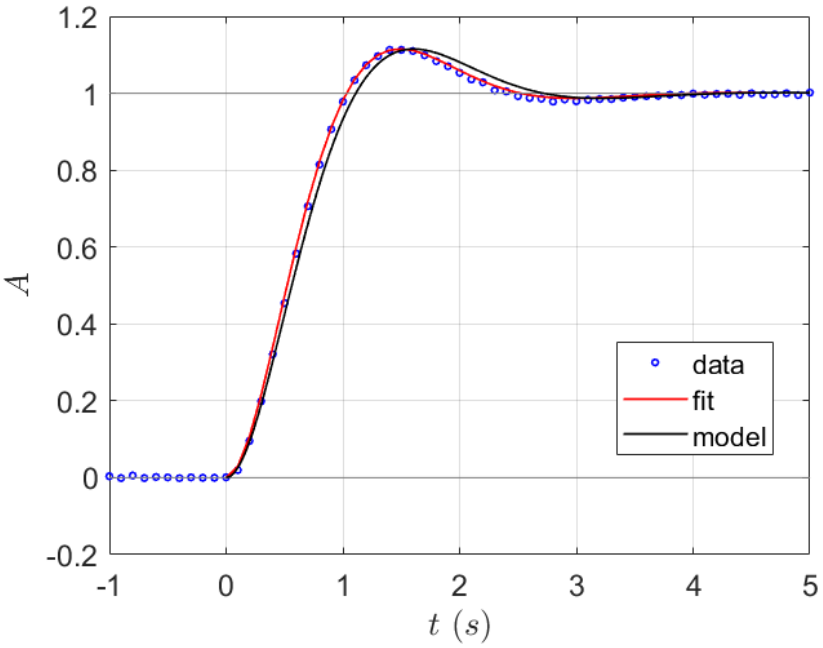

Figure 4.5: Comparison of calculated and measured step response. Time dependent normalized amplitude A as a function of time t.

in 4 points per value of s. The damping coefficient b can be converted to ζ using:

$$\zeta = \frac{(nL)^2}{2\sqrt{\kappa I}} \cdot b \tag{4.23}$$

which follows from eq. (4.15) and (4.17). The results are plotted in Fig. 4.6. The experimental data (ζ) is scaled using eq. (4.23) with 2.97 s/kg (thruster) and 4.08 s/kg (no thruster). From the figure it is clear that the FEM model accurately predicts the damping ratio. As a control we also measured the magnetic field in the centre between the magnets for varying magnet spacing and compared it to the simulated value; this was also found to be in good agreement ($R^2 = 0.995$ and an RMSE (root mean squared error), normalized to the mean, of 2%). The damping system is capable of providing a damping ratio from 0.1 to more than 1 which is more than sufficient for practical application. We did find a slight difference between the results obtained from the positive and the negative edges, most clearly seen at $s = 10$ mm of the blue curve in Fig. 4.6. This is probably due to the fact that for the negative edge the plate does not start centered on the magnet. Regardless, this minor difference does not affect the previous conclusions.

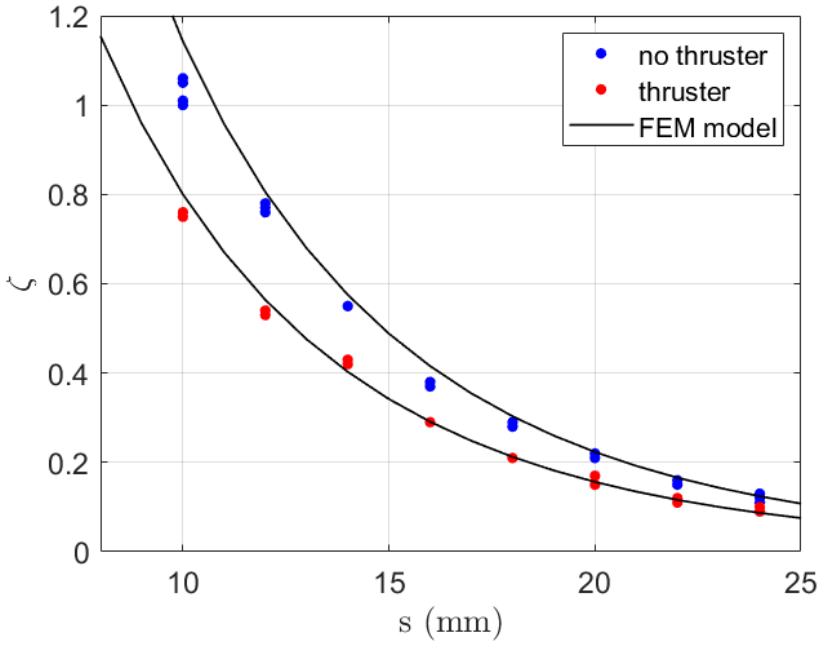

Figure 4.6: Comparison of calculated and measured damping ratio. The model output is scaled using eq. (4.23) with 2.97 s/kg (thruster) and 4.08 s/kg (no thruster).

The optimal damping ratio is that for which the settling time is minimal. The settling time is defined as the time it takes for a step response to fall within 2% of the final value. Using the parameters derived from our Lagrangian model we simulated the settling time for different values of the normalized damping coefficient ζ, resulting in the plot of Fig. 4.7. The optimal damping ratio is about $\zeta = 0.78$ with a settling of time 1.8s. We also inferred the settling time and damping ratio from the measured response of the system to a step input for various separation distances of the magnets which are the red circles in Fig. 4.7. As is apparent the measurement and simulation agree well. These results were obtained without a thruster mounted on the balance. Including the thruster mass in the model yields similar results, the optimum ζ is still 0.78 and the settling time is slightly lower at 1.5 seconds. The discontinuities in the graph are due to the definition of the settling time and can be explained as follows: for a given value of ζ there is a point where the step response $A(t)$ will have crossed the lines $A = 0.98$ or $A = 1.02$ for the last time. This is the settling time. When ζ is increased there will be a point at which this ultimate crossing will occur one half-period earlier, the settling time

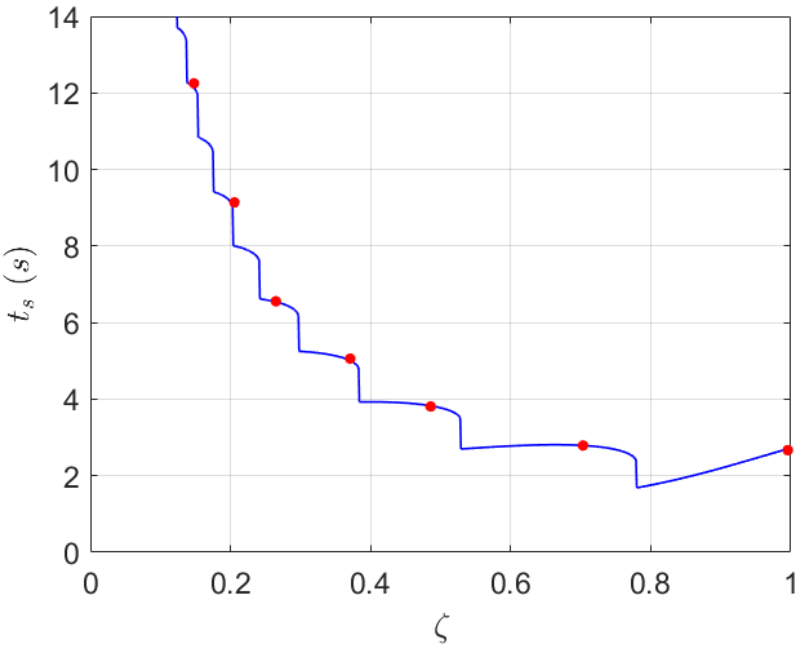

Figure 4.7: Settling time t_s as a function of damping ratio ζ.

will then be reduced discontinuously by a half-period.

4.5.2 Calibration

Calibration of the system is necessary to obtain the actual stiffness of the balance which is needed for post-processing measurement data. Comparison of the calibrated stiffness with the stiffness predicted by the model also provides another venue for validation.

For the HPTx a maximum thrust level of around 8 mN was expected and therefore we intended to calibrate up to 20 mN. The force per current ratio of 0.29 N/A implies that the current applied to the voice coil should be varied from 0 to 70 mA. To verify this we first performed a linear fit of the applied current versus measured force of the voice coil and found instead a force per current ratio of 0.35 N/A a 21% difference. This significant difference could indicate that the calibration of the voice coil is affected by the horizontal orientation and the lateral loading due to the voice coil magnet. This could explain at least part of the difference in the predicted and measure thrust balance stiffness. Despite the different force per current value we maintained the maximum current at 70 mA for a calibration range of slightly

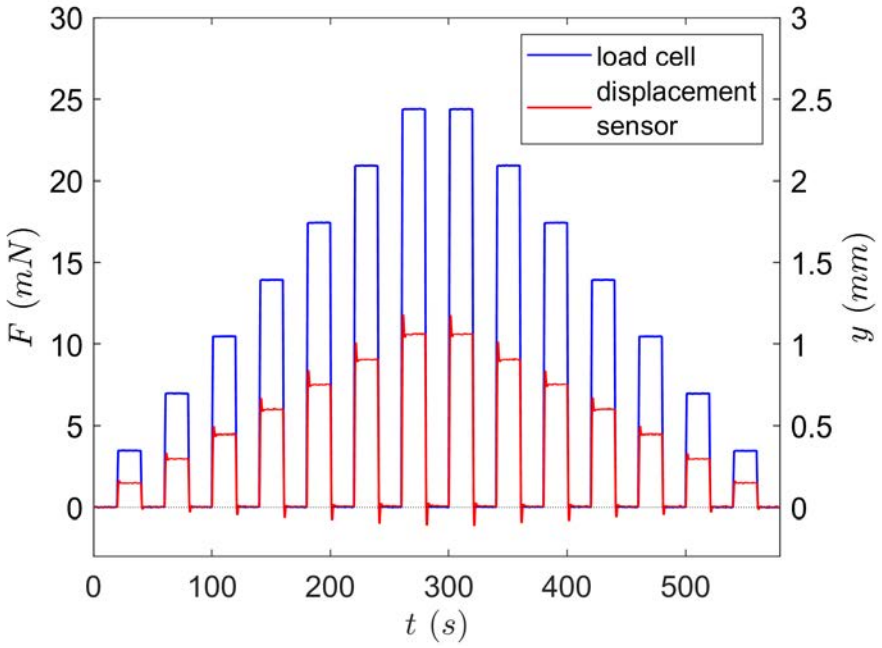

Figure 4.8: Raw calibration data. Applied force F and displacement y as a function of time t.

less than 25 mN.

The calibration protocol was as follows: 0 to 70 mA is applied in steps of 10 mA. Each step lasts for about 20 seconds to allow the balance to settle and to be able to average sufficient data points in one step. To account for drifts, each current step is followed by a zero step that also lasts 20 seconds. In this way each step has its own zero value. Furthermore, to check for hysteresis the procedure is repeated from 70 mA down to 0 mA. The displacement data is sampled at 10 Hz and the load cell data is sampled at 2 Hz. The resulting data is shown in Fig. 4.8. This data was taken with the HPTx mounted on the balance and with the cooling water running. The data is processed as follows. At each step as well as the subsequent 'zero'-step, 150 displacement sensor data points and 30 load cell data points are taken. The displacement data is then averaged every 5 points to reduce it to 30 points. The zero values are subtracted from the preceding 'high' values. We then use a least squares fitting procedure to obtain a linear fit of the data. This results in the plot shown in Fig. 4.9, where we plotted the displacement versus the force, as well as the linear fit. In the upper window of the plot the standardized residuals are

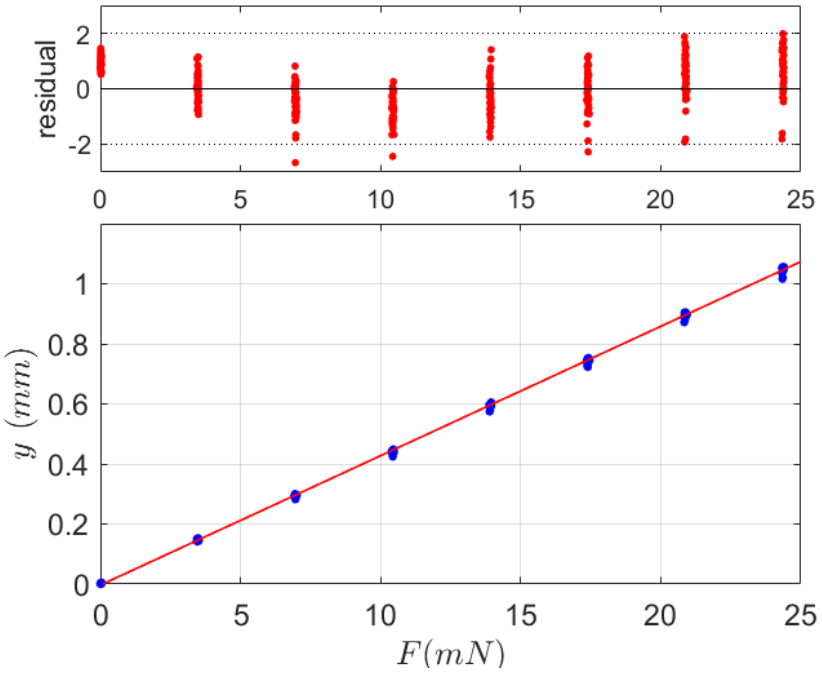

Figure 4.9: Processed calibration curve. Top: standardized residuals. Bottom: displacement y as a function of applied force F.

shown. These residuals should be normally distributed around zero. It can be seen that there is a pattern in the residuals. This is indicative of non-linearity. When doing a quadratic fit the residuals were normally distributed. We quantified the non-linearity as the largest deviation of the quadratic fit with respect to the linear fit, relative to the full scale which resulted in a 0.4% non-linearity error. Since this uncertainty is so small we find the use of the linear fitting justified as it yields a single calibration constant that is easy to use.

The inverse of the slope of the fit is $k_{cal} = 23.21 \pm 0.02$ mN/mm. However, this is the stiffness for forces applied at the position of the voice coil. This needs to be scaled by the ratio between the distance from O to the voice coil (368 mm) and the distance from O to the point of action of the thrust force L_T (generally, but not necessarily: $L_T = L_4$) which is 674 mm; this ratio is 0.546. The stiffness of the thrust balance is therefore 12.7 mN/mm which is about 20% higher than that predicted by either model.

In this particular calibration the relative uncertainty on the calibration constant is about 0.07%. In general we have found that the relative uncertainty is $\leq 1\%$.

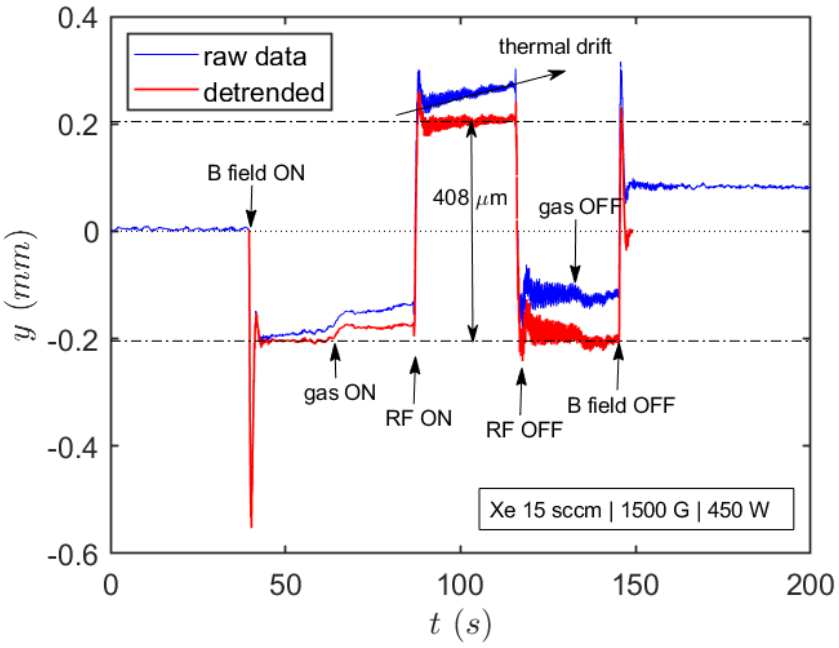

Figure 4.10: Measurement of the HPTx operating at 450W, peak magnetic field of 1500G and 15 sccm of Xenon. Displacement y as a function of time t.

4.5.3 Thrust Measurements

In this section we explain how the thrust measurement results are obtained from the raw thrust balance data. In Fig. 4.10 the output of the displacement sensor during a firing of the HPTx is shown. The operating point was 15 sccm of Xenon, 450 W of RF power and a magnetic field of 1500 G. The blue line shows the raw data; as can be seen there is a thermal drift from the moment the magnetic field is turned on, which in first approximation is linear. It was found that subtracting the slope of the line connecting the point of the curve, right before turning on the magnetic field (40 s) and the point right after turning it off again (150 s) removed most of the drift as evidenced by the red line.

In Fig. 4.10 several events can be distinguished. Firstly at around 40 seconds the magnetic field is turned on, resulting in a negative thrust. This can be explained by the magnetic force between the solenoid and the magnet of the voice coil. A linear relationship was found between the magnetic field of the solenoid and the negative thrust generated, which seems to support this hypothesis. It is important to note that this negative thrust level is considered the 'zero level' of the measurement.

At about 64 seconds the propellant flow is turned on leading to a small increase in the thrust value, the so-called cold gas effect. Little after 86 seconds the RF power is turned on starting the plasma discharge. This is the largest contribution to the thrust. A small overshoot can be seen after which the thrust stabilizes. The increased noise possibly comes from the cooling system. Currently the water cooling circuit for the thrust balance and that of the RF generator are both supplied from the facility water lines. The thrust balance cooling water runs continuously but the RF generator has a valve which opens/closes when the RF is on/off. Although they are connected at outlets several meters apart we suspect that opening and closing the valve causes pressure waves that induce vibrations in the thrust balance. The vibrations are worse when the valve closes (RF OFF), probably due to the induced water hammer, at 132 s. Then subsequently at 145 s and 166 s propellant flow and magnetic field are turned off. Despite the oscillations when turning off and on the thruster the thrust balance signal is appreciably more stable than that of other thrust balances running a HPT [51, 115, 128].

To obtain the net displacement we first obtain the zero level by taking the mean of a 150 data points of the (detrended) data set, after turning on the magnetic field and before turning on the propellant flow where the curve is 'flat', between 45 and 60 seconds; we then obtain the mean of 330 data points of the steady-state part of the data between turning on and off the RF power, between 92 and 115 seconds. The mean values are denoted by the dash-dotted lines in Fig. 4.10. The difference between these values is the net displacement, 408 μm. Given the calibration constant of 12.7 mN/mm this is equal to 5.1 mN.

4.5.4 Uncertainty Estimate

In this section we report the analysis of the experimental uncertainty estimation. The final thrust value is the product of the following variables:

$$F = y \cdot k_{cal} \cdot \frac{L_{vc}}{L_T} \tag{4.24}$$

where $L_{vc} = 368$ mm is the distance from the voice coil to O and y the displacement measured by the sensor. All of these quantities come with an uncertainty. The uncertainty in L_F and L_{vc} are those in the measurement of both lengths and is $\sigma_{L_F} = \sigma_{L_{vc}} = 1$ mm. The uncertainty in k_{cal} is obtained concurrently with k_{cal}

and for this particular measurement is $\sigma_{k_{cal}} = 0.1$ mm/mN. According to [97] the uncertainty in y, σ_y, can be estimated from the calibration data. However, we are of the opinion that in our case this underestimates the uncertainty. Therefore, we use the root sum of squares of the standard deviation of the zero level and thrust level. In this measurement of Fig. 4.10 this results in an uncertainty of 8 μm. The uncertainty in the thrust measurement is calculated from the root sum of squares of all the relative uncertainties.

$$\frac{\sigma_T}{F} = \sqrt{\left(\frac{\sigma_y}{y}\right)^2 + \left(\frac{\sigma_{k_{cal}}}{k_{cal}}\right)^2 + \left(\frac{\sigma_{L_T}}{L_T}\right)^2 + \left(\frac{\sigma_{L_{vc}}}{L_{vc}}\right)^2} \tag{4.25}$$

For the measurement of Fig. 4.10 the relative uncertainty in the thrust measurement is 2% which is dominated by the uncertainty in the displacement measurement. The thrust value is then $T = 5.1 \pm 0.1$ mN.

4.6 Thrust Measurement Results

Although a full thrust measurement campaign is outside of the scope of this work in this section we will present some results that are representative of the HPTx performance at 400W and 1500G. The thrust balance calibration constant was found to be 14.0±0.4 mN/mm. A series of 9 measurements was performed at 5,10 and 20 sccm of which 5 were useful. The results are tabulated in Table 4.5 and plotted in Figure 4.11. From these results it can be concluded that both the balance and the thruster operate with good repeatability; results taken at the same operating point produce the same results within the measurement uncertainty. Furthermore it can be concluded that the thrust and efficiency increase with the mass flow rate, while the specific impulse decreases. The thrust to power ratio varies between 4.4-12.7 mN/kW. Overall the specific impulse is low for EP devices, and is rather in the range typical of chemical propulsion. Lastly the efficiency is dramatically low, ranging from 1-2%.

4.7 Mechanically Decoupled RF System

The power source of a helicon plasma thruster is primarily the RF system which generates a high power AC signal at 13.56 MHz that is coupled to the plasma by the helicon antenna. In the power ranges considered here, 10^2W, the coaxial

$\dot{m}$ (sccm)	F (mN)	I_{sp} (s)	η (%)
5	2.0 ± 0.2	421 ± 41	1.0 ± 0.2
5	2.1 ± 0.2	427 ± 41	1.1 ± 0.2
5	2.2 ± 0.2	447 ± 41	1.2 ± 0.2
10	3.9 ± 0.2	401 ± 21	1.9 ± 0.2
20	5.7 ± 0.2	298 ± 10	2.1 ± 0.1
20	5.7 ± 0.3	296 ± 16	2.1 ± 0.2

Table 4.5: Performance of the HPTx operating at 450W, 1500G and different mass flow rate as measured with the thrust balance.

cables used to transfer the RF power from the power supply in the ambient to the antenna in the vacuum chamber are type LM-400, RG214/U or similar which are thick and rigid. Their rigidity would nullify the carefully engineered compliance of the thrust balance. In the current prototype the antenna can be mechanically decoupled from the rest of the thruster in a way that allows the magnetic coil and the thrust chamber to move freely while hanging from the balance; the antenna is fixed to the vacuum chamber. Once the prototype reaches a more mature phase, where both the antenna as well as the RF system are integrated into the thruster, the rigidity of the RF cables will also be circumvented. However during a major part of the development, the prototype will have the antenna integrated but not the RF system. Therefore a solution is needed to mechanically decouple the RF cable from the thruster without separating the antenna.

Mechanically decoupling the power system for thrust balance measurements has been done before with electron cyclotron thrusters (ECR). ECR thrusters operate in the microwave range and use wave guides instead of coax cables, at least for some part of the power line. In this case it is sufficient to cut a wave guide in two parts and align them with a separation sufficiently small compared to the wavelength. This way power transfer is uninterrupted but the two parts of the wave guide are mechanically decoupled. Since the helicon plasma thruster operates in the radio-frequency domain the solution is less trivial. However research into wireless power coupling has increased over the years due to an interest in wireless charging of both mobile devices and electric vehicles.

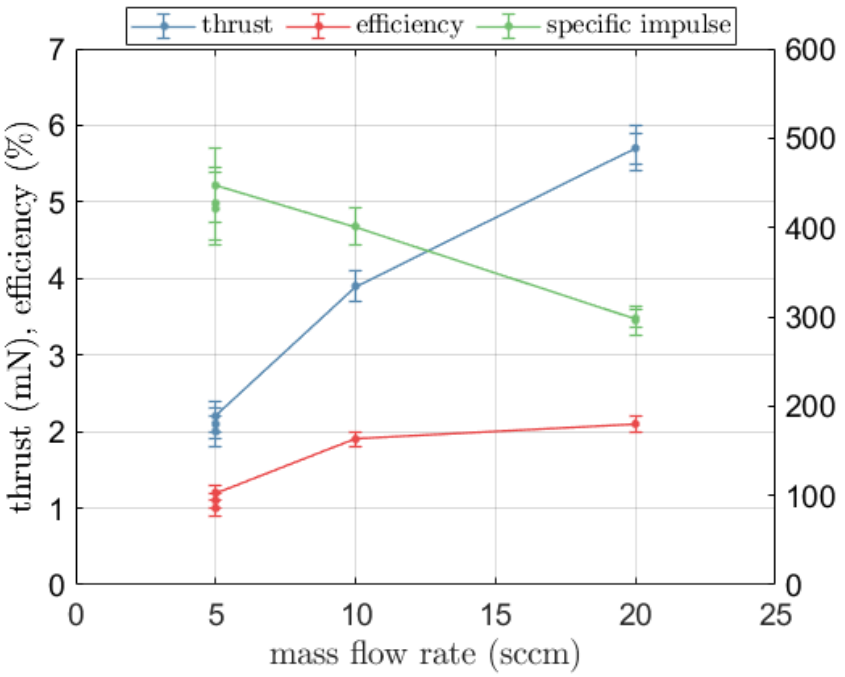

Figure 4.11: Performance of the HPTx operating at 450W, 1500G and different mass flow rate as measured with the thrust balance.

4.7.1 Wireless Power Transfer

Wireless power transfer technologies use energy containing fields to transfer power contactlessly. Although technologies using acoustic fields exist most technologies use either electric or magnetic fields. In the latter case a further division can be made between radiative or far-field technologies such as optical or microwave power transfer and non-radiative or near-field technologies, most importantly inductive power transfer. When using electric fields one speaks of capacitive power transfer.

Far-field technologies are used for power transfer over long range, even over several kilometers, and generally have lower coupling efficiency than near-field technologies. Of the latter category both inductive power transfer (IPT) and capacitive power transfer (CPT) are use for electric charging applications although the former have been studied in more depth over the past decades.

Although IPT technologies are more mature and generally have a higher efficiency and power density, they tend to operate a lower frequencies < 1 MHz. At high frequencies the Eddy current losses induced in the magnetic core material and the conduction losses due to skin-effects reduce the overall efficiency [73]. Air core

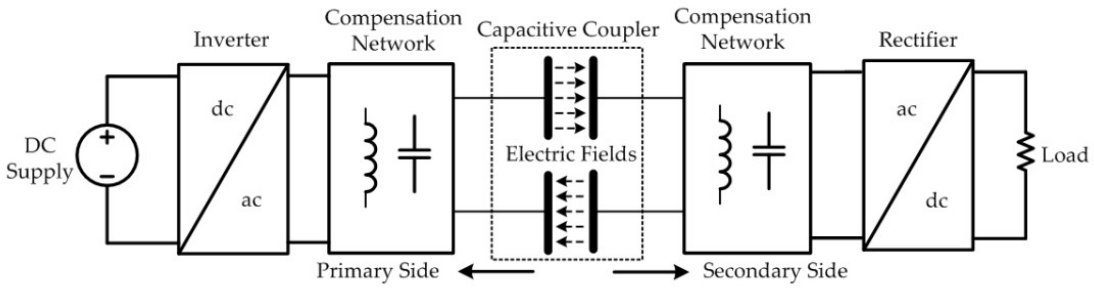

Figure 4.12: A schematic of a CPT system. Figure from [73].

coils using Litz wire mitigate this partially but even at the 13.56 MHz operating frequency of the helicon these do not completely solve the issue. On a practical note, achieving design parameters with custom wound coils is notoriously difficult while doing the same for capacitors is very simple as it only requires two plates and the correct spacing between them. Another downside of IPT technologies is the fact that it can induces Eddy currents in nearby metals further increasing losses and leading to unwanted heating of surrounding surfaces.

The main drawbacks of CPT technologies are, lower power density, lower efficiency and emission of electric fields [73]. However these low power densities are mainly of concern at 'long distances' i.e. of the order of 100's of millimeters which are not relevant to our particular application. Efficiencies of up to 92% have been reported, which would equal a 10% reflection that can be tolerated in the case of the RF generator. Lastly regarding the electric fields, this is mostly of importance at larger distances, furthermore the setup will be contained inside the grounded vacuum chamber effectively shielding the operator of these fields.

Due to the high operating frequency of 13.56 MHz and the difficulty of manufacturing custom coils we consider CPT a better solution for our particular application. However IPT technologies outperform CPT in many other applications; an in-depth review about IPT can be found in [151].

4.7.2 Capacitive Power Transfer

As aforementioned CPT uses electric fields for contactless power transfer. The electric fields are generally established between two parallel plates which act as a capacitor. In Figure 4.12 a schematic of a general CPT system is shown. CPT

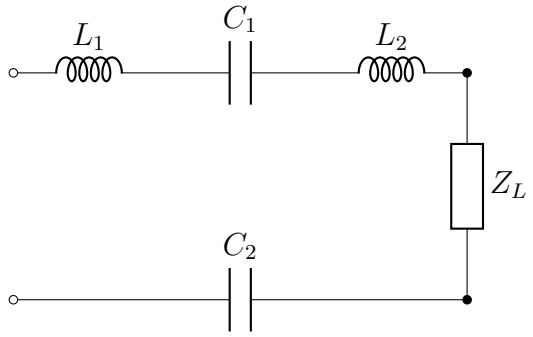

Figure 4.13: Equivalent circuit of a CPT system.

is mostly considered for DC-DC power transfer which requires an inverter at the primary side to generate an AC signal and a rectifier at the secondary to convert back to DC power. For our particular application these can be left out, which is a boon as these elements generally introduce some extra losses. The simplest compensation circuit is the double sided L-compensation. Here two inductors are added in series with the capacitors to induce a resonance. An equivalent circuit of such a system including a load impedance Z_L is given in Figure 4.13. The equivalent impedance of this ideal circuit is easy to calculate.

$$Z(\omega) = Z_L + \left(\frac{C_1 + C_2}{\omega C_1 C_2}\right)\left[\frac{\omega^2}{\omega_0^2} - 1\right] \tag{4.26}$$

Where we introduced the resonance frequency ω_0.

$$\omega_0 = \sqrt{\frac{C_1 + C_2}{C_1 C_2 (L1 + L2)}} = \frac{1}{\sqrt{LC}} \tag{4.27}$$

Here the second equality holds if $L_1 = L_2 = L$ and $C_1 = C_2 = C$. When the operating frequency is equal to the resonance frequency the second term in Equation 4.26 becomes zero and $|Z| = Z_L$ i.e. the equivalent impedance is equal to the load impedance of the system and the coupling system is virtually invisible for the source. Such a system would be of use if the thruster presents itself as a 50Ω load. For this system to work it is important that the components L_1, L_2 and C_1, C_2 are size correctly. To account for any manufacturing tolerances it would also be of interest to have at least either the capacitances or the inductors be (somewhat) variable.

The previous analysis however does not account for stray capacitances. The are not only capacitances between the opposing electrodes of each of the capacitors but

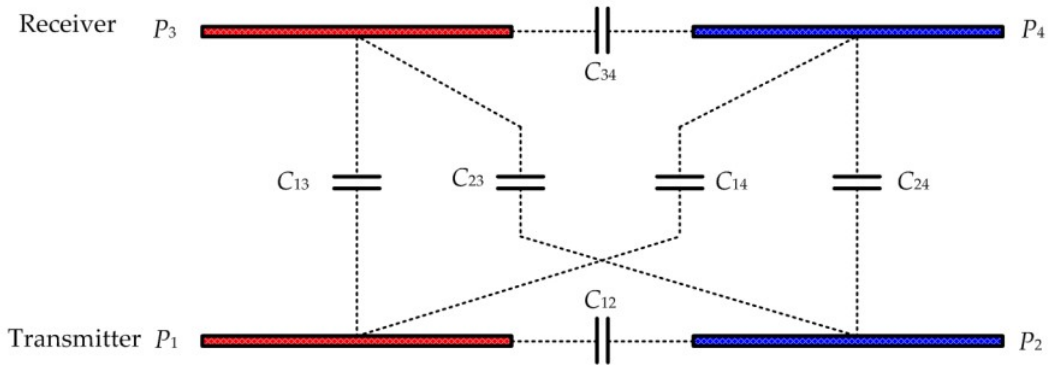

Figure 4.14: Equivalent circuit of capacitive coupler including stray capacitances. Figure from [73].

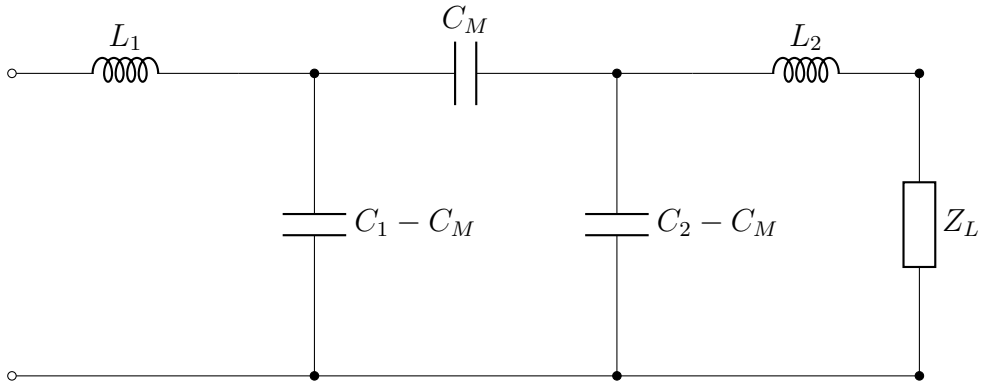

Figure 4.15: Equivalent π-model of the circuit shown in Figure 4.14.

also between the electrodes on the same side as well as between opposing electrodes of different capacitors. In Figure 4.14 a circuit with all the stray capacitances is shown It is possible to transform the capacitive coupler consisting of two series capacitances into two parallel capacitances and a coupling capacitance, i.e. an equivalent π-model taking into account all (stray) capacitances between the four electrodes, shown here in Figure 4.15 including the double-side L-compensation. The values for C_1, C_2 and C_M are as follows [150].

$$C_1 = \frac{(C_{13}+C_{14})(C_{23}+C_{24})}{C_{13}+C_{14}+C_{23}+C_{24}} + C_{12} \tag{4.28}$$

$$C_2 = \frac{(C_{13}+C_{23})(C_{14}+C_{24})}{C_{13}+C_{14}+C_{23}+C_{24}} + C_{34} \tag{4.29}$$

$$C_M = \frac{C_{12}C_{34} - C_{14}C_{23}}{C_{13}+C_{14}+C_{23}+C_{24}} \tag{4.30}$$

The equivalent impedance of the circuit shown in Figure 4.15 is significantly more complicated than that of Equation 4.26.

$$Z(\omega) = \frac{1-\omega^2(L_1C_1+L_2C_2)+\omega^4L_1L_2C_1C_2(1-k_c^2)+\mathrm{i}\omega Z_L C_2[1-\omega^2L_1C_1(1-k_c^2)]}{-\omega^2C_1C_2(1-k_c^2)Z_L+\mathrm{i}\omega C_1[1-\omega^2L_2C_2(1-k_c^2)]} \tag{4.31}$$

In the equation above we have introduced a coupling constant $k_c = C_M/\sqrt{C_1C_2}$. This can be somewhat simplified if we assume that the system is symmetric, and that the inductors are of equal size i.e. $C_{13} = C_{24} \equiv C_S$, $C_{12} = C_{34} \equiv C_P$, $C_{14} = C_{23} \equiv C_D$ and $L_1 = L_2 \equiv L$. It follows then that $C_1 = C_2 \equiv C$, and the expressions for C and C_M then become:

$$C_C = \frac{(C_S+C_D)^2}{2(C_P+C_S)} + C_P \tag{4.32}$$

$$C_M = \frac{C_S^2 - C_D^2}{2(C_P+C_S)} \tag{4.33}$$

We can then write the equivalent impedance as:

$$Z(\omega) = \frac{1-2\omega^2LC+\omega^4L^2C^2(1-k_c^2)+\mathrm{i}\omega CZ_L[1-\omega^2LC(1-k_c^2)]}{-\omega^2C^2(1-k_c^2)Z_L+\mathrm{i}\omega C[1-\omega^2LC(1-k_c^2)]} \tag{4.34}$$

We can then normalize the frequency to $\hat{\omega} = \omega/\omega_0$, with $\omega_0 = 1/\sqrt{LC}$ and $\Lambda = \sqrt{C/L}$. Note that for this ω_0 to be equal to that of Equation 4.27 we need to set here $C = C_S/2$. We also drop the subscript on k_c.

$$Z(\omega) = \frac{1-2\hat{\omega}^2+\hat{\omega}^4(1-k^2)+\mathrm{i}\hat{\omega}\Lambda Z_L[1-\hat{\omega}^2(1-k^2)]}{-\hat{\omega}^2\Lambda^2(1-k^2)Z_L+\mathrm{i}\omega\Lambda[1-\hat{\omega}^2(1-k^2)]} \tag{4.35}$$

In the limit that the stray capacitances $C_P, C_D \to 0$, we find that $k \to 1$ and $C \to \frac{1}{2}C_S$. Substituting this in Equation 4.34 we recover Equation 4.26. For maximum power transfer the impedance of the system should be equal to that of the RF generator, i.e. $Z_0 = 50\Omega$. This can best be quantified in the form of the transmission coefficient T, when $T = 1$ all power is coupled to the load.

$$T = \frac{2Z_0}{Z+Z_0} \tag{4.36}$$

4.7.3 CPT Design

For the design of the CPT system the following requirements should be kept in mind: operating frequency 13.56 MHz, and a reasonable system volume of about 1L or $10\times10\times10\text{cm}^3$ with maximal power coupling, but at least $T > 0.9$. The total power it should be able to handle should be around 500W. To size the components we do the following back of the envelop calculation: the largest area within the volume is about 100×100 mm^2 which should fit 2 capacitors, so a single electrode is about $5{\cdot}10^{-}3$ m^2. As as starting point we can use Equation 4.27 with $\omega_0/2\pi = 13.56$ MHz. A reduced inter-electrode distance leads to larger capacitances, and therefor lower required inductances. Inductors with lower inductances generally have less windings and therefore also less resistance. We estimate a practical inter-electrode distance to be of the order of $10^{-}3$ m, which can be somewhat varied with a micrometer stage. The capacitance of two parallel plates can be approximated with:

$$C = \frac{\epsilon_0 A}{d} \tag{4.37}$$

Where $\epsilon_0 = 8.85 \cdot 10^{-12}$ Fm^{-1} the permittivity of free space, A the area of the electrode and d the inter-electrode distance. Using the aforementioned estimates, we can calculate $C \approx 44$ pF, the corresponding inductance is then about $L \approx 3$ μH. This inductance can be adjusted somewhat, within order unity to adapt to what's commercially available, while adjusting C by varying d.

At the frequency of 13.56 MHz the inductor most certainly should be an air-core inductor to avoid losses in the magnetic core. Increased AC resistance due to the skin-effect are another source of losses to be avoided. When current travels through a conductor with a high varying frequency it is confined to a thin layer near the surface called the skin-depth δ which is frequency dependent.

$$\delta_s(\omega) = \sqrt{\frac{2}{\mu_0 \sigma \omega}} \tag{4.38}$$

where $\mu_0 = 4\pi \cdot 10^{-7}$ Hm^{-1} is the permeability of vacuum and ρ is the resistivity of the conductor. For a copper conductor at 13.56 MHz the skin depth is about 1.8 μm. Therefore using thick solid conductors for high frequency currents does nothing to reduce induction losses. Hollow copper tubes are sometimes use but they lead to bulky inductors. Litz wire is another solution, which consist of multi-stranded wires where all strands are electrically isolated from each other. However Litz wire

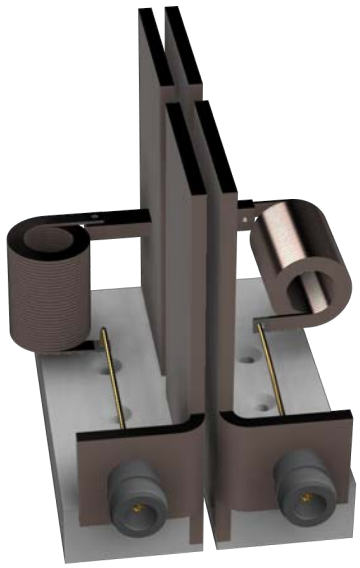

Figure 4.16: CAD of the CPT.

Figure 4.17: Photo of capacitive coupler setup.

is expensive and generally used up to about 2 MHz. A third solution is flat wire coils, which are flat copper wires wound in such a way that the large surface is parallel to the normal plane of the coil. This results in relatively compact coils with low AC resistance.

The 500W requirement translates roughly into a 3 A current requirement in the case that the system is properly tuned i.e. $Z \simeq 50\Omega$. For a safety margin and taking into account that heat dissipation in the vacuum environment happens by conduction only, we set the current requirement at 10 A current for the inductors. We found a commercial flat wire coil air core inductor with 5.3 μH inductance, a 10 A current carrying capacity. It consists of a 5 mm wide, 1 mm thick enamelled flat copper wire, wound in a coil with 29.5 windings, 33 mm tall and 15 mm inner diameter. Using these inductors and four copper plates we designed the setup shown in Figure 4.16. Before constructing the setup we first calculated the capacitances C_P, C_D and C_S using FEM software. We created 4 electrodes of 117 x 50 mm in sets of two, spaced 10 mm apart and both sets facing each other. We then varied the distance between both sets of electrodes and calculated the capacitances. The resulting data are plotted in Figure 4.18 and Figure 4.19. As can be seen in Figure 4.18 over the first millimeter or so the theoretical Equation 4.37 agrees

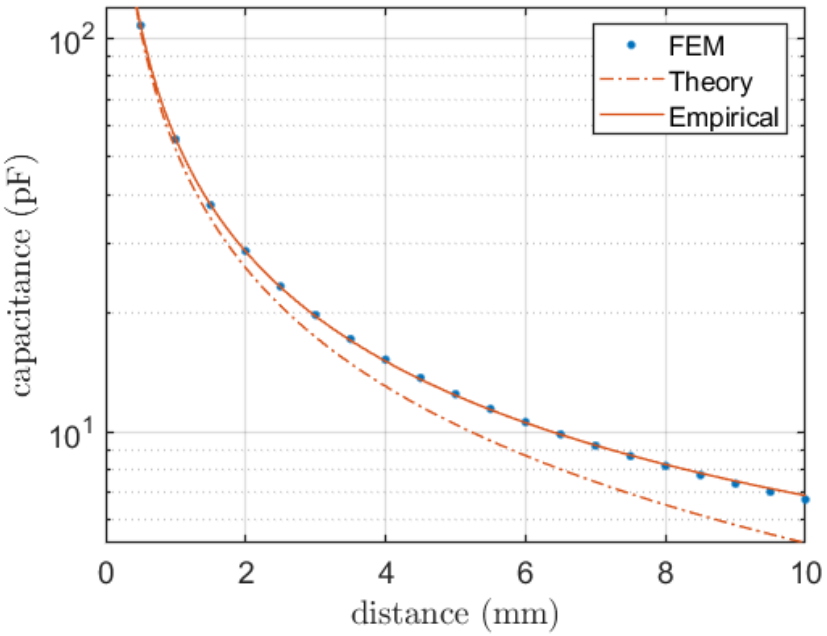

Figure 4.18: Series capacitance as a function of electrode separation, obtained from FEM analysis.

well with the FEM results. However, as the inter-electrode distance increases, edge effects become more important and the results deviate from theory. Instead we find that a rational with a first order numerator and first order denominator are a better fit.

All three fitting formulas are given in Equation 4.39.

$$C_S = \left(\frac{0.1554 \cdot d + 6.244}{d + 1.977 \cdot 10^{-2}}\right)\epsilon_0 \tag{4.39}$$

$$C_P = (-199.3 \cdot d^2 + 7.387 \cdot d + 0.1601)\epsilon_0 \tag{4.40}$$

$$C_D = (-31.47 \cdot d^2 + 0.8474 \cdot d + 8.089 \cdot 10^{-2})\epsilon_0 \tag{4.41}$$

$$\tag{4.42}$$

Using the empirical expressions for the capacitances we can then calculate Z as a function of d using Equation 4.32 to 4.34. The result is plotted in figure Figure 4.20. The transmission peaks at an inter-electrode distance of about $d = 4.55$ mm, with $T = 1$; the series capacitance corresponding to that position is 13.51 pF. After having proven that high transmission is possible and can be adjusted by changing

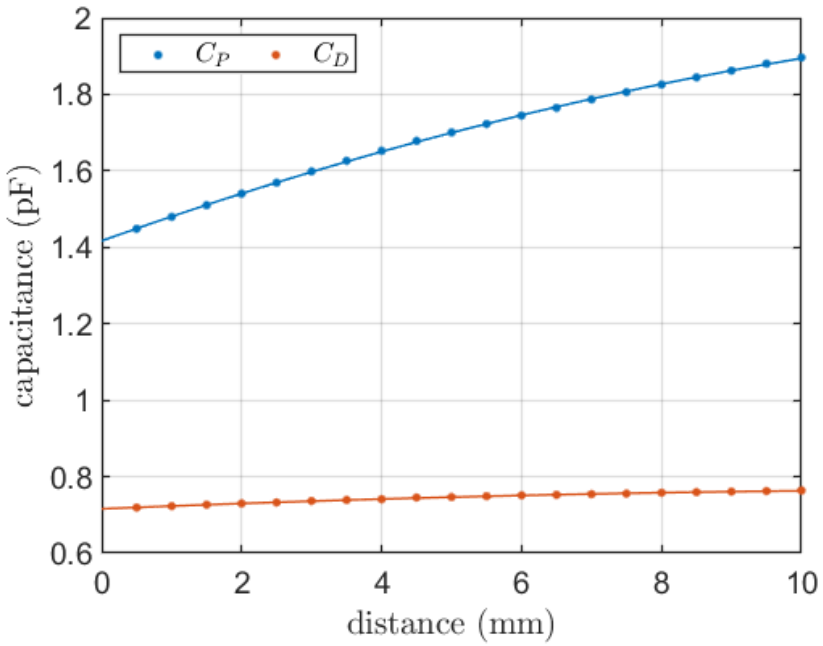

Figure 4.19: Parallel and diagonal capacitances as a function of electrode separation, obtained from FEM analysis.

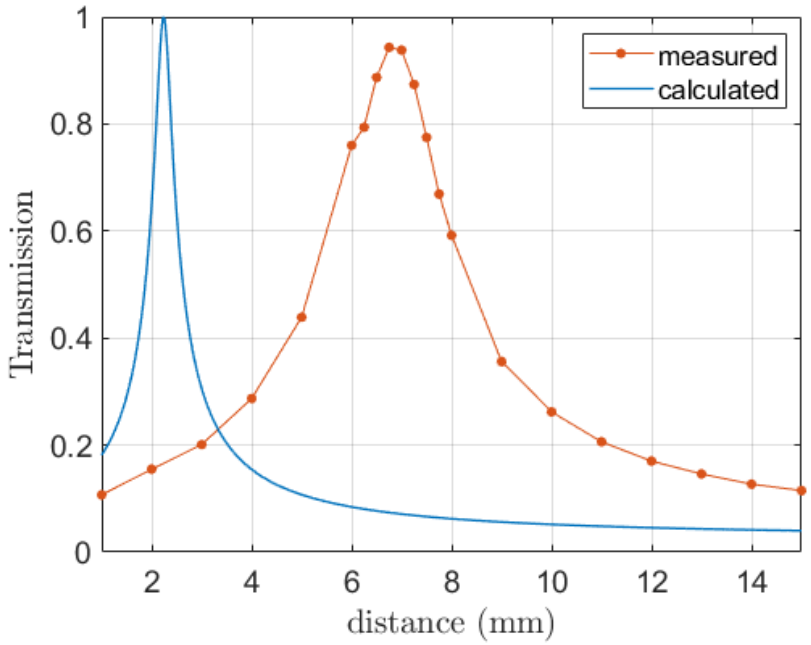

Figure 4.20: Calculated and measured transmission coefficient T as a function of inter-electrode distance d.

the inter-electrode distance we manufactured the CPT. One half of the coupler was mounted on a micrometer linear stage as shown in figure Figure 4.17.

The transmission coefficient was obtained by measuring the S_{21} parameter using a network analyzer, while varying the inter-electrode distance d. The measured results are also plotted in Figure 4.20. Surprisingly the distance of maximum transmission is significantly different than calculated, at $d = 6.8$ mm. The peak value of the transmission is about 0.95 which exceeds the requirement of > 0.90. Furthermore the measured response is also significantly broader than the calculated one. One explanation could be that the N-type coaxial connectors have a capacitance that is not included in the model. Although they are matched to 50Ω their capacitance plays a role when the system is not perfectly matched which would show up as an increase of C_{12} and a capacitance in parallel with Z_L. Despite the discrepancy between measurement and calculation it can be concluded that the experimental CPT is capable of reaching a transmission in excess of 90%.

The CPT setup has also been tested up to 50W with a load and no significant loss of transmissibility was seen. Next steps would include testing the system at higher powers: 100-300W, ideally in vacuum and measure the temperature of various parts to assess whether it maintains its transmissibility even at those powers and to assess whether the system would need active cooling. The latter can be easily achieved by welding copper tubes to the electrodes and connect them to the water cooling circuit of the balance. Car has to be taken that one uses non-conductive tubing. The addition of the cooling circuit may affect the performance of the coupling circuit due to additional stray capacitances and it would therefore have to be characterized again. Once having past these tests the system would have to be integrated into the thrust balance, which would be fairly straightforward. The biggest drawback of this system is that it requires a thruster that presents itself as a 50Ω load. Unfortunately this is not the case for the current version of the HPT, however it is expected that for a future iteration this will be the case.

CHAPTER

FIVE

Optical Emission Spectroscopy

"To try to make a model of an atom by studying its spectrum is like trying to make a model of a grand piano by listening to the noise it makes when thrown downstairs."

— Anonymous - Atoms and Rays (1924)

5.1 Introduction

Numerous diagnostic methods are available to measure relevant physical quantities for characterizing plasma production and acceleration. As we have seen in chapter 3, charged particle density, energy distribution and flux as well as electron temperature are conventionally obtained by means of probes. Although well-suited for the plume region, such intrusive diagnostics are less applicable to the source region of a thruster, where any probe would irremediably perturb the plasma production and transport processes and therefore yield non-representative measurements. Optical diagnostics, which are intrinsically non-intrusive, overcome these drawbacks and therefore present a valuable alternative for plasma characterization. Optical techniques are based on electromagnetic (EM) waves, often visible light but also infrared and ultraviolet as well micro- and millimeter waves and even x-rays. Another distinction that can be made is between passive techniques that rely on natural emission from the plasma and active techniques that probe the plasma with EM waves while measuring the absorbed, scattered or fluoresced light. Techniques that are common in plasma diagnostics in general and electric propulsion testing in particular are: optical emission spectroscopy (OES), laser induced fluorescence (LIF) Doppler velocimetry, (tunable diode) laser absorption spectrometry (TDLAS) and

microwave interferometry. Active techniques are generally able to more directly measure desired plasma properties but at the expense of more complex and costly equipment. Passive techniques like OES are less costly but rely on extensive modelling to interpret the results and extract the desired quantities. Optical Emission Spectroscopy (OES) is commonly applied to probe excited state densities and from them derive the electron temperature.

5.2 Atomic Physics

Optical emission relies on the fact that energetic states in atoms and molecules are quantized, that is to say there are only discrete energetic states that a system can occupy. For energy to be conserved in a transition between two states a photon with a wavelength $\Delta E = hc/\lambda$ is emitted or absorbed. These states are either electronic, rotational or vibrational in nature. The latter two states are particular to molecules only and are due to vibration of atomic bonds within the molecule or rotation of the molecule around some axis. Emission due to rovibrational transitions occur in the infrared only, because $\Delta E \leq 0.12$ eV. Since the vast majority of electric thrusters use noble gases as a propellant, rovibrational transitions are not of interest for electric propulsion testing.

Electronic states are a result of the fact that bound electrons of an atom can only occupy discrete orbitals defined by total energy (E), angular momentum (L) and the projection (L_z) of that angular momentum along an arbitrary (although conventionally the z-) axis. Electronic states are generally defined by the principle quantum numbers (n, l, m) where $E = n\hbar$, $L^2 = l(l+1)\hbar$ and $L_z = m\hbar$ with $\hbar$, Planck's constant divided by 2π. These principle quantum numbers are eigenvalues of the energy and angular momentum and it's projection operator.[1] They can be derived by solving the time-independent Schrödinger equation in spherical coordinates for the potential of a hydrogen atom. The quantum numbers denote the possible orbitals of an atom. For multi-electron atoms these orbits are filled starting with the lowest energy orbital, until all bound electrons occupy an orbital. It is important to note that the values of the principle quantum numbers are bound by: $n = 0, 1, 2, ...,$ $l = 0, 1, 2, .., n-1$ and the magnetic quantum number by $m = -l, -l+1, ..., l-1, l$. It is conventional to label the orbitals with the same value of l with letters: s, p, d, f

[1] Note that the quantum number m is also referred to as the magnetic quantum number.

for $l = 0, 1, 2, 3$, while maintaining the numbers for n. So the orbital with $n = 2$ and $l = 1$ is referred to as the $2p$ orbital which contains three different states, since for $l = 1 \rightarrow m = -1, 0, 1$. According to the Pauli exclusion principle two or more fermions (which include electrons) cannot occupy the same state. However there is an additional quantum number, the electron spin s which can either have the value *up*, or *down* $(+\frac{1}{2}, -\frac{1}{2})$. So each state n, l, m can be occupied by two electrons, one with spin *up* and one with spin *down*. (Alternatively one could speak of unique states (n, l, m, s). Therefore, the $2p$ orbital can be filled with at most 6 electrons. For multi-electron atoms one can then write the electronic configuration as follows. For example, the electronic configuration for the ground state of argon, which has 18 electrons, is: $1s^2 2s^2 2p^6 3s^2 3p^6$. The exponents denote how many electrons reside in a given orbital. Although the majority of atoms (and ions) in a low temperature plasma are in their ground state, at any given time a fraction of them are in an excited state. This means that one (or more) of the outer electrons has moved to a higher orbital. (In most cases it's only the outermost electron.) One can also write an electronic configuration for such an excited state. For an argon atom of whom one of it's 3p electrons has been excited to the 4s orbital the configuration would be: $1s^2 2s^2 2p^6 3s^2 3p^5 4s$. For the noble gases this very often abbreviated using the preceding noble gas in the periodic table, this case: $[Ne]3s^2 3p^5 4s$.

5.2.1 Nomenclature of Excited States

Due to interaction between the many electrons in a multi-electron atom the electronic configuration is not sufficient to describe an electronic state. For smaller atoms the coupling scheme is the Russel-Saunders or LS-coupling since both the total orbital angular momentum and the total spin of the atom are good quantum numbers. This coupling is denoted with a term symbol which is derived as follows. For a given atom (in the ground state) one fills up the shells according to Hund's rules. Take the electronic configuration and discard all the full orbitals. For the remaining orbitals fill them each with one electron, starting with the highest m and assign all of these electrons $s = +\frac{1}{2}$. Then do the same with the remaining electrons assigning them a spin of $-\frac{1}{2}$. The angular momentum is then $L = \sum_i m_i$ and the spin $S = \sum_i s_i$ where is a sum over the electrons in the partially filled orbital. Lastly we calculate the total angular momentum J, where $J = |L - S|$ if the orbital

is less than have full, $J = L + S$ when it is more than half full and $J = 0$ when it is exactly half full. The term symbol is then ${}^{2S+1}L_J$ where L is expressed with the same letters as in the orbitals, only now capitalized. As an example, for fluorine the electronic configuration is $1s^2 2s^2 2p^5$. We discard the first two orbitals and keep the partially filled $2p^5$ orbital. We then first fill that orbital with 3 electrons all with spin $+\frac{1}{2}$ and magnetic quantum numbers $m = +1, 0, -1$ we then add the remaining two electrons with spin $-\frac{1}{2}$ and $m = +1, 0$. Doing the sums we end up with $L = 1$ and $S = +\frac{1}{2}$. Since the orbital is more than half full $J = \frac{3}{2}$. The term symbol for the ground state for fluorine is then ${}^2P^\circ_{3/2}$. The circle denotes the parity $\pi = (-1)^{\sum_i l_i}$ with $\pi = -1$ odd and $\pi = +1$ even. Term symbols with odd parity have a $^\circ$ while even ones do not. Unfortunately all noble gases starting from neon do not strictly follow the LS-coupling scheme, but rather have a mix of LS-coupling and J_1L_2-coupling. From it follows the spectroscopic Racah notation which is used to describe singly excited states of noble gas atoms (and ions). The LS-coupling is applied to the parent ion while the J_1L_2-coupling applies to the excited electron. The Racah notation has the form: $({}^{2S_1+1}L_{1J_1})nl[K]^0_J$ where all the variables with subscript 1 relate to the parent ion, nl is for the excited electron and $K = J_1 + l$ and $J = K + s$, where l and s are the angular momentum and the spin of the excited electron. It has to be noted that Hund's rules only apply for finding the term symbol of the ground state. For an excited state the open orbital can be filled in any way. For example for an excited argon atom with configuration $[Ne]3p^5 4p$ we find that $L_1 = 1$ and $S_1 = +\frac{1}{2}$ and $J = \frac{3}{2}$ or $J = \frac{1}{2}$, while $n = 4$ and $l = 1$. It then follows that $K = \frac{5}{2}$ and either $J = 2$ or $J = 3$ depending on the spin of the excited electron. The term symbol is then either $({}^2P^\circ_{3/2})4p[K]_J$ or $({}^2P^\circ_{1/2})4p[K]_J$ where $K = \frac{1}{2}, \frac{3}{2}, \frac{5}{2}$ and $J = 0, 1, 2$ resulting in total 10 possible states. From this example it may be clear why the electronic configuration alone is not sufficient to denote an excited state. Apart from the Racah notation there is the Paschen notation which is simpler, but less informative. The notation for a given excited state is $n'l_k$ where $n' = n - N + l$ with N the highest value of n in the ground state, while k denotes the degenerate states of a particular configuration. To take again the example of excited argon $[Ne]3p^5 4p$: here $N = 3$ and $l = 1$ so $n' = 2$. So this electronic configuration would be referred to as the $2p$ levels. However, as we've seen there are 10 different possible states, meaning $k = 1, 2, ..., 10$ where the highest value of k has the lowest energy. For example $2p_{10}$ corresponds to $({}^2P^\circ_{1/2})4p[1/2]_1$

in Racah notation. Now we're familiar with the structure of atoms, excited states and the spectroscopic notations we can have a look at the energy diagrams of the elements studied in this thesis, argon and xenon, the latter being the most ubiquitous propellant for electric thrusters. The levels are denoted using the Paschen notation. Each level has a corresponding energy. An extensive list of all levels and corresponding energies of all elements can by found in the NIST atomic database [93].

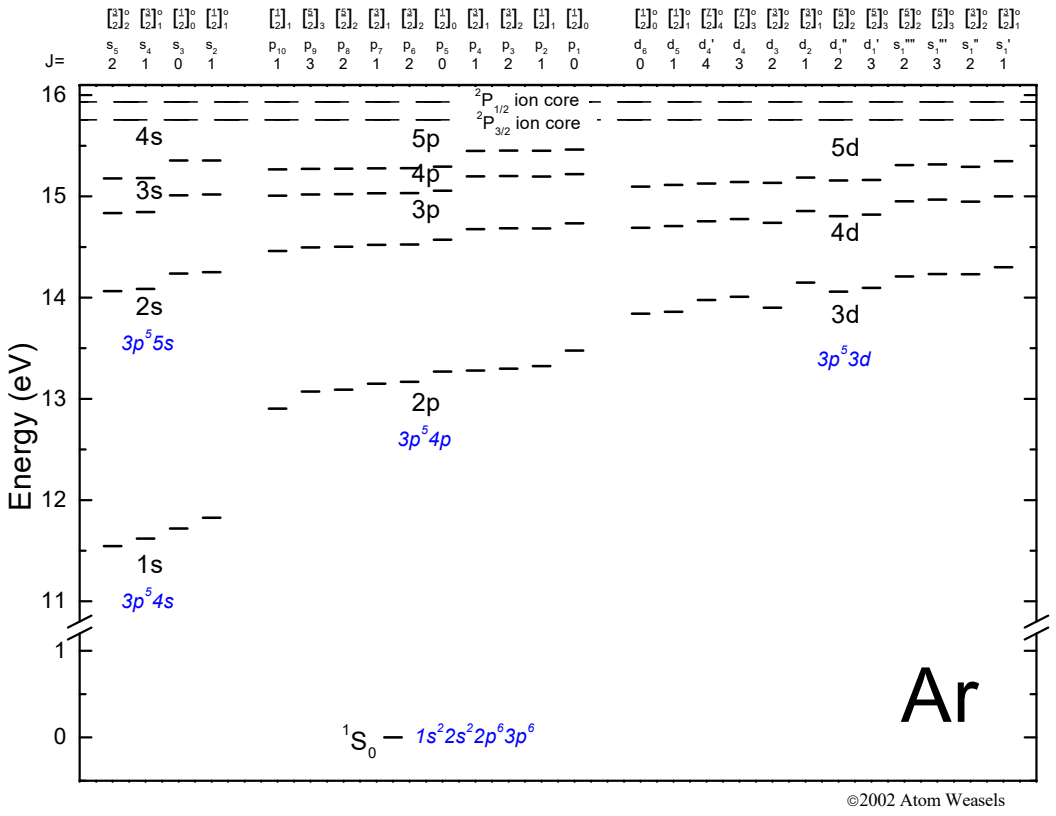

Figure 5.1: Energy level diagram of atomic Argon. [94]

5.2.2 Optical Emission

Emission due to an excited state i decaying to a lower state j is called spontaneous emission. The emission rate is proportional to $\partial N/\partial t = -A_{ij}N(t)$ where A_{ij} is the Einstein coefficient for spontaneous emission. This coefficient is a measure of the probability of emission and inversely proportional to the lifetime $A_{ij} = 1/\tau_{ij}$.

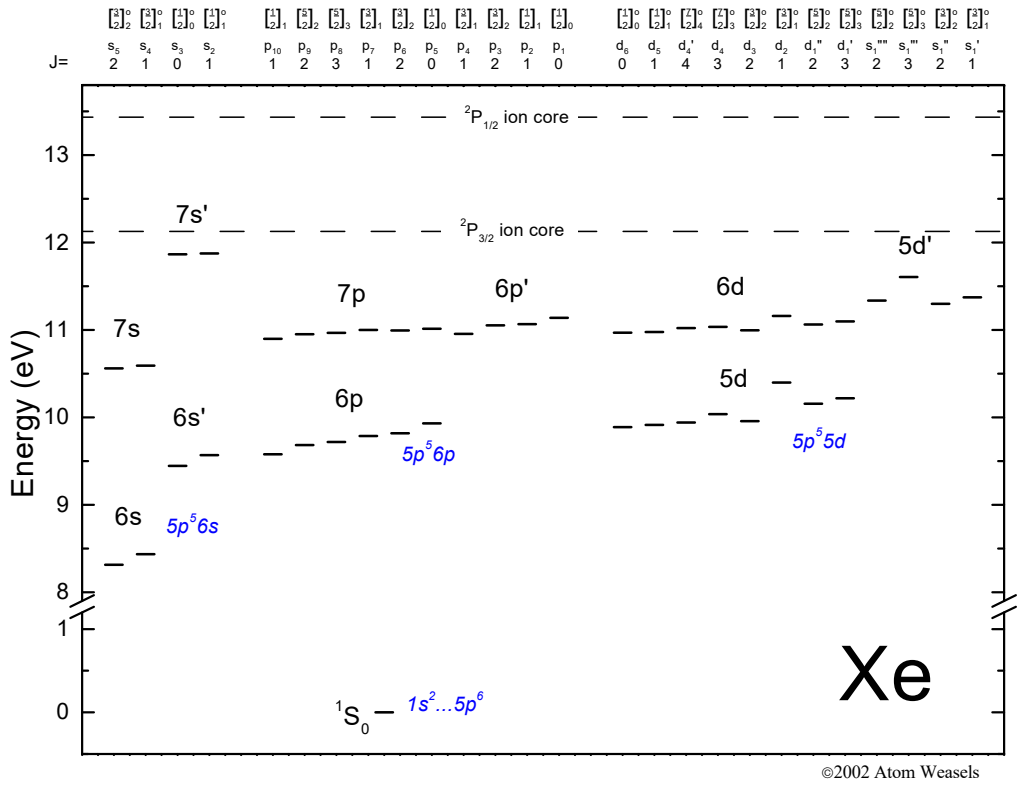

Figure 5.2: Energy level diagram of atomic Xenon. [94]

The Einstein coefficient is particular to a transition $i \rightarrow j$. As mentioned before, emission occurs due to conservation of energy and the energy difference of the initial and final states determines the wavelength.

$$\Delta E = \frac{hc}{\lambda} \tag{5.1}$$

Emission occurring at a particular wavelength is called an emission line, as it corresponds to a particular 'line' in the spectrum. Apart from energy, angular momentum must also be conserved. This leads to several selection rules. In general radiation can be classified as electric (Eq) or magnetic (Mq) multipoles of order 2^q. E1 is for example electric dipole radiation. The selection rules depend on the type of radiation and are as follows. The change in total angular momentum is constrained by $\Delta J = 0, \pm 1, ..., \pm q$. Furthermore $J : 0 \not\leftrightarrow 0$ for all types of radiation and additionally for $q = 1, 2$, $J : 0 \not\leftrightarrow 1, \frac{1}{2} \not\leftrightarrow \frac{1}{2}$ and for $q = 2$ also $J : 0 \not\leftrightarrow 2, \frac{1}{2} \not\leftrightarrow \frac{3}{2}$ and $J : 1 \not\leftrightarrow 1$. Parity is also preserved during a transitions: $\pi(Eq) = \pi_i \pi_j = (-1)^q$ and

$\pi(Mq) = (-1)^{q+1}$, meaning that the parity remains the same for E-even or M-odd multipoles and changes for E-odd and M-even. Dipole transitions overwhelmingly dominate all the radiation. Transitions that do not comply with the selection rules for $q = 1$ are called '(dipole) forbidden transitions'. These transitions can still occur through quadrupole or octupole radiation but this occurs at a much lower rate, often several orders of magnitude lowe. All emission lines both theoretically allowed as well as measured, including their Einstein coefficients are also tabulated in the NIST atomic database [93].

5.3 Plasma Spectroscopy

Spectroscopy is the study of the interaction between matter and electromagnetic radiation as a function of the wavelength or frequency of the radiation. Since the refraction of EM radiation is wavelength dependent, by using prisms or gratings incident radiation can be resolved into a spectrum of wavelengths. The resulting spectrum is a measure of the (relative) intensity per wavelength interval. In optical emission spectroscopy of (atomic) plasmas the emission spectra is studied to infer information about the state of the plasma, in particular the electron temperature and particle densities. The relationship between plasma parameters and the emission spectrum however, is not straightforward and more or less elaborate models are necessary to interpret the data.

The total radiation emitted by the plasma is the radiant flux Φ in units of Watts. Another important quantity is the radiance L defined as the radiant flux per unit project area per solid angle. The radiance from surface element dA at an angle θ from the normal is given by:

$$L_{e,\Omega} = \frac{d^2\Phi}{\cos\theta \mathrm{d}A \mathrm{d}\Omega} \tag{5.2}$$

Its units are $\mathrm{W} \cdot \mathrm{m}^{-2} \cdot \mathrm{sr}$. The local emission at a position $\mathbf{r}$ in the plasma is characterized by the local emission coefficient $\epsilon(\mathbf{r})$:

$$\epsilon(\mathbf{r}) = \frac{\mathrm{d}^2\Phi(\mathbf{r})}{\mathrm{d}V \mathrm{d}\Omega} \tag{5.3}$$

It is the radiant intensity from a volume dV per solid angle $d\Omega$, assuming isotropic radiation [62]. The units are $\mathrm{W} \cdot \mathrm{m}^{-3} \cdot \mathrm{sr}$. Spectral quantities are derivative quantities and are denoted with a subscript λ (ν or ω). They are related to the total

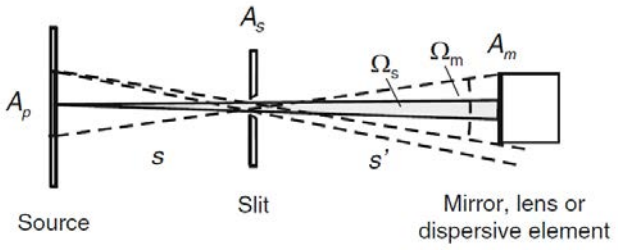

Figure 5.3: Measured radiation in the presence of an entrance slit. Figure from [62].

quantity as follows:

$$\epsilon(\mathbf{r}) = \int_0^\infty \epsilon_\lambda(\mathbf{r},\lambda)\,\mathrm{d}\lambda \qquad \text{or} \qquad \epsilon(\mathbf{r},\lambda_0,\Delta\lambda) = \int_{\lambda_0+\Delta\lambda/2}^{\lambda_0-\Delta\lambda/2} \epsilon_\lambda(\mathbf{r},\lambda)\,\mathrm{d}\lambda \qquad \text{or} \quad (5.4)$$

For a spectrometer the measured radiant flux is limited by the entrance slit and the detector [62]. As can be seen in figure 5.3 the area of the source surface A_p from which radiation is collected is determined by the area of the detector A_m.

$$\Phi = L_{e,\Omega} A_p \Omega_s = L_{e,\Omega} A_p \frac{A_s}{s^2} = L_{e,\Omega} \frac{A_m}{s'^2} = L_{e,\Omega} A_s \Omega_m \tag{5.5}$$

The product $A_s\Omega_d$ is called the throughput or etendúe and this is conserved. For this reason it is possible to calibrate the spectrometer with a source with a known radiance $\lambda_{0,\lambda}$ to obtain a signal S_0 at the spectrometer, which can then be used to obtain the spectral radiance $L_{x\lambda}(\lambda)$ of an unknown source from the measured signal S_x.

$$L_{x\lambda}(\lambda) = \frac{S_x}{S_0} L_{0\lambda}(\lambda) \tag{5.6}$$

In a plasma where the whole volume is emitting we can replace A_p with slice of plasma of thickness ds. For an optically thin plasma, i.e. without re-absorption of radiation, the flux is given by:

$$\Phi = \iiint \epsilon(s)\mathrm{d}A_p(s)\,\mathrm{d}s\mathrm{d}\Omega = \left(\int \epsilon(s)\,\mathrm{d}s\right) A_p\Omega_s = LA_s\Omega_m \tag{5.7}$$

So the (spectral) irradiance is a line integrated measurement of the local emission coefficient $\epsilon(\mathbf{r})$.

The second integral in equation 5.4 is of importance since emission at a wavelength λ_0 in reality always occurs over a small wavelength interval. This is a result of line broadening. Line broadening can occur through various mechanisms, mainly

natural broadening and Doppler broadening. Other broadening mechanisms exist such as pressure and Stark broadening but they are not relevant for plasmas common in electric propulsion devices.

5.3.1 Line Broadening

Natural broadening is always present and is due to Heisenberg's uncertainty principle; it places a limit on the accuracy with which two canonically conjugate variables can be known. The Heisenberg's uncertainty principle usually is invoked when talking about the position x and momentum p of a particle. However, energy E and time t are also conjugate variables. The uncertainty principle in this case reads:

$$\Delta_E \Delta_t \leq \hbar/2 \tag{5.8}$$

Since there is an uncertainty in the lifetime of a state, there is a corresponding finite, non-zero uncertainty in the energy and therefore in the wavelength. Please note that this is not an uncertainty in the measurement of the wavelength that can be improved by improving the measurement setup, but rather an inherent uncertainty in the actual value of the wavelength. The probability distribution of the wavelength due to natural broadening is given by a Lorentz distribution. [[62]]

$$\mathcal{L}_L(\lambda; \lambda_0, \gamma) = \frac{1}{\pi} \frac{\gamma/2}{(\lambda - \lambda_0)^2 + (\gamma/2)^2} \tag{5.9}$$

Where γ is the full-width at half-maximum (FWHM), with τ_i, τ_j the lifetimes of states i, j.

$$\gamma = \frac{\lambda_0^2}{2\pi c} \left(\frac{1}{\tau_i} + \frac{1}{\tau_j} \right) \tag{5.10}$$

Doppler broadening occurs due to the random thermal motion of the atoms. The velocity of the thermal motion produces a Doppler shift in the wavelength.

$$\frac{\lambda - \lambda_0}{\lambda_0} = \frac{v}{c} \tag{5.11}$$

For a given temperature the velocity of particles in a given direction, e.g. along the line of sight of the measurement is normally distributed.

$$f(v_x) = \sqrt{\frac{m}{2\pi k_B T}} \exp\left(-\frac{m v_x^2}{2 k_B T} \right) \tag{5.12}$$

By subsituting (5.11) into (5.12) we find the Gaussian line profile $G(\lambda; \lambda_0, \sigma)$.

$$\mathcal{L}_G(\lambda; \lambda_0, \sigma) = f(v)\frac{dv}{d\lambda} = \sqrt{\frac{mc^2}{2\pi k_B T}} \exp\left(-\frac{mc^2}{2k_B T}\frac{(\lambda - \lambda_0)^2}{\lambda_0^2}\right) \tag{5.13}$$

Which is another Gaussian distribution with standard deviation σ and FWHM $2\sqrt{2\ln 2}\sigma_G$.

$$\sigma_G = \sqrt{\frac{k_B T}{mc^2}}\lambda_0 \tag{5.14}$$

Usually both mechanisms are present and the resulting line shape is a Voigt profile.

$$\mathcal{L}_V(\lambda; \lambda_0, \sigma, \gamma) = \int_{-\infty}^{\infty} \mathcal{L}_G(\lambda' - \lambda_0)\mathcal{L}_L(\lambda - \lambda')d\lambda' = \frac{1}{\sigma\sqrt{2\pi}}V(x, a) \tag{5.15}$$

Where $V(x, a)$ is the Voigt function:

$$V(x, a) = \frac{a}{\pi}\int_{-\infty}^{\infty} \frac{e^{-t^2}}{a^2 + (x - t)^2}dt \tag{5.16}$$

With:

$$x = \frac{\lambda - \lambda_0}{\sqrt{2}\sigma_G}, \qquad a = \frac{\gamma}{2\sqrt{2}\sigma_G} \tag{5.17}$$

Line broadening is relevant for optical emission spectroscopy because it implies that the emission due to a given transmission is spread out over a part of the spectrum. In practice it is therefore not sufficient to obtain the intensity at a given wavelength but rather one has to integrate the area under the line shape function as we will see shortly. It also implies difficulties in processing emission lines of which the line shape functions overlap.

5.4 Collisional-Radiative Models

In an optically thin plasma the total emitted power [W$\cdot$ m$^{-3}\cdot$ sr^{-1}] for a given transition $i \to j$ is given by:

$$I_{ij}(\mathbf{r}) = \frac{hc}{4\pi\lambda_{ij}}A_{ij}n_i(\mathbf{r}) \tag{5.18}$$

The wavelength λ_{ij} and the Einstein coefficient A_{ij} are constants particular to the transition $i \to j$. The emission is then linearly dependent on the population

density of state i. Note that this is the local density at a position $\mathbf{r}$ in the plasma. To obtain any physical quantity of interest from an emission spectrum a model is needed to relate the quantity of interest to the population density of the excited states. Such a model is called a collisional-radiative model.

The population and depopulation of excited states are effectuated by a great variety of collisional and radiative processes and for a given equilibrium result in a distribution population densities. Which processes are relevant depends on the local plasma conditions. Collisional processes can be due to impact by an electron or by an ion, respectively referred to as an electron-impact or an ion-impact collision. Collisional processes can be further divided into excitation, de-excitation and ionization. Radiative processes can be broken down into spontaneous emission and (re-)absorption. An extensive list of processes follows below. The asterisks denote an excited state.

i. electron-impact excitation and de-excitation

$$e^- + \mathrm{Xe} \leftrightarrow \mathrm{Xe}^* + e^- \tag{5.19}$$

$$e^- + \mathrm{Xe}^* \leftrightarrow \mathrm{Xe}^{**} + e^- \tag{5.20}$$

$$e^- + \mathrm{Xe}^+ \leftrightarrow \mathrm{Xe}^{+*} + e^- \tag{5.21}$$

$$e^- + \mathrm{Xe}^{+*} \leftrightarrow \mathrm{Xe}^{+**} + e^- \tag{5.22}$$

ii. ion-impact excitation

$$\mathrm{Xe}^+ + \mathrm{Xe} \rightarrow \mathrm{Xe}^{+*} + \mathrm{Xe}^* \tag{5.23}$$

$$\mathrm{Xe}^{2+} + \mathrm{Xe} \rightarrow \mathrm{Xe}^{2+*} + \mathrm{Xe}^* \tag{5.24}$$

iii. electron-impact ionization

$$e^- + \mathrm{Xe} \rightarrow \mathrm{Xe}^{+*} + 2e^- \tag{5.25}$$

$$e^- + \mathrm{Xe}^* \rightarrow \mathrm{Xe}^{2+*} + 2e^- \tag{5.26}$$

$$e^- + \mathrm{Xe}^+ \rightarrow \mathrm{Xe}^{2+*} + 2e^- \tag{5.27}$$

iv. ion-impact ionization

$$\mathrm{Xe}^+ + \mathrm{Xe} \rightarrow \mathrm{Xe}^{+*} + \mathrm{Xe}^{+*} + e^- \tag{5.28}$$

$$\mathrm{Xe}^{2+} + \mathrm{Xe} \rightarrow \mathrm{Xe}^{2+*} + \mathrm{Xe}^{+*} + e^- \tag{5.29}$$

v. spontaneous emission and self-absorption

$$\mathrm{Xe} \leftrightarrow \mathrm{Xe}^{*} + h\nu \tag{5.30}$$

$$\mathrm{Xe}^{*} \leftrightarrow \mathrm{Xe}^{**} + h\nu \tag{5.31}$$

$$\mathrm{Xe}^{+} \leftrightarrow \mathrm{Xe}^{+*} + h\nu \tag{5.32}$$

$$\mathrm{Xe}^{+*} \leftrightarrow \mathrm{Xe}^{+**} + h\nu \tag{5.33}$$

$$\tag{5.34}$$

A full CR-model results in a coupled system of equations that have to be solved simultaneously; it also requires a great many excitation cross sections some of which are not readily available. Multiple Xenon CR-models for the application of electric propulsion and Hall-thrusters in particular have been developed over the last two decade, mainly differing in the theoretical excitation cross sections used. Zhu et al. [157] use cross sections from [141] obtained with the Dirac B-spline R-matrix (BSR) method, Priti et al. [43] use fine-structure resolved cross sections obtained with the relativistic distorted wave (RDW) method, Yang et al. [146] uses the cross sections developed by the Los Alamos National Laboratory (LANL) (but for which no reference could be found) and Chaplin et al. [26][61] use the same cross sections as Zhu et al. However, simpler CR-models are possible, such as those of Karabadzhak et al. [58] who focuses on near-infrared (NIR) emission of Xenon I and uses experimentally obtained optical cross sections from Chiu et al. [32]. This work was continued by Dressler et al. [37] in 2009, who included a proper treatment of excitation from the meta-stable levels.

5.4.1 Excitation Cross sections

The concept of collision cross sections comes from the treatment of hard-sphere collisions. To calculate the collision frequency ν of a sphere of radius r traveling with a velocity v through a medium with density n, note that the sphere traces a tube with a cross section $\sigma = \pi(2r)^2$ and it follows that $\nu = \sigma n v$. The collision frequency of a population particles with density n_1 colliding with a population of particles of density n_2 is just $\nu = \sigma n_1 n_2 v$ where now $\sigma = \pi(r_1 + r_2)^2$ and v is the relative velocity.

However, collisions of atomic and sub-atomic particles the collision cross section is no longer constant but rather a function of the velocity $\sigma(v)$. For collisions of

electrons with atoms, the former is generally much faster and the the latter can be regarded stationary with respect to the former. The relative velocity is then approximately equal to the velocity of the electrons. However, a population of electrons does not have a mono-disperse velocity but rather follow a distribution, most often a Maxwell-Boltzmann distribution.

$$f(v) = \left(\frac{m}{2\pi k_B T}\right)^{3/2} \exp\left(-\frac{mv^2}{2k_B T}\right) \tag{5.35}$$

$$f(\mathcal{E}) = 2\sqrt{\frac{\mathcal{E}}{\pi}}\left(\frac{1}{k_B T}\right)^{3/2} \exp\left(-\frac{\mathcal{E}}{k_B T}\right) \tag{5.36}$$

Instead of a single cross section one can speak of a velocity averaged cross section $\langle\sigma(v)v\rangle$. Generally it is easier to work in terms of energy, and the most useful quantity to work with is the excitation rate coefficient k (in $m^6 \cdot s^{-1}$) such that $\nu = n_n n_e k$. The equation for the rate coefficient of an electron impact collision with cross section $\sigma(E_e)$ (and assuming a Maxwellian distribution) is then:

$$k(T_e) = \sqrt{\frac{2}{\pi m_e (k_B T_e)^3}} \int_0^\infty 2E_e \exp\left(-\frac{\mathcal{E}_e}{k_B T_e}\right)\sigma(\mathcal{E}_e) d\mathcal{E}_e \tag{5.37}$$

In the literature four main types of electron excitation cross sections can be found [15]: apparent cross sections, optical emission cross sections, direct cross sections and cascade cross sections. Consider an atom initially in level j that gets excited into level i and then decays to level k. The optical emission cross section is directly related to the photon flux emerging from the radiative transition $i \rightarrow j$. The apparent cross section is the sum of all optical emission cross sections over a all decay channels of level i i.e. not just to k but also to other levels k'. It is thus related to the *apparent* rate at which level i is populated. The direct cross section is the cross section for the transition $j \rightarrow i$. The difference with the apparent cross section is that the latter also includes the contribution of excitation of level i into higher levels $n > i$ that then decay to level i, also referred to as cascades. The cascade cross section is then the difference between the apparent and the direct cross section. The relationship between all cross sections can be described as follows [14]:

$$\sigma_i^{dir} = \sigma_i^{app} - \sigma_i^{casc} = \sum_{j<i} \sigma_{ij}^{opt} - \sum_{k>i} \sigma_{ki}^{opt} \tag{5.38}$$

The relationship between the apparent and optical emission cross sections is given by:

$$\sigma^{opt} = \Gamma_{ij} \sigma_i^{app} \tag{5.39}$$

Where Γ_{ij} is the branching ratio, the ratio of the Einstein coefficient of transition $i \rightarrow j$ to the sum of all Einstein coefficients out of the level i

$$\Gamma_{ij} = \frac{A_{ij}}{\sum_{l<i} A_{il}} \tag{5.40}$$

When using cross sections from the literature it is important to note which type of cross sections are being reported. Chiu et al. for example have measured optical cross sections, while Wang et al. [141] have calculated direct cross sections and in [57] and [56] apparent cross sections are reported. Different cross sections can be combined if the proper relationships between them are taken into account, e.g. by scaling with the branching ratio.

Apart from electron impact excitation, ion impact excitation also can play a role. Generally in electric propulsion devices ions can be considered mono-energetic, which simplifies the calculation of the rate coefficient since now $f(\mathcal{E}_i) = 1$. The ion energy however should be known for this to work. In Hall-effect thrusters for example it is generally the electrostatic energy due to the anode voltage V. Note that the energy is different for different charge states $z = +1, +2, ...$

$$k_z(V) = \sigma_z(zeV)\sqrt{\frac{2zeV}{m_i}} \tag{5.41}$$

5.4.2 Xenon Excited States and NIR emission lines

Quite a few different excited states are considered and mentioned throughout this thesis, although a schematic overview can be found in Figure 5.2 we will list all relevant states in both Racah and Paschen notation in Table 5.1. Please note that we used the short form of the Racah notation. For example $6p[\frac{5}{2}]_3$ in full would be $5p^5(^2P^\circ_{3/2})6p$ with term $^2[\frac{5}{2}]$ and $J = 3$. Note that the prime in for example $6s'[\frac{3}{2}]_1$ denotes that the parent ion is $(^2P^\circ_{1/2})$ while al states without the prime have parent ion $(^2P^\circ_{3/2})$.

There are 11 NIR emission lines originating from the Xe I $2p$ levels that are considered in this work. All emission lines emanating from the $2p$ levels are summarized in Table 5.2 specifying also the upper and lower level of the corresponding transition and the Einstein coefficient, the NIR lines used in this work are in bold.

Table 5.1: Energy levels of Xe I in Racah and Paschen notation.

Racah	Paschen	E (eV)	Racah	Paschen	E (eV)
$5p^6$	$1s_0$	0.000	$7p[\frac{1}{2}]_1$	$3p_{10}$	10.902
$6s[\frac{3}{2}]_2$	$1s_5$	8.315	$7p[\frac{5}{2}]_2$	$3p_9$	10.954
$6s[\frac{3}{2}]_1$	$1s_4$	8.437	$7p[\frac{5}{2}]_3$	$3p_8$	10.969
$6s'[\frac{1}{2}]_0$	$1s_3$	9.447	$7p[\frac{3}{2}]_1$	$3p_7$	11.003
$6s'[\frac{1}{2}]_1$	$1s_2$	9.570	$7p[\frac{3}{2}]_2$	$3p_6$	10.996
			$7p[\frac{1}{2}]_0$	$3p_5$	11.015
$6p[\frac{1}{2}]_1$	$2p_{10}$	9.580	$5d[\frac{1}{2}]_0$	$3d_{12}$	9.890
$6p[\frac{5}{2}]_2$	$2p_9$	9.686	$5d[\frac{1}{2}]_1$	$3d_{11}$	9.917
$6p[\frac{5}{2}]_3$	$2p_8$	9.721	$5d[\frac{7}{2}]_4$	$3d_{10}$	9.943
$6p[\frac{3}{2}]_1$	$2p_7$	9.789	$5d[\frac{7}{2}]_3$	$3d_9$	10.039
$6p[\frac{3}{2}]_2$	$2p_6$	9.821	$5d[\frac{3}{2}]_2$	$3d_8$	9.959
$6p[\frac{1}{2}]_0$	$2p_5$	9.933	$5d[\frac{3}{2}]_1$	$3d_7$	10.401
$6p'[\frac{3}{2}]_1$	$2p_4$	10.958	$5d[\frac{5}{2}]_2$	$3d_6$	10.158
$6p'[\frac{3}{2}]_2$	$2p_3$	11.055	$5d[\frac{5}{2}]_3$	$3d_5$	10.220
$6p'[\frac{1}{2}]_1$	$2p_2$	11.069	$5d'[\frac{5}{2}]_2$	$3d_4$	11.301
$6p'[\frac{1}{2}]_0$	$2p_1$	11.141	$5d'[\frac{5}{2}]_3$	$3d_3$	11.375
			$5d'[\frac{3}{2}]_2$	$3d_2$	11.338
			$5d'[\frac{3}{2}]_1$	$3d_1$	11.607

5.5 Karabadzhak-Chiu-Dressler Model

The collisional radiative model by Karabadzhak et al. [58] referenced earlier is relatively simple and easier to use than the more extensive CR-models of [157][146][61][43]. Furthermore it relies mainly on optical emission cross sections which are more accurate than the theoretically obtained direct cross sections. Using optical emission cross sections also greatly reduces the number of equations to be considered. A drawback of this particular model is that it only considers Xe I emission lines in the NIR region, although this is sufficient to obtain the electron temperature. Dressler et al. [37] expanded on the KCD model by more accurately accounting for excitation from the metastable states which has a significant contri-

bution due to the lower threshold energy. In their work they found that the most accurate model was obtained by using a combination of cross sections obtained by BSR and RDW methods, supplemented by experimentally obtained cross sections [56][57] when available. Because of its simplicity this model was selected to interpret optical emission spectra obtained from the Helicon Plasma thruster. In this section we outline the model.

5.5.1 Model Assumptions

Any model always rests on certain assumptions. The model validity rest in part on the validity of the assumptions. The KCD model is a simplified CR-model that is also referred to as a Corona model. The main assumption here is that population happens *solely* by collisions and depopulation happens by radiation *only*, which is the case as long as the spontaneous emission probability is much larger than the collisional quenching frequency: $\sum_j A_{ij} \gg \nu_i^{dex}$. The de-excitation rates can be obtained from the excitation rates using the principle of detailed balance [62, p. 117]. For de-excitation from a higher level i to a lower level j

$$k_{ij}^{dex}(T_e) = k_{ji}^{ex}(T_e)\frac{g(j)}{g(i)}\exp\left(\frac{E_i - E_j}{k_B T_e}\right) \tag{5.42}$$

However the dominant depopulation collisions for the $5p^5 6p$ levels would be to the more nearby $5p^5 7s$ and $5p^5 5d$ levels; since the energy difference is smaller the rate coefficients are larger. Although detailed cross sections are not available (neither for population or depopulation) Karabadzhak [58] estimates them to be of the order of $10^{-19} - 10^{-18}$ m^2 using a generalized Born approximation. Assuming a σ independent of the energy and of the order aforementioned, we can estimate ν_i^{dex} using (5.37) which for an electron density $n_e < 10^{18}$ m^{-3} and an electron temperature $T_e < 20$ eV results in: $A_i \gg 3{\cdot}10^6$ s. Note that these plasma conditions (n_e, T_e) are quite extreme and in most cases will be below these values [90]. In any case, all $2p$ levels have at least one emission line with a probability of one order of magnitude higher, meaning the assumption is valid even in the most extreme case.

Dressler makes two additional assumptions regarding the metastable balance equation [37]: (1) that the diffusion loss of the metastables can be neglected and (2) that the $1s_5$ level is the only level to affect the spectrum. Assumption (1) is justified by Karabadazhak et al. [58] by assuming that the diffusion frequency of the

metastables is negligible compared to the collision loss frequency, i.e. $\nu_{dm} \ll \nu_{cm}$. To estimate ν_{dm} Karabadzhak et al. use $\nu_{dm} = v_m/R$ where v_m is the thermal velocity of the metastables and R the radius of the plasma. On the other hand ν_{cm} is estimated from cross-sections of Jung et al. [56] and the Born approximation. Although the values are not made explicit it is stated that for both the conditions in the discharge (>3 eV, $>10^{17}$ m^{-3}) and the plume (>1.8 eV, $>10^{16}$ m^{-3}) the condition holds. Dressler et al. merely refers to Karabadzhak et al. for justification of this assumption. We repeat this exercise here for conditions expected in the HPT. The collisional loss frequency we obtain from the sum of all collisional loss channels of the $1s_5$ level, i.e. everything inside the parentheses on the RHS of Equation 5.46 multiplied by the electron density $n_e = 10^{17} - 10^{18}$ m^{-3} [90]. The rate coefficient of the sum of all loss channels is $2 - 7 \cdot 10^{-13}$ $m^3 \cdot s^{-1}$. Therefore we estimate that $10^4 < \nu_{cm} < 10^6$ s^{-1}. Estimating the diffusion loss frequency is slightly trickier. Karabadzhak's approximation of ν_{dm} is valid for low neutral densities (10^{18} m^{-3}, [19]), typical in Hall-effect thrusters, however the diffusion loss frequency in a cylindrical discharge is more accurately represented by [157][68, p.134,314]:

$$\nu_{dm}^{-1} = \left[D_m \left(\frac{\chi_0}{R} \right)^2 \right]^{-1} + \left[\frac{u_m}{R} \right]^{-1} \tag{5.43}$$

The first term on the RHS is the diffusion loss time and the second term is the wall loss time. For the velocity of the metastables we take the thermal velocity assuming a temperature of 600K which results in a velocity of about 300 $m \cdot s^{-1}$. The plasma radius near the exit of the HPT is about 15 mm. The wall loss rate is about $2 \cdot 10^4$ s^{-1}. In the second term we have the diffusion coefficient D_m and $\chi_0 = 2.405$ the first zero of the zeroth order Bessel function. The diffusion constant can be obtained from Smirnov [117, p.113] which for Xe($^3P_2$) is $D_0 = 2.4 \cdot 10^{-6}$ $m^2 \cdot s^{-1}$. However this value is valid for the standard normal density $n_0 = 2.687 \cdot 10^{25}$ m^{-3} and room temperature, 300K and therefore needs to be scaled according to:

$$D(n, T) = D_0 \left(\frac{n_0}{n} \right) \left(\frac{T}{300\text{K}} \right)^{1.5} \tag{5.44}$$

We estimate a neutral density near the exit of about 10^{21} m^{-3} (10 Pa at 600K) and a temperature of 600K which yields $D_m = 0.152$ $m^2 \cdot s^{-1}$. With this value the first term on the RHS is about $4 \cdot 10^3$ s^{-1}. The total diffusion loss rate is then about $3 \cdot 10^3$ s^{-1}. Even is the neutral density is an order of magnitude lower the diffusion loss rate

is at most 10^4 s^{-1}. The conclusion that $\nu_{dm} \ll \nu_{cm}$ cannot be made unequivocally as it depends on the plasma conditions. If the electron density near the exit plane of the thruster indeed is 10^{18} m^{-3} then the condition holds, however if it is closer to 10^{17} m^{-3} whether the condition is met then depends on the neutral density.

Assumption (2) is justified by Dressler et al. on the basis that the other metastable level $1s_3$ is populated by optically weak transitions from the $2p_2$ and $2p_4$ levels. The optical emission cross sections from the ground state to $2p_2, 2p_4$ and subsequent decay to the $1s_3$ level are about an order of magnitude smaller than those populating the $1s_5$ level [41]. The population density of the $1s_3$ level can therefore be assumed to be an order of magnitude smaller than that of the $1s_5$ level and thus neglected. The results from Zhu et al.in particular Figure 12 of [157] confirm this.

5.5.2 Model Equations

The excitation rate in W$\cdot$ m$^{-3}\cdot$ sr^{-1} for an emission line with wavelength λ can be given by [58]:

$$J_\lambda(\mathrm{XeI}) = \frac{hc}{4\pi\lambda} n_n n_e \left(k_{e0}^\lambda + \frac{n_m}{n_n} k_{em}^\lambda + \alpha k_1^\lambda + \frac{1-\alpha}{2} k_2^\lambda \right) \tag{5.45}$$

Here h is Planck's constant, c the speed of light and n_n, n_e, n_m are the ground state, electron and metastable densities. Furthermore k_{e0}^λ is the rate coefficient for the optical emission due to electron impact of the ground state and k_{em}^λ for impact from the metastable states. Lastly k_1^λ,k_2^λ are rate coefficients of ion impact excitation and $\alpha = n_1/n_e$ is the ratio of singly ionized ions to the total density of ions; note that $n_e = n_1 + 2n_2$ because of quasi-neutrality. Such a simple model is principally possible because of the Corona model assumptions and the use of optical emission cross sections.

The difficulty of this model lies mostly in determining the metastable density which is not a priori known. Of course one could measure this using tunable laser absorption spectrometry (TDLAS) but this would defy the simplicity of using optical emission spectroscopy. Due to a lack of cross sections from the metastable levels Karabadzhak made some approximations, mainly by assuming that the metastable levels were predominantly populated by cascades from the $6p$ levels as well as by assuming that the rate coefficients were $k_{em} \propto (2J+1)\Gamma^\lambda$ with J the total quantum

number and Γ^{λ} the branching ratio for the line λ. However due to the availability of new cross sections Dressler [37] used a more accurate balance equation to obtain the metastable fraction. The metastable state is mainly populated through two channels: direct excitation from the ground state and cascades from the $2p$ levels which were themselves excited from the ground state (sum over i in Equation 5.46). The loss channels on the other hand are: excitation to the $2p$ levels followed by radiative decay to levels coupled to the ground state (sum over j), excitation to higher levels that have negligible re-population rates to the $1s_5$ level (sum over k), and ionization. The balance equation reads [37]:

$$n_n n_e \left(k_{0m} + \sum_i \left\{ k_{e0}^i + \alpha k_1^i + \frac{1-\alpha}{2} k_2^i \right\} \right) = n_m n_e \left(\sum_j \Gamma_j k_{2pm}^j + \sum_k k_{dm}^k + k_{ion} \right) \tag{5.46}$$

In [37] Dressler et al. define Γ_j as the branching ratio of emission to the $1s_4$ level only, most likely because in the preceding work of Karabadhzak et al. [58] they only considered the transitions to the $2p_{10} - 2p_6$ levels which decay to either the $1s_5$ or the $1s_4$ level. However since we are including all the $2p$ levels we define $\Gamma_j = 1 - \Gamma_{1s_5}$ where Γ_{1s_5} is the branching ratio of the transition $2p_j \rightarrow 1s_5$ [16, eq. 28]. Karabadzhak et al. and presumably Dressler et al. used the emission cross section from Fons and Lin [41] to derive the branching ratios. We instead have used the Einstein coefficients found in the NIST atomic spectra database [93] to calculate the branching ratios according to Equation 5.40 which yields the following table:

This equation can then be solved for n_m/n_n:

$$\frac{n_m}{n_n} = \left(k_{0m} + \sum_i \left\{ k_{e0}^i + \alpha k_1^i + \frac{1-\alpha}{2} k_2^i \right\} \right) \times \left(\sum_j \Gamma_j k_{2pm}^j + \sum_k k_{dm}^k + k_{ion} \right)^{-1} \tag{5.47}$$

5.6 Cross Section Set

The success of a CR model rests in large part on the accuracy of the cross-sections used. Generally experimentally cross sections are more practical for diagnostic applications since the apparent and optical cross sections already include all the cascade contributions[14]. To manually account for these using direct cross sections one would have to include the cross sections to a given level as well as all the cross sections to higher levels that decay into it as well as the corresponding branching

ratios. Theoretical calculations generally produce direct cross sections only, while experimental techniques can produce apparent, optical emission and in some cases even direct cross sections.

The KCD model relies primarily on a set of optical emission cross sections for electron impact excitation of NIR and VIS lines of primarily Xe(I) as well as some Xe(II) lines, obtained from an accompanying paper[32]. Cross sections were obtained from beam luminescence measurements using electron beams of energies up to 70 eV Optical emission cross sections for ion impact excitation by Xe^+, Xe^{2+} (at 300 eV) of the same lines were also measured. Karabhadzak[58] extended these cross sections with the results from Fons and Lin [41] for E >70 eV to be able to handle electron temperatures over 20 eV. For this thesis we received cross sections used in [37] directly from Dr. Dressler. These cross sections were zero-pressure adjusted and included the extension up to 150 eV as well as data for three additional NIR lines (841.0 nm, 895.0 nm, 992.3 nm) not reported in either [32][58][37].

Although Chiu[32] presents ion impact cross sections for 300 eV, Sommerville et al. [118] have measured cross sections with 100< E <900 eV for Xe^+ and 200< E <1800 for Xe^{2+} impact excitation for the same lines as reported as in [32] plus the 3 additional NIR lines mentioned before. The cross sections used in the calculation of the metastable fraction[37] are a more complicated mix. Dressler et al. uses theoretical cross-sections obtained with BSR calculations from Allan et al.[6] for energies up to 72 eV and extends these with results from RDW calculations by Srivastava et al.[119] and Sharma et al.[111]. For the $1s_5 \rightarrow 2p$ transitions he replaces the BSR cross sections with experimental cross sections from Jung et al.[56]. The 'higher' levels (the sum over k in 5.46) considered by Dressler are the other $1s$, $3p$ and $3d$ levels. For ionization of the metastable level he uses the cross sections of Ton-That and Flannery[134].

For this thesis we largely used the same cross-sections although we use more recent BSR calculations[149] from the same research group as [6], which can also be found on the LXCat database[102]. The RDW calculations of both [119] and [111] are available in a newer paper by Priti et al.[43] in parameterized form. Lastly, we also replace BSR cross sections by experimental cross sections from Jung et al.[57] for the $1s_5 \rightarrow 3p$ transitions.

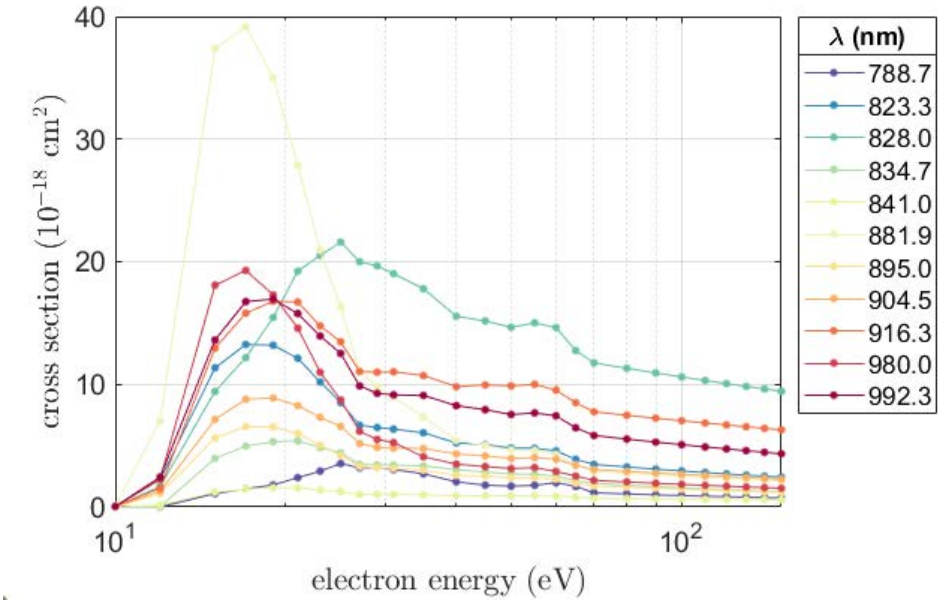

Figure 5.4: Optical emission cross section (in 10^{-18} cm^2) for NIR emission lines due to electron impact excitation of the Xe(I) $2p$ levels, corresponding to data in Table C.1. All curves of the same color originate from the same upper level.

5.6.1 Emission Cross Sections for Xe(I) NIR Lines

The emission cross sections for NIR emission from the $2p$ levels of Xe(I) where obtained were provided to us by Dr. Dressler and are pressure scaled emission cross sections from [32] extended with RDW calculations from [41] and include data for three additional lines not reported before. The data can be found in table C.1 below and is visualized in figure 5.4. Optical emission cross-sections for the same lines due to ion impact excitation are obtained from [118] and are tabulated in Table Table C.2 and Table C.3.

5.6.2 B-Spline R-Matrix Direct Cross Sections

Direct cross-sections obtained using a B-Spline R-matrix calculations, obtained from the work of Zatsarinny and Bartschat [149] were used when not experimental cross-sections were available. Cross-section data was obtained directly from Dr. Zatsarinny (although some cross-sections are available on LXCat [102]) for the following transitions $1s_0 \rightarrow 1s_5$; $1s_5 \rightarrow 1s_i, i = 2, 3, 4$; $1s_5 \rightarrow 2p$; $1s_5 \rightarrow 3p$ and $1s5 \rightarrow 3d$.

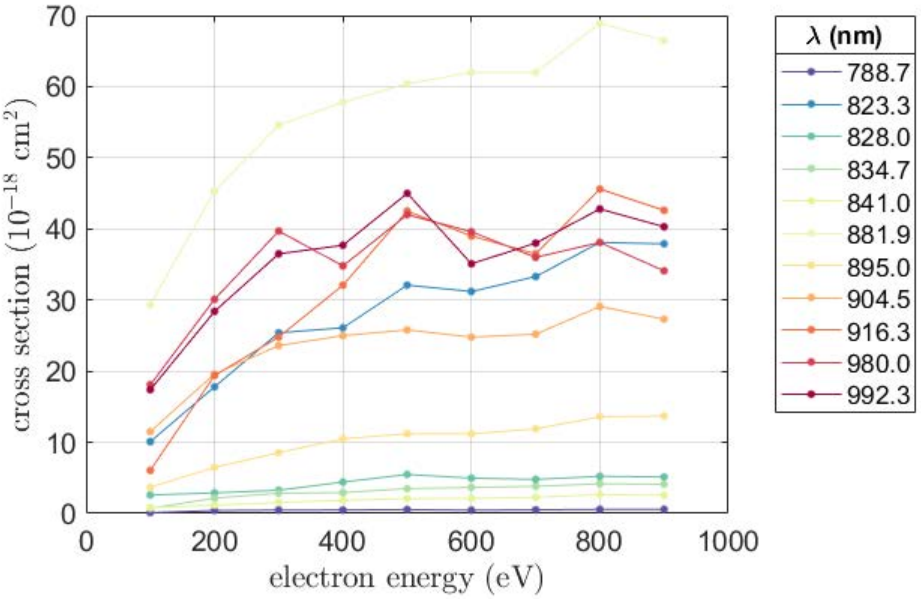

Figure 5.5: Optical emission cross section (in 10^{-18} cm^2) for NIR emission lines due to ion impact excitation by Xe^+ of the Xe(I) $2p$ levels, corresponding to data in Table C.1 in section C.2.

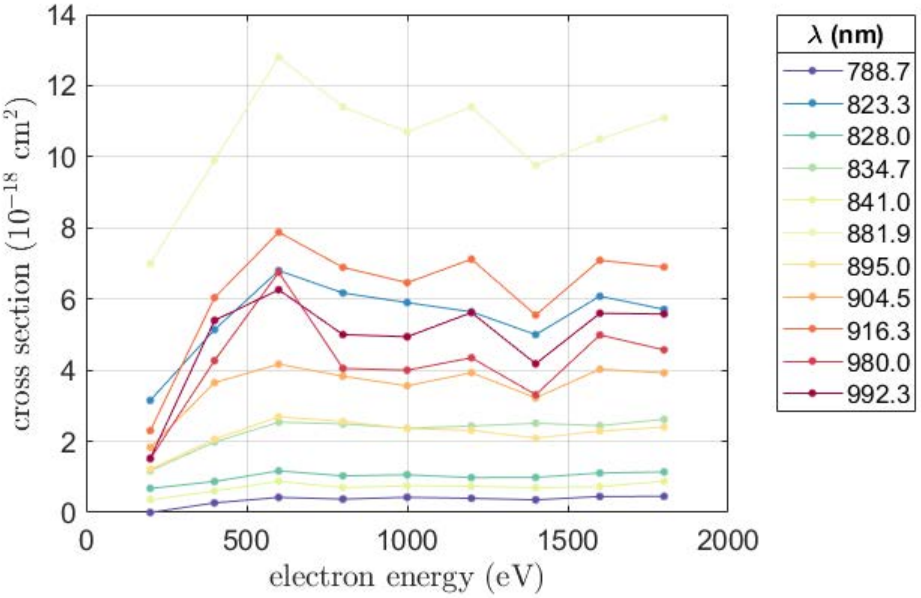

Figure 5.6: Optical emission cross section (in 10^{-18} cm^2) for NIR emission lines due to ion impact excitation by Xe^{+2} of the Xe(I) $2p$ levels , corresponding to data in Table C.1 in section C.2.

The BSR cross-section comes in the following format: two columns, electron energy E in electron-Volt and cross section $\sigma(E)$ as a multiple of the Bohr radius a_0 squared ($a_0^2 = 0.28 \cdot 10^-16$ cm^2). The electron energy is always given with respect to the ground state, for cross-sections from the $1s_5$ level therefore its energy (8.315 eV) is subtracted. The column with the cross section values is multiplied with a_0^2. All cross sections are tabulated in Table C.1 to C.16 in appendix C.2. Plots of the cross sections can be found below.

5.6.3 Relativistic Distorted Wave Cross Sections

Similar to Dressler et al. we've used RDW values to extend the BSR cross-sections to higher energies. However as mentioned before we used a more recent work from the same author. Srivastava et al. [43],[44] present their calculated cross sections in the form of two fitting formulas and and a table of fitting coefficient which we have reproduced below. The formulas are:

$$\sigma(\mathcal{E}) = b_0 \mathcal{E}^{b_1} a_0^2 \tag{5.48}$$

$$\sigma(\mathcal{E}) = \frac{\sum_{n=0}^{N} b_n \mathcal{E}^n}{c_0 + c_1 \mathcal{E} + c_2 \mathcal{E}^2} a_0^2 \tag{5.49}$$

Where a_0 again is the Bohr radius and $\mathcal{E}$ is scaled by two times the Rydberg energy (2 Ry = 27.211 eV). Practically all fits use equation 5.49 except for some range of the transition $1s_0 \rightarrow 2p_4$ and $1s_0 \rightarrow 2p_7$ as marked with a † in Table C.4 in section C.2. However we found that there were errors in several of the fitting constants and were not able to reproduce the cross-sections as shown in the corresponding articles [43][44]. Instead the original RDW cross-sections were provided to us by the authors and are plotted below.

5.6.4 Experimental Apparent Cross Sections

Experimental cross sections of electron impact excitation of Xenon, both from the ground state and from the metastable states to the $2p$ and $3p$ manifolds have been measured by the Atomic Collisions group of Prof. Lin at the university of Wisconsin, including work mainly carried out by Jung et al. [41][56][57]. All measurement data can be found at the website of the research group [94]. The data for transitions from the $1s_5$ level to the $2p$ and $3p$ manifolds, can be found in tabled form in Table C.14 and Table C.15 in section C.2 and in graphical form below.

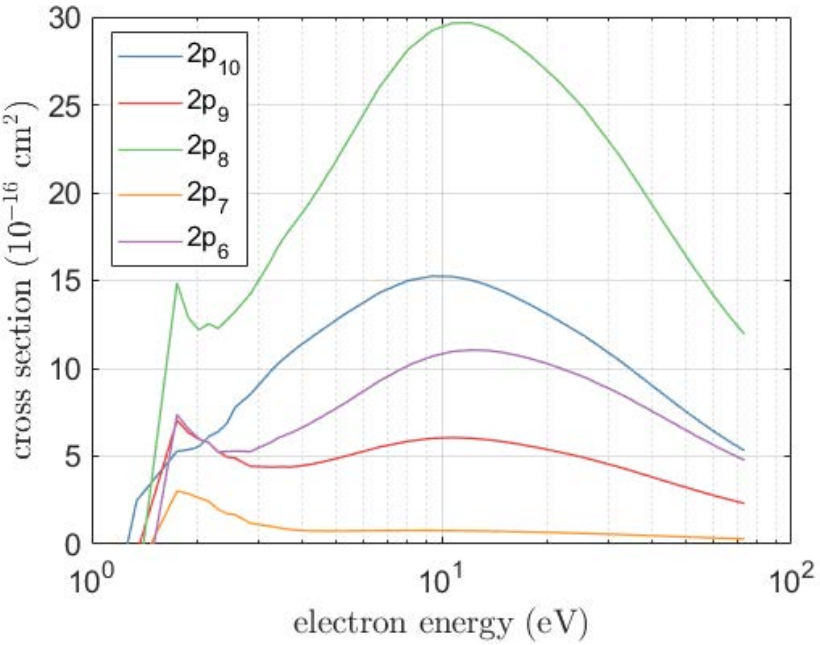

Figure 5.7: BSR direct cross sections (in 10^{-16} cm^2) for excitation from $1s_5$ to the $2p_{10} - 2p_6$ levels. Corresponding to data in Table C.8

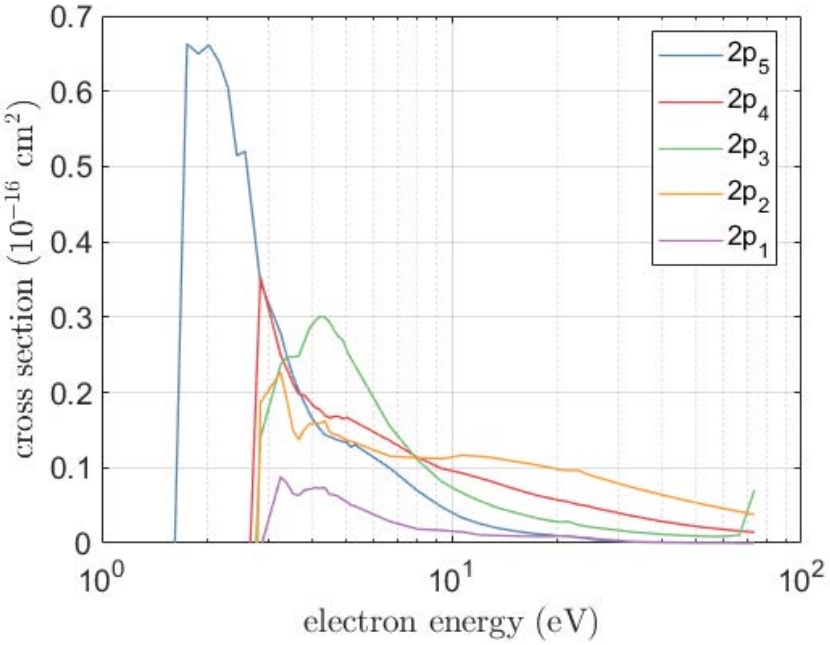

Figure 5.8: BSR direct cross sections (in 10^{-16} cm^2) for excitation from $1s_5$ to the $2p_5 - 2p_1$ levels. Corresponding to data in Table C.9

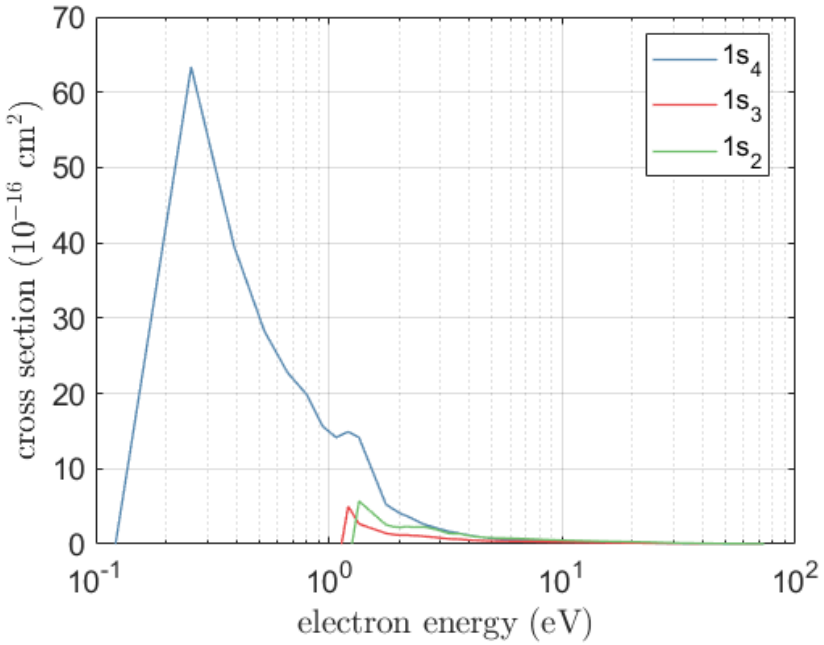

Figure 5.9: BSR direct cross sections (in 10^{-16} cm^2) for excitation from $1s_5$ to the other $1s$ levels. Corresponding to data in Table C.13

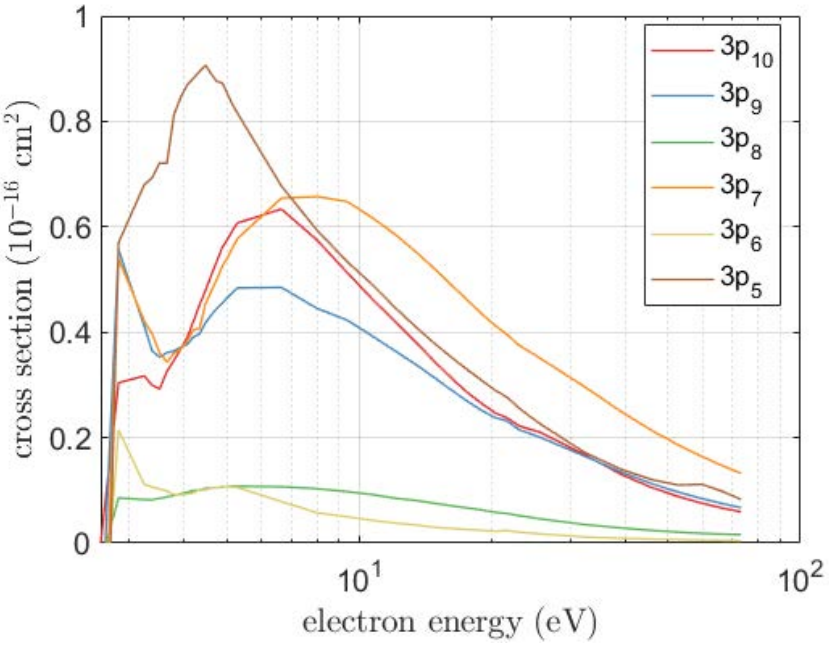

Figure 5.10: BSR direct cross sections (in 10^{-16} cm^2) for excitation from $1s_5$ to the $3p$ levels. Corresponding to data in Table C.10

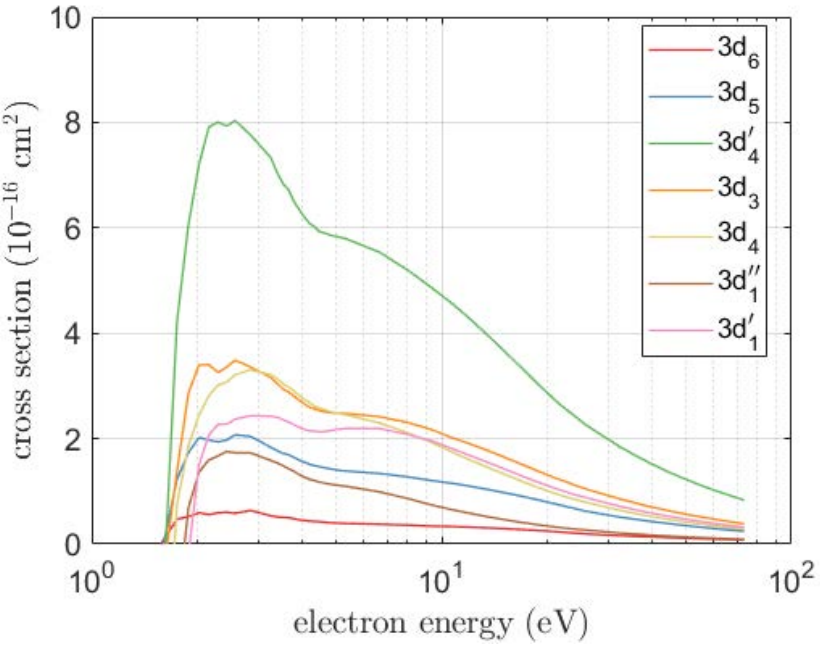

Figure 5.11: BSR direct cross sections (in 10^{-16} cm^2) for excitation from $1s_5$ to the $3d_6 - 3d'_1$ levels. Corresponding to data in Table C.11

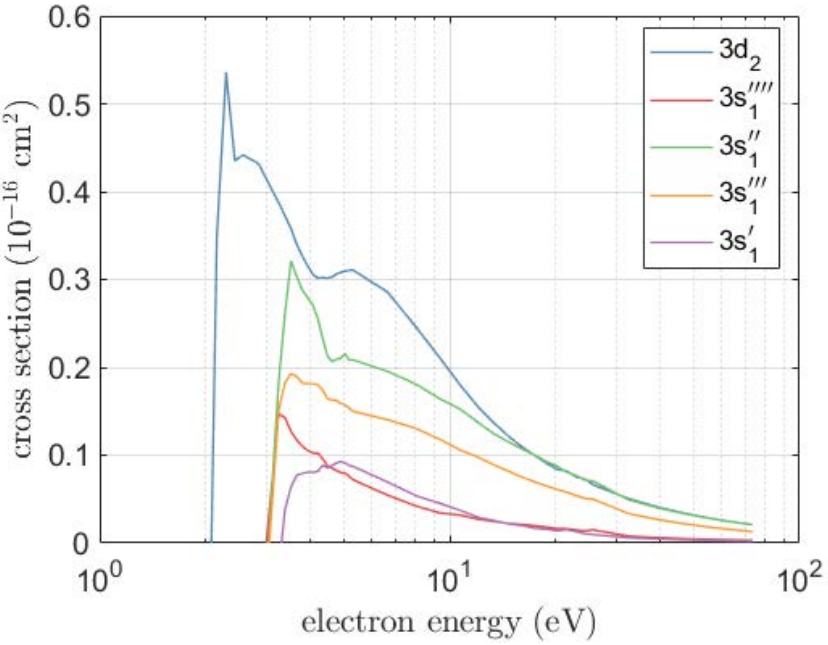

Figure 5.12: BSR direct cross sections (in 10^{-16} cm^2) for excitation from $1s_5$ to the $3d_2 - 3s'_1$ levels. Corresponding to data in Table C.12

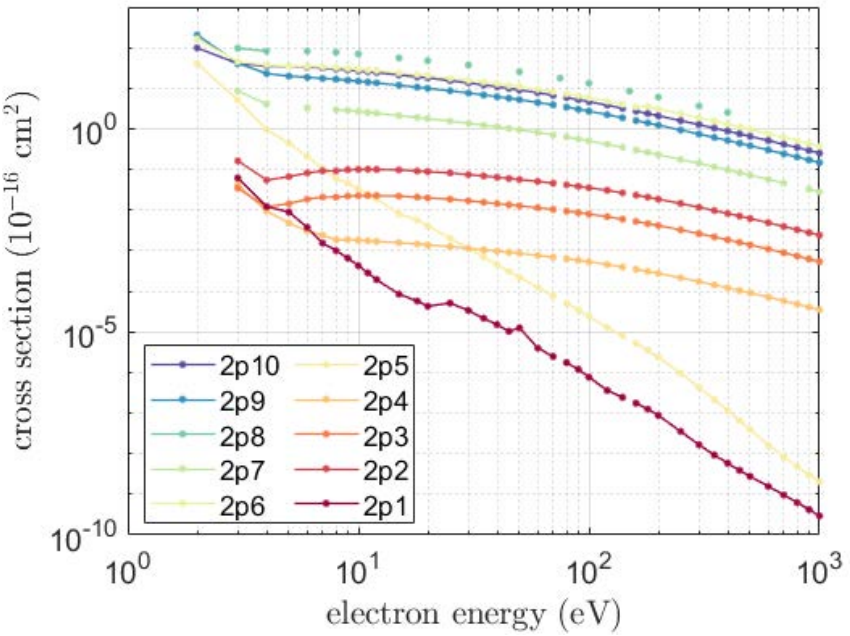

Figure 5.13: Relativistic Distorted Wave cross sections for the $1s_5 \rightarrow 2p$ transitions, corresponding to data in Table C.6 and C.7 in section C.2. Data from [43]

5.6.5 Ionization Cross Section

One of the loss channels for the $1s_5$ level is ionization. Dressler et al. use the cross sections from Ton-That and Flannery [133] who use the Born approximation and the binary encounter method. Dressler's argument for choosing this cross section was that is had the intermediate values of three sets of cross sections available to them. We use the same cross section in thesis for the same reason as well for the fact that it was available in digital form on LXCat [102]. Although this data set refers to the paper of Meunier et al. [87], in this paper it is specified that the ionization cross section from the $1s_5$ of Xenon is in fact that of Ton-That and Flannery. The cross section is plotted in Figure 5.16.

5.6.6 Processed Cross Sections

To be able to facilitate easy use of the cross-section data in the model all cross section data from the $1s_5$ level is interpolated to the same (semi-)regular grid of 491 points: 0 to 1 eV with 0.1 eV spacing, 1 to 3 eV with 0.01 eV spacing and 3

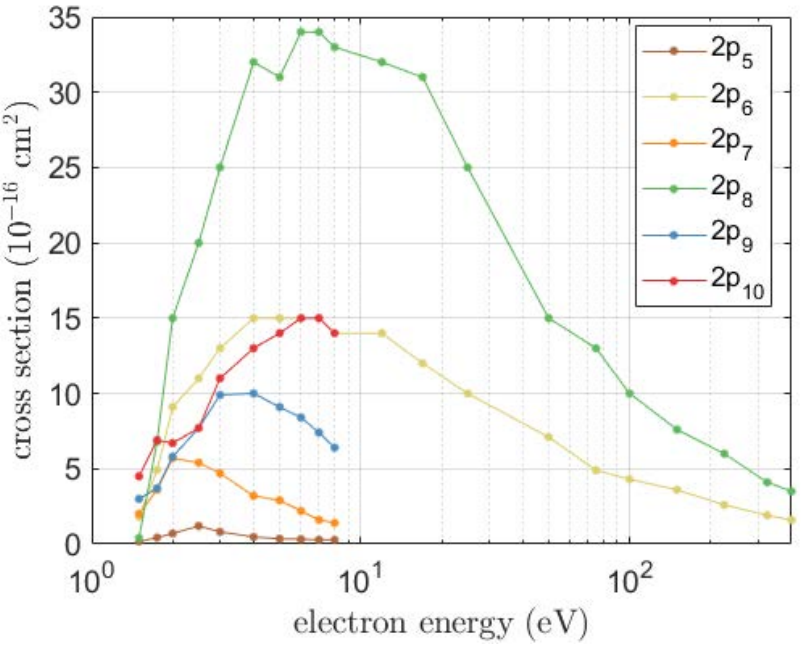

Figure 5.14: Experimental apparent cross sections for the $1s_5 \rightarrow 2p$ transitions, corresponding to data in Table C.14 in section C.2. Data from [56].

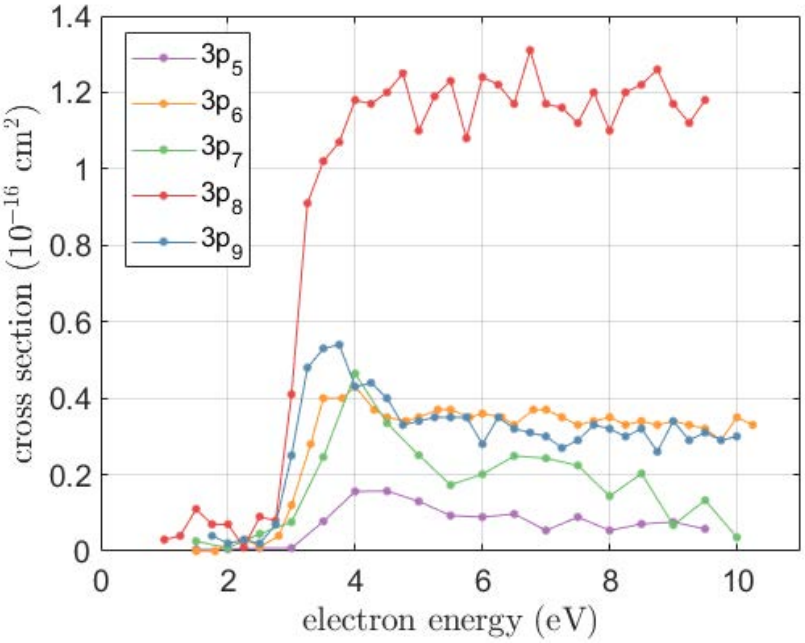

Figure 5.15: Experimental apparent cross sections for the $1s_5 \rightarrow 3p$ transitions, corresponding to data in Table Table C.15 in section C.2. Data from [57].

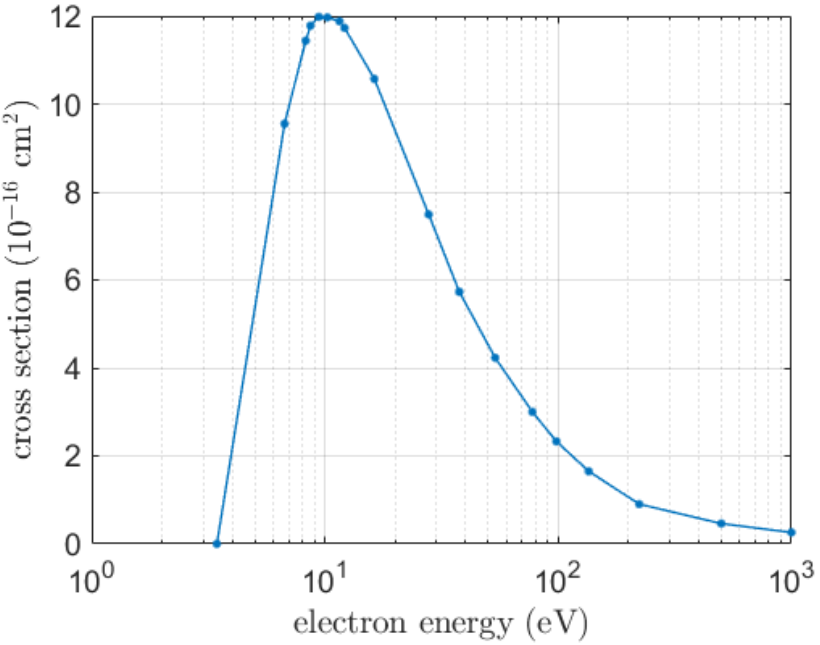

Figure 5.16: Ionization cross section of the $1s_5$ level.

to 10 eV with 0.1 eV spacing and 10 to 200 eV with 1 eV spacing. This grid was chosen to have sufficient resolution in the threshold region (1-3 eV) while reducing the amount of points in the high energy region >10 eV where the cross sections vary less with energy.

For the $1s_5 \rightarrow 2p$ cross sections the BSR values where used as a baseline and replaced with Jung's cross sections where available. Jung's cross sections have non-zero values below the threshold energy which is non-physical therefore we forced the cross sections to zero below the threshold energy. We extended the cross sections with the RDW values for energies over 70 eV. For the $1s_5 \rightarrow 3p$ cross sections we use the values from Jung extended with RDW values, except for $3p_{10}$ where Jung does not provide any data. For both $2p$ and $3p$ to achieve a smooth extension the RDW data is scaled with a constant to ensure the BSR/Jung value and the RDW values are equal at the merging point (around 70 eV when using BSR data and around 10 eV for Jung's data). For the $1s5 \rightarrow 3d$ and $1s5 \rightarrow 1s$ cross sections we use the BSR data. In for transitions to the $1s$ manifold we extend these with RDW data, but for transitions to the $3d$ manifold these are not available. Instead we adopted an approach similar to [111] and fitted the BSR curves from 30-70 eV

with the Born-Bethe approximation (see Equation 5.50to extend the cross section to 200 eV.

$$Q_{BB}(\mathcal{E}) = \frac{1}{\mathcal{E}} \left[c_0 + c_1 \ln\left(\mathcal{E}\right)\right] a_0^2 \tag{5.50}$$

All cross-sections are plotted in the figures below. The cross sections for the $1s_5 \rightarrow 3p$ and $1s_5 \rightarrow 3d$ transitions have been summed into one and are plotted in Figure 5.17 together with the $1s_5 \rightarrow 1s$ cross sections and the ionization cross-section as a for a comparison of the loss channels of the metastable level. For comparison we also show the same plot from [37].

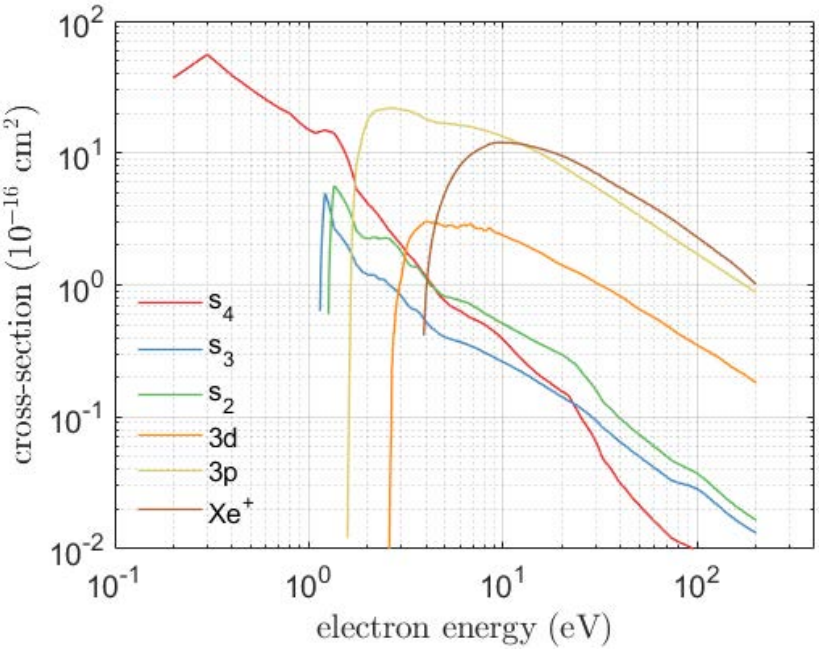

Figure 5.17: Comparison of cross sections for $1s_5$ loss channels.

5.7 MATLAB Code of KCD Model

KCD model is code in MATLAB script to allow for fast and efficient processing of obtained spectra. The code can be found verbatim in appendix C.1. Here we will give a functional description of the code. The code consists of 5 sections and uses two functions.

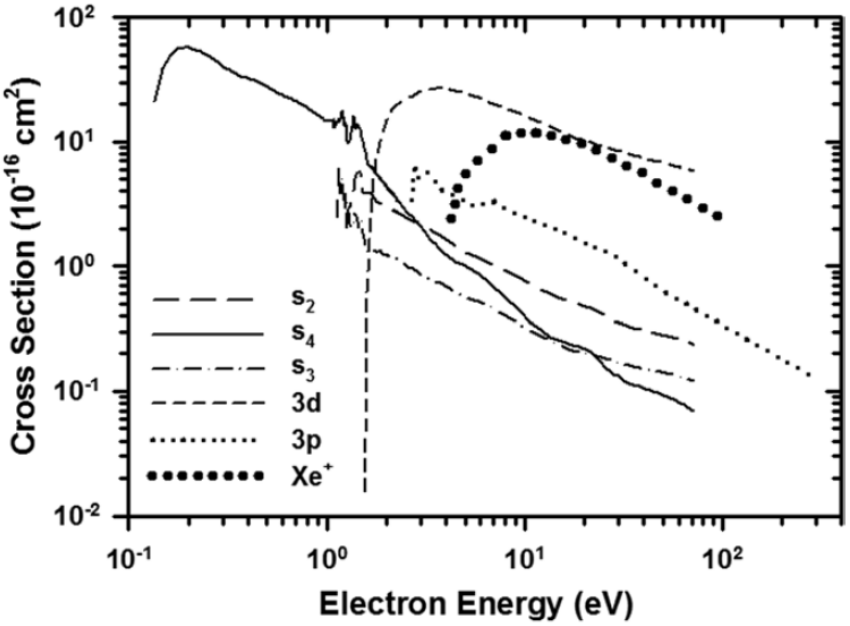

Figure 5.18: Comparison of cross sections for $1s_5$ loss channels. From [37]

Constants and Variables

The first section is called *Constants and Variables* and is used to declare two global variables V, M (`V,M`) the acceleration voltage and the ion mass (131 Da in the case of xenon) and one local variable: α (`alpha`), the fraction of singly charged ions. In this section also the experimental data to be processed is loaded.

Load Cross Sections

In the second section all the relevant cross sections are loaded using the `load` function. In total nine different cross sections sets are loaded. All cross sections were processed as mentioned in the previous section, interpolated on the same grid and stored in MATLAB tables. The branching ratio for $2p \rightarrow 1s_4$ transitions for each $2p$ level (`Xe_2p_gamma`) is also loaded. And furthermore we define a vector of electron temperatures: `T = [1:0.01:30]`. All cross section sets as they appear in the code are listed in Table 5.4.

Rate Coefficients

In this section the rate coefficients are calculated for all values of T_e. This is done in a for loop over `T` while calling the function `ratecoef`. The function `ratecoef` does no more than calculate the cross section weighted first moment of the (Maxwellian) velocity distribution according to Equation 5.37 using the `trapz` function. The rate coefficients for ion impact excitation are calculated using the `ionimpact` function which interpolates the corresponding cross section to the value of `V` and calculates the rate coefficient according to Equation 5.41. This leads to the following list of rate coefficients, in vector or table format. All rate coefficients as they appear in the code are listed in Table 5.4.

Calculate Metastable Fraction

In this section of the code the metastable $1s_5$ fraction `Nm` as function of the electron temperature is calculated. This is done by solving Equation 5.47. The numerator consists of `k0m` and the subset of NIR lines with $1s_5$ as the lower level of `ke0,k1,k2`, while the denominator consists of `k2pm,k1s,k3p,k3d,kion`. Note that `k2pm` is multiplied by the branching ratio of emission to states that are **not** coupled to the $1s_5$ state, i.e. $1 - \Gamma(1s_5)$. This can be calculated from the values in table 5.3.

Calculate Line Intensity

Having calculated the metastable fraction as a function of temperature we can now calculate the line intensity of each of the NIR lines as a function of temperature by solving Equation 5.45. Since the electron and neutral density are not known a priori we assume 10^{18} m^{-3} and 10^{21} m^{-3} respectively, mainly to offset the value of h which is of the order of $\mathcal{O}(10^{-34})$. For the calculation of the electron temperature only the relative line intensities matter and the values for n_n, n_e cancel out anyway. To facilitate calculations even more each of the line intensities is normalized to the sum of all intensities.

Estimate Electron Temperature

In this last section the calculated line intensities as a function of temperature are used to estimate the electron temperature from a set of measured line intensities.

Firstly the measured line intensities are normalized to their sum and then the χ^2 is calculated according to:

$$\chi^2(T_e) = \sum_{\lambda} \left(\frac{J_\lambda(T_e) - J_{\lambda,exp}}{J_{\lambda,exp}} \right)^2 \tag{5.51}$$

The χ^2 is a measure of the relative mean squared error as a function of electron temperature. The electron temperature for which χ^2 reaches a minimum the calculated line intensities *best* match the measured line intensities and it is assumed that this electron temperature is a good approximation of the actual value.

Apart from the electron temperature there is another variable, the singly charged ion fraction α. Currently this value is estimated and the calculation can be repeated for different α. However it is not difficult to extend the code to instead calculate a surface $\chi^2(T_e, \alpha)$ and find a minimum. However the current application of the code is to Helicon Plasma Thrusters where the ion energy near the throat is of the order of the electron temperature (i.e. $E_i \ll 100$ eV) and the ion impact processes are not significant. In general for processing HPT spectra we set `V` $= 0$ to make sure `k1,k2` are zero and therefore the value of α is irrelevant.

5.8 Methodology

5.8.1 Experimental Setup

The diagnostic setup in this work is based on an OceanOptics HR4000 spectrometer which has a spectral range of 200-1100 nm and a resolution of < 1.0 nm FWHM (full-width at half maximum). An optical fiber was outfitted with a custom 3D printed collimator (2 mm inner diameter and 100 mm length, i.e. a bit over 1° collection angle). The collimator was parallel to the exit plane of the thruster and aligned with the center of the plasma column; the other side of the fiber was connected to the spectrometer (via a vacuum feedthrough). A second fiber was mounted on the translation staged (see section 3.6) and aligned with the axial axis of the thruster. The spectrometer was connected to a laptop via USB and operated with the accompanying OceanView software. A schematic of the complete setup can be seen in figure 5.19.

Spectra were obtained with an integration time of 500 ms and averaged over 10 measurements. Care was taken to prevent saturation of the CCD chip. Pre-

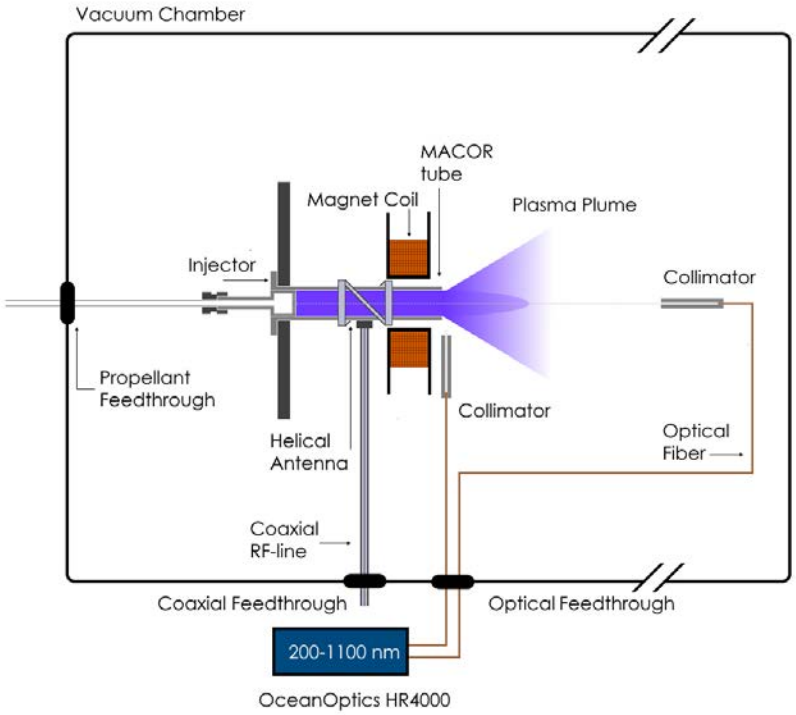

Figure 5.19: Spectrometry setup for the HPTx prototype at the EP^2 vacuum facility.

ceding every series of measurements the spectrometer was configured to subtract a background spectrum and correct the sensitivity with a calibration curve. This calibration was obtained by comparing the measured spectra of a halogen and a deuterium lamp from an Ocean Optics DH-2000-CAL calibration with its documented irradiance. All spectra were processed using MATLAB.

5.8.2 Xenon Emission Spectrum

The emission spectrum obtained from the HPT running with Xenon (450W, 10 sccm, 0.2T) can be seen in Figure 5.20 which is a close up of the NIR region of $750-1000$ nm and Figure 5.21 which is a close-up of the violet-blue-green region of $400-650$ nm. In both cases prominent peaks have been marked with the corresponding wavelength. In case of the NIR region particularly the 11 lines used for diagnostic purposes have been marked. The lines marked in the blue region are not used in the KCD model, but it is notable to point out that they all come from transitions of Xe II, i.e. from ions. Although the magnitude of the emission lines are a factor

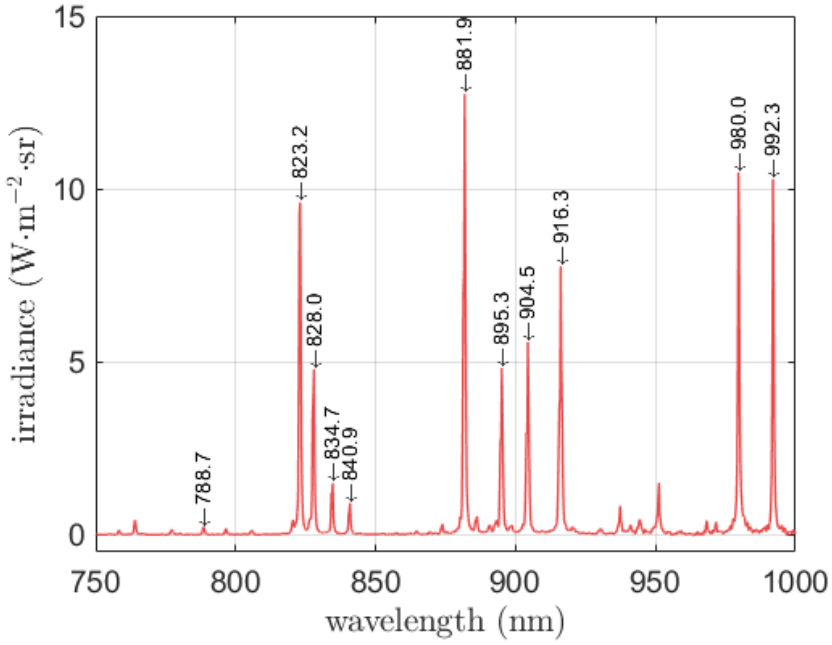

Figure 5.20: Example spectrum of Xenon in NIR region 750-1000 nm.

5 or so lower than in the NIR region, this still points to a sizeable fraction of ions.

5.8.3 Extracting Line Emission Values

Line emission theoretically occurs at a specific wavelength. However, due to different broadening mechanisms, emission lines actually occupy a range of wavelengths. Apart from the broadening mechanisms described in section 5.3.1 significant broadening is due to the instrument, something referred to as instrument broadening and this is mainly due to the finite resolution of the spectrometer as well as the grating and entrance slits. The broadening is apparent in figure 5.20 and is overwhelmingly due to instrument broadening. Fitting a Gaussian to for example the 882 nm line, results in a standard deviation of about $\sigma = 0.35$ which according to equation 5.14 would imply a neutral temperature of $2.1 \cdot 10^8$ K which is clearly non-physical. Furthermore the measured standard deviation corresponds to a FWHM of 0.82 nm which corresponds to actual measurements of the instrument broadening of the same spectrometer as reported in [88].

To extract the value of the line emission one of several approaches can be used. One can simply take the value corresponding to the maximum of the emission peak,

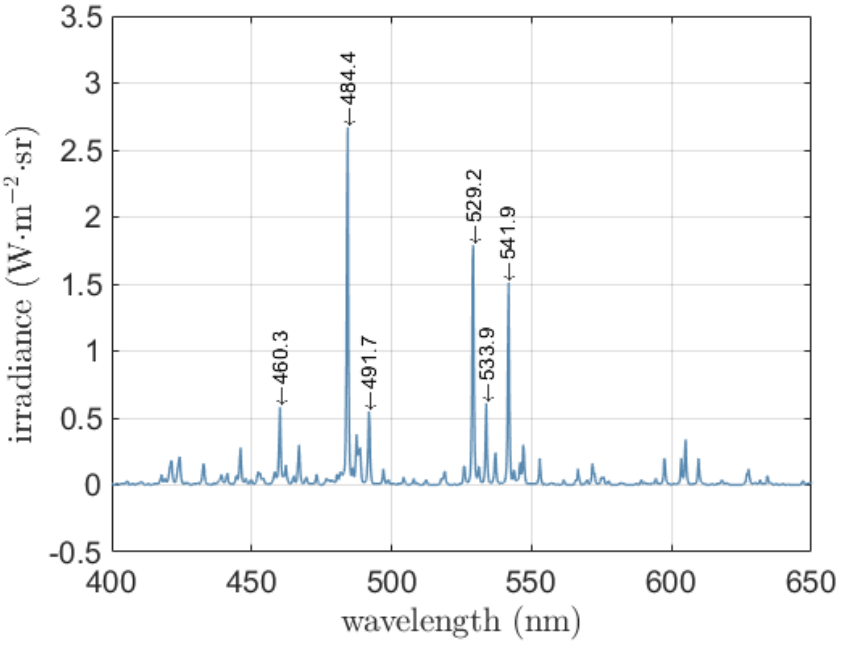

Figure 5.21: Example spectrum of Xenon in visible region 400-650 nm.

integrate the spectral peak around the emission line, one can fit the peaks with a Gaussian or Voigt profile and obtain the amplitude or one can use a technique from compressed sensing called a super-resolution algorithm [54].

The first approach is the most simple and can be achieved by using a simple trapezoidal numerical integration scheme on the spectral data. The main disadvantage is in the case of two emission lines that are too close to properly resolve and one can only obtain the cumulative line emission of the two.

The second approach is slightly more involved but can be used even for relatively closely spaced lines in which case on simply fits two profiles to the wavelength interval of the corresponding peaks. We found that although the Gaussian profile is a decent fit, particularly for the upper part of the peaks, it does not capture very well the wider tails of the emission peaks. Instead it was found that a Voigt profile is a better fit. Although Voigt profiles are a convolution of a Gaussian and a Lorentzian profile and therefore don't provide a straightforward fitting function there is an approximation given by [36].

$$V(x) = (1-\mu)G(x,\sigma) + \mu L(x,\gamma) \tag{5.52}$$

Even though the Gaussian and Lorentzian functions $G(x)$ and $L(x)$ in the above

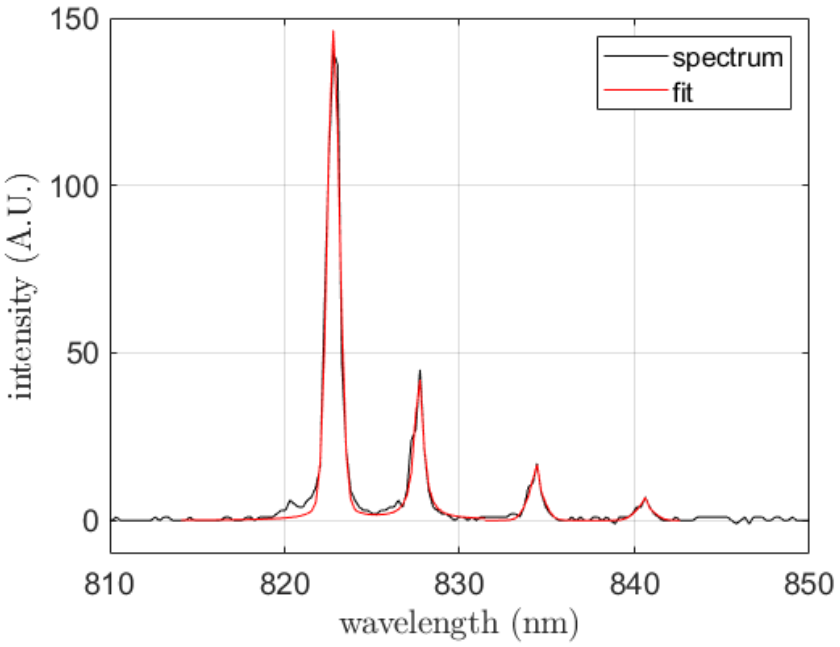

Figure 5.22: Example of empirical Voigt fit to spectral data in 810-850 nm range.

equation are not the same as those whose convolution would produce the same Voigt profile, this is not a problem as we are not interested in these real profiles, but rather in an empirical fit to extract the amplitude. The fitting function that we use is:

$$V_{fit}(\lambda) = A\left(\frac{1-\mu}{\sigma_G\sqrt{2\pi}}\exp\left[-\frac{(\lambda-\lambda_0)^2}{2\sigma_G^2}\right] + \frac{\mu}{\pi\gamma}\left[\frac{\gamma^2}{(\lambda-\lambda_0)^2+\gamma^2}\right]\right) \tag{5.53}$$

The resulting fit matches very well the data, as can be glimpsed from the example shown in Figure 5.22.

The third and last approach is the most complicated but also the most interesting. The theory of super-resolution (SR) algorithms is as follows. Assume we have a measured spectrum $y(\lambda)$ which is the result of acquiring the 'real' spectrum $x(\lambda)$ with an instrument function $H(\lambda)$. The relation between y and x is then given by:

$$y(\lambda) = \int_0^\infty H(\lambda - s)x(s)ds + w(\lambda) \tag{5.54}$$

where s is an integration constant and $w(\lambda)$ is an arbitrary stochastic or deterministic noise term that conforms to:

$$\|w(\lambda)\|_1 = \int_0^\infty |w(\lambda)|\, d\lambda < \epsilon \tag{5.55}$$

Here $\|w(\lambda)\|_1$ is the continuum version of the vector norm. Taking the Fourier transform we can write:

$$\hat{y}(\nu) = \begin{cases} \hat{H}(\nu)\hat{x}(\nu) + \hat{w}(k), & \text{for} \quad k \in [-\nu_c, \nu_c] \\ \hat{w}(\nu), & \text{otherwise} \end{cases} \tag{5.56}$$

Here $\nu = \lambda^{-1}$ is the wave-number, usually given in cm^{-1}. The function H can be seen as a low-pass filter with cutoff ν_c. The goal of a SR algorithm is then to find an estimate x' of x such that:

$$\begin{cases} i) & \mathcal{F}(H * x') = \mathcal{F}(H * x) \quad \text{on} \quad [-\nu_c, \nu_c] \\ ii) & \hat{x}' \quad \text{is supported on} \quad [-\nu_{hi}, \nu_{hi}] \end{cases} \tag{5.57}$$

This problem is severely ill-posed unless the and x' may not exist or not be unique unless it is consist of a series of well separated point sources. Particularly in the case that:

$$x(\lambda) = \sum_{j \in N} \alpha_j \delta(\lambda - \lambda_j) \tag{5.58}$$

the solution is tractable. Here $\delta(\lambda)$ is the Dirac delta function and j iterates over all point sources, or in our case emission lines. Even though in reality the pure emission lines (x) have a finite width due to the various broadening mechanisms, this width is negligible with respect to the instrument broadening as we've shown before and Equation 5.58 is a good approximation. Furthermore, if the minimum separation between two spectral lines,

$$\Delta\lambda = \min_{i,j \in T} |\lambda_j - \lambda_i| \tag{5.59}$$

is larger than twice the inverse of ν_c, i.e. $\Delta\lambda \geq 2/\nu_c$ then there is a unique solution $x' = x$ that can be found. Note that Equation 5.54 uses continuous functions, however in our case we have discrete vectors with a finite number of values, i.e. $y = (y_1, y_2, ..., y_N$ and correspondingly $x = (x_1, x_2, ..., x_N)$ and we can write:

$$y_n = \sum_{j=1}^{N} H(\lambda_n - s_j)\alpha_j, \quad |\lambda_n| \geq \nu_c^{-1} \quad \text{for} \quad n \in 0, ..., N-1. \tag{5.60}$$

Alternatively we can also write $y = Hx$ where H is an $N \times N$ matrix with $H_{nj} = H(\lambda_n - s_j)$. The problem to solve to obtain $x' = x$ is now reduced to the following

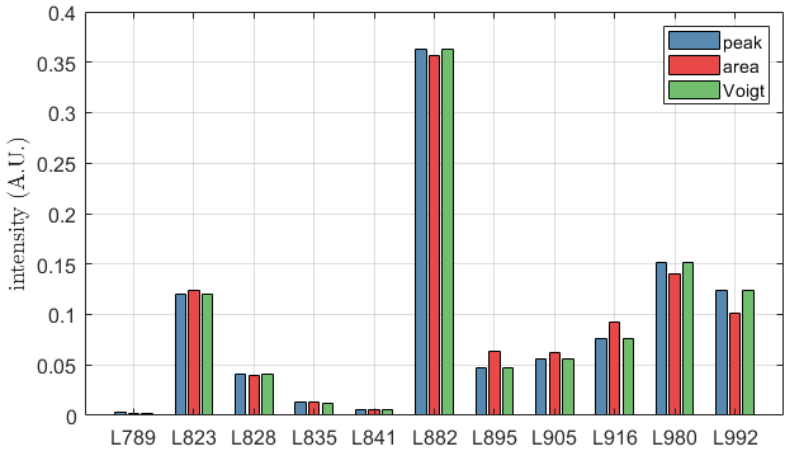

Figure 5.23: Comparison of extraction method for line emission values.

convex minimization problem:

$$\begin{cases} \min_{\tilde{x}} \|\tilde{x}\|_{L^1}, \\ \text{subject to} \quad H\tilde{x} = y \end{cases} \tag{5.61}$$

where $\|\tilde{x}\|_{L^1} = \sum_{j=1}^{N} \alpha_j$.

Although the super-resolution algorithm is a very interesting method for extracting the line emission data unfortunately to date, we have not been able to successfully implement the method.

For comparison we show the results of all four methods in extracting the emission line values for a given spectrum in Figure 5.23.

All methods give reasonably comparable results, in particular the peak and Voigt fit methods are very similar.

5.9 Results

In this section we present the results obtained by post-processing several spectra obtained from the helicon plasma thruster.

5.9.1 Model Validation

Firstly we will try to validate the model as best as possible. However, there is not that many 'intermediate' data available from [37] and [58]. To recap the differences

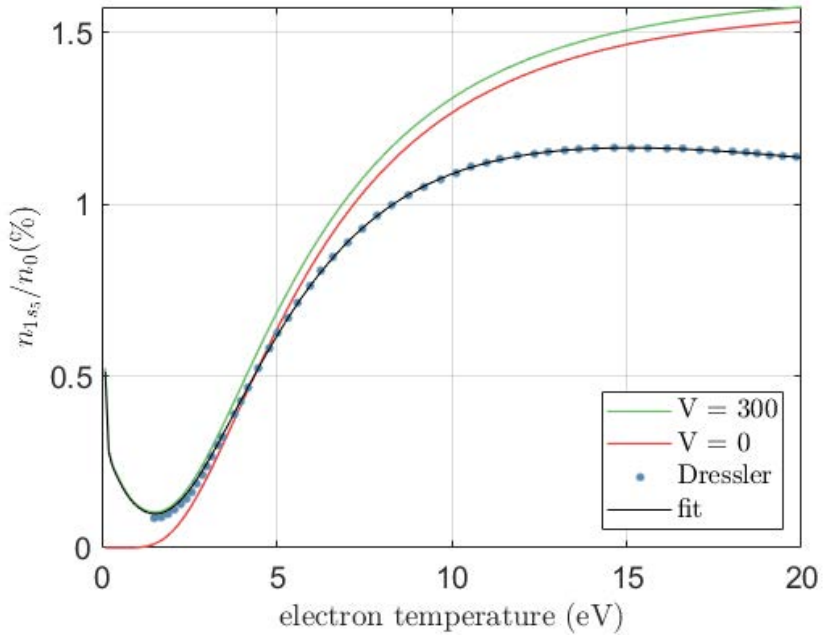

Figure 5.24: Calculated metastable fraction as function of electron temperature, with ($V = 300$) and without ($V = 0$) ion-impact, compared to results of [37].

between the BSR-RDW-Jung model of [37] and the model developed in this thesis is mainly the inclusion of $1s_5 \rightarrow 3p$ cross-sections of Jung, and updated BSR and RDW cross-sections for the other metastable excitations. Another difference is that Dressler et al., just like Karabadzhak et al. seem to only take into account the levels $2p_{6-10}$ in the summation over j in equation 4 in [37]. This is justified because the metastable cross sections to these levels are more than an order of magnitud larger (which becomes apparent when comparing Figure 5.7 and Figure 5.8). This is also the reason why P_j in the same equation is defined as the branching fraction of lines radiating to the $1s_4$ level, since the $2p_{6-10}$ only radiate to either the $1s_5$ or the the $1s_4$ levels. We however include all $2p$ levels in this summation and use the branching fraction to all levels other than the $1s_5$ level, because some of the $2p_{1-5}$ levels do radiate to the $1s_3$ and $1s_2$ levels.

As a first comparison we can look at the calculated metastable fraction as a function of the electron temperature which is reported in Figure 5. of [37]. We have digitalized this data and plotted it together with our results with ($V = 300$) and without ($V = 0$) ion impact which can be seen in Figure 5.24.

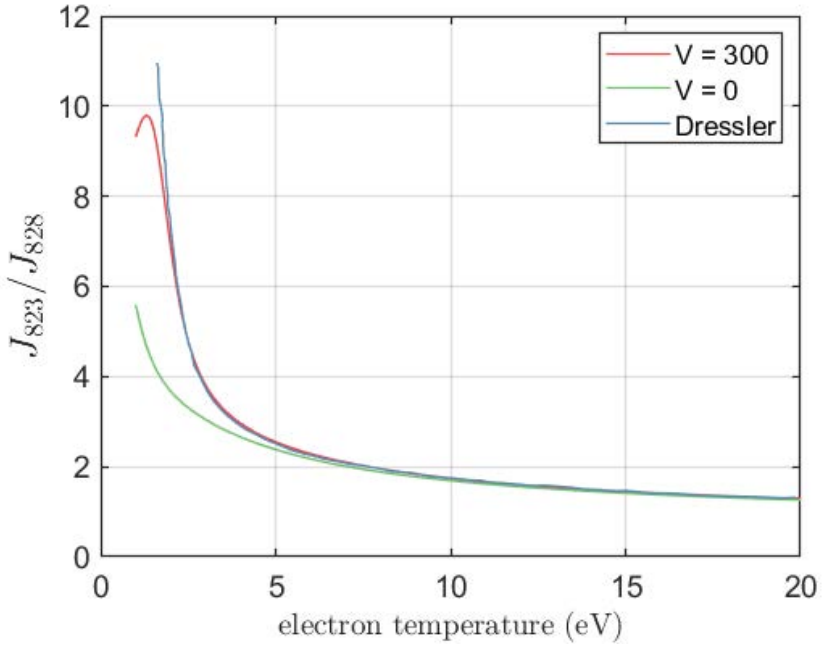

Figure 5.25: Calculated line ratio of the 823 nm and 828 nm lines, with ($V = 300$) and without ($V = 0$) ion-impact, compared to results of [37].

Up to 5 eV the our results with ion-impact agree well with those of Dressler et al., within about 10%. Also the effect at lower temperatures < 3 eV, of including ion-impact can also be clearly seen. However after 5 eV the results start to deviate and the relative difference increases linearly from 10% at 5 eV up to 35% at 20 eV. In fact the relationship is so markedly linear where the ratio between Dressler's curve and ours is given by $\mathcal{R} = 1.018 + 0.0184T_e$ that we've plotted our curve divided by this ratio, $n_{1s_5}/\mathcal{R}$ in the same graph (the black dashed line) and it results in a near perfect fit with Dressler's results. This shows that for some reason the metastable fraction as calculated by our model is equal to that of Dressler et al. plus another term proportional to T_e and to the results of Dressler.

Dressler et al. also report a plot of the modeled line ratio of the 823 nm and 828 nm line as a function of electron temperature. In Figure 5.25 we compare their results (digitalized, from Figure 4. in [37]) to our results, both with and without ion-impact.

In this case also there is a very good agreement between the data of Dressler et al. and our case with ion impact, and even without ion impact for temperatures

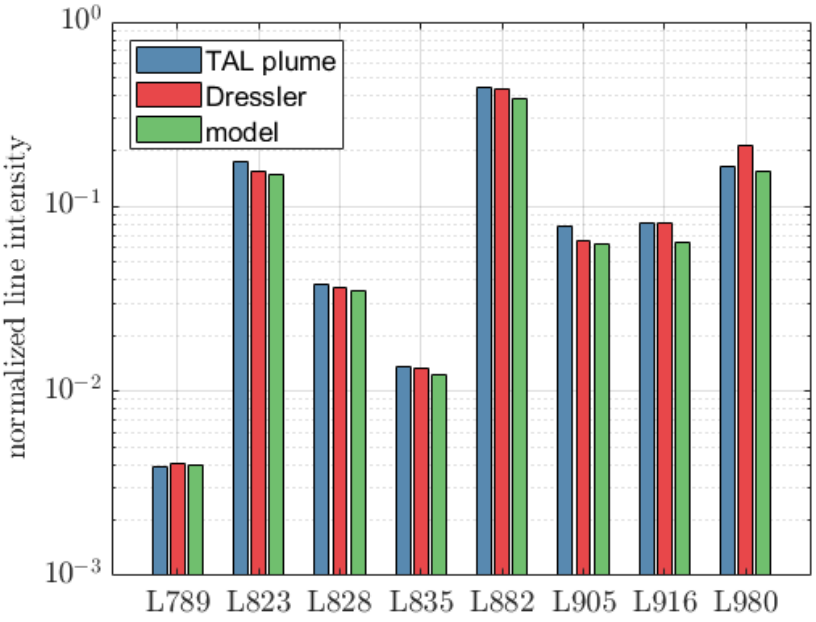

Figure 5.26: Comparison of measured and calculated line intensities from a D-55 TAL plume data set as reported in [37].

above 7 eV. This confirms that the inclusion of ion impact is of most importance at lower temperatures where the ion impact rate coefficients are similar to the electron impact rate coefficients. Below 2 eV the results of Dressler and ours start to diverge slightly. It is not clear what cause this discrepancy. It is unlikely to be due to the difference in metastable fraction, which is small as we have seen. Even though the 823 nm line emission is dominated by excitation from the metastable, manually increase the metastable fraction by +20% was insufficient to reproduce the data of Dressler at below 2 eV.

Lastly, Dressler et al. report one set of measured emission lines from the plume of the D-55 TAL Hall-effect thruster, compared to the best fitting calculated line intensities. We digitalized the plot if Figure 6. of [37] and obtained the measured line intensities as well as the calculated line intensities corresponding to the BSR-RDW-Jung model and we plot it together with the best fitting line intensities as obtained from our model. Note that some uncertainty is introduced due the digitalization process. Also note that the 841 nm, 895 nm and 992 nm lines are not used in [37]. The results are shown in Figure 5.26.

Figure 5.26 shows overall similar or slightly worse agreement with the measurement data than those of Dressler. Although due to the logarithmic scale and errors introduced by digitalization of the original plot it is hard to quantify. We also report the electron temperature obtained from our model using the 8 lines as well as from the 823/828 line ratio and the 834/828 line ratio which are: 3.0 eV, 2,8 eV and 2.8 eV compared to 2.7 eV, 2.5 eV and 2.8 eV. There is a slight discrepancy between the results of Dressler et al. and ours here, although our results seem more internally consistent. At the very least our model seems to produce results that are similar if not comparable to those of Dressler et al.

Intermediate Results

Before reporting the final results in terms of electron temperature for different operating conditions we will look at the intermediate results. This will provide some insight into how the experimental data is interpreted and how reliable the model is. As mentioned before the model yields a set of curves $J_\lambda(T_e)$ which are the normalized (to the sum of all lines) line intensities for each line under consideration, as a function of the electron temperature. To extract find the most probable electron temperature we compare the measured line intensity with the model one and look for the best agreement, i.e. where the square of the difference is minimum. This is done for all 11 lines and average measure of the discrepancy is taken in the form of the χ^2, which is basically the sum of the relative square errors as defined in Equation 5.51. The assumption is that the most likely electron temperature is for which χ^2 is at a minimum.

We'll first look at the line intensities calculated by the model for the HPT case where we neglect ion impact, i.e. $V = 0$ and also for the case presented in [37] and[58], i.e. $V = 300$ and $\alpha = 0.8$. The results are shown in Figure 5.27 below.

From Figure 5.27 it can be seen that the emission of some lines, such as the 823 nm,895 nm and 992 nm are rather unchanging over the range of electron temperatures and particularly at higher temperatures, while other such as the 789 nm, 828 nm and 835 nm lines vary markedly. It can also be seen that the effect of ion-impact for most lines results in higher line emission at low electron temperatures, < 2 eV.

As mentioned before the χ^2 is the sum of the squared difference of the measured and modeled line intensities. Here we look first at the squared difference for each

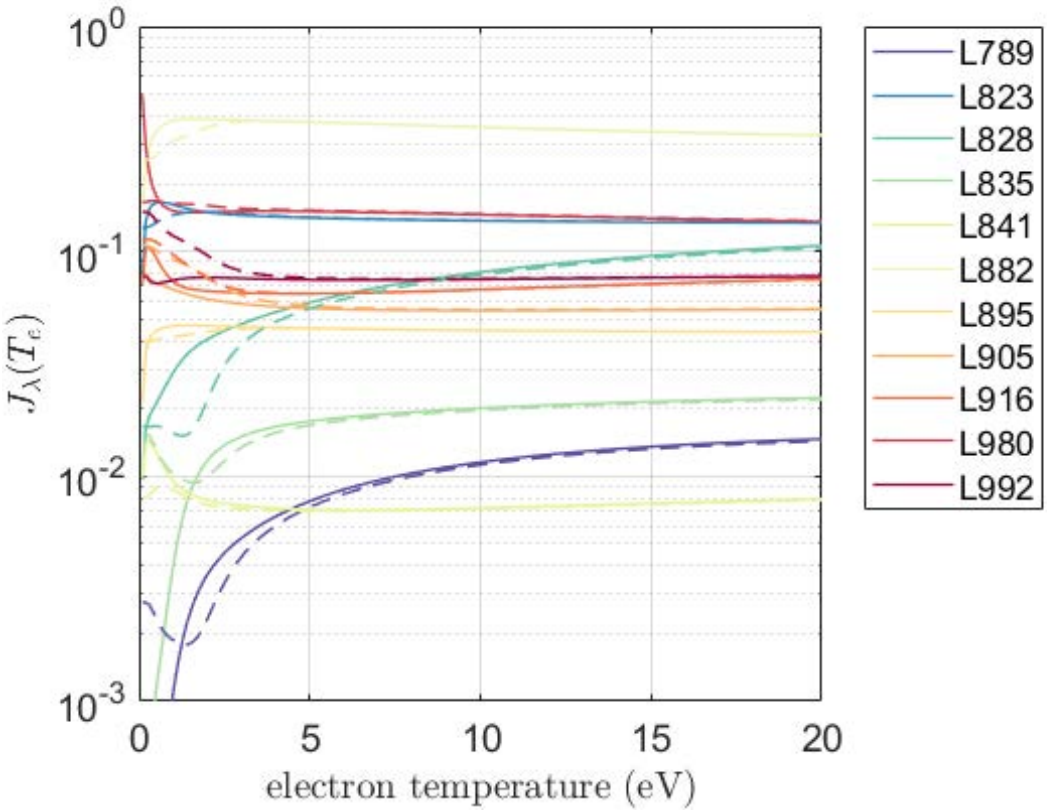

Figure 5.27: Calculated line emission of Xe I NIR lines as a function of electron temperature, with (dashed) and without (solid) ion-impact. Assuming an ion acceleration voltage of 300V.

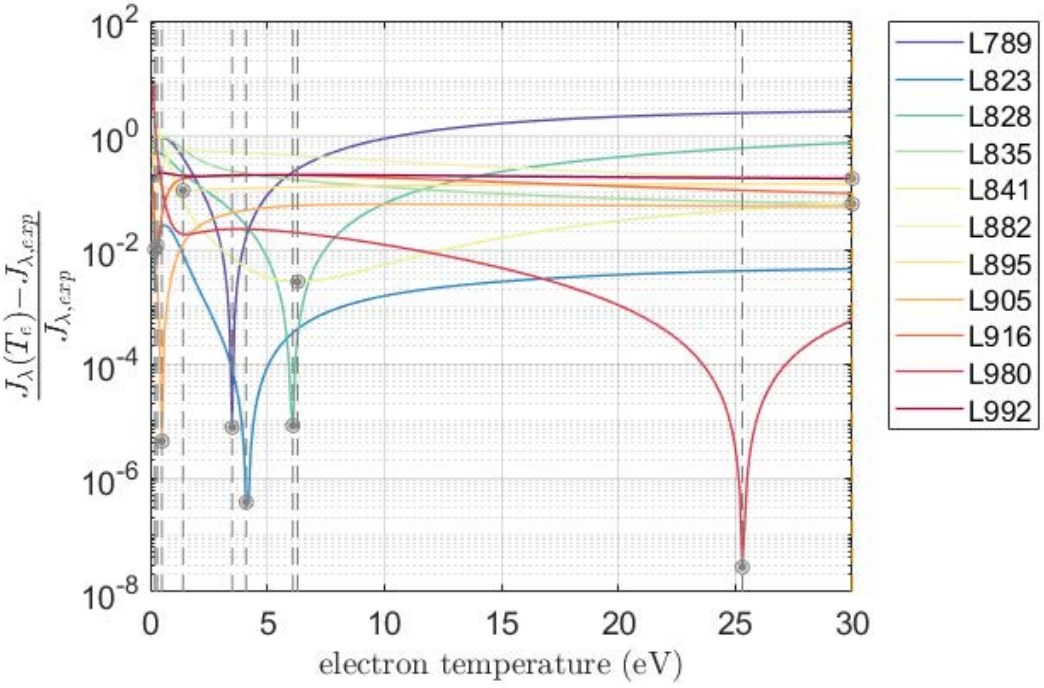

Figure 5.28: Squared difference of measured and calculated line emission as a function of electron temperature for a HPT operating at 300W, 2 kG, and 2.5 sccm.

of the line separately. The measured data is obtained in the radial direction, at the exit plane of the helicon plasma thruster operating at 300W RF power, a magnetic field of 2 kG and a mass flow rate of 2.5 sccm of Xenon.

Several things are immediately apparent from Figure 5.29. Firstly almost all lines have their minimum at a different location. Furthermore some lines such as the 835 nm, 882 nm, 905 nm, 916 nm and 992 nm don't have a minimum inside the interval 1-30 eV. Curiously the 980 nm has a minimum at 25 eV while the remaining lines (789 nm, 823 nm, 828 nm and 841 nm have similar minima, clustered around 5 eV. The line 895 nm has a minimum at 1.4 eV. For comparison we show a similar plot obtained at 20 sccm in Figure 5.28.

Now the picture is significantly different. The lines 882 nm, 905 nm, 916 nm and 992 nm still don't have a minimum within the interval, but now 823 nm and 841 nm do neither ($T_e < 1$). The 789 nm and 895 nm now have a similar minimum at 1.5 and 1.4 eV respectively while 828 and 835 nm have the same minimum at 5.4 eV. The 980 nm line still has a minimum significantly higher than the other lines, but not as much as before with $T_e = 10.8$ eV. It is clear that some line are less

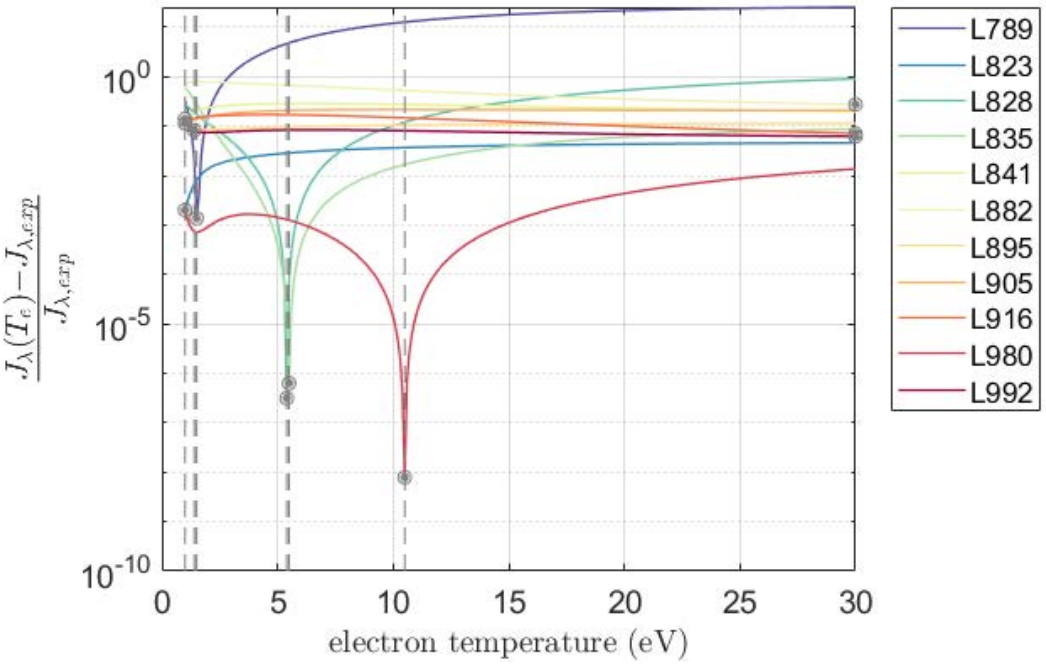

Figure 5.29: Squared difference of measured and calculated line emission as a function of electron temperature for a HPT operating at 300W, 2 kG, and 20 sccm.

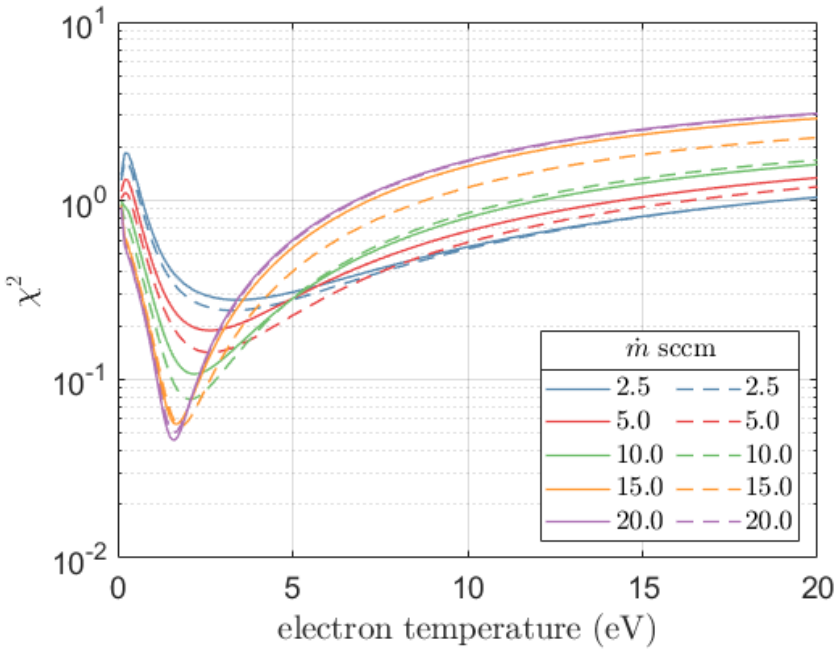

Figure 5.30: χ^2 as a function of electron temperature for a HPT operating at 300W, 2 kG, and 2 sccm.

relevant for determination of T_e while others are more prominent. The 823 nm and 828 nm seem a good candidate for a line ratio as they feature in two very distinct spectra and yield electron temperatures that are, at least between them, in good agreement .

5.9.2 Measurements with Varying Mass Flow Rate

In this section we present the results of applying the CR model to a set of measured spectra obtained from the HPTx for different mass flow rates. The measurements were taking, while operating at 300 W of RF power, 2 kG of magnetic field and the following mass flow rates of Xenon: 2.5, 5, 10, 15 and 20 sccm. Note that the orientation of the magnetic field was north upstream/south downstream. Measurements were taken both at the exit plane in the radial direction and axially (as shown in Figure 5.19). Two measurements were taken for each value of the mass flow rate.

First we show the results obtained along the radial direction. In Figure 5.30 the value of χ^2 as a function T_e can be seen for the various measurements. In Figure 5.31 a close up of Figure 5.30 around 0-5 eV in shown.

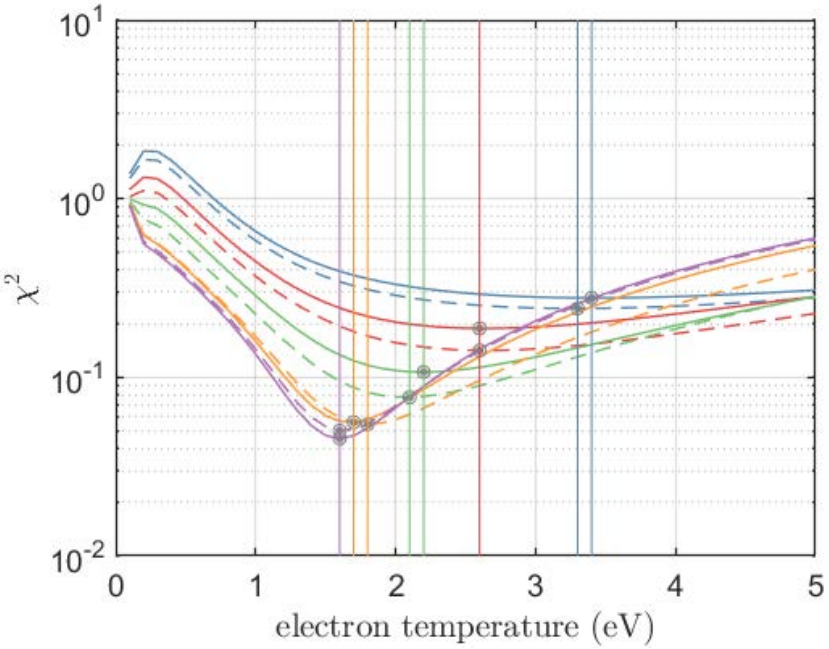

Figure 5.31: Close up of Figure 5.30.

As is apparent, the minima in χ^2 are occur in the range 1-4 eV. Furthermore there is good agreement between the results of spectra obtained under similar conditions, with at most a 0.1 eV difference. The resulting electron temperature as a function of mass flow rate is plotted in Figure 5.32, together with probe measurements. RPA measurements are of the most probable ion energy (i.e. the peak in the first derivative of the measured $I(V)$). In a magnetic nozzle expansion the ion energy at infinity $\mathcal{E}_{i,\infty}$ is related to the electron temperature at the source. For a cold plasma, i.e. $T_i/T_e \sim 0.1$ this is expressed by [2]:

$$\mathcal{E}_{i,\infty} = \frac{1}{2}\left[0.168 \ln\left(\frac{m_i}{m_e}\right) + 1.95\right]^2 T_{e0} \tag{5.62}$$

where m_i, m_e are the ion and electron masses and T_{e0} is the electron temperature at the source. For Xenon this results in $\mathcal{E}_{i,\infty} = 8.12 \times T_{e0}$. In Figure 5.32 The ion energy is shown on the right y-axis while the electron temperature is shown on the left. The RPA measurement corresponds to both axis, where for the left axis it has been scaled by 8.12

Several things can be gleaned from Figure 5.32. Firstly the probe measurements LP, RPA, seem to agree well. Note that the electron temperature derived from the

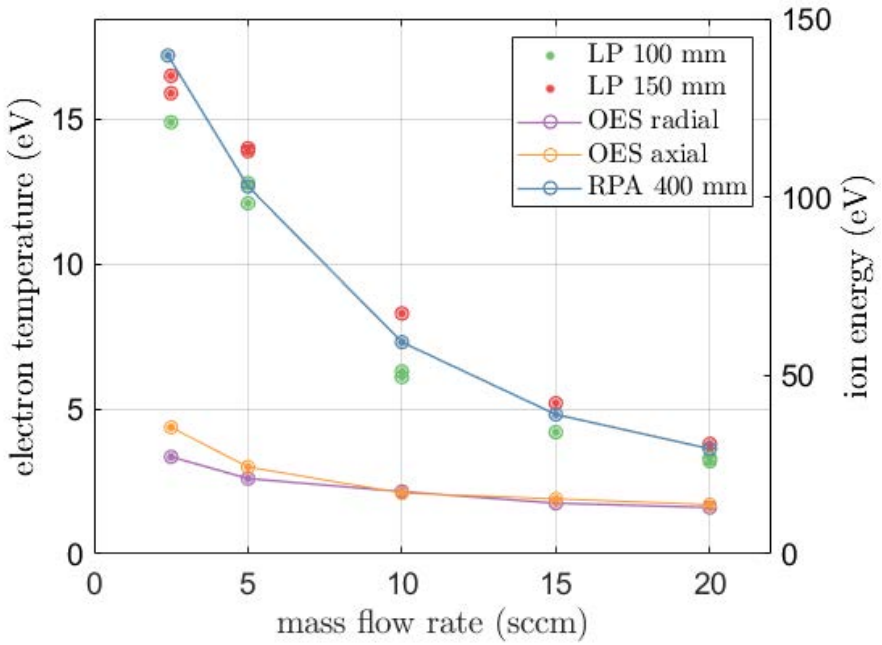

Figure 5.32: Comparison of electron temperature as a function of mass flow rate, obtained from Langmuir probe measurements at 100 mm and 150 mm downstream, derived from the ion energy as measured by an RPA and from radial and axial OES measurements.

RPA measurements should correspond to the electron temperature at the source, while those obtained from the LP measurements are the local electron temperature at 100 mm and 150 mm. Generally the electron temperature decreases along the expansion due to cooling. One would therefore expect the temperatures at 150 mm and 100 mm to be less than those at the source, and likewise the temperature at 150 mm to be lower than 100 mm. There may be several explanations for why this is not the case. Firstly the relationship $E_{i,\infty} = 8.12T_{e0}$ assumes that the plume has fully expanded, which may not yet be the case at 400 mm. If so, then E_i should be divided by a factor lower than 8.12 which would result in higher corresponding T_{e0}. LP measurements in RF plasmas are notoriously difficult and require RF-compensated probes and while those have used here, it is very much dependent on the local plasma properties whether the RF fluctuations are properly filtered out. It could be the case that at 150 mm the filtering does not work sufficiently resulting in an overestimation of T_e. Regardless, both RPA and LP measurements both agree well in trend as well as magnitude of the electron temperature. The OES measurements though, both taken along the radial and axial direction agree well with each other, except at low mass flow rates where they deviate about 1 eV but have little to no correlation to the probe measurements, except perhaps that both monotonically decrease with the mass flow rate.

5.9.3 Discussion

It is not immediately clear why there is no good agreement between the OES results and the probe results. The OES measurements plotted in Figure 5.32 are obtained from the χ^2 method including all eleven lines. However we also could not find a single line ratio that yielded results in agreement with the probe measurements. Multiple line ratios yielded nonsensical results, including the 823/828 nm line used in [58]. Several explanations are possible. 1) There could be an error in the code or the processing of the cross-sections and rate coefficients. However we have revised the code and the data multiple times and have not been able to find any errors. 2) The updated cross-sections used in this work somehow results in very different outcomes. However the updates in general should lead to an improvement and are of a similar nature as those of [37] over [58], that is to say for example the inclusion of experimentally obtained $1s_5 \rightarrow 3p$ cross-sections from Jung et al. instead of

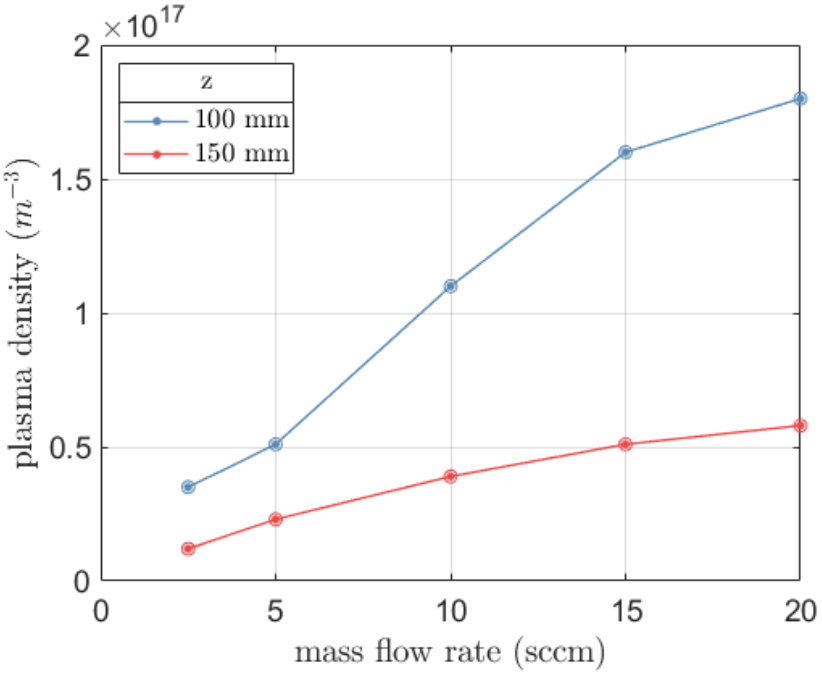

Figure 5.33: Plasma density as a function of mass flow rate as measured with a Langmuir probe, at $z = 100$ mm and $z = 150$ mm.

calculated BSR cross-sections. 3) The helicon plasma has a fundamentally different structure than for example a hall effect thruster. Simulations of the plasma inside a HPT [153, p.38] have shown for example streams of high electron temperature near the edges of the plasma, with lower electron temperatures in the center. It could be that the line integrated measurement of OES is a combination of spectra with different density and temperature and therefore do not result in an a good fit when post processing. Taking multiple spectra at different angles or different positions and using a mathematical transform such as the Abel or Radon transform to obtain more localized information could solve this issue if it is indeed the cause. 4) The helicon plasma is fundamentally different such that the assumptions underlying the model are no longer valid. One example could be the assumption to neglect the metastable diffusion. As argued in subsection 5.5.1 for a plasma density of 10^{18} m^{-3} the assumption holds. However plasma density measurements obtained from the same Langmuir probe measurements as used in Figure 5.32 yield densities ranging anywhere from the 10^{17} m^{-3} to as low as 10^{16} m^{-3} at low mass flow rates as shown in Figure 5.33.

Note that this is the downstream density, which drops rapidly along the expansion. A relatively simple 1D model [3, eq.37] for plasma expansion yields a relatively good approximation for the plasma density. It shows that at a distance of 10 times the source radius the plasma density is about 1 order of magnitude lower then at the source. It is likely that for higher mass flow rates the density at the source is of the order of 10^{18} m^{-3} and the assumption holds, however at the low end, 2.5-5 sccm this might not be the case. In that case it depends on the neutral density. To estimate the neutral density we can do a simple mass balance of the source: $\dot{m} = \dot{m}_i + \dot{m}_n$, i.e. the total mass flow going into the thruster is equal to the mass flow of ions and neutrals leaving the thruster. The mass flow of ions can be obtained from angular current density profiles as measured with a Faraday probe. The mass flow of neutrals is given by $\dot{m}_n = m_n n_n v_n A_e$ where m_n,n_n and v_n are the mass, density and velocity of the neutrals and A_e the cross sectional area of the thruster. For the velocity we assume expansion into vacuum at the thermal velocity, and we assume a neutral temperature of about 600K. We can then solve for n_n:

$$n_n = \frac{\dot{m}(1-\eta_u)}{A_e}\sqrt{\frac{\pi m}{8 m_n k_B T_n}} \tag{5.63}$$

where η_u is the utilization efficiency as obtained from Faraday probe measurements. The utilization efficiency and the resulting neutral density are plotted in Figure 5.34. The utilization efficiency can be seen to decrease proportionally to $\dot{m}^{-1}$ while the neutral density increases linearly and is of the order of $10^{19} - 10^{20}$ m^{-3}; one to two orders lower than our original estimate in subsection 5.5.1. Due to the combination of low plasma density and low neutral density it is likely that metastable diffusion is not negligible at lower mass flow rates.

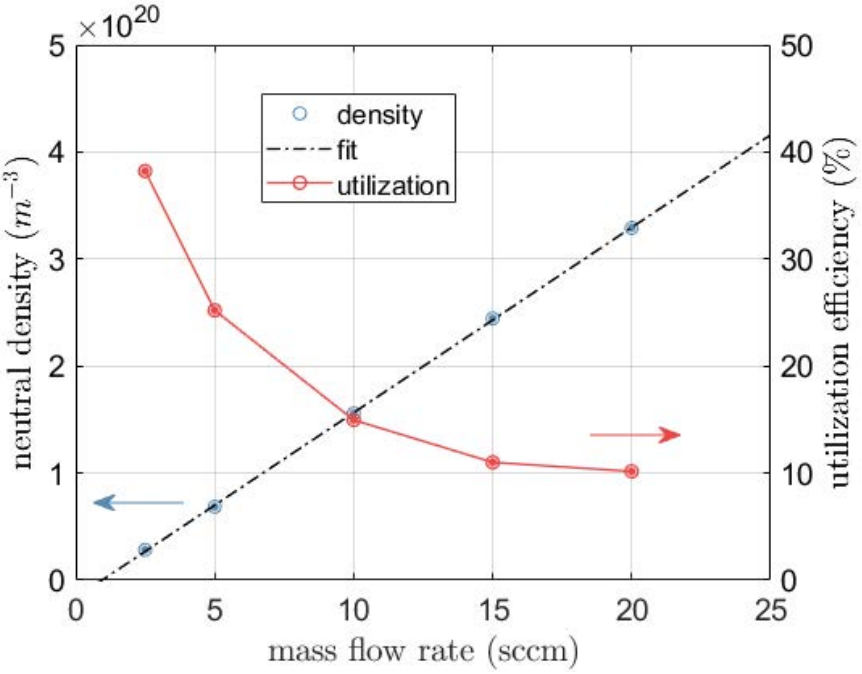

Figure 5.34: Utilization efficiency and neutral density as a function of mass flow rate.

Table 5.2: Emission lines originating in from the Xe I $2p$ levels. Data from [93].

upper	lower	λ (nm)	A ($\times 10^6$ s^{-1})
$2p_{10}$	$1s_5$	**979.9697**	31.10
	$1s_4$	1083.8340	1.80
$2p_9$	$1s_5$	**904.5447**	12.40
	$1s_4$	**992.3198**	13.00
$2p_8$	$1s_5$	**881.9411**	30.00
$2p_7$	$1s_5$	**840.9189**	3.06
	$1s_4$	**916.2652**	24.00
$2p_6$	$1s_5$	**823.1634**	28.60
	$1s_4$	**895.2251**	8.10
$2p_5$	$1s_4$	**828.0116**	36.90
$2p_4$	$1s_5$	469.0970	0.28
	$1s_4$	491.6507	1.60
	$1s_3$	820.6336	20.00
	$1s_2$	893.0830	22.00
$2p_3$	$1s_5$	452.4681	0.46
	$1s_4$	473.4152	1.38
	$1s_2$	**834.6822**	42.00
$2p_2$	$1s_5$	450.0978	1.46
	$1s_3$	764.2023	21.00
	$1s_2$	826.6520	12.00
$2p_1$	$1s_4$	458.2737	1.30
	$1s_2$	**788.7393**	35.00

Table 5.3: Branching ratio for all $2p \rightarrow 1s$ transitions. Data from [93].

	$\mathbf{1s_5}$	$\mathbf{1s_4}$	$\mathbf{1s_3}$	$\mathbf{1s_2}$
$\mathbf{2p_{10}}$	0.945	0.055	0.000	0.000
$\mathbf{2p_9}$	0.488	0.512	0.000	0.000
$\mathbf{2p_8}$	1.000	0.000	0.000	0.000
$\mathbf{2p_7}$	0.113	0.887	0.000	0.000
$\mathbf{2p_6}$	0.779	0.221	0.000	0.000
$\mathbf{2p_5}$	0.000	1.000	0.000	0.000
$\mathbf{2p_4}$	0.006	0.036	0.456	0.501
$\mathbf{2p_3}$	0.010	0.031	0.000	0.958
$\mathbf{2p_2}$	0.042	0.000	0.609	0.348
$\mathbf{2p_1}$	0.000	0.036	0.000	0.964

Table 5.4: Overview of cross section sets and calculated rate coefficients as they appear in the MATLAB code.

transition	**cross sections**	**impact**	**type**	**rate coef.**	**format**	**type**
$1s_0 \rightarrow 2p \rightarrow 1s$	`Xe_2p_optical`	e	optical	`ke0`	table	individual
$1s_0 \rightarrow 2p \rightarrow 1s$	`Xe_2p_ion1`	Xe^+	optical	`k1`	vector	individual
$1s_0 \rightarrow 2p \rightarrow 1s$	`Xe_2p_ion2`	Xe^{2+}	optical	`k2`	vector	individual
$1s_0 \rightarrow 1s_5$	`Xe_1s5`	e	BSR+RDW	`k0m`	vector	individual
$1s_5 \rightarrow 1s$	`Xe_1s_met`	e	BSR+RDW	`k1s`	vector	cumulative
$1s_5 \rightarrow 2p$	`Xe_2p_met`	e	BSR+RDW+Exp.	`k2pm`	table	individual
$1s_5 \rightarrow 3p$	`Xe_3p_met`	e	BSR+RDW+Exp.	`k3p`	vector	cumulative
$1s_5 \rightarrow 3d$	`Xe_3d_met`	e	BSR+RDW	`k3d`	vector	cumulative
$1s_5 \rightarrow Xe^+$	`Xe_ion_met`	e	Born-approx.	`kion`	vector	individal

CHAPTER

SIX

Conclusions

"To succeed jump as quickly at opportunities as you do at conclusions."

— Benjamin Franklin

In this last chapter we will summarize the work that has been presented in this thesis as well as the conclusions that can be drawn from them. The chapter is divided according to the three chapters (3-5) containing the original contributions of this work related to plasma probes, the thrust balance and optical emission spectroscopy respectively.

6.1 Plasma Probes

Plasma probes are the oldest plasma diagnostic tool, yet they are still relevant today. This due to the fact that they are the least expensive and most simple method yet can provide a wealth of information on the local plasma parameters.

In this work several plasma diagnostic probes were manufactured: an RF-compensated Langmuir probe, a Faraday Probe and emissive probe a capacitive probe additionally a commercial retarding potential analyser was used. Furthermore a robotic arm system was developed to position the plasma probes in a 2D polar plane in the thruster exhaust plume.

The Langmuir probe was used to measure the ion density, electron temperature and the plasma potential. (Langmuir probes can also be used to measure the electron density however in magnetized plasmas this may not yield correct values.)

In plasmas with strong RF potential fluctuations, as is the case for helicon plasmas RF compensation of the Langmuir probe is necessary for correct measurements of the electron temperature which can otherwise be significantly overestimated. RF

compensation was achieved by the implementation of a series of RF chokes close to the probe tip in combination with a capacitively coupled secondary electrode, also close to the tip and exposed to the plasma. Measurements of the local plasma potential fluctuations as well as the Debye length, (which is dependent on the plasma density and electron temperature) are necessary to verify whether the compensation circuit is appropriately sized.

The plasma potential oscillations can be measured with the capacitive probe and an oscilloscope, which will show the base frequency and several harmonics of the radio frequency of the thruster, in this case 13.56 MHz. In the measurements performed in this work, the amplitude of the first harmonic was about 8% with 4% and 1% for the second and third harmonic from which it is clear that the oscillations are dominated by the base frequency. The electron temperature and plasma density however, are measured with the probe whose correct operation is to be verified. To correctly assess whether the obtained Langmuir probe measurements are correct they have to be combined with capacitive probe measurements and a post hoc analysis should be performed to verify correct compensation of the RF oscillations. Furthermore it is important to perform this verification procedure at various downstream positions as the both the Debye length and the amplitude of the oscillations change in the plasma plume. Here we found that although the Debye length increases downstream which reduces the efficacy of the compensation, the amplitude of the oscillations decreased sufficiently such that the requirement for compensation was met. However, this cannot be assumed a priori and should therefore be assessed when operating conditions change. Most plasma parameters (ion density, electron temperature and plasma potential) were obtained from fitting the $I-V$ curve. However, some attempts were made to obtain the electron energy distribution function (EEDF) from the second derivative of the $I-V$ curve. These attempts resulted in long duration measurements with high precision (i.e. long measurement times) and sufficient points as well as smoothing in post processing to mitigate the noise amplification inherent in numerical differentiation of noisy signals. Despite this effort only in a small number of cases did this yield useful EEDFs. Other methods, such as the Boyd-Twiddy method should be pursued for this purpose.

Although not the purpose of this work, some characterization of the HPTx plume was performed, to demonstrate the utility of the plasma probes, from which some

conclusions can be drawn. Firstly the plasma density is has a Gaussian shape near the axis ($\pm 20°$) with a constant density beyond that. The density in the source is estimated to be of the order of $10^{18}\mathrm{m}^{-3}$, consistent with a helicon plasma, dropping about two orders of magnitude over the first 300 mm. Increasing the magnetic field helps focus the plasma, leading to a higher on- and near-axis densities. On the contrary the electron temperature showed a double peaked profile, with typical peak values of 15-25 eV depending on the operating conditions and measurement location. The electron temperature decreases downstream, while the peaks then to merge downstream. This results in non-monotonic on-axis electron temperature curve with a local maximum somewhere 100-200 mm downstream. Increasing the magnetic field resulted in higher overall electron temperatures. Increasing the RF power did no noticeably affect neither the density nor the temperature. The plasma potential also has a slightly double peak profile, but less pronounced than the electron temperature and it tends to flatten further downstream. Increasing the magnetic field makes the potential peaks more pronounced. It has to be noted that Langmuir probe measurements were only obtained from 100-400 mm downstream. Measurements closer to the thruster yielded the non-sensible results and showed perturbation of the plasma, such as plasma stream tubes visibly connecting to the probe tip. In some case, for example for higher magnetic fields strength, even measurements in the 100-200 mm region were difficult or impossible. Lastly also has to be noted that it is imperative that the (cylindrical) Langmuir probe is aligned with the plasma flow, for which the polar coordinate system (as opposed to a Cartesian system) of the robotic arm system are a necessity.

The Faraday probe is probably the most simple measurement of all the plasma probes both in execution as well as in post processing. A custom made probe, was used to obtain ion current density measurements of the plasma plume, in particular its azimuthal distribution in the far plume (300-400 mm downstream). These measurements were used to infer both the total beam current and from it the utilization efficiency as well as the plume divergence angle and divergence efficiency. The azimuthal ion current density profile is well fitted with a central Gaussian with a half-width at half maximum (HWHM) of 16-18° and two smaller Gaussians centered at $\pm 40°$ with each a HWHM of around 26-28°. The parameters of the off-axis peaks can differ somewhat depending on the operating point (mass flow rate, magnetic field, etc.) However the HWHM of the central peak seems to be independent

of the operating point and rather a feature of the magnetic topology. In fact, normalized (with the peak value) curves of different operating points result in a similar curve for the near axis (±20°) range. Decreasing the magnetic field seems to shift the off-axis peaks more towards the center to around ±30°. The amplitude of these off-axis peaks varies between 10-20% of the central peak, depending on the mass flow rate and the magnetic field.

Generally both increasing the mass flow rate and the magnetic field lead to higher beam currents, while higher mass flow rates leads to lower utilization efficiency, while a higher magnetic field leads to a lower utilization efficiency. The utilization efficiency of Xenon is higher, by about a factor 2 for Xenon, with respect to Argon.

6.2 Thrust Balance

In chapter 4 a mechanically amplified thrust balance was presented, designed specifically for helicon thrusters. This design has several advantages such as increased sensitivity; a more compact form factor; a displacement sensor mounted on the main structure, far away from the source of disturbances; among other advantages mentioned throughout this work.

A dynamic model of the balance was developed based on Lagrangian mechanics. This model was able to reproduce the results of the static analysis of earlier work while also able to calculate the time-response of the thrust balance and analyze the required damping force.

The model predicted an angular magnification of 31°/° and a stiffness of 9.65 mN/mm in agreement with the static model. It also showed that the system is equivalent to a damped harmonic oscillator and predicts a natural frequency of 0.38 Hz when loaded with a 5.2 kg thruster (6.9 kg including the 1.7 kg mounting structure), within 8% of the measured value of 0.41 Hz.

The thrust balance includes a viscous damping system based on eddy currents, with a variable damping ratio. The damping system was modeled using Comsol and the calculated damping ratio was in good agreement with the measured value. It was shown that a damping ratio of 0.78 is optimal resulting in the lowest settling time of 1.8 s.

The balance was equipped with a calibration system based on a voice-coil

mounted on a load-cell. The addition of the load cell mitigates any uncertainties in the voice coil's force constant. Calibration of the balance yielded a stiffness 20% larger than predicted by the model. Coincidentally, when verifying the force constant using this setup it was found that it is 21% higher than specified in the data sheet. This could indicate that the load cell calibration is affected by the fact that it is loaded laterally. If the load cell indeed over-predicts the force it could explain the difference between the model and the measurement. However, this needs be verified, e.g., by cross-comparison with a different calibration system.

Coupling between the solenoid of the helicon thruster and the magnet of the voice coil was observed, which poses a minor inconvenience during thrust measurements. The stiffness of the thrust balance loaded with a 5 kg thruster and corrected for relative position of the calibration system and the thruster is 12.7 mN/mm, almost 20% higher than expected from the models. However, correcting the stiffness with the ratio between the force per current ratio of the voice coil as reported by the manufacturer and the measured one, yields a stiffness of 10.4 mN/mm in exact agreement with the prediction of our model. This lends credence to the hypothesis that the load cell sensitivity has increased 20%, probably due to loading and orientation, and thereby over-predicting the stiffness.

The design further includes liquid metal connectors to mitigate the contribution of the power cables to the overall stiffness, on-board electronics to minimize electrical feed-through connections, leveling system to keep the balance aligned with the local horizontal, and a confocal chromatic displacement sensor with 0.4 μm resolution and 12 mm range that is impervious to EMI. Another novelty is the active water cooling of the thruster mounting plate. This acts as a thermal sink for the thruster shielding the thrust balance from the heat load. We have shown that the water cooling increases the noise by a factor 6 from 0.5 μm to 2.9 μm (equivalent to 6 and 37 μN). Currently the water cooling is supplied from the facility's water net which does not have a regulated outlet pressure. This could be improved with a closed loop, dedicated chiller with more accurate pressure control.

The thrust balance performance has been validated by testing the HPTx platform. The relative uncertainty on the thrust measurement was 2% in this particular case and dominated by the noise induced by the opening and closing of the RF generator valve which generated a water hammer that reverberated through the cooling lines. It is expected that this can be reduced to $\leq 1\%$ by decoupling the water cool-

ing system. A set of thrust measurements was performed at 450W and different mass flow rates for a first direct characterization of the HPTx prototype. For a mass flow rate of 5-20 sccm, thrust ranges from 2.0-5.7 mN, specific impulse from 296-421 s and the efficiency from 1.0-2.1%.

Current thrust measurements require the antenna to be decoupled from the moving part of the balance. Although possible in the current prototypes this will no longer be the case for future versions where the antenna will be fully integrated. A contactless power coupling mechanism was proposed that allows for mechanically decoupling the RF power line from the thruster provided the thruster presents itself as a 50Ω load. The system is based on capacitive power coupling, with inductive compensation. It was shown by simulation and measurement that the system can effectively couple power (up to 50W) with over 90% transmission efficiency. The transmission can be fine-tuned by varying the distance between the capacitive electrodes.

6.3 Optical Emission Spectroscopy

The third diagnostic developed in this work and documented in chapter 5 of this thesis was a Xenon collisional-radiative model for the extraction of the electron temperature from low resolution optical emission spectroscopy data. The model was a refined implementation of Karabadzhak-Chiu-Dressler (KCD) model which was successfully applied to Hall-effect thrusters. The main advantage of OES is the ability to access the source region of the thruster without perturbing the plasma.

The model is a reduced collisional-radiative model, i.e. a Corona model and considers 11 NIR lines emanating from the Xe I $2p$ levels for which optical emission cross sections are available both from the ground state (due to electron impact and ion impact) as well as the metastable state (only electron impact). To estimate the metastable state a rate balance equation is solved considering direct excitation from the ground state as well as cascades from the $2p$ levels as a source channel. The loss channels are excitation to the $3p, 3d$ and other $1s$ levels as well as to $2p$ levels scaled with the branching ratio of decay to $1s$ levels other than the $1s_5$ level and lastly ionization. The model produces the lines emission as a function of electron temperature for the 11 NIR lines.

The main assumptions of the model are: a) collisional quenching is negligible

with respect to spontaneous emission which was found to be the case for $T_e < 20$ eV, $n < 10^{18}$ m^{-3}; b) diffusion loss of the metastable level is negligible, which doesn't unequivocally hold for all cases and was found to depend on the plasma conditions; c) excitation from the $1s_3$ level can be neglected, which was found to be true; d) the electrons follow a Maxwell-Boltzmann distribution, a common and reasonable assumption in the absence of relevant data.

Cross sections for all processes are obtained from a variety of sources and include apparent cross sections obtained from B-spline R-matrix and Relativistic Distorted Wave calculations as well as experimentally obtained apparent and optical emission cross-sections. In many cases multiple cross-sections sets were combined to span a sufficient range of impact energies. The rate coefficients are calculated assuming a Maxwellian energy distribution for the electrons. All calculations are performed in a MATLAB script.

All cross sections used are either those of the original work, or updated data sets of the same sources. For example, optical emission cross sections for $1s_5 \rightarrow 3p$ not available at the time of the original work have been added to replace theoretical cross sections. Three more lines, not included in the KCD model (992.3 nm, 980.0 nm, 895.2 nm) have been added.

The model was implemented in MATLAB to automatize processing of emission spectra. All cross section data is stored into `.mat` files. A MATLAB script loads the cross sections, calculates the rate coefficients, metastable fraction and the corresponding line intensities for a range of electron temperatures. This array of line intensities as a function of electron temperature is then compared to the experimental spectra by calculating the χ^2. The temperature for which χ^2 is minimum is assumed to be the actual electron temperature.

The model has been validated as much as possible against data available in the work of Dressler et al. Using the model to process the only line emission data set published yielded similar results as the KCD model, within 10%. However comparison of the $1s_5$ population fraction as a function of the electron temperature as calculated by our model and the KCD model yielded noticeable results above 5 eV, with the results diverging by more than 20%, the cause of which has not been identified.

The model was subsequently applied to spectroscopic data from the HPT05M thruster, obtained radially at the exit plane as well as on axis. Looking at the

relative difference between the calculated and measured line intensities as a function of electron temperature showed that several lines did not produce a minimum in the 1-30 eV range, while others produced a minimum a disparate temperatures. In other words there was little internal consistency between the different emission lines.

As set of measurements obtained at different mass flow rates were processed and the resulting electron temperatures were compared to estimates from Langmuir probe and RPA data. Although the trend seemed reasonable: decreasing temperature with mass flow rate, the magnitude of the measurements where off by a factor 3-4. Where RPA and LP data showed temperatures between 4-16 eV the OES measurements reported results in the range of 2-4 eV. The reason for this unacceptably large discrepancy has not yet been established.

Multiple possible reasons were considered: the new cross sections used yield different if not incorrect results; the structure of the HPT plasma results in line integrated measurements combining light produced by very different plasma conditions that doesn't fit well to a single temperature and lastly: the assumptions of the model do not hold for the conditions of the HPT plasma, in particularly neglecting the metastable diffusion. The first two reasons are easy to check for, while the latter two require further investigation.

6.4 Future Work

Although much has been accomplished in this work, it is by no means conclusive. The topics treated in this thesis require further investigation. A general comment valid in all cases is that this work has focused on the development of diagnostic tools for characterization of helicon plasma thrusters, rather than on their application to the latter. The diagnostics developed in this work should be used to investigate and improve the performance of the helicon plasma thruster in particular as well as other thrusters developed at EP2.

In the area of probe diagnostics, it would be of interest to develop a setup implementing the Boyd-Twiddy method to measure directly the electron energy distribution function. Measurements which are not only interesting in and of themselves but could also inform the collisional-radiative model for the OES. Furthermore a comparison of indirect thruster characterization (combining FP and RPA data) and

direct thruster measurements are interesting to see if indirect characterization can be reliably used for performance estimates.

Regarding the thrust balance, firstly a proper thrust measurement campaign of the helicon thruster is in order. Furthermore it would be of interest to implement a second, ideally gravimetric calibration method, for cross calibration of the current calibration system as well as for use with thrusters using permanent magnets. Interaction of the latter with the voice coil interferes with the correct operation of the calibration system. And thirdly, the wireless power coupling module should be tested at high power (>50W) and implemented on the thrust balance to mechanically decouple the RF line. Lastly, decoupling of the thrust balance cooling circuit from the facility would help improve the noise.

Future work on the collisional-radiative model should focus on improving the model until it yields sensible results. Another check of all cross sections used as well as the code implementation would be the first step to identify any overlooked errors. Secondly the code could be updated to include only the original cross sections used by Dressler et al. If possible more data could be obtained from Dressler et al. to compare both models more in depth, although it is doubtful that after 10+ years much data can be obtained. (For this work the authors have already provided us with the cross section data.) Applying the model to measurements from a better understood plasma source such as a simple ICP or CCP discharge would help identify whether the issue is with the model or with the plasma. In case the line integration over different plasma conditions is the culprit, augmenting the experimental setup to be able to take measurements at different angles and/or different chords and using a Radon or Abel transform to obtain localized data could be a solution.

Bibliography

[1] E. Ahedo. Plasma dynamics in a helicon thruster. In *Proceedings of EUCASS 2011, 4-8 July 2011, Saint Petersburg, Russia*, paper 118, 2011.

[2] Eduardo Ahedo, Sara Correyero, Jaume Navarro, and Mario Merino. Macroscopic and parametric study of a kinetic plasma expansion in a paraxial magnetic nozzle. *Plasma Sources Science and Technology*, 29(4):045017, 2020.

[3] Eduardo Ahedo and Mario Merino. Two-dimensional supersonic plasma acceleration in a magnetic nozzle. *Physics of Plasmas*, 17(7):073501, 2010.

[4] Eduardo Ahedo and Mario Merino. Two-dimensional plasma expansion in a magnetic nozzle: separation due to electron inertia. *Physics of Plasmas*, 19(8):083501, 2012.

[5] Eduardo Ahedo and Jaume Navarro-Cavallé. Helicon thruster plasma modeling: Two-dimensional fluid-dynamics and propulsive performances. *Physics of Plasmas*, 20(4):043512, 2013.

[6] Michael Allan, Oleg Zatsarinny, and Klaus Bartschat. Near-threshold absolute angle-differential cross sections for electron-impact excitation of argon and xenon. *Physical Review A*, 74(3):030701, 2006.

[7] S.A. Andersen, V.O. Jensen, P. Nielsen, and N D'Angelo. Continuous supersonic plasma wind tunnel. *The Physics of Fluids*, 12(3):557–560, 1969.

[8] BM Annaratone and N St J Braithwaite. A comparison of a passive (filtered) and an active (driven) probe for rf plasma diagnostics. *Measurement Science and Technology*, 2(8):795, 1991.

[9] Marcelo Renato Anselmo and R Intini Marques. Torsional thrust balance for electric propulsion application with electrostatic calibration device. *Measurement Science and Technology*, 30(5):055903, 2019.

[10] Jae-Sung Bae, Moon K Kwak, and Daniel J Inman. Vibration suppression of a cantilever beam using eddy current damper. *Journal of Sound and Vibration*, 284(3-5):805–824, 2005.

[11] O.V. Batishchev. Minihelicon plasma thruster. *IEEE Transactions on Plasma Science*, 37(8):1563–1571, 2009.

[12] Brian E Beal, Alec D Gallimore, and William A Hargus Jr. Plasma properties downstream of a low-power hall thruster. *Physics of plasmas*, 12(12):123503, 2005.

[13] Paul M Bellan. *Fundamentals of plasma physics*. Cambridge University Press, 2008.

[14] John B Boffard, RO Jung, LW Anderson, and CC Lin. Electron-impact excitation of rare-gas atoms from the ground level and metastable levels. *Advances in Atomic Molecular and Optical Physics*, 54:320, 2007.

[15] John B Boffard, Chun C Lin, and Charles A DeJoseph Jr. Application of excitation cross sections to optical plasma diagnostics. *Journal of Physics D: Applied Physics*, 37(12):R143, 2004.

[16] John B Boffard, Chun C Lin, and Amy E Wendt. Application of excitation cross-section measurements to optical plasma diagnostics. In *Advances In Atomic, Molecular, and Optical Physics*, volume 67, pages 1–76. Elsevier, 2018.

[17] Federico Boni, Julien Jarrige, and Victor Désangles. A numerical and experimental study of the curling probe: application to electron density measurements in ecr and icp plasma sources. In *47th EPS Conference on Plasma Physics*, volume 45, pages O1–301, 2021.

[18] A Boschi and F Magistrelli. Effect of an rf signal on the characteristic of a langmuir probe. *Il Nuovo Cimento (1955-1965)*, 29(2):487–499, 1963.

[19] I.D. Boyd. Computation of the plume of an anode-layer Hall thruster. *J. Propulsion Power*, 16(5):902–909, 2000.

[20] Robert Lewis Fullarton Boyd and ND Twiddy. Electron energy distributions in plasmas. i. *Proceedings of the Royal Society of London. Series A. Mathematical and Physical Sciences*, 250(1260):53–69, 1959.

[21] GR Branner, EM Friar, and G Medicus. Automatic plotting device for the second derivative of langmuir probe curves. *Review of Scientific Instruments*, 34(3):231–237, 1963.

[22] Daniel L Brown, Mitchell LR Walker, James Szabo, Wensheng Huang, and John E Foster. Recommended practice for use of faraday probes in electric propulsion testing. *Journal of Propulsion and Power*, 33(3):582–613, 2016.

[23] Juan F Caneses and Boyd Blackwell. Rf compensation of double langmuir probes: modelling and experiment. *Plasma Sources Science and Technology*, 24(3):035024, 2015.

[24] Enrico Canuto and Andrea Rolino. Nanobalance: An automated interferometric balance for micro-thrust measurement. *ISA transactions*, 43(2):169–187, 2004.

[25] Leonard Cassady, Benjamin Longmier, Chris Olsen, Maxwell Ballenger, Greg McCaskill, Andrew Illin, Mark Carter, Tim Glover, Jared Squire, Franklin Chang Diaz, et al. Vasimr performance results. In *46th AIAA/ASME/SAE/ASEE Joint Propulsion Conference & Exhibit*, page 6772, 2010.

[26] Vernon H Chaplin, Mary Konopliv, Timothy Simka, Lee K Johnson, Robert B Lobbia, and Richard E Wirz. Insights from collisional-radiative models of neutral and singly-ionized xenon in hall thrusters. In *AIAA Propulsion and Energy 2021 Forum*, page 3378, 2021.

[27] C. Charles, R.W. Boswell, and M.A. Lieberman. Xenon ion beam characterization in a helicon double layer thruster. *Applied Physics Letters*, 89(26):261503, 2006.

[28] C. Charles, R.W. Boswell, and K. Takahashi. Boltzmann expansion in a radiofrequency conical helicon thruster operating in xenon and argon. *Applied Physics Letters*, 102:223510, 2013.

[29] F.F. Chen. Plasma ionization by helicon waves. *Plasma Physics and Controlled Fusion*, 33(4):339, 1991.

[30] Francis F Chen. Time-varying impedance of the sheath on a probe in an rf plasma. *Plasma Sources Science and Technology*, 15(4):773, 2006.

[31] Xin Chen and J.R. Sanmartin. Low work-function thermionic emission and orbital-motion-limited ion collection at bare-tether cathodic contact. *Physics of Plasmas*, 22(5):053504, 2015.

[32] Yu-hui Chiu, Brad L Austin, Skip Williams, Rainer A Dressler, and George F Karabadzhak. Passive optical diagnostic of xe-propelled hall thrusters. i. emission cross sections. *Journal of applied physics*, 99(11):113304, 2006.

[33] Anthony G Cofer, Stephen D Heister, and Alina Alexeenko. Improved design and characterization of micronewton torsional balance thrust stand. In *49th AIAA/ASME/SAE/ASEE Joint PropulsionConference*, page 3856. 2013.

[34] B Crowley and S Dietrich. A langmuir probe system incorporating the boyd–twiddy method for eedf measurement applied to an inductively coupled plasma source. *Plasma Sources Science and Technology*, 18(1):014010, 2008.

[35] K Dannenmayer, P Kudrna, M Tichỳ, and S Mazouffre. Measurement of plasma parameters in the far-field plume of a hall effect thruster. *Plasma Sources Science and Technology*, 20(6):065012, 2011.

[36] Héctor Oscar Di Rocco and Alicia Cruzado. The voigt profile as a sum of a gaussian and a lorentzian functions, when the weight coefficient depends only on the widths ratio. *Acta Physica Polonica A*, 122, 2012.

[37] Rainer A Dressler, Yu-hui Chiu, Oleg Zatsarinny, Klaus Bartschat, Rajesh Srivastava, and Lalita Sharma. Near-infrared collisional radiative model for xe plasma electrostatic thrusters: the role of metastable atoms. *Journal of Physics D: Applied Physics*, 42(18):185203, 2009.

[38] Mari Johan Druyvesteyn. Der niedervoltbogen. *Zeitschrift für Physik*, 64(11-12):781–798, 1930.

[39] Casey C Farnell, Cody C Farnell, Shawn C Farnell, and John D Williams. Recommended practice for use of electrostatic analyzers in electric propulsion testing. *Journal of Propulsion and Power*, 33(3):638–658, 2017.

[40] U Flender, BH Nguyen Thi, K Wiesemann, NA Khromov, and NB Kolokolov. Rf harmonic suppression in langmuir probe measurements in rf discharges. *Plasma Sources Science and Technology*, 5(1):61, 1996.

[41] John T Fons and Chun C Lin. Measurement of the cross sections for electron-impact excitation into the 5 p 5 6 p levels of xenon. *Physical Review A*, 58(6):4603, 1998.

[42] A Ganguli, BB Sahu, and RD Tarey. A new structure for rf-compensated langmuir probes with external filters tunable in the absence of plasma. *Plasma Sources Science and Technology*, 17(1):015003, 2007.

[43] RK Gangwar, Rajesh Srivastava, et al. Collisional-radiative model of xenon plasma with calculated electron-impact fine-structure excitation cross-sections. *Plasma Sources Science and Technology*, 28(2):025003, 2019.

[44] RK Gangwar, Rajesh Srivastava, et al. Electron excitation cross sections of fine-structure (5p 5 6s–5p 5 6p) transitions in xenon. In *Quantum Collisions and Confinement of Atomic and Molecular Species, and Photons*, pages 172–179. Springer, 2019.

[45] BE Gilchrist, Shawn G Ohler, and Alec D Gallimore. Flexible microwave system to measure the electron number density and quantify the communications impact of electric thruster plasma plumes. *Review of Scientific Instruments*, 68(2):1189–1194, 1997.

[46] Robert J Goldston and Paul Harding Rutherford. *Introduction to plasma physics*. CRC Press, 1995.

[47] V. Gómez, A. Gimńez, M. Ruiz, J. Navarro-Cavallé, P. Fajardo, M. Wijnen, and E. Ahedo. Rf power-plasma coupling experimental results in a helicon plasma thruster prototype. In 36^{th} *International Electric Propulsion Conference*, number IEPC-2019-365, Vienna, Austria, 2019. Electric Rocket Propulsion Society.

[48] Ph Guittienne, E Chevalier, and Ch Hollenstein. Towards an optimal antenna for helicon waves excitation. *Journal of Applied Physics*, 98(8):083304, 2005.

[49] WE Harbaugh. Tungsten, thoriated-tungsten, and thoria emitters. *Electron Tube Design*, pages 90–98, 1962.

[50] T Harle, SJ Pottinger, and VJ Lappas. Helicon double layer thruster operation in a low magnetic field mode. *Plasma Sources Science and Technology*, 22(1):015015, 2012.

[51] T Harle, SJ Pottinger, VJ Lappas, C Charles, RW Boswell, and M Perren. Thrust measurements of a small scale helicon double layer thruster. In *32th International Electric Propulsion Conference*, IEPC 2011-103, 2011.

[52] Franz Georg Hey, Andreas Keller, Claus Braxmaier, Martin Tajmar, Ulrich Johann, and Dennis Weise. Development of a highly precise micronewton thrust balance. *IEEE Transactions on Plasma Science*, 43(1):234–239, 2014.

[53] GD Hobbs and JA Wesson. Heat flow through a langmuir sheath in the presence of electron emission. *Plasma Physics*, 9(1):85, 1967.

[54] LM Hoyos-Campo, AM Juarez, and A Capella. Enhanced resolution in argon and neon spectra using a super-resolution algorithm. *EPL (Europhysics Letters)*, 113(4):43001, 2016.

[55] Pedro Jiménez, Mario Merino, and Eduardo Ahedo. Wave propagation and absorption in a helicon plasma thruster and its plume. *Plasma Sources Science and Technology*, 31(4):045009, 2022.

[56] RO Jung, John B Boffard, LW Anderson, and Chun C Lin. Electron-impact excitation cross sections from the xenon j= 2 metastable level. *Physical Review A*, 72(2):022723, 2005.

[57] RO Jung, John B Boffard, LW Anderson, and Chun C Lin. Excitation into 5 p 5 7 p levels from the ground level and the j= 2 metastable level of xe. *Physical Review A*, 80(6):062708, 2009.

[58] George F Karabadzhak, Yu-hui Chiu, and Rainer A Dressler. Passive optical diagnostic of xe propelled hall thrusters. ii. collisional-radiative model. *Journal of applied physics*, 99(11):113305, 2006.

[59] Andrea Kodys, Robert Murray, Leonard Cassady, and Edgar Choueiri. An inverted-pendulum thrust stand for high-power electric thrusters. In *42nd AIAA/ASME/SAE/ASEE Joint Propulsion Conference & Exhibit*, page 4821, 2006.

[60] K.O.N. *Semion Single/Multi System Installation and User Guide*. Impedans Plasmas Measurment.

[61] Mary Konopliv, Lee K Johnson, Vernon H Chaplin, Robert B Lobbia, Anirudh Thuppul, Timothy Simka, and Richard E Wirz. Collisional-radiative models of neutral and singly-ionized xenon in hall thrusters: Experimental validation and model investigations. In *AIAA Propulsion and Energy 2021 Forum*, page 3390, 2021.

[62] Hans-Joachim Kunze. *Introduction to plasma spectroscopy*, volume 56. Springer Science & Business Media, 2009.

[63] Daisuke Kuwahara, Shunjiro Shinohara, and Kazuki Yano. Thrust characteristics of high-density helicon plasma using argon and xenon gases. *Journal of Propulsion and Power*, 33(2):420–424, 2017.

[64] Trevor Lafleur. Helicon plasma thruster discharge model. *Physics of Plasmas*, 21(4):043507, 2014.

[65] James G Laframboise. Theory of spherical and cylindrical langmuir probes in a collisionless, maxwellian plasma at rest. Technical report, Toronto University Downsview (Ontario) Institute for Aerospace Studies, 1966.

[66] JA Lehane and PC Thonemann. An experimental study of helicon wave propagation in a gaseous plasma. *Proceedings of the Physical Society (1958-1967)*, 85(2):301, 1965.

[67] Dan Lev, Roger M Myers, Kristina M Lemmer, Jonathan Kolbeck, Hiroyuki Koizumi, and Kurt Polzin. The technological and commercial expansion of electric propulsion. *Acta Astronautica*, 159:213–227, 2019.

[68] Michael A Lieberman and Alan J Lichtenberg. *Principles of plasma discharges and materials processing*. John Wiley & Sons, 2005.

[69] JM Little and EY Choueiri. Critical condition for plasma confinement in the source of a magnetic nozzle flow. *IEEE Transactions on Plasma Science*, 43(1):277–286, 2014.

[70] JM Little and EY Choueiri. Electron cooling in a magnetically expanding plasma. *Physical review letters*, 117(22):225003, 2016.

[71] Justin M Little and Edgar Choueiri. Influence of the applied magnetic field strength on flow collimation in magnetic nozzles. In *50th AIAA/ASME/SAE/ASEE Joint Propulsion Conference*, page 3912, 2014.

[72] Robert B Lobbia and Brian E Beal. Recommended practice for use of langmuir probes in electric propulsion testing. *Journal of Propulsion and Power*, pages 1–16, 2017.

[73] Fei Lu, Hua Zhang, and Chris Mi. A review on the recent development of capacitive wireless power transfer technology. *Energies*, 10(11):1752, 2017.

[74] Ch Lukas, M Müller, V Schulz-von der Gathen, and HF Döbele. Spatially resolved electron density distribution in an rf excited parallel plate plasma reactor by 1 mm microwave interferometry. *Plasma Sources Science and Technology*, 8(1):94, 1999.

[75] Mirko Magarotto, Marco Manente, Fabio Trezzolani, and Daniele Pavarin. Numerical model of a helicon plasma thruster. *IEEE Transactions on Plasma Science*, 48(4):835–844, 2020.

[76] M Martinez-Sanchez, J Navarro-Cavallé, and E Ahedo. Electron cooling and finite potential drop in a magnetized plasma expansion. *Physics of Plasmas*, 22(5):053501, 2015.

[77] M. Martínez-Sánchez and J.E. Pollard. Spacecraft electric propulsion — an overview. *Journal of Propulsion and Power*, 14(5):688–699, September 1998.

[78] Stéphane Mazouffre. Laser-induced fluorescence diagnostics of the cross-field discharge of hall thrusters. *Plasma Sources Science and Technology*, 22(1):013001, 2012.

[79] Stéphane Mazouffre. Electric propulsion for satellites and spacecraft: established technologies and novel approaches. *Plasma Sources Science and Technology*, 25(3):033002, 2016.

[80] Davide Melazzi, D Curreli, M Manente, J Carlsson, and Daniele Pavarin. Spires: A finite-difference frequency-domain electromagnetic solver for inhomogeneous magnetized plasma cylinders. *Computer Physics Communications*, 183(6):1182–1191, 2012.

[81] Davide Melazzi and Vito Lancellotti. Adamant: A surface and volume integral-equation solver for the analysis and design of helicon plasma sources. *Computer Physics Communications*, 185(7):1914–1925, 2014.

[82] Mario Merino and Eduardo Ahedo. Simulation of plasma flows in divergent magnetic nozzles. *IEEE Transactions on Plasma Science*, 39(11):2938–2939, 2011.

[83] Mario Merino and Eduardo Ahedo. Two-dimensional quasi-double-layers in two-electron-temperature, current-free plasmas. *Physics of Plasmas*, 20(2):023502, 2013.

[84] Mario Merino and Eduardo Ahedo. Plasma detachment in a propulsive magnetic nozzle via ion demagnetization. *Plasma Sources Science and Technology*, 23(3):032001, 2014.

[85] Mario Merino and Eduardo Ahedo. Influence of electron and ion thermodynamics on the magnetic nozzle plasma expansion. *IEEE Transactions on Plasma Science*, 43(1):244–251, Jan 2015.

[86] Mario Merino, Javier Mauriño, and Eduardo Ahedo. Kinetic electron model for plasma thruster plumes. *Plasma Sources Science and Technology*, 27(3):035013, 2018.

[87] J Meunier. Ph. belenquer, and j.-p. boeuf. *J. Appl. Phys*, 78:731, 1995.

[88] Andrew J Morin, Rebecca Osborn, Jeff C Schindler, Precious Jagun, Douglas G Fletcher, and Jason M Meyers. Inductively coupled facility qualification for electron transpiration cooling investigations. In *AIAA Scitech 2020 Forum*, page 0921, 2020.

[89] G Narasimhan and Ch Steinbrüchel. Analysis of langmuir probe data: Analytical parametrization, and the importance of the end effect. *Journal of Vacuum Science & Technology A: Vacuum, Surfaces, and Films*, 19(1):376–378, 2001.

[90] J Navarro-Cavallé, M Wijnen, P Fajardo, and E Ahedo. Experimental characterization of a 1 kw helicon plasma thruster. *Vacuum*, 149:69–73, 2018.

[91] J Navarro-Cavallé, M Wijnen, P Fajardo, and E Ahedo. Experimental characterization of a 1 kw helicon plasma thruster. *Vacuum*, 149:69–73, 2018.

[92] Jaume Navarro-Cavallé, Mick Wijnen, Pablo Fajardo, Eduardo Ahedo, V. Gómez, A. Giménez, and M. Ruiz. Development and characterization of the helicon plasma thruster prototype hpt-03. In 36^{th} *International Electric Propulsion Conference*, number IEPC-2019-596, Vienna, Austria, 2019. Electric Rocket Propulsion Society.

[93] National Institute of Standards and Technology (NIST). Atomic spectra database. https://www.nist.gov/pml/atomic-spectra-database. Accessed: 2022-05-29.

[94] University of Wisconsin. Atomic collisions group. http://raptor.physics.wisc.edu/. Accessed: 2022-05-25.

[95] Yuya Oshio, Tomohiro Shimada, and Hiroyuki Nishida. Experimental investigation of thrust performance on position relationship between rf antenna and magnetic cusp of rf plasma thruster. In *35th international electric propulsion conference, Atlanta, Georgia, USA. IEPC-2017-344*, 2017.

[96] Dillon O'Reilly, Georg Herdrich, and Darren F Kavanagh. Electric propulsion methods for small satellites: A review. *Aerospace*, 8(1):22, 2021.

[97] A Pancotti, T Haag, S King, and M Walker. Recommended practices in thrust measurements. In *33rd International Electric Propulsion Conference*, IEPC-2013-440, 2013.

[98] RB Piejak, J Al-Kuzee, and N St J Braithwaite. Hairpin resonator probe measurements in rf plasmas. *Plasma Sources Science and Technology*, 14(4):734, 2005.

[99] Kurt A Polzin, Carrie S Hill, Peter J Turchi, Rodney L Burton, Sarah Messer, Ralph H Lovberg, and Ashley K Hallock. Recommended practice for use of inductive magnetic field probes in electric propulsion testing. *Journal of Propulsion and Power*, 33(3):659–667, 2017.

[100] Kurt A Polzin, Thomas E Markusic, Boris J Stanojev, Amado DeHoyos, and Benjamin Spaun. Thrust stand for electric propulsion performance evaluation. *Review of Scientific Instruments*, 77(10):105108, 2006.

[101] S. Pottinger, V. Lappas, C. Charles, and R. Boswell. Performance characterization of a helicon double layer thruster using direct thrust measurements. *Journal of Physics D: Applied Physics*, 44(23):235201, 2011.

[102] LXCat project. Lxcat database. https://nl.lxcat.net/home/. Accessed: 2022-05-11.

[103] A Qayyum, N Ahmad, S Ahmad, Farah Deeba, Rafaqat Ali, and S Hussain. Time-resolved measurement of plasma parameters by means of triple probe. *Review of Scientific Instruments*, 84(12):123502, 2013.

[104] Francesco Romano, Y-A Chan, Georg Herdrich, C Traub, S Fasoulas, PCE Roberts, K Smith, S Edmondson, S Haigh, NH Crisp, et al. Rf helicon-based inductive plasma thruster (ipt) design for an atmosphere-breathing electric propulsion system (abep). *Acta Astronautica*, 176:476–483, 2020.

[105] Aiko K Ruprecht, Christof Pruss, Hans J Tiziani, Wolfgang Osten, Peter Lucke, Arndt Last, Jurgen Mohr, and Peter Lehmann. Confocal micro-optical distance sensor: principle and design. In *Optical Measurement Systems for Industrial Inspection IV*, volume 5856, pages 128–135. International Society for Optics and Photonics, 2005.

[106] Álvaro Sánchez-Villar, Jiewei Zhou, Eduardo Ahedo, and Mario Merino. Coupled plasma transport and electromagnetic wave simulation of an ecr thruster. *Plasma Sources Science and Technology*, 30(4):045005, 2021.

[107] Adam Shabshelowitz and Alec D Gallimore. Performance and probe measurements of a radio-frequency plasma thruster. *Journal of Propulsion and Power*, 29(4):919–929, 2013.

[108] Adam Shabshelowitz and Alec D Gallimore. Performance and probe measurements of a radio-frequency plasma thruster. *Journal of Propulsion and Power*, 29(4):919–929, 2013.

[109] Adam Shabshelowitz, Alec D Gallimore, and Peter Y Peterson. Performance of a helicon hall thruster operating with xenon, argon, and nitrogen. *Journal of Propulsion and Power*, 30(3):664–671, 2014.

[110] Konstantin P Shamrai and Vladimir B Taranov. Volume and surface rf power absorption in a helicon plasma source. *Plasma Sources Science and Technology*, 5(3):474, 1996.

[111] Lalita Sharma, Rajesh Srivastava, and AD Stauffer. Electron impact excitation of the 5p57p levels of xenon from 5p56s metastable states. 185(1):012042, 2009.

[112] JP Sheehan and N Hershkowitz. Emissive probes. *Plasma Sources Science and Technology*, 20(6):063001, 2011.

[113] JP Sheehan, Yevgeny Raitses, Noah Hershkowitz, and Michael McDonald. Recommended practice for use of emissive probes in electric propulsion testing. *Journal of Propulsion and Power*, 33(3):614–637, 2016.

[114] Shunjiro Shinohara. Helicon high-density plasma sources: Physics and applications. *Advances in Physics: X*, 3(1):1420424, 2018.

[115] M. Umair Siddiqui, C. Cretel, J. Synowiec, Andrea G. Hsu, Jason A. Young, and R. Spektor. First performance measurements of the phase four rf thruster. In *35th International Electric Propulsion Conference, Atlanta, GA.*, IEPC-2017-431, 2017.

[116] Umair Siddiqui and Chris Cretel. Updated performance measurements and analysis of the phase four rf thruster. In *2018 Joint Propulsion Conference*, page 4817, 2018.

[117] Boris M Smirnov. *Reference data on atomic physics and atomic processes*, volume 51. Springer Science & Business Media, 2008.

[118] Jason D Sommerville, Lyon B King, Yu-Hui Chiu, and Rainer A Dressler. Ion-collision emission excitation cross sections for xenon electric thruster plasmas. *Journal of Propulsion and Power*, 24(4):880–888, 2008.

[119] Rajesh Srivastava, AD Stauffer, and Lalita Sharma. Excitation of the metastable states of the noble gases. *Physical Review A*, 74(1):012715, 2006.

[120] Isaac D Sudit and Francis F Chen. Rf compensated probes for high-density discharges. *Plasma Sources Science and Technology*, 3(2):162, 1994.

[121] K. Takahashi. Helicon-type radiofrequency plasma thrusters and magnetic plasma nozzles. *Reviews of Modern Plasma Physics*, 3:3, 2019.

[122] K. Takahashi, T. Lafleur, C. Charles, P. Alexander, and R.W. Boswell. Electron diamagnetic effect on axial force in an expanding plasma: Experiments and theory. *Physical Review Letters*, 107(23):235001, 2011.

[123] K. Takahashi, T. Lafleur, C. Charles, P. Alexander, R.W. Boswell, M. Perren, R. Laine, S. Pottinger, V. Lappas, T. Harle, et al. Direct thrust measurement of a permanent magnet helicon double layer thruster. *Applied Physics Letters*, 98:141503, 2011.

[124] Kazunori Takahashi. Helicon-type radiofrequency plasma thrusters and magnetic plasma nozzles. *Reviews of Modern Plasma Physics*, 3(1):1–61, 2019.

[125] Kazunori Takahashi, Christine Charles, and Rod Boswell. Approaching the theoretical limit of diamagnetic-induced momentum in a rapidly diverging magnetic nozzle. *Physical review letters*, 110(19):195003, 2013.

[126] Kazunori Takahashi, Christine Charles, Rod Boswell, and Akira Ando. Effect of magnetic and physical nozzles on plasma thruster performance. *Plasma Sources Science and Technology*, 23(4):044004, 2014.

[127] Kazunori Takahashi, Christine Charles, Rod Boswell, and Rikizo Hatakeyama. Radial characterization of the electron energy distribution in a

helicon source terminated by a double layer. *Physics of plasmas*, 15(7):074505, 2008.

[128] Kazunori Takahashi, Christine Charles, Rod W Boswell, and Akira Ando. Demonstrating a new technology for space debris removal using a bi-directional plasma thruster. *Scientific reports*, 8(1):1–10, 2018.

[129] Kazunori Takahashi, Atsushi Komuro, and Akira Ando. Effect of source diameter on helicon plasma thruster performance and its high power operation. *Plasma Sources Science and Technology*, 24(5):055004, 2015.

[130] Kazunori Takahashi, Trevor Lafleur, Christine Charles, Peter Alexander, and Rod W Boswell. Axial force imparted by a current-free magnetically expanding plasma. *Physics of Plasmas*, 19(8):083509, 2012.

[131] Bin Tian, Mario Merino, and Eduardo Ahedo. Two-dimensional plasma-wave interaction in an helicon plasma thruster with magnetic nozzle. *Plasma Sources Science and Technology*, 27(11):114003, 2018.

[132] M Tichỳ, A Pétin, P Kudrna, M Horkỳ, and S Mazouffre. Electron energy distribution function in a low-power hall thruster discharge and near-field plume. *Physics of Plasmas*, 25(6):061205, 2018.

[133] D Ton-That and MR Flannery. Cross sections for ionization of metastable rare-gas atoms (ne*, ar*, kr*, xe*) and of metastable n 2*, co* molecules by electron impact. *Physical Review A*, 15(2):517, 1977.

[134] D Ton-That and MR Flannery. Cross sections for ionization of metastable rare-gas atoms (ne*, ar*, kr*, xe*) and of metastable n 2*, co* molecules by electron impact. *Physical Review A*, 15(2):517, 1977.

[135] F Trezzolani, M Manente, A Selmo, D Melazzi, M Magarotto, D Moretto, P De Carlo, M Pessana, and D Pavarin. Development and test of an high power rf plasma thruster in project sapere-strong. In *Proc. 35th Int. Electr. Propuls. Conf.*, pages 1–9, 2017.

[136] F Trezzolani, M Manente, E Toson, A Selmo, M Magarotto, D Moretto, F Bosi, P De Carlo, D Melazzi, and D Pavarin. Development and testing of a

miniature helicon plasma thruster. In *Proc. 35th Int. Electr. Propuls. Conf.*, pages 1–9, 2017.

[137] S Tsikata, C Honore, and D Gresillon. Collective thomson scattering for studying plasma instabilities in electric thrusters. *Journal of Instrumentation*, 8(10):C10012, 2013.

[138] O Tudisco, A Lucca Fabris, C Falcetta, L Accatino, R De Angelis, M Manente, F Ferri, M Florean, C Neri, C Mazzotta, et al. A microwave interferometer for small and tenuous plasma density measurements. *Review of Scientific Instruments*, 84(3):033505, 2013.

[139] Théo Vialis, Julien Jarrige, Ane Aanesland, and Denis Packan. Direct thrust measurement of an electron cyclotron resonance plasma thruster. *Journal of Propulsion and Power*, 34(5):1323–1333, 2018.

[140] Benjamin Vincent, Sedina Tsikata, Stéphane Mazouffre, Tiberiu Minea, and Jérôme Fils. A compact new incoherent thomson scattering diagnostic for low-temperature plasma studies. *Plasma Sources Science and Technology*, 27(5):055002, 2018.

[141] Yang Wang, Yan-Fei Wang, Xi-Ming Zhu, Oleg Zatsarinny, and Klaus Bartschat. A xenon collisional-radiative model applicable to electric propulsion devices: I. calculations of electron-impact cross sections for xenon ions by the dirac b-spline r-matrix method. *Plasma Sources Science and Technology*, 28(10):105004, 2019.

[142] Mick Wijnen. Magnetic nozzels - experimental characterisation of the plume expansion in the magnetic nozzel of a helicon plasma thruster. Master's thesis, Delft University of Technology, Delft, The Netherlands, May 2017.

[143] Logan T Williams and Mitchell LR Walker. Thrust measurements of a radio frequency plasma source. *Journal of Propulsion and Power*, pages 1–8, 2013.

[144] Logan T Williams and Mitchell LR Walker. Initial performance evaluation of a gridded radio frequency ion thruster. *Journal of Propulsion and Power*, 30(3):645–655, 2014.

[145] Kunning G Xu and Mitchell LR Walker. High-power, null-type, inverted pendulum thrust stand. *Review of Scientific Instruments*, 80(5):055103, 2009.

[146] Juan Yang, Shigeru Yokota, Ryotaro Kaneko, and Kimiya Komurasaki. Diagnosing on plasma plume from xenon hall thruster with collisional-radiative model. *Physics of Plasmas*, 17(10):103504, 2010.

[147] Yuan-Xia Yang, Liang-Cheng Tu, Shan-Qing Yang, and Jun Luo. A torsion balance for impulse and thrust measurements of micro-newton thrusters. *Review of Scientific Instruments*, 83(1):015105, 2012.

[148] CV Young, A Lucca Fabris, NA MacDonald-Tenenbaum, WA Hargus, and MA Cappelli. Time-resolved laser-induced fluorescence diagnostics for electric propulsion and their application to breathing mode dynamics. *Plasma Sources Science and Technology*, 27(9):094004, 2018.

[149] Oleg Zatsarinny and Klaus Bartschat. Benchmark calculations for near-threshold electron-impact excitation of krypton and xenon atoms. *Journal of Physics B: Atomic, Molecular and Optical Physics*, 43(7):074031, 2010.

[150] Hua Zhang, Fei Lu, Heath Hofmann, Weiguo Liu, and Chunting Chris Mi. A four-plate compact capacitive coupler design and lcl-compensated topology for capacitive power transfer in electric vehicle charging application. *IEEE Transactions on Power Electronics*, 31(12):8541–8551, 2016.

[151] Zhen Zhang, Hongliang Pang, Apostolos Georgiadis, and Carlo Cecati. Wireless power transfer—an overview. *IEEE Transactions on Industrial Electronics*, 66(2):1044–1058, 2018.

[152] J. Zhou, A. Domínguez-Vázquez, D. Pérez-Grande, P. Fajardo, and E. Ahedo. An axisymmetric hybrid model for the plasma transport in a helicon plasma thruster. In *Space Propulsion Conference 2018*, number 00308, Seville, Spain, 2018. Association Aéronautique et Astronautique de France.

[153] Jiewei Zhou. *Modeling and simulation of the plasma discharge in a radiofrequency thruster*. PhD thesis, Universidad Carlos III de Madrid, 2021.

[154] Jiewei Zhou, Adrián Domínguez-Vázquez, P Fajardo, and E Ahedo. Magnetized fluid electron model within a two-dimensional hybrid simulation code

for electrodeless plasma thrusters. *Plasma Sources Science and Technology*, 31(4):045021, 2022.

[155] Jiewei Zhou, Pedro Jiménez, Mario Merino, Pablo Fajardo, and Eduardo Ahedo. Numerical Simulations of the Plasma discharge in a Helicon Plasma Thruster. In 36^{th} *International Electric Propulsion Conference*, number IEPC-2019-330, Vienna, Austria, 2019. Electric Rocket Propulsion Society.

[156] Jiewei Zhou, Daniel Pérez-Grande, Pablo Fajardo, and Eduardo Ahedo. Numerical treatment of a magnetized electron fluid model within an electromagnetic plasma thruster simulation code. *Plasma Sources Science and Technology*, 28(11):115004, 2019.

[157] Xi-Ming Zhu, Yan-Fei Wang, Yang Wang, Da-Ren Yu, Oleg Zatsarinny, Klaus Bartschat, Tsanko Vaskov Tsankov, and Uwe Czarnetzki. A xenon collisional-radiative model applicable to electric propulsion devices: Ii. kinetics of the 6s, 6p, and 5d states of atoms and ions in hall thrusters. *Plasma Sources Science and Technology*, 28(10):105005, 2019.

APPENDIX

A

Plasma Probes

A.1 Langmuir Probe Post-processing

```
% Langmuir Probe Post-processing
% Based on "Recommended best practices for Langmuir probe
% measurements in Electric Propulsion", Lobbia, 2007
%
% Version:  1.1
% Date:     05/12/2022
% Author:   M. Wijnen
%-------------------------------------------------------%
close all;
clc;
clearvars -except data
%% Input Parameters
%--------------------Probe properties-------------------%
Rp =  0.127;  %[mm] probe radius
Lp =  1.1;    %[mm] probe length
% Gas properties
AN = 131; %39.95;     %[amu] atomic mass number

%% Preprocessing
%------------------Physical constants-----------------%
e    = 1.60217662e-19;         %[C]   electron charge
me   = 9.109382910e-31;        %[kg]  electron mass
eps0 = 8.854187817e-12;        %[F/m] Vacuum permittivity
```

```
u = 1.660539040e-27;          %[kg]  atomic mass unit
% Calculate secondary constants
Rp = Rp/1e3;                  % scale probe radius
Lp = Lp/1e3;                  % scale probe length
Ap   = 2*pi*Rp*Lp;            %[m^2]  probe surface
AR  = 1+Rp/2/Lp;              %[1]    aspect ratio
mi  = AN*u;                   %[kg]   ion mass
a0  = exp(-0.5);              %[1]    correction factor
%-------------------Data management-------------------%
% Import data as MATLAB table named 'data'
% with column V and column I
V = data.V;          % initialize voltage array
Vmin = V(1);
I = data.I;          % initialize raw current array
I = I/AR;            % correct for front area collection
% Compute number of datapoints & resolution
len = length(I);
dV = V(2)-V(1);
% Plot I-V curve
IVcurve = figure('Name','IV-curve','NumberTitle','off');
figure(IVcurve)
plot(V,I,'o','MarkerSize',3)
hold on; grid on;
xlabel('$V\ [V]$','Interpreter','latex','FontSize',14)
ylabel('$I\ [A]$','Interpreter','latex','FontSize',14)
%------------------Floating Potential-----------------%
% find the index of V <= 0
idxV0 = find(V>=0,1);
% find the index of the first I > 0
idxVf = find(I>0,1);
% interpolate the floating potential
Vf = V(idxVf-1) - I(idxVf-1)*(V(idxVf)-V(idxVf-1))/...
                  (I(idxVf)-I(idxVf-1));
%disp floating potential
```

```
disp(['Floating potential Vf = ' num2str(Vf,'%.1f') 'V'])
%----------------------Ion current----------------------%
% Plot ion collection region
ions = figure('Name','Ion Collection Region','NumberTitle
    ','off');
plot(V(1:idxVf),I(1:idxVf),'o','MarkerSize',3)
hold on; grid on;
xlabel('$V\ [V]$','Interpreter','latex','FontSize',14)
ylabel('$I\ [A]$','Interpreter','latex','FontSize',14)
% Limit ion saturation fit range
disp('Choose right limit for fitting the ion current.')
[x,~] = ginput(1);
[~,idxi] = min(abs(V-x));
% Linear fit of ion saturation current
Ci = polyfit(V(1:idxi),I(1:idxi),1);
%Compute ion current
Ii = Ci(1)*V+Ci(2);
% Plot ion current fit
plot(V,Ii)
xlim([Vmin Vf])
% Compute electron current
Ie = I-Ii;
%--------------------Derivatives----------------------%
% smooth the IV-curve with a moving average filter
Ies = smooth(V,Ie,round(0.02*length(I)),'moving');
% generate the first derivative dI/dV
dIdV = gradient(Ies,V);
%--------------------Estimate phi---------------------%
% Plot derivative dI/dV
deriv = figure('Name','1st Derivative','NumberTitle','off
    ');
plot(V,dIdV)
ylim([0 1.05*max(dIdV)])
xlabel('$V\ [V]$','Interpreter','latex','FontSize',14)
```

```
ylabel('$\frac{dI}{dV}$','Rotation',0,'Interpreter','
   latex','FontSize',18)
grid on; hold on;
% Find plasma potential
[x,~] = ginput(1);
[~,idxPhi] = min(abs(V-x));
Phi = V(idxPhi);
plot(Phi,dIdV(V == Phi),'o');
%disp plasma potential
disp(['Plasma potential phi = ' num2str(Phi,'%.1f') 'V'])
%------------------Electron Current------------------%
%Plot the logarithm of the electron current
electrons = figure('Name','Electron Collection Region','
   NumberTitle','off');
plot(V(idxVf:min(idxPhi+(5/dV),length(V))),...
    log(Ie(idxVf:min(idxPhi+(5/dV),length(V)))),...
    'o','MarkerSize',3)
hold on; grid on;
xlabel('$V\ [V]$','Interpreter','latex','FontSize',14)
ylabel('I\ [A]','Interpreter','latex','FontSize',14)
% Fit electron current
Ce = polyfit(V(idxVf+15/dV:idxPhi),...
             log(Ie(idxVf+15/dV:idxPhi)),1);
Iefit = Ce(1)*V+Ce(2);
% Plot electron current fit
plot(V,Iefit)
xlim([Vf-5 Phi+5]);
ylim([round(min(log(Ie(idxVf:idxPhi))))-1 ...
      round(max(real(log(Ie(idxVf:idxPhi)))))+1]);
ylabel('$\ln(I_e)$','Interpreter','latex','FontSize',14)
xlabel('$V\ [V]$','Interpreter','latex','FontSize',14)
%-------------Estimate plasma parameters------------%
% Compute electron temperature
Te0 = 1/Ce(1);
```

```
disp(['First guess Electron Temperature Te = ' ...
      num2str(Te0,'%0.1f') ' eV'])
% Compute electron density
Ne = (I(idxPhi)/Ap/e)*sqrt(2*pi*me/e/Te0);
disp(['Electron Density ne = ' num2str(Ne,'%0.1e') 'm-3'
   ])
disp('Warning! Electron density underestimated ...
      in magnetized plasmas')
% Compute ion density
Iisat = Ii(idxVf);
Ni0 = -(Iisat/a0/Ap/e)*sqrt(mi/e/Te0);
disp(['First guess Ion Density ni = ' ...
      num2str(Ni0,'%0.1e') ' m-3'])
% Compute Debeye length
LD = sqrt(eps0*Te0/Ni0/e);
if LD > 99e-6
    disp(['Debeye length LD = ' ...
          num2str(LD*1e3,'%0.2f') ' mm'])
else
    disp(['Debeye length LD = ' ...
          num2str(LD*1e6,'%0.2f') ' um'])
end
% Compute probe parameter
Xi = Rp/LD;
if Xi > 50
    disp(['Probe parameter Xi = ' num2str(Xi,'%0.1f')])
    disp('Xi > 50: Thin Sheath Limit')
    theory = 'thin sheath limit';
elseif Xi < 3
    disp(['Probe parameter Xi = ' num2str(Xi,'%0.1f')])
    disp('Xi < 3: Thick Sheath Limit')
    theory = 'thick sheath limit';
else
    disp(['Probe parameter Xi = ' num2str(Xi,'%0.1f')])
```

```
    disp('3 < Xi < 50: Transitional Regime')
    theory = 'transitional regime';
end
%-----------------------------------------------------%
% Initialize relative differential parameters
dTe = 1;
dNi = 1;

while dTe > 0.001 && dNi > 0.001

switch theory
    case 'thin sheath limit'
    % Compute Child-Langmuir sheath
    Xs = (LD*sqrt(2)/3)*((Phi-V)/Te).^(3/4);
    Xs = Xs.*(V<=Vf);
    %IiCL = I./(1+Xs/Rp);
    % Linear fit of ion saturation current
    Ci = polyfit(V(1:idxi),Ii(1:idxi),1);
    % Compute ion density
    Iisat = Ci(1)*Vf+Ci(2);
    % Iisat = mean(IiCL(1:idxVf-(10/dV));
    Ni = -(Iisat/a0/Ap/e)*sqrt(mi/e/Te0);
    %Compute ion current
    Ii = Ci(1)*V+Ci(2);
    % Ii = Iisat*(1+Xs/Rp);

    case 'thick sheath limit'
    % Fit a quadratic curve to the ion current
    Ci = polyfit(V(1:(idxVf-(5/dV))), ...
                 I(1:(idxVf-(5/dV))).^2,1);
    % Compute ion density
    Ni = (pi/Ap)*sqrt(mi/2)*e^(-3/2)*sqrt(-Ci(1));
    % Compute plasma potential
    Vp = Ci(2)/(e*Ni*Ap/pi)^2/(2*e/mi);
```

```
    %Compute ion current
    Ii = -real(sqrt(Ci(1)*V+Ci(2)));

    case 'transitional regime'
    a = 1.18-0.00080*(Rp/LD)^1.35;
    b = 0.0684-(0.722+0.928*(Rp/LD))^-0.729;
    % Fit I^1/b to the ion current
    Ci = polyfit(V(1:idxi),(-I(1:idxi)).^(1/b),1);
    % Compute ion density
    Ni = (1/Ap/a)*sqrt(2*pi*mi)*e^(-3/2)*Te^(b-1/2)* ...
         (-Ci(1))^b;
    %Compute ion current
    Ii = (e*Ni*Ap)*sqrt(e*Te/2/pi/mi)*a*((Phi-V)/Te).^b;
    Ii = Ii.*(V<=Phi);
end
% Compute electron current
Ie = I-Ii;
% Fit electron current
Ce = polyfit(V(idxVf+15/dV:idxPhi),log(Ie(idxVf+15/dV:
   idxPhi)),1);
Iefit = Ce(1)*V+Ce(2);
% Compute electron temperature
Te = 1/Ce(1);
% Compute Debeye length
LD = sqrt(eps0*Te/Ni/e);
% Compute probe parameter
Xi = Rp/LD;
    if LD > 50
        theory = 'thin sheath limit';
    elseif LD < 3
        theory = 'thick sheath limit';
    else
        theory = 'transitional regime';
    end
```

```
% Compute relative errors for last iteration
dTe = abs(Te-Te0)/Te0;
dNi = abs(Ni-Ni0)/Ni0;
% Update Te0,Ni0
Te0 = Te;
Ni0 = Ni;
end

disp(['Ion Density ni = ' num2str(Ni,'%0.1e') ' m-3'])
disp(['Electron Temperature Te = ' num2str(Te0,'%0.1f') '
    eV'])
if exist('Vp')
   disp(['OML Plasma Potential phi = ' num2str(Vp,'%0.1f'
      ) ' V'])
end
figure(ions)
plot(V,Ii)
xlim([Vmin Vf])

figure(electrons)
hold off
plot(V,real(log(Ie)),'o','MarkerSize',3)
hold on; grid on;
plot(V,Iefit)
xlim([Vf-10 Phi+10]);
ylim([round(min(log(Ie(idxVf:idxPhi))))-1 ...
      round(max(real(log(Ie(idxVf:idxPhi)))))+1]);
xlabel('$V\ [V]$','Interpreter','latex','FontSize',14)
ylabel('$\ln{I_e}$','Interpreter','latex','FontSize',14)

%----------------Druyvestein Method-----------------%
% Smooth electron current
Ies = smooth(V,I,'moving',0.02*len);
% Transform to electron energy
```

```
E = Phi-V(idxV0:idxPhi);
Ies = Ies(idxV0:idxPhi);
% Calculate and smooth 1st derivative
dIdV = gradient(Ies,E);
dIdVs = smooth(E,dIdV,'moving',0.05*len);
% Calculate 2nd derivative
d2IdV2 = gradient(dIdVs,E);
% Compute EEDF
EEDF = (2/e^2/Ap)*sqrt(2*me*e*E).*d2IdV2;
% Compute EEPF
EEPF = (2/e^2/Ap)*sqrt(2*me*e).*d2IdV2;
% Plot EEDF
EEDFplot = figure('Name','EEDF','NumberTitle','off');
semilogy(E,EEDF,'o','MarkerSize',3)
grid on
xlabel('$\mathcal{E}\ [eV]$','Interpreter','latex', ...
       'FontSize',14)
ylabel('$EEDF(\mathcal{E})$','Interpreter','latex', ...
       'FontSize',14)
% Plot EEPF
EEPFplot = figure('Name','EEPF','NumberTitle','off');
semilogy(E,EEPF,'o','MarkerSize',3)
grid on
xlabel('$\mathcal{E}\ [eV]$','Interpreter','latex','
   FontSize',14)
ylabel('$EEPF(\mathcal{E})$','Interpreter','latex','
   FontSize',14)
% Compute 0th and 1st moments
N = -trapz(E,EEDF);
T = -(2/3/N)*trapz(E,E.*EEDF);

disp(['Computing EEDF using Druyvestein method'])
disp(['Electron Density = ' num2str(N,'%0.1e') 'm-3'])
disp(['Electron Temperature = ' num2str(T,'%0.1f') 'eV'])
```

APPENDIX

B

Thrust Balance

B.1 Static Model

$$
\begin{aligned}
y &= 2L_{AE}\sin\left(\frac{\theta_2}{2}\right) && \text{(B.1)}\\
\theta_2 &= \theta_1+\theta_3+\theta_4-\pi && \text{(B.2)}\\
\theta_1 &= 2\sin^{-1}\left(\frac{x}{2L_4}\right) && \text{(B.3)}\\
\theta_3 &= \cos^{-1}\left(\frac{L_{OB}^2+L_{AB'}^2-L_{OA}^2}{2L_{OB}L_{AB'}}\right) && \text{(B.4)}\\
&+ \cos^{-1}\left(\frac{L_{AB'}^2+L_{BC}^2-L_{AC}^2}{2L_{AB'}L_{BC}}\right) && \text{(B.5)}\\
\theta_4 &= \cos^{-1}\left(\frac{L_{AC}^2+L_{BC}^2-L_{AB'}^2}{2L_{AC}L_{BC}}\right) && \text{(B.6)}\\
L_{AB'}^2 &= L_{OB}^2+L_{OA}^2-2L_{OB}L_{OA}\cos\left(\gamma+\theta_1\right) && \text{(B.7)}\\
\gamma &= \cos^{-1}\left(\frac{L_{OA}^2+L_{OB}^2-L_{BC}^2-L_{AC}^2}{2L_{OA}L_{OB}}\right) && \text{(B.8)}
\end{aligned}
$$

where $\gamma \equiv \angle AOB$.

The variables L_i denote the length from the centre of mass r_i to its corresponding point of rotation, while L_{jk} is the length between the points j, k.

Note that in the previous equations, it is implicit that θ_3, θ_4 are initially right angles. It can be seen that y is a function of θ_2 which is in turn a function of θ_1, which is a function of x.

The stiffness of the thrust balance can be obtained from a force balance at all four pivots (O, A, B, and C in Fig. 4.1). The resulting relationship between the applied thrust T and the angle θ_1 is given by:

$$
T = \frac{\tau_O+\tau_{B'}}{L_4} + Mg\sin(\theta_1) + \frac{\left(\tau_A+\tau_{C'}\right)L_{OB}\cos\left(\frac{\pi}{2}-\theta_3\right)}{L_4L_{AC}\cos\left(\frac{\pi}{2}-\theta_4\right)} \qquad \text{(B.9)}
$$

where,

$$\tau_O = \kappa_1\theta_1 \qquad \tau_{B'} = \kappa_3\left(\theta_3 - \frac{\pi}{2}\right) \tag{B.10}$$
$$\tau_A = \kappa_2\theta_2 \qquad \tau_{C'} = \kappa_4\left(\theta_4 - \frac{\pi}{2}\right)$$

B.2 Linearized Equations

We can use a Taylor expansion to the first order to linearize the angles θ_2, θ_3 and θ_4 around $\theta = 0$.

$$\theta_3 = \theta_3(0) + [\theta_3'(0)] \cdot \theta \tag{B.11}$$
$$\theta_4 = \theta_4(0) + [\theta_4'(0)] \cdot \theta \tag{B.12}$$
$$\theta_2 = \theta_3(0) + \theta_4(0) - \pi + [1 + \theta_3'(0) + \theta_4'(0)] \cdot \theta \tag{B.13}$$

Here the primes denote a derivative to θ. We simplify this notation by introducing the following nomenclature: $n_3 = \theta_3'$, $n_4 = \theta_4'$ and $n = 1 + \theta_3'(0) + \theta_4'(0)$. We already have the equations for θ_3, θ_4 (eq. (B.5),(B.6)) we only need to find their derivatives. To this end we start by normalizing L_{OA}, L_{BC} and L_{AC} with L_{OB}.

$$p = \frac{L_{OA}}{L_{OB}} \qquad q = \frac{L_{BC}}{L_{OB}} \qquad s = \frac{L_{AC}}{L_{OB}} \tag{B.14}$$

We also introduce the substitution:

$$z(p, \theta, \gamma) = 1 + p^2 - 2p\cos(\theta + \gamma) \tag{B.15}$$

We then rewrite eq. (B.8), (B.5) and (B.6) using the above expressions.

$$\gamma = \cos^{-1}\left(\frac{1 + p^2 - q^2 - s^2}{2p}\right) \tag{B.16}$$
$$\theta_3 = \cos^{-1}\left(\frac{1 - p\cos(\theta + \gamma)}{\sqrt{z(p, \theta, \gamma)}}\right) \tag{B.17}$$
$$+ \cos^{-1}\left(\frac{z(p, \theta, \gamma) + q^2 - s^2}{2q\sqrt{z(p, \theta, \gamma)}}\right) \tag{B.18}$$
$$\theta_4 = \cos^{-1}\left(\frac{s^2 + q^2 - z(p, \theta, \gamma)}{2qs}\right) \tag{B.19}$$

We then take the derivative to θ.

$$\frac{d\theta_3}{d\theta} = \frac{1 - p\cos(\theta + \gamma)}{z(p, \theta, \gamma)} - 1 \tag{B.20}$$

$$- \quad \frac{p\sin(\theta+\gamma)\left[1-\frac{q^2-s^2}{z(p,\theta,\gamma)}\right]}{\sqrt{4q^2s^2-[z(p,\theta,\gamma)-q^2-s^2]^2}} \tag{B.21}$$

$$\frac{d\theta_4}{d\theta} = \frac{2p\sin(\theta+\gamma)}{\sqrt{4q^2s^-[q^2+s^2-z(p,\theta,\gamma)]^2}} \tag{B.22}$$

When we evaluate θ_3, θ_4 and their derivatives at $\theta = 0$ all cosines and sines become a function of γ. When we substitute in eq. (B.8) we get rid of these trigonometric functions and are left with the following:

$$\theta_3(0) = \cos^{-1}\left(\frac{1-p^2+q^2+s^2}{2\sqrt{q^2+s^2}}\right) \tag{B.23}$$

$$+ \quad \cos^{-1}\left(\frac{q^2}{\sqrt{q^2+s^2}}\right) \tag{B.24}$$

$$\theta_3'(0) = \frac{1-p^2-q^2-s^2}{2(q^2+s^2)} \tag{B.25}$$

$$- \quad \frac{s\sqrt{4p^2-(1+p^2-q^2-s^2)^2}}{2q(q^2+s^2)} \tag{B.26}$$

$$\theta_4(0) = \frac{\pi}{2} \tag{B.27}$$

$$\theta_4'(0) = \frac{\sqrt{4p^2-(1+p^2-q^2-s^2)^2}}{2qs} \tag{B.28}$$

For the dimensions given in Tab. 4.4 we find that $p = 0.9786$, $q = 0.1452$ and $s = 0.0323$ resulting in $\theta_3(0) = \pi/2$, $\theta_3'(0) = -1$ and $\theta_4'(0) = 31$. The fac that $\theta_3(0)$ and $\theta_4(0)$ are right angles is something that is designed for on purpose. In that case $\theta_3(0) + \theta_4(0) - \pi$ is zero and the linearized θ_2 does not have an intercept. We can furthermore see that $\theta_3'(0)$ cancels out the 1 and that the angular magnification $n = n_4 = \theta_4'(0) = 31$. If we look at the differential angles for this case we find that:

$$\delta_1(\theta) = \theta \tag{B.29}$$

$$\delta_2(\theta) = \theta_2 = n \cdot \theta \tag{B.30}$$

$$\delta_3(\theta) = \theta_3 - \theta_3(0) = n_3 \cdot \theta \tag{B.31}$$

$$\delta_3(\theta) = \theta_3 - \theta_3(0) = n_4 \cdot \theta \tag{B.32}$$

$$\tag{B.33}$$

APPENDIX

C

Optical Emission Spectroscopy

C.1 Spectrometry MATLab Code

```
clearvars -except data
close all
clc

%% Constants and Variables
global V M
% [1] ion charge fraction: Xe(+)/[Xe(2+) + Xe(+)]
alpha = 0.8;
% [V] ion acceleration voltage
V = 0; %300;
% [u] ion mass
M = 131;
% [m^2*kg/s] Planck constant
h = 6.62607015E-34;
% [m/s] speed of light
c = 299792458;
% Branching fraction for 2p -> 1s_x where x != 5
P = [0.055 0.512 0.000 0.887 0.221
     1.000 0.994 0.990 0.962 1.000];

% Load measurement data.
% Ensure data is stored in table format named 'data.mat'.
% First column is the variable 'Var' i.e. data.Var,
```

```
% other columns correspond to emission lines.
% load('measurements/....')

%% Load cross sections
load('xsections/processed/Xe_2p_optical')
load('xsections/processed/Xe_2p_ion1')
load('xsections/processed/Xe_2p_ion2')
load('xsections/processed/Xe_2p_gamma');
load('xsections/processed/Xe_1s5')
load('xsections/processed/Xe_met_1s')
load('xsections/processed/Xe_met_2p')
load('xsections/processed/Xe_met_3p')
load('xsections/processed/Xe_met_3d')
load('xsections/processed/Xe_met_ion')
% Generate array of T_e values
T = (0:0.1:30)';
% Value for x-form distribution: 1 < x < 2
% 1: Maxwellian, 2: Druyvestein
x = 1;

%% Rate Coefficients
line =  fieldnames(Xe_2p_optical.lines);
level = Xe_met_2p.Properties.VariableNames(2:end);
ke0 = zeros(length(T),length(line));

clear ke0 k0m k2pm k1s k3p k3d kion

for n = 1:length(T)
    % Rate coefficient optical transitions g -> 2p -> g
    for j = 1:length(line)
        ke0(n,j) = ratecoef(Xe_2p_optical.E,
                 Xe_2p_optical.lines.(line{j}).Q,T(n),x);
    end
```

```
    % Rate coefficient ground state to 1s5
    k0m(n) = ratecoef(Xe_1s5.E,Xe_1s5.Q,T(n),x);
    % Rate coefficient 1s5 to 2p levels
    for j = 1:size(Xe_met_2p,2)-1
        k2pm(n,j) = ratecoef(Xe_met_2p.E,
                    Xe_met_2p.(level{j}),T(n),x);
    end
    % Rate coefficients 1s5 to 3d, 3p and other 1s
    k1s(n) = ratecoef(Xe_met_1s.E,Xe_met_1s.Q,T(n),x);
    k3p(n) = ratecoef(Xe_met_3p.E,Xe_met_3p.Q,T(n),x);
    k3d(n) = ratecoef(Xe_met_3d.E,Xe_met_3d.Q,T(n),x);
    % Metastable 1s5 ionization rate coefficient
    kion(n) = ratecoef(Xe_met_ion.E,Xe_met_ion.Q,T(n),x);
end
% Turn array into table.
ke0 = array2table(ke0);
ke0.Properties.VariableNames = line;
k2pm = array2table(k2pm);
k2pm.Properties.VariableNames = level;
% Ion impact rate coefficients
k1 = ionimpact(Xe_2p_ion1,1);
k2 = ionimpact(Xe_2p_ion2,2);

%% Calculate metastable fraction
met = {};
for j = 1:length(line)
    if Xe_2p_optical.lines.(line{j}).lower == '1s5'
       met = [met; line{j}];
    end
end
Nm = (k0m + sum(ke0{:,met},2) +
      sum(alpha*k1{:,met} + 0.5*(1-alpha)*k2{:,met}))
   ./(sum(k2pm{:,:}.*P,2) + k3p + k3d + k1s + kion);
```

```
% Plot metastable fraction vs electron temperature
figure(1)
plot(T,100*Nm)
xlabel('Electron Temperature [eV]','interpreter','Latex')
ylabel('1s$_5$ fraction [\%]', 'Interpreter','Latex')
grid on

%% Calculate Line Intensity
for i = 1:size(Xe_2p_gamma,1)
    kem(:,i) = k2pm.(['p' num2str(Xe_2p_gamma.level(i),
               '%d')])*Xe_2p_gamma.gamma(i);
end
% Define wavelength.
lambda = Xe_2p_gamma.line;
% Line intensity.
J = 1E38*(h*c./lambda').*(ke0{:,:} + Nm.*kem
    + alpha*k1{:,:} + 0.5*(1-alpha)*k2{:,:});
% Note that 1E38 is an estimate of n_e*n_n ~ 1E18*1E20
% Normalize to sum of intensities.
J = J./sum(J,2);

%% Estimate Electron Temperature
for ii = 1:height(data)
    Iexp = data{ii,2:end};
    Iexp = Iexp/sum(Iexp);
    % Calcualte chi-squared.
    Q = J./Iexp;
    Chi2 = mean((Q-1).^2,2);

    % Plot chi-squared vs electron temperature
    figure(3)
    semilogy(T,Chi2,'LineWidth',1)
    hold on; grid on;
```

```
    xlabel('electron temperature (eV)','Interpreter','
       latex')
    ylabel('$\chi^2$','Interpreter','latex')
    ax = gca;
    ax.FontSize = 14;

    % Find minimum
    [~,idx] = min(Chi2);
    % Find electron temperature
    Te(ii) = T(idx);
    % Display electron temperature
    disp(['Te = ' num2str(Te(ii),'%.1f') ' eV'])
end

% Plot electron temperature vs variable (mfr, power,
   magnetic field etc.)
figure(4)
plot(data.Var,Te,'LineWidth',1)
grid on
ylabel('electron temperature (eV)','Interpreter','latex')
ax = gca;
ax.FontSize = 14;

%% Functions
function k = ratecoef(E,sigma,T,x)
% Function for calculating the electron impact excitation
    rate coefficient.
    % [C] elementary charge
    e = 1.60217662E-19;
    % [kg] electron mass
    m = 9.10938356E-31;
    % Coefficients for x-form distribution.
    c1 = x*(2/3)^(3/2)*(gamma(5/2/x))^(3/2)
         /(gamma(3/2/x))^(5/2);
```

```
    c2 = (2/3)^x*(gamma(5/2/x)/gamma(3/2/x))^x;
    % Calculate distribution function.
    f = c1*sqrt(E)*T^(-3/2).*exp(-c2*(E/T).^x);
    % Define velocity.
    v = sqrt(2*e*E/m);
    % Calculate rate coefficient.
    k = trapz(E,v.*f.*sigma);
    k = k';
end

function k = ionimpact(xsection,Z)
% Function for calculating the ion impact excitation rate
    coefficient
% Z: ion charge number
    global V M
    % [kg] atomic mass unit
    u = 1.66053906660E-27;
    % [C] elementary charge
    e = 1.60217662E-19;
    % Define velocity.
    v = sqrt(2*Z*e*V/M/u);
    % Get line.
    line = fieldnames(xsection.lines);
    % Calculate rate coefficient.
    for j = 1:length(line)
        k(j) = v*interp1(xsection.E,
              xsection.lines.(line{j}).Q,Z*V,'linear',0);
    end
    % Turn array into table.
    k = array2table(k);
    k.Properties.VariableNames = line;
end
```

C.2 Cross Section Data

Table C.1: Optical emission cross section (in 10^{-18} cm^2) for NIR emission lines due to electron impact excitation of the Xe(I) $2p$ levels, by courtesy of Dr. Dressler.

	λ (nm)										
E (eV)	788.7	823.3	828.0	834.7	841.0	881.9	895.0	904.5	916.3	980.0	992.3
10.00	0.0020	0.0371	0.0230	0.0100	0.0035	0.0928	0.0183	0.0237	0.0381	0.0468	0.0453
12.00	0.0058	2.2328	1.6786	0.0219	0.1428	7.0132	1.1047	1.2763	1.5370	2.2854	2.4340
15.00	1.0865	11.3480	9.4240	3.9624	1.2040	37.3971	5.6146	7.1417	12.9547	18.0855	13.6191
17.00	1.4906	13.2517	12.1735	4.9641	1.4692	39.1529	6.5565	8.7819	15.8084	19.2895	16.7469
19.00	1.7946	13.1893	15.4613	5.3211	1.5591	35.0386	6.5256	8.8905	16.7763	17.2973	16.9541
21.00	2.3927	12.1278	19.2323	5.3845	1.5526	27.8657	6.0004	8.2724	16.7062	14.5840	15.7753
23.00	2.9210	10.1916	20.5231	4.8581	1.3721	20.9357	5.0425	7.3109	14.7641	10.9819	13.9418
25.00	3.5438	8.4996	21.6009	4.4111	1.2520	16.2899	4.2053	6.5670	13.4719	8.7267	12.5231
27.00	3.1894	6.6695	19.9992	3.4787	1.0267	11.0207	3.2998	5.1746	11.0475	6.1669	9.8678
29.00	3.2124	6.4770	19.6604	3.4300	1.0213	9.8119	3.2046	4.8588	10.9894	5.5082	9.2656
31.00	3.0457	6.3478	19.0282	3.4179	1.0248	8.9634	3.1407	4.7934	11.0263	5.2555	9.1408
35.00	2.7061	6.0516	17.7971	3.3556	0.9959	7.3442	2.9941	4.7695	10.7162	4.0951	9.0952
40.00	2.0491	5.2202	15.5515	3.0411	0.9123	5.4240	2.5828	4.3346	9.8160	3.4960	8.2659
45.00	1.7792	5.0911	15.1699	2.8583	0.9254	5.0250	2.5189	4.1613	9.9568	3.2946	7.9355
50.00	1.6962	4.8109	14.6547	2.6891	0.9174	4.6590	2.3803	3.9538	9.8708	3.1310	7.5397
55.00	1.7674	4.7905	15.0114	2.6633	0.9296	4.6239	2.3702	4.0229	10.0028	3.2128	7.6716
60.00	1.9835	4.5722	14.6261	2.5198	0.8855	4.2861	2.2622	3.8972	9.5281	2.8947	7.4318
65.00	1.6673	3.8939	12.7551	2.1524	0.7897	3.4409	1.9266	3.3848	8.4976	2.5226	6.4547
70.00	1.1603	3.4716	11.7506	1.9153	0.7213	2.9182	1.7177	3.0577	7.7611	2.1706	5.8310
80.00	1.0658	3.2609	11.3072	1.7755	0.6952	2.7595	1.6134	2.9037	7.4801	2.0411	5.5373
90.00	0.9909	3.0857	10.9300	1.6606	0.6729	2.6266	1.5267	2.7743	7.2408	1.9334	5.2905
100.00	0.9297	2.9370	10.6033	1.5642	0.6536	2.5133	1.4531	2.6635	7.0331	1.8418	5.0791
110.00	0.8786	2.8087	10.3161	1.4818	0.6367	2.4149	1.3896	2.5670	6.8505	1.7628	4.8952
120.00	0.8351	2.6964	10.0608	1.4104	0.6215	2.3285	1.3341	2.4820	6.6878	1.6935	4.7331
130.00	0.7975	2.5971	9.8315	1.3478	0.6080	2.2517	1.2849	2.4063	6.5416	1.6323	4.5887
140.00	0.7646	2.5084	9.6238	1.2922	0.5956	2.1829	1.2411	2.3382	6.4091	1.5775	4.4590
150.00	0.7356	2.4285	9.4344	1.2426	0.5844	2.1207	1.2016	2.2766	6.2882	1.5282	4.3415

Table C.2: Optical emission cross section (in 10^{-18} cm^2) for NIR emission lines due to ion impact excitation by Xe^+ of the Xe(I) $2p$ levels, from [118]

	λ (nm)										
E (eV)	788.7	823.3	828.0	834.7	841.0	881.9	895.0	904.5	916.3	980.0	992.3
100	0.112	10.1	2.60	0.73	0.83	29.3	3.67	11.5	6.05	18.1	17.4
200	0.416	17.8	2.90	2.16	1.16	45.3	6.49	19.6	19.4	30.1	28.4
300	0.475	25.4	3.27	2.85	1.55	54.6	8.55	23.6	24.8	39.7	36.5
400	0.493	26.1	4.42	2.94	1.86	57.8	10.5	25.0	32.1	34.8	37.7
500	0.547	32.1	5.49	3.49	2.08	60.4	11.2	25.8	42.5	42.0	45.0
600	0.464	31.2	4.97	3.67	2.12	62.0	11.2	24.8	39.0	39.6	35.1
700	0.515	33.3	4.79	3.82	2.28	62.0	11.9	25.2	36.5	36.0	38.0
800	0.573	38.1	5.22	4.18	2.66	68.9	13.6	29.1	45.6	38.1	42.8
900	0.589	37.9	5.14	4.11	2.57	66.5	13.7	27.3	42.6	34.1	40.3

Table C.3: Optical emission cross section (in 10^{-18} cm^2) for NIR emission lines due to ion impact excitation by Xe^{2+} of the Xe(I) $2p$ levels, from [118]

	λ (nm)										
E (eV)	788.7	823.3	828.0	834.7	841.0	881.9	895.0	904.5	916.3	980.0	992.3
200	0.000	3.15	0.68	1.17	0.360	6.99	1.22	1.83	2.30	1.51	1.52
400	0.270	5.14	0.87	1.98	0.606	9.90	2.06	3.65	6.04	4.27	5.40
600	0.425	6.80	1.17	2.54	0.877	12.8	2.69	4.17	7.88	6.75	6.26
800	0.376	6.17	1.03	2.49	0.702	11.4	2.56	3.83	6.89	4.05	5.00
1000	0.427	5.90	1.06	2.37	0.748	10.7	2.36	3.56	6.46	4.00	4.94
1200	0.398	5.64	0.98	2.43	0.740	11.4	2.31	3.93	7.12	4.35	5.62
1400	0.356	5.00	0.99	2.51	0.696	9.76	2.09	3.22	5.55	3.31	4.18
1600	0.449	6.08	1.11	2.44	0.728	10.5	2.29	4.03	7.09	4.99	5.60
1800	0.452	5.71	1.14	2.62	0.876	11.1	2.4	3.92	6.9	4.57	5.58

Table C.4: Fitting coefficients of RDW results for excitation from the ground state. From [43][44].

transition	E (eV)	b_0	b_1	b_2	b_3	c_0	c_1	c_2
$1s_0 \rightarrow 1s_5$	$E_{th} - 90$	7.8866×10^{-2}				3.0361	−6.6126	4.0172
	90 - 1000	4.6820×10^{-2}				5.2838×10^{-1}	-3.8888×10^{-1}	8.0583
$1s_0 \rightarrow 2p_{10}$	$E_{th} - 80$	1.9910×10^{-2}	-9.7100×10^{-3}	7.4665×10^{-4}	-5.0700×10^{-2}	-6.0716×10^{1}	1.0757×10^{2}	-5.1772×10^{1}
	$80 - 200$	1.0984				3.3189×10^{2}	-4.1172×10^{2}	1.2918×10^{2}
	$200 - 1000$	-3.1026×10^{-5}	2.2590×10^{-7}	6.8979×10^{-5}		1.8031×10^{2}	-5.3398×10^{1}	4.1852
$1s_0 \rightarrow 2p_9$	$E_{th} - 100$	−1.8521	1.0219×10^{1}	-4.2500×10^{-3}	1.4679×10^{4}	-1.0289×10^{2}	-2.5139×10^{2}	-1.4409×10^{3}
	$100 - 1000$	1.3479				2.1317	3.9210	7.6264×10^{-4}
$1s_0 \rightarrow 2p_8$	$E_{th} - 100$	-5.4400×10^{-3}	1.5916×10^{5}			3.2681×10^{6}	-6.7930×10^{6}	7.7521×10^{6}
	$100 - 200$	-6.2454×10^{-4}	5.1328×10^{-1}			-1.3194×10^{3}	3.6997×10^{2}	6.0326×10^{1}
	$200 - 1000$	-2.6894×10^{-5}	2.0128×10^{-7}	6.3865×10^{-5}		1.6995×10^{2}	-5.3516×10^{1}	4.4449
$1s_0 \rightarrow 2p_7$	$E_{th} - 80$	3.4010×10^{-2}				1.2815×10^{1}	-1.8149×10^{1}	9.2537
	$80 - 300$	3.576×10^{-2}	−3.5608					
	$300 - 1000^{\dagger}$	3.011×10^{-2}	−3.5337					
$1s_0 \rightarrow 2p_6$	$E_{th} - 50$	-3.0920×10^{-2}	-8.4500×10^{-3}	3.4707×10^{1}		1.7348×10^{2}	-3.3769×10^{2}	4.9717×10^{2}
	$50 - 1000$	7.5561×10^{-1}				4.5032	5.8817	1.2570×10^{-2}
$1s_0 \rightarrow 2p_5$	$E_{th} - 70$	1.0818	2.5260×10^{-2}			9.3725×10^{-1}	−1.5712	6.8408×10^{-1}
	$70 - 200$	-3.8067×10^{-1}	3.5950×10^{-2}	8.6913×10^{-1}		1.5012×10^{1}	-1.1588×10^{1}	2.8564
	$200 - 1000$	−2.8506	-2.1500×10^{-3}	4.4474		3.5587	−1.5891	1.4977
$1s_0 \rightarrow 2p_4$	$E_{th} - 25$	2.9106×10^{-4}	2.9840×10^{-2}			5.1557	-1.5350×10^{1}	1.3424×10^{1}
	$25 - 80$	2.015 95				2.7279×10^{2}	-3.6703×10^{2}	2.7466×10^{2}
	$80 - 200^{\dagger}$	5.2600×10^{-2}	−3.4736					
	$200 - 1000^{\dagger}$	5.5250×10^{-2}	−3.5000					
$1s_0 \rightarrow 2p_3$	$E_{th} - 100$	2.6500×10^{-3}	1.2460×10^{-1}			2.2344	−1.4046	1.3265
$1s_0 \rightarrow 2p_2$	$E_{th} - 20$	2.5758×10^{-4}				5.4381	-2.2118×10^{1}	2.2498×10^{1}
	$20 - 100$	-1.4955×10^{-1}	4.0044×10^{-1}	-2.3700×10^{-3}	3.3853	−3.7074	−1.3743	−8.9987
	$100 - 300$	-3.7367×10^{-5}	1.1530×10^{-2}			1.7725×10^{2}	-1.4612×10^{2}	3.1877×10^{1}
	$300 - 1000$	3.6810×10^{-2}	−3.3045					
$1s_0 \rightarrow 2p_1$	$E_{th} - 50$	1.9487×10^{-1}	-1.1222×10^{-1}	7.7131×10^{-1}		1.1674	−1.9697	1.2195
	$50 - 100$	4.2434				1.3417	7.8567×10^{-1}	-2.9950×10^{-2}
	$100 - 1000$	7.2682×10^{-1}	-2.2216×10^{-1}	-1.2071×10^{-5}	1.2406	-7.6469×10^{1}	1.4519×10^{1}	5.6388

Table C.5: Fitting coefficients of RDW results for excitation from the $1s_5$ level. From [43][44].

transition	E (eV)	b_0	b_1	b_2	c_0	c_1	c_2
$1s_5 \rightarrow 1s_4$	$E_{th} - 20$	4.6855×10^{-1}			-8.9910×10^{-1}	8.2880×10^{-1}	8.6022×10^{-1}
	$20 - 1000$	9.0147×10^{-4}	2.8059×10^{10}		-2.1069×10^{10}	6.0095×10^{9}	9.4849×10^{10}
$1s_5 \rightarrow 1s_3$	$E_{th} - 10$	2.0797×10^{-1}	1.7685×10^{2}		9.0259×10^{1}	-1.1643×10^{3}	4.8841×10^{3}
	$10 - 1000$	8.4943×10^{-1}			8.5920×10^{-1}	2.9539	-1.2770×10^{-2}
$1s_5 \rightarrow 1s_2$	$E_{th} - 10$	4.0006×10^{-1}	4.9601×10^{-1}		2.1633×10^{-1}	−2.8644	1.0807×10^{-1}
	$10 - 100$	1.5210×10^{-2}	1.2785		6.9435×10^{-1}	−1.5859	4.1219
	$100 - 1000$	1.4229			−2.7520	4.3649	-3.1040×10^{-2}
$1s_5 \rightarrow 2p_{10}$	$E_{th} - 1000$	2.6098×10^{1}			1.5121×10^{-1}	3.2918×10^{-1}	1.6700×10^{-2}
$1s_5 \rightarrow 2p_9$	$E_{th} - 10$	3.9755×10^{-4}	7.2257×10^{5}		-3.0221×10^{3}	2.5272×10^{4}	8.0034×10^{4}
	$10 - 1000$	1.0122×10^{1}			1.0684×10^{-1}	2.3120×10^{-1}	7.4400×10^{-2}
$1s_5 \rightarrow 2p_8$	$E_{th} - 1000$	3.6499×10^{2}	1.2666×10^{-1}	-3.9480×10^{4}	6.1273	6.5354×10^{1}	1.0580×10^{2}
$1s_5 \rightarrow 2p_7$	$E_{th} - 10$	7.0814			1.9165×10^{-1}	2.3946	−2.5172
	$10 - 1000$	2.5173			1.531×10^{-1}	3.1449×10^{-1}	8.6500×10^{-3}
$1s_5 \rightarrow 2p_6$	$E_{th} - 10$	7.3764×10^{-6}	1.8704×10^{8}		-2.4360×10^{5}	3.6945×10^{6}	6.2914×10^{6}
	$10 - 1000$	2.3404×10^{1}			1.3008×10^{-1}	2.5480×10^{-1}	4.5500×10^{-3}
$1s_5 \rightarrow 2p_5$	$E_{th} - 10$	1.2579×10^{1}	-3.1775×10^{1}		4.0798×10^{1}	-5.4764×10^{2}	2.0071×10^{3}
	$10 - 200$	4.9200×10^{-3}	-4.1720×10^{1}				
	$200 - 1000$	3.4700×10^{-2}					
$1s_5 \rightarrow 2p_4$	$E_{th} - 10$	4.8510×10^{-2}			−2.6937	$2.423\,88 \times 10^{1}$	2.8147×10^{1}
	$10 - 200$	2.0074×10^{1}	-4.1720×10^{1}		2.2740×10^{2}	$2.373\,48 \times 10^{2}$	−1.1196
	$200 - 1000$	1.4891×10^{2}			7.0555×10^{3}	$1.644\,23 \times 10^{4}$	4.3993×10^{2}
$1s_5 \rightarrow 2p_3$	$E_{th} - 10$	1.6970×10^{-2}	1.6418×10^{-1}	1.2860×10^{-2}	1.1657	−9.5431	2.0322×10^{1}
	$10 - 1000$	-2.1300×10^{-3}	-4.1720×10^{1}		4.8117×10^{4}	6.0709×10^{5}	5.5174×10^{5}
$1s_5 \rightarrow 2p_2$	$E_{th} - 10$	9.0160×10^{-2}	6.7293×10^{-1}	6.7626×10^{-1}	1.0771×10^{1}	-8.7902×10^{1}	1.8948×10^{2}
	$10 - 1000$	8.2549×10^{-1}			1.8115	1.1182	4.6650×10^{-2}
$1s_5 \rightarrow 3p_{10}$	$E_{th} - 10$	1.266 31			7.6023×10^{-1}	-5.0730×10^{-2}	8.9156×10^{-1}
	$10 - 100$	1.236 49			4.8765×10^{-1}	9.2608×10^{-1}	2.8600×10^{-3}
	$100 - 1000$	4.476 78			1.639 97	3.198 58	4.5610×10^{-2}
$1s_5 \rightarrow 3p_9$	$E_{th} - 10$	$8.316\,90 \times 10^{-1}$	5.364 77		−1.534	6.807 79	$1.774\,60 \times 10^{1}$
	$10 - 100$	1.221 65			3.5609×10^{-1}	1.363 13	-1.0080×10^{-2}
	$100 - 1000$	3.185 83			8.8656×10^{-1}	3.368 55	2.2290×10^{-2}
$1s_5 \rightarrow 3p_8$	$E_{th} - 20$	5.522 53	−4.727 01	$1.479\,64 \times 10^{2}$	$-8.440\,78 \times 10^{1}$	$4.633\,67 \times 10^{2}$	-2.5418×10^{2}
	$20 - 1000$	1.2855			$1.512\,10 \times 10^{-1}$	$4.301\,80 \times 10^{-1}$	-3.5833×10^{-4}
$1s_5 \rightarrow 3p_7$	$E_{th} - 100$	1.871 87			$2.862\,40 \times 10^{-1}$	$6.557\,20 \times 10^{-1}$	1.1090×10^{-2}
	$100 - 1000$	8.9062			1.186 47	3.163 57	2.8930×10^{-2}
$1s_5 \rightarrow 3p_6$	$E_{th} - 10$	3.836 32			−6.770 63	$3.856\,29 \times 10^{1}$	$3.920\,73 \times 10^{1}$
	$10 - 100$	$6.861\,20 \times 10^{-1}$			$9.012\,00 \times 10^{-2}$	6.001 36	-2.6719×10^{-1}
	$100 - 1000$	1.430 78			2.069 97	9.867 59	4.8690×10^{-2}

Table C.6: RDW direct cross sections for excitation from the $1s_5$ metastable to $2p_5$-$2p_1$ levels, values in 10^{-16} cm^2. From Priti et. al. [43]. Note the difference in order of magnitude $\mathcal{O}(10^2)$ with the next table.

E (eV)	$2p_{10}$	$2p_9$	$2p_8$	$2p_7$	$2p_6$
10	26.7	14.9	69.6	2.7	29.4
11	25.4	14.1		2.5	28.1
12	24.4	13.5		2.4	27.2
15	21.2	11.8	55.8	2.1	23.8
18	19.0	10.6		1.9	21.6
20	18.0	9.9	47.5	1.8	20.5
25	15.3	8.6		1.6	17.6
30	13.5	7.6	37.4	1.4	15.6
35	12.0	6.8		1.2	14.1
40	10.9	6.2		1.1	12.8
45	9.9	5.7		1.0	11.7
50	9.1	5.2	25.4	0.9	10.8
60	7.7	4.5		0.8	9.3
70	6.7	3.9		0.7	8.2
75			17.7		
80	5.9	3.4		0.6	7.2
90	5.2	3.0		0.6	6.4
100	4.7	2.7	13.3	0.5	5.8
120	3.8	2.2		0.4	4.8
140	3.2	1.9		0.4	4.0
150			8.5		
160	2.7	1.6		0.3	3.5
180	2.4	1.4		0.3	3.5
200	2.1	1.2	6.1	0.2	3.1
250	1.6	0.9	0.0	0.2	2.4
300	1.3	0.7	3.7	0.1	1.9
350	1.0	0.6		0.1	1.6
400	0.9	0.5	2.5	0.1	1.3
450	0.8	0.4		0.1	1.1
500	0.7	0.4		0.1	1.0
600	0.5	0.3		0.1	0.8
700	0.4	0.2		0.0	0.6
800	0.3	0.2			0.5
900	0.3	0.2		0.0	0.4
1000	0.3	0.1		0.0	0.4

Table C.7: RDW direct cross sections for excitation from the $1s_5$ metastable to $2p_5$-$2p_1$ levels, values in 10^{-18} cm^2. From Priti et al. [43]. Note the difference in order of magnitude $\mathcal{O}(10^{-2})$ with the previous table.

E (eV)	$2p_5$	$2p_4$	$2p_3$	$2p_2$	$2p_1$
10	3.32	0.18	2.26	10.00	0.04
11	2.46	0.18	2.28	10.10	0.03
12	1.88	0.17	2.27	10.00	0.02
15	0.81	0.16	2.20	9.74	0.01
18	0.57	0.15	2.08	9.18	0.01
20	0.40	0.14	1.99	8.81	0.00
25	0.20	0.13	1.85	8.21	0.01
30	0.11	0.11	1.69	7.48	0.00
35	0.07	0.11	1.55	6.90	0.00
40	0.04	0.10	1.44	6.41	0.00
45	0.03	0.09	1.35	6.00	0.00
50	0.02	0.09	1.27	5.64	0.00
60	0.01	0.08	1.14	5.05	0.00
70	0.01	0.07	1.03	4.57	0.00
80	0.01	0.06	0.94	4.18	0.00
90	0.00	0.06	0.86	3.84	0.00
100	0.00	0.05	0.80	3.54	0.00
120	0.00	0.05	0.69	3.05	0.00
140	0.00	0.04	0.60	2.65	0.00
160	0.00	0.03	0.52	2.33	0.00
180	0.00	0.03	0.47	2.07	0.00
200	0.00	0.03	0.42	1.85	0.00
250	0.00	0.02	0.33	1.45	0.00
300	0.00	0.02	0.26	1.17	0.00
350	0.00	0.01	0.22	0.97	0.00
400	0.00	0.01	0.18	0.82	0.00
450	0.00	0.01	0.16	0.71	0.00
500	0.00	0.01	0.14	0.62	0.00
600	0.00	0.01	0.11	0.49	0.00
700	0.00	0.01	0.09	0.39	0.00
800	0.00	0.00	0.07	0.33	0.00
900	0.00	0.00	0.06	0.28	0.00
1000	0.00	0.00	0.05	0.24	0.00

Table C.8: BSR direct cross sections for excitation from the $1s_5$ metastable to $2p_{10}$-$2p_6$ levels, values in 10^{-16} cm^2. From Zatsarinny and Bartschat [149]. Note the difference in order of magnitude $\mathcal{O}(10^2)$ with the next table.

E (eV)	$2p_{10}$	$2p_9$	$2p_8$	$2p_7$	$2p_6$
E_0	1.265	1.371	1.406	1.474	1.506
1.35	2.48				
1.75	5.28	7.05	14.86	3.01	7.37
1.89	5.37	6.34	12.87	2.87	6.56
2.03	5.55	5.97	12.19	2.62	6.00
2.16	6.12	5.78	12.54	2.42	5.75
2.30	6.38	5.27	12.27	1.97	5.23
2.43	6.86	4.96	12.76	1.73	5.27
2.57	7.78	4.89	13.23	1.67	5.29
2.84	8.53	4.43	14.24	1.18	5.26
3.25	9.84	4.39	16.13	1.01	5.79
3.39	10.21	4.40	16.83	0.94	6.00
3.52	10.51	4.40	17.36	0.88	6.15
3.66	10.78	4.39	17.83	0.84	6.28
3.79	11.04	4.41	18.23	0.80	6.42
3.93	11.28	4.44	18.65	0.78	6.57
4.07	11.50	4.48	19.05	0.76	6.71
4.20	11.69	4.53	19.45	0.75	6.86
4.34	11.90	4.58	19.87	0.75	7.02
4.47	12.08	4.63	20.27	0.74	7.16
4.61	12.27	4.70	20.71	0.74	7.32
4.75	12.44	4.76	21.12	0.74	7.47
4.88	12.61	4.81	21.48	0.74	7.60
5.02	12.77	4.88	21.89	0.74	7.74
5.15	12.93	4.94	22.28	0.74	7.88
5.29	13.09	5.00	22.66	0.75	8.02
6.65	14.31	5.52	26.02	0.76	9.29
8.01	14.99	5.85	28.14	0.77	10.16
9.37	15.24	6.02	29.23	0.77	10.68
10.73	15.22	6.06	29.65	0.76	10.96
12.09	15.03	6.02	29.66	0.75	11.04
13.45	14.75	5.95	29.41	0.74	11.02
14.81	14.42	5.84	28.99	0.72	10.92
16.18	14.07	5.73	28.49	0.71	10.77
17.54	13.71	5.60	27.95	0.69	10.60
18.90	13.37	5.48	27.39	0.68	10.42
20.26	13.04	5.36	26.84	0.66	10.23
21.62	12.71	5.24	26.31	0.65	10.04
22.98	12.39	5.13	25.76	0.63	9.85
24.34	12.10	5.02	25.23	0.62	9.66
25.70	11.82	4.91	24.70	0.61	9.48
32.50	10.40	4.36	22.02	0.54	8.53
39.30	9.12	3.86	19.53	0.48	7.64
46.11	8.06	3.43	17.42	0.43	6.87
52.91	7.18	3.07	15.66	0.39	6.20
59.71	6.44	2.78	14.18	0.35	5.64
66.52	5.83	2.53	12.95	0.32	5.17
73.32	5.32	2.32	11.94	0.30	4.78

Table C.9: BSR direct cross sections for excitation from the $1s_5$ metastable to the $2p_5$-$2p_1$ levels, values in 10^{-18} cm^2. From Zatsarinny and Bartschat [149]. Note the difference in order of magnitude $\mathcal{O}(10^{-2})$ with the previous table.

E (eV)	$2p_5$	$2p_4$	$2p_3$	$2p_2$	$2p_1$
E_0	1.619	2.661	2.763	2.790	2.872
1.75	66.29				
1.89	64.98				
2.03	66.12				
2.16	63.99				
2.30	60.45				
2.43	51.44				
2.57	52.04				
2.84	34.51	35.37	13.97	18.67	
3.25	27.80	24.89	23.71	22.65	8.81
3.39	24.68	23.08	24.69	18.92	7.90
3.52	22.17	21.14	24.72	14.94	6.54
3.66	20.24	19.79	24.83	13.73	6.34
3.79	18.66	19.64	26.79	15.11	7.02
3.93	17.15	18.79	28.55	15.84	7.17
4.07	16.01	18.02	29.46	15.91	7.33
4.20	15.13	17.70	30.08	15.90	7.27
4.34	14.41	16.99	29.98	16.24	7.37
4.47	14.15	16.60	29.40	14.82	6.49
4.61	13.87	16.81	28.31	14.43	6.39
4.75	13.66	16.81	27.40	14.28	6.19
4.88	13.46	16.50	27.02	13.94	5.78
5.02	13.38	16.69	25.53	13.64	5.48
5.15	12.74	16.35	24.50	13.53	5.04
5.29	13.05	16.11	23.61	13.33	4.91
6.65	9.97	13.60	15.53	11.53	2.87
8.01	6.90	11.36	10.99	11.31	1.85
9.37	4.77	9.89	8.13	11.20	1.68
10.73	3.35	9.28	6.64	11.65	1.47
12.09	2.54	8.60	5.54	11.51	1.07
13.45	2.01	7.96	4.73	11.25	1.00
14.81	1.67	7.32	4.17	10.90	0.94
16.18	1.40	6.79	3.72	10.64	0.91
17.54	1.21	6.32	3.31	10.34	0.90
18.90	1.11	6.00	3.00	10.07	0.89
20.26	0.91	5.68	2.80	9.76	0.91
21.62	0.89	5.47	2.83	9.63	0.96
22.98	0.73	5.10	2.41	9.65	0.75
24.34	0.62	4.95	2.20	9.16	0.73
25.70	0.42	4.64	2.06	8.81	0.57
32.50	0.16	3.64	1.49	7.44	0.20
39.30	0.08	2.92	1.18	6.47	0.11
46.11	0.05	2.43	1.00	5.71	0.07
52.91	0.04	2.07	0.89	5.10	0.05
59.71	0.03	1.81	0.87	4.60	0.04
66.52	0.02	1.60	1.05	4.17	0.03
73.32	0.02	1.44	7.01	3.79	0.02

Table C.10: BSR direct cross sections for excitation from the $1s_5$ metastable to the $3p$ levels, values in 10^{-18} cm^2. From Zatsarinny and Bartschat [149].

E (eV)	$3p_{10}$	$3p_9$	$3p_8$	$3p_7$	$3p_6$	$3p_5$
E_0	2.56	2.65	2.66	2.70	2.72	2.73
2.84	30.40	55.67	8.55	53.95	21.47	56.99
3.25	31.72	41.22	8.24	42.10	11.12	67.97
3.39	29.92	36.43	8.22	39.70	10.60	69.31
3.52	29.24	35.27	8.48	36.06	10.23	72.10
3.66	32.56	36.12	8.76	34.31	9.86	72.06
3.79	34.62	36.45	9.02	36.00	9.19	81.20
3.93	36.80	37.12	9.30	36.79	9.16	84.56
4.07	38.95	37.69	9.66	38.36	9.31	86.91
4.20	42.08	39.09	9.98	40.47	9.51	88.20
4.34	45.21	39.70	10.04	40.70	10.14	89.43
4.47	47.93	41.80	10.38	45.38	10.07	90.65
4.61	50.81	43.23	10.44	47.82	10.40	88.98
4.75	53.43	44.51	10.50	49.95	10.51	87.57
4.88	56.03	45.49	10.64	52.50	10.51	87.30
5.02	57.63	46.60	10.69	54.11	10.69	85.22
5.15	59.34	47.54	10.81	56.04	10.64	83.13
5.29	60.72	48.41	10.77	57.79	10.54	81.51
6.65	63.36	48.50	10.69	65.43	7.87	67.72
8.01	57.46	44.50	10.31	65.72	5.75	59.33
9.37	51.32	42.28	9.76	64.78	4.97	53.39
10.73	46.12	39.18	9.17	61.62	4.29	48.89
12.09	41.85	36.33	8.48	58.43	3.77	44.51
13.45	38.00	33.82	8.06	55.17	3.42	40.89
14.81	34.38	31.33	7.53	51.98	2.98	37.82
16.18	31.26	28.99	7.06	48.90	2.77	35.19
17.54	28.60	26.96	6.67	46.14	2.57	32.92
18.90	26.52	25.16	6.29	43.53	2.41	30.89
20.26	24.73	23.83	5.85	41.32	2.25	29.03
21.62	23.73	23.15	5.60	39.55	2.39	27.65
22.98	22.26	21.50	5.19	37.53	2.06	25.61
24.34	21.57	20.77	4.90	36.27	1.91	24.03
25.70	21.02	20.06	4.58	35.04	1.74	22.58
32.50	16.67	16.44	3.49	29.56	1.15	17.10
39.30	12.98	13.41	2.85	24.87	0.90	13.94
46.11	10.50	11.22	2.40	21.30	0.74	12.01
52.91	8.79	9.64	2.07	18.58	0.63	11.01
59.71	7.57	8.44	1.84	16.44	0.55	11.14
66.52	6.63	7.48	1.68	14.69	0.49	9.81
73.32	5.90	6.70	1.60	13.23	0.44	8.25

Table C.11: BSR direct cross sections for excitation from the $1s_5$ metastable to the $3d_6 - 3d'_1$ levels, values in 10^{-16} cm^2. From Zatsarinny and Bartschat [149].

E (eV)	$3d_6$	$3d_5$	$3d'_4$	$3d_3$	$3d_4$	$3d''_1$	$3d'_1$
E_0	1.58	1.60	1.63	1.64	1.72	1.84	1.91
1.75	0.47	1.23	4.22	1.38	0.75		
1.89	0.52	1.73	6.05	2.86	1.86	0.68	
2.03	0.59	2.02	7.20	3.40	2.44	1.36	1.50
2.16	0.56	1.97	7.91	3.40	2.81	1.60	2.07
2.30	0.59	1.94	8.01	3.26	3.02	1.67	2.27
2.43	0.60	1.97	7.93	3.36	3.07	1.76	2.27
2.57	0.58	2.07	8.03	3.49	3.21	1.73	2.37
2.84	0.64	2.04	7.76	3.36	3.30	1.73	2.44
3.25	0.54	1.84	7.33	3.16	3.21	1.59	2.42
3.39	0.52	1.77	7.05	3.05	3.14	1.54	2.41
3.52	0.51	1.72	6.83	2.94	3.04	1.48	2.36
3.66	0.50	1.69	6.71	2.88	2.98	1.43	2.31
3.79	0.48	1.64	6.49	2.80	2.90	1.37	2.26
3.93	0.46	1.59	6.33	2.72	2.81	1.31	2.21
4.07	0.45	1.55	6.19	2.65	2.74	1.27	2.17
4.20	0.44	1.51	6.08	2.59	2.67	1.23	2.15
4.34	0.43	1.48	6.02	2.56	2.61	1.20	2.14
4.47	0.42	1.47	5.93	2.53	2.58	1.18	2.13
4.61	0.42	1.45	5.90	2.51	2.55	1.16	2.14
4.75	0.41	1.43	5.87	2.50	2.52	1.14	2.14
4.88	0.40	1.42	5.85	2.49	2.50	1.13	2.16
5.02	0.40	1.41	5.83	2.48	2.49	1.12	2.18
5.15	0.39	1.39	5.82	2.48	2.47	1.11	2.18
5.29	0.39	1.39	5.80	2.48	2.46	1.10	2.19
6.65	0.38	1.34	5.54	2.42	2.30	0.99	2.19
8.01	0.36	1.27	5.19	2.30	2.11	0.86	2.08
9.37	0.34	1.20	4.86	2.17	1.92	0.74	1.96
10.73	0.33	1.15	4.56	2.01	1.74	0.65	1.81
12.09	0.32	1.10	4.26	1.90	1.59	0.58	1.68
13.45	0.31	1.04	3.98	1.78	1.46	0.52	1.56
14.81	0.29	0.99	3.72	1.67	1.35	0.47	1.45
16.18	0.28	0.93	3.47	1.57	1.24	0.43	1.35
17.54	0.27	0.89	3.24	1.47	1.15	0.40	1.25
18.90	0.26	0.84	3.03	1.38	1.07	0.37	1.17
20.26	0.24	0.79	2.84	1.30	1.00	0.34	1.10
21.62	0.23	0.74	2.67	1.23	0.94	0.32	1.03
22.98	0.22	0.70	2.52	1.17	0.88	0.30	0.98
24.34	0.21	0.66	2.40	1.10	0.84	0.28	0.93
25.70	0.19	0.63	2.27	1.05	0.80	0.27	0.89
32.50	0.16	0.51	1.83	0.85	0.63	0.21	0.71
39.30	0.14	0.43	1.54	0.71	0.53	0.17	0.59
46.11	0.12	0.38	1.32	0.61	0.45	0.15	0.51
52.91	0.11	0.33	1.16	0.53	0.39	0.13	0.44
59.71	0.09	0.30	1.03	0.47	0.35	0.11	0.39
66.52	0.09	0.27	0.92	0.42	0.31	0.10	0.35
73.32	0.08	0.24	0.83	0.38	0.28	0.09	0.32

Table C.12: BSR direct cross sections for excitation from the $1s_5$ metastable to the $3d_2 - 3s'_1$ levels, values in 10^{-18} cm^2. From Zatsarinny and Bartschat [149].

E (eV)	$3d_2$	$3s''''_1$	$3s''_1$	$3s'''_1$	$3s'_1$
E_0	2.09	2.99	3.04	3.05	3.31
2.16	34.84				
2.30	53.59				
2.43	43.53				
2.57	44.18				
2.84	43.19				
3.25	38.71	14.73	18.52	15.24	
3.39	37.24	14.24	26.23	18.24	3.82
3.52	35.80	12.70	32.10	19.30	6.38
3.66	34.00	11.71	30.33	18.92	7.73
3.79	32.64	11.02	28.78	18.20	7.92
3.93	31.54	10.53	27.93	18.14	8.06
4.07	30.59	10.25	27.08	18.15	8.04
4.20	30.16	10.21	25.53	18.00	8.17
4.34	30.23	9.60	23.28	17.42	8.83
4.47	30.15	8.81	21.33	16.44	8.58
4.61	30.29	8.50	20.66	16.27	8.81
4.75	30.60	8.27	20.89	16.23	9.13
4.88	30.82	8.02	21.03	15.91	9.27
5.02	30.94	7.96	21.58	15.75	9.14
5.15	31.03	7.63	20.84	15.40	8.85
5.29	31.08	7.21	20.85	15.00	8.73
6.65	28.56	5.44	19.54	14.04	6.94
8.01	24.59	4.22	18.09	13.04	5.38
9.37	21.09	3.43	16.43	11.80	4.52
10.73	17.95	3.18	15.22	10.59	3.71
12.09	15.46	2.70	13.70	9.75	2.91
13.45	13.59	2.46	12.37	8.86	2.54
14.81	12.08	2.21	11.48	8.13	2.17
16.18	10.89	2.10	10.66	7.48	1.97
17.54	9.95	1.96	9.99	6.95	1.68
18.90	9.10	1.81	9.28	6.51	1.58
20.26	8.40	1.65	8.75	6.11	1.40
21.62	8.18	1.63	8.08	5.78	1.53
22.98	7.51	1.48	7.69	5.40	1.30
24.34	7.29	1.38	7.18	5.08	1.07
25.70	6.64	1.51	7.04	4.99	0.97
32.50	5.05	0.78	4.93	3.35	0.60
39.30	4.10	0.61	4.01	2.68	0.46
46.11	3.45	0.51	3.40	2.23	0.38
52.91	2.98	0.44	2.94	1.91	0.32
59.71	2.61	0.38	2.59	1.66	0.27
66.52	2.32	0.34	2.31	1.47	0.24
73.32	2.09	0.30	2.09	1.31	0.21

Table C.13: BSR direct cross sections for excitation from the $1s_5$ metastable to the other $1s$ levels, values in 10^{-16} cm^2. From Zatsarinny and Bartschat [149].

E (eV)	$1s_4$	$1s_3$	$1s_2$	E (eV)	$1s_4$	$1s_3$	$1s_2$
E_0	0.122	1.132	1.255				
0.257	63.347			⋮	⋮	⋮	⋮
0.393	39.469			4.746	0.819	0.420	0.856
0.529	28.281			4.882	0.787	0.410	0.832
0.665	22.757			5.019	0.757	0.402	0.823
0.801	19.890			5.155	0.731	0.397	0.807
0.937	15.672			5.291	0.699	0.391	0.803
1.073	14.156			6.651	0.573	0.350	0.725
1.209	14.899	4.997	0.000	8.012	0.500	0.307	0.609
1.345	14.145	2.681	5.696	9.372	0.421	0.273	0.533
1.753	5.293	1.423	2.566	10.733	0.343	0.247	0.479
1.889	4.622	1.251	2.294	12.093	0.284	0.224	0.434
2.025	4.062	1.191	2.234	13.454	0.244	0.204	0.398
2.161	3.699	1.193	2.310	14.815	0.215	0.187	0.368
2.297	3.310	1.107	2.248	16.175	0.194	0.173	0.345
2.433	2.941	1.101	2.266	17.536	0.180	0.160	0.328
2.570	2.608	1.007	2.260	18.896	0.166	0.149	0.308
2.842	2.185	0.896	1.970	20.257	0.154	0.141	0.294
3.250	1.685	0.691	1.431	21.617	0.148	0.133	0.274
3.386	1.598	0.659	1.376	22.978	0.125	0.126	0.258
3.522	1.496	0.650	1.374	24.339	0.108	0.121	0.238
3.658	1.385	0.630	1.361	25.699	0.093	0.113	0.211
3.794	1.287	0.587	1.233	32.502	0.048	0.083	0.130
3.930	1.201	0.547	1.156	39.305	0.032	0.065	0.099
4.066	1.120	0.512	1.083	46.108	0.024	0.055	0.081
4.202	1.049	0.482	1.003	52.910	0.019	0.047	0.069
4.338	0.991	0.466	0.956	59.713	0.016	0.041	0.060
4.474	0.916	0.452	0.937	66.516	0.014	0.037	0.053
4.610	0.862	0.433	0.891	73.319	0.012	0.033	0.047

Table C.14: Experimental apparent cross section (in 10^{-18} cm^2) for $1s_5 \rightarrow 2p$ transitions. From Jung et al. [56].

E (eV)	$2p_5$	$2p_6$	$2p_7$	$2p_8$	$2p_9$	$2p_{10}$
1.50	0.2	1.8	2.0	0.4	3.0	4.5
1.75	0.4	4.9	3.6	6.8	3.7	6.9
2.00	0.7	9.1	5.7	15.0	5.8	6.7
2.50	1.2	11.0	5.4	20.0	7.7	7.7
3.00	0.8	13.0	4.7	25.0	9.9	11.0
4.00	0.5	15.0	3.2	32.0	10.0	13.0
5.00	0.4	15.0	2.9	31.0	9.1	14.0
6.00	0.3	15.0	2.2	34.0	8.4	15.0
7.00	0.3	15.0	1.6	34.0	7.4	15.0
8.00	0.3	14.0	1.4	33.0	6.4	14.0
12.00		14.0		32.0		
17.00		12.0		31.0		
25.00		10.0		25.0		
50.00		7.1		15.0		
75.00		4.9		13.0		
100.00		4.3		10.0		
150.00		3.6		7.6		
225.00		2.6		6.0		
325.00		1.9		4.1		
400.00		1.6		3.5		

Table C.15: Experimental apparent cross section (in 10^{-18} cm^2) for $1s_5 \rightarrow 3p$ transitions. From Jung et al. [57].

E (eV)	$3p_5$	$3p_6$	$3p_7$	$3p_8$	$3p_9$
1.00	3.0				
1.25	4.0				
1.50	0.4	0.0	2.6	11.0	
1.75	0.0	7.0	4.0		
2.00	0.5	2.0	0.8	7.0	2.0
2.25	3.0	1.0	3.0		
2.50	0.8	1.0	4.5	9.0	2.0
2.75	4.0	8.0	7.0		
3.00	0.8	12.0	7.6	41.0	25.0
3.25	28.0	91.0	48.0		
3.50	7.8	40.0	24.6	102.0	53.0
3.75	40.0	107.0	54.0		
4.00	15.6	43.0	46.4	118.0	43.0
4.25	37.0	117.0	44.0		
4.50	15.7	35.0	33.5	120.0	40.0
4.75	34.0	125.0	33.0		
5.00	13.0	35.0	25.1	110.0	34.0
5.25	37.0	119.0	35.0		
5.50	9.3	37.0	17.3	123.0	35.0
5.75	35.0	108.0	35.0		
6.00	8.9	36.0	20.1	124.0	28.0
6.25	35.0	122.0	35.0		
6.50	9.7	33.0	24.9	117.0	32.0
6.75	37.0	131.0	31.0		
7.00	5.4	37.0	24.3	117.0	30.0
7.25	35.0	116.0	27.0		
7.50	8.9	33.0	22.4	112.0	29.0
7.75	34.0	120.0	33.0		
8.00	5.4	35.0	14.4	110.0	32.0
8.25	33.0	120.0	30.0		
8.50	7.1	34.0	20.3	122.0	32.0
8.75	33.0	126.0	26.0		
9.00	7.6	34.0	6.8	117.0	34.0
9.25	33.0	112.0	29.0		
9.50	5.8	32.0	13.3	118.0	31.0
9.75	29.0	29.0			
10.00	35.0	3.6	30.0		
10.25	33.0				

Table C.16: Cross section for ionization from the $1s_5$ level (in 10^{-16} cm^2). Data from [133] via [102].

E (eV)	Xe^+	E (eV)	Xe^+
3.44	0.00	⋮	⋮
6.71	9.55	37.66	5.73
8.27	11.44	53.66	4.23
8.67	11.78	77.50	3.00
9.41	11.98	98.16	2.33
10.24	11.97	135.20	1.65
11.54	11.88	222.40	0.90
12.13	11.73	500.00	0.46
16.28	10.57	1000.00	0.26
27.84	7.49		